Dating Early Archean partial melting events: insights from Re-Os dating of micrometric Os-minerals from Kalahari Craton mantle xenoliths

Dissertation
zur
Erlangung des Doktorgrades (Dr. rer. Nat.)
der
Mathematisch-Naturwissenschaftlichen Fakultät
der
Rheinischen Friedrich-Wilhelms-Universität Bonn

vogelegt von
Ashlea N. Wainwright
aus Melbourne

Bonn,
Dezember 2014

Angefertigt mit Genehmigung der Mathematisch-Naturwissenschaftlichen Fakultät der
Rheinischen Friedrich-Wilhelms-Universität Bonn

1. Gutachter: Prof. Dr. Ambre Luguet
2. Gutachter: Dr. Raúl Fonseca

Tag der Promotion: 20.02.2015

Erscheinungsjahr: 2015

Contents

List of Tables

List of Figures

Abstract

Our understanding on the formation, mechanism and timing of the formation of the Earth's earliest continents hinges on obtaining robust and accurate ages of melt depletion and lithosphere stabilisation. The Re-Os geochronometer has been used to obtain such information. However, recent advances indicate that metasomatism can impact on the signatures obtained. This thesis utilises the combination of Re-Os and highly siderophile element (HSE) systematics to accurately assess the impact secondary mineralisation has on the Re-Os ages determined. A suite of samples from the Kalahari craton (Kaapvaal and Zimbabwe cratons) are investigated in terms of their metasomatic overprint and Re-Os systematics. The sub-suite of peridotites from the Kaapvaal craton are first analysed for whole-rock major and trace elements, Re-Os and HSE systematics. The peridotites were also analysed for the $^{187}Os/^{188}Os$ compositions at the single grain base metal sulphide (BMS) and platinum-group mineral (PGM) scale. These analyses indicate that the Kaapvaal peridotites have experienced high degrees of melt depletion followed by variable and significant enrichment in the incompatible trace elements and HSE. The enrichment of HSE led to the precipitation of metasomatic BMS which impact on the Re-Os ages determined. As such, the whole-rock and single grain BMS T_{RD} (rhenium depletion model age) indicate that the mantle was pervasively metasomatised as early as 3.2 Ga. Nano-particle PGM (Pt-alloys) with radiogenic $^{187}Os/^{188}Os$ (0.1294-0.1342) were found included within unradiogenic BMS ($^{187}Os/^{188}Os$ 0.1066-0.1084). This signifies that the PGM formed in the presence of Re and evolved to high $^{187}Os/^{188}Os$ compositions over a long time scale. The Os composition of the Pt-alloys, combined with their nano-particle nature and the Os dichotomy with the host BMS signifies that the Pt-alloys formed in a HSE-Si-rich melt. This provides further evidence for the metasomatic overprinting of the Kaapvaal peridotites.

Despite the high degree of metasomatism experienced by the Letlhakane peridotites (Zimbabwe craton), as evidenced by their re-enriched HSE-Se-Te systematics, single grain BMS preserve evidence of partial melting events. The $^{187}Os/^{188}Os$ analyses of the BMS provide ages >2.5 Ga older than the whole-rock. The oldest BMS T_{RD} age of 3.7 Ga is preserved in a metasomatic BMS associated with secondary clinopyroxene and phlogopite. The attainment of an Eoarchean age from a metasomatic BMS suggests that the metasomatic fluid is able to entrain or nucleate on residual BMS. As such, the obtained ages reflect a mixing between the two different Os signatures. Whereas older ages reflect the dominance of

the residual PGM on the bulk Os composition, younger ages are due to the control from the metasomatic melt. The 3.7 Ga T_{RD} obtained age also pushes the age of initial stabilisation of the Zimbabwe lithosphere to within the age of the oldest crustal rocks in this region.

The combined results of the Letlhakane and Kaapvaal peridotites indicate that whilst the Re-Os system can be affected by the metasomatic addition of BMS, the combination of HSE and Re-Os at the whole-rock and micro-scale can still resolve geologically significant ages.

Chapter 1

Introduction

1.1 The Early Earth

Understanding the evolution of the Earth is an important constraint for our understanding of the present day mantles geochemical composition. Constraining the timing and extent of partial melting within the Early Earth as well as constraining the implications of accretion on the early mantle will further our understanding of how the Earth was created, how it evolved to its present form, and how to fully interpret and understand modern day mantle signatures. The Early Earth is known as the Hadean era, spanning the time from the beginnings of the Earth at 4.56 Ga to the age of the first rocks currently preserved (3.8Ga). The subsequent era is the Archean which extends to 2.5 Ga, when life is first recorded. These two eras were witness to the formation of the first continents, oceans, and potentially plate tectonics and life (cf. Harrison, 2008). However our understanding of this time span, especially anything older than 3.5 Ga, is limited due to the scarcity of samples available. With only two known examples of Hadean rocks preserved on today's Earth (Bowring et al., 1989; O'Neil et al., 2008).

Our understanding of the early Earth is highly limited by the scarcity of samples available, and by the complex history ancient samples have faced. Therefore, geochemical systems that can trace primary processes are invaluable tools. The Re-Os system is one such tool, as it can be utilised to date the age of formation of the oldest lithosphere (crust + the upper elastic section of the mantle) and hence further our understanding of the formation of the earliest continents (cf. Walker et al., 1989). The most stable parts of the Earth's lithosphere are cratons, which are generally found in the interiors of continental plates and have been stable for hundreds of millions of years. The remnants of the Earths earliest continents are found today on Archean cratons. Archean cratons are currently distributed across the Earth (Figure 1.1), and have been the subject of extensive exploration. Nonetheless, constraining the timing of the stabilisation of the lithosphere – and hence formation of the Earth's earliest continents – has not been achieved, due to apparent crust-mantle decoupling (Carlson and Moore 2004; Griffin et al., 2004; Schmitz et al., 2004; Luguet et al., 2009). This is mainly due to the impact of re-enrichment that has obscured the primary compositions of the sub-cratonic mantle. Therefore, geochronological studies of mantle samples need to include a complete and thorough investigation of the geochemical

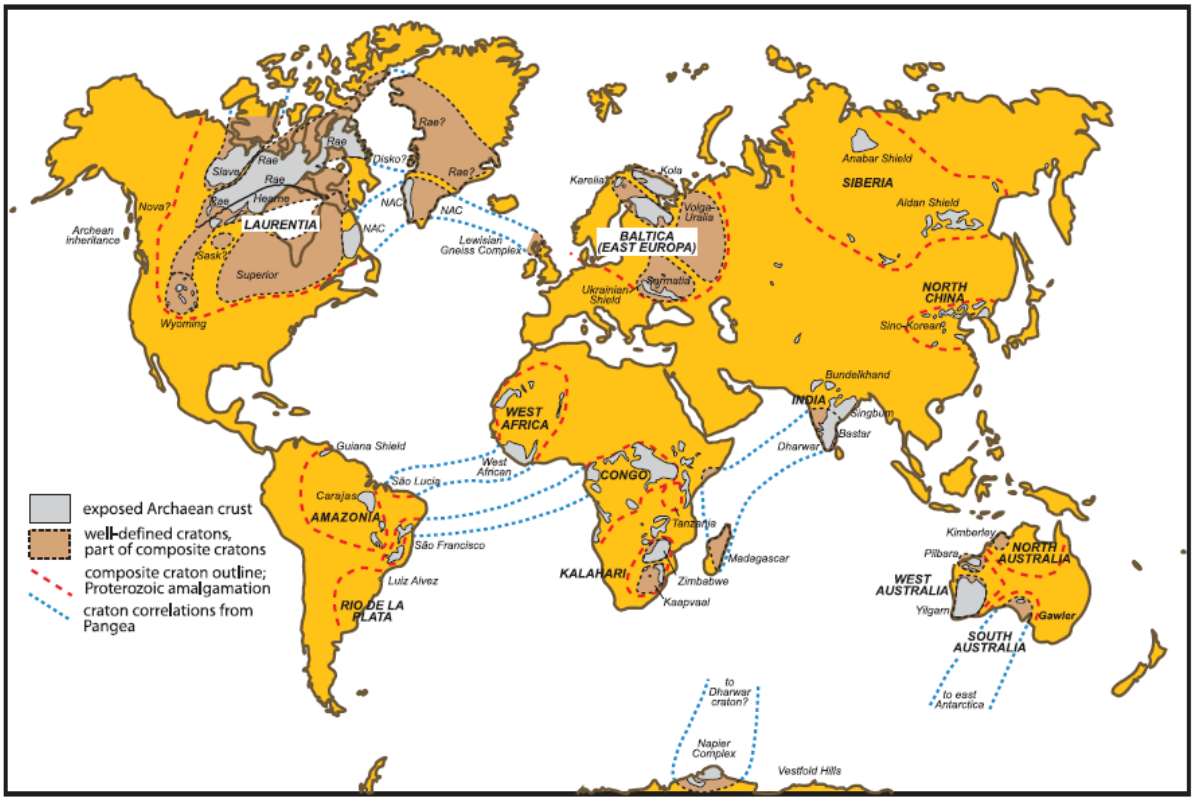

Figure 1.1. The distribution of Archean cratons on Earth, from Pearson and Wittig (2008). Well-defined cratons are in brown, exposed Archean crust is indicated in grey, red lines indicate composite cratons that were amalgamated during the Proterozoic, blue lines are the correlations of cratons for the super-continent Pangea. NAC – North Atlantic Craton.

history of the sample so that robust constraints can be applied to the geochronological data obtained.

The Kalahari Craton of southern Africa (Figure 1.2) is one of the most widely researched Archean cratons on Earth, due to the volume of kimberlite borne mantle xenoliths (cf. Boyd, 1989). The Kalahari craton is composed of two separate Archean cratons that collided during the Mesoarchean. The northern craton, situated predominately in Zimbabwe, is the Zimbabwe Craton (Figure 1.2). Whilst to the south, predominantly in South Africa, is the Kaapvaal craton (Figure 1.2). The xenoliths from the Kalahari Craton are diverse in their composition and rather large (up to 100's cm; cf. Boyd and Nixon, 1978; Smith, 1983; Walker et al., 1989). Despite the well-studied nature of Kalahari xenoliths, a disparity in the ages obtained is evident, with a mismatch between mantle and crustal ages (2.9 vs 3.7 Ga cf. Carlson and Moore, 2004). If the crust and mantle are genetically linked this is unexpected. Recent advances in techniques for determining Re-Os ages in peridotite xenoliths have seen the advent of Eoarchean and Hadean ages being determined in the region, but not to the extent expected. It is therefore required that the Re-Os systematics of the xenoliths be looked

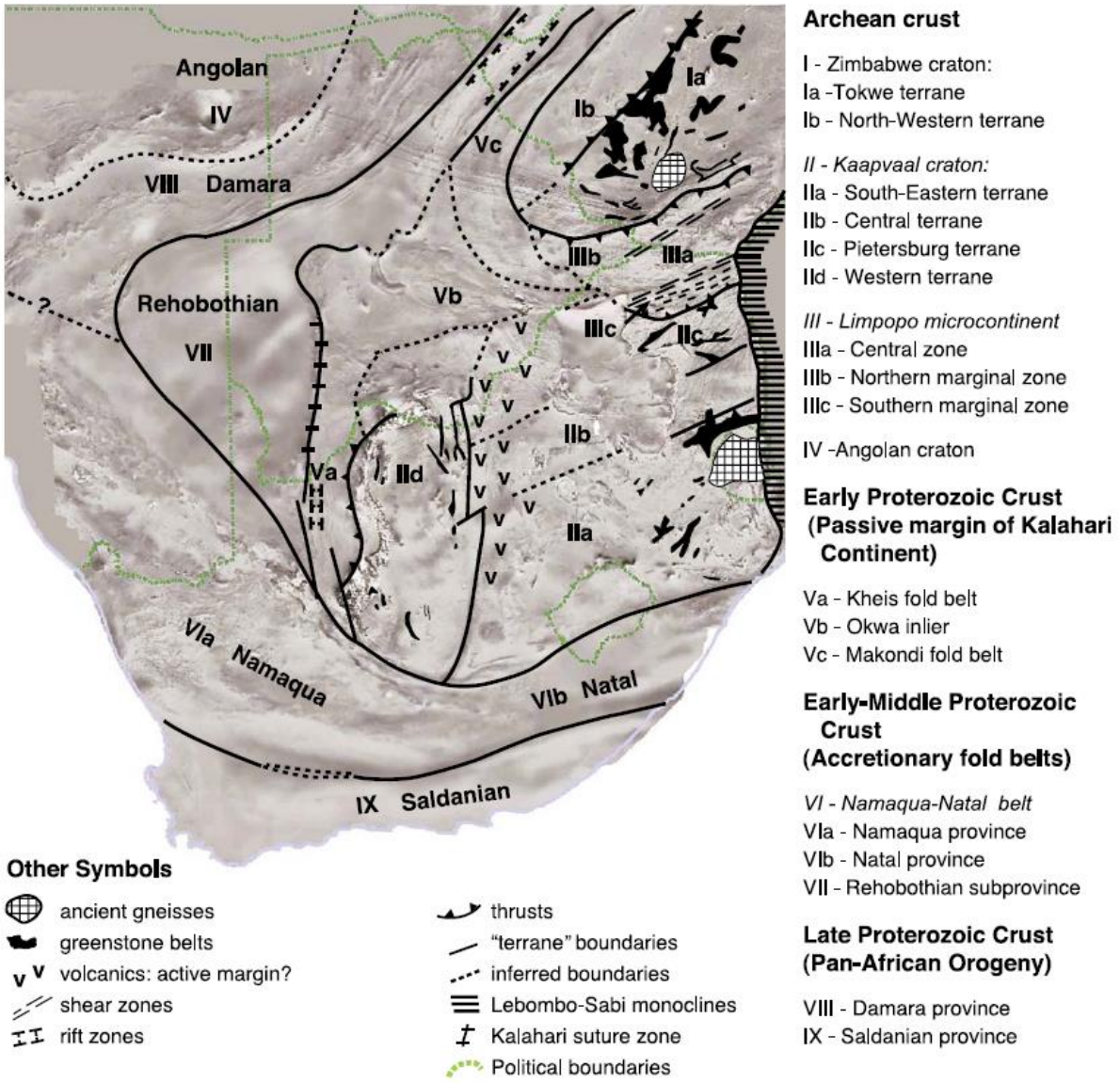

Figure 1.2. The extent and structural units of the Kalahari craton, southern Africa, from Griffin et al. (2003).

at in more detail, in an attempt to further constrain the timing of stabilisation and the mechanism for the formation of Archean continents.

There are two main models for the formation of cratonic crust and its highly depleted mantle, with each having a different implication for the variation in the age of the mantle. The first model utilises a mantle plume, i.e. a rising funnel of hot mantle from either the asthenosphere or the core-mantle boundary. As the plume ascends and is capped by the lithosphere the plume head bulges out and begins to melt the surrounding mantle, which rises to the surface and begins the formation of the cratonic crust (cf. Lee et al, 2011). Due to the difference in temperature between the mantle plume and the surrounding mantle, the surrounding mantle is very quickly consumed and depleted, this leads to a highly depleted lithosphere, with a homogenous distribution of ages with depth (Figure 1.3; Aulbach, 2012).

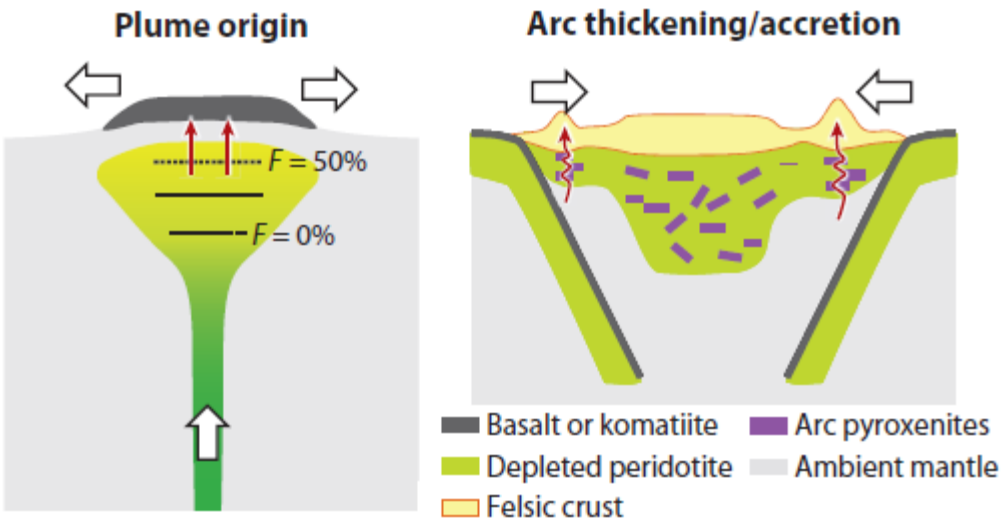

Figure 1.3. Schematic drawing of the two models for the formation of continental mantle, plume origin or arc thickening/accretion, modified from Lee et al. (2011). *F*, average degree of melting, red arrows indicate extraction of partial melt, white arrows are direction of motion.

The second model can be broken into two phases, the first being the creation of the crust at an arc setting. With the depletion of the mantle due to the down-welling of a subducting slab, causing the formation of continental arcs. The continued subduction and plate tectonics leads to the accretion and stacking of these arcs, which will thicken to the point that it becomes a stable continent (Figure 1.3; Pearson and Wittig, 2013). This stacking and accretion of the arcs will create a lateral and vertical variation in mantle ages. The lateral and vertical distribution of mantle ages in cratonic lithosphere enables the differentiation of these two models. As such, the robust determination of the age of stabilisation of Archean lithosphere provides an opportunity to determine the mechanism for the formation of the Earth's earliest continents.

1.2 Re-Os – The Basics

The Re-Os decay system functions via the β-decay of ^{187}Re to ^{187}Os over a half-life of 42 billion years. Despite this relatively long half-life, the large abundance of ^{187}Re (62.2% of all Re isotopes) compared to the very small abundance of ^{187}Os (1.96% of all Os isotopes) ensures that even the presence of a small amount of Re will create a large variation in the amount of ^{187}Os over time.

The Re-Os decay system is a powerful tool for dating mantle melting events due to the different chemical affinities of the parent and daughter isotopes. Whilst both elements are considered to be Fe-loving (siderophile), they behave differently during mantle melting. As a

melt is produced, Re will readily partition into the melt (i.e. it is incompatible in the residue) whilst the Os will stay within the residue (i.e. it is compatible in the residue). This creates a natural fractionation of the parent from the daughter over time and creates a Re-depleted unradiogenic mantle and a Re-enriched radiogenic crust. Importantly, it requires 15-20% of partial melting at depth to extract all of the Re from the rock into the melt (Fonseca et al., 2011); this complete extraction of Re effectively locks in the ^{187}Os content of the residual highly depleted rock (e.g. harzburgite) allowing us to calculate the age of partial melting of the residual rock.

For the determination of how radiogenic a sample is, the measured ^{187}Os content of the sample is compared to a stable isotope i.e. an isotope that is not created or destroyed by radioactive decay and has a constant naturally occurring content. For the Re-Os system the ^{188}Os isotope is utilised, so all Os compositions are reported in the format: ^{187}Os/^{188}Os. A ^{187}Os/^{188}Os composition is considered to be radiogenic when it is above the present day assumed mantle composition of 0.1296 (Becker et al., 2006), if it is below this number then it is unradiogenic.

The ages determined for mantle rocks using the Re-Os system in this thesis are in a model age format, where an age is deduced from a previously constrained parameter. For the Re-Os system the parameter is either meteorites (CI-chondrite) or primitive mantle. As such, the initial ^{187}Os/^{188}Os composition of the Earth has been calculated from meteorites and mantle rocks (Smoliar et al., 1996); from these the initial ^{187}Re/^{188}Os composition has also been calculated. Through the combination of these ratios it is possible to calculate a mantle or chondrite evolution line for the ^{187}Os/^{188}Os composition with time (see Figure 1.4 and eq. 1). This mantle evolution line gives the ^{187}Os/^{188}Os composition of the mantle at each point over the history of the Earth, which is then utilised to calculate model ages. The equation requires unradiogenic ^{187}Os/^{188}Os compositions to calculate an age, therefore anything with a radiogenic composition is said to give a "future age", as the mantle has not yet evolved to that composition. There are three different types of model ages used for Re-Os geochronometry. The first is a standard model age and is referred to as the "T_{MA}" (see equation 2).

$$\left[\frac{^{187}Os}{^{188}Os}\right]_{CHON} = \left[\frac{^{187}Os}{^{188}Os}\right]_{i} - \left[\frac{^{187}Re}{^{188}Os}\right]_{CHON} \times \left[e^{\lambda t} - 1\right] \qquad \text{Eq. 1}$$

$$T_{MA} = \frac{1}{\lambda}\ln\left[1 + \frac{\left(\frac{^{187}Os}{^{188}Os}\right)_{CHON} - \left(\frac{^{187}Os}{^{188}Os}\right)_{SMP}}{\left(\frac{^{187}Re}{^{188}Os}\right)_{CHON} - \left(\frac{^{187}Re}{^{188}Os}\right)_{SMP}}\right] \qquad \text{Eq. 2.}$$

Where *i* refers to the initial composition of the Chondrite, CHON is the present day chondritic composition, SMP is the sample measured ratios and λ is the decay constant for the Re-Os system ($\lambda = 1.666 \times 10^{-11}$, Smoliar et al., 1996).

In the T_{MA} calculation, any Re contained within the sample is assumed to have been there since the melting event being dated, i.e. not all of the Re was removed due to partial melting. By determining the amount of Re in the sample it is possible to determine how much ^{187}Os has been added to the sample over time due to the decay of ^{187}Re, as this would occur at a constant rate, enabling a decay line to be calculated (Figure 1.4). Equation 2 above calculates at what point the Os composition in the sample intersects the mantle evolution line and subsequently the age related to this composition. It is then inferred that the calculated composition was the $^{187}Os/^{188}Os$ composition of the mantle at the time of melting and therefore correlates with a given age determined from the mantle evolution line (Figure 1.4); this is the T_{MA} age.

However, since cratonic mantle rocks have generally experienced a high degree of melting (i.e. >20%), they would therefore no longer host any Re (cf. McDonough, 1994; Reisberg and Lorand, 1995). Therefore, any Re within the sample must have been added to the sample at a later point in time. As such, there are two other model ages that can be used to calculate a more conservative estimate on the age of depletion: "rhenium depletion (T_{RD})" and "rhenium depletion eruption (T_{RDerup})". To calculate a T_{RD} age it is assumed that all of the Re has been removed from the sample via the melting event and that there has been no in-growth of ^{187}Os over time. In this scenario the model age equation becomes:

$$T_{RD} = \frac{1}{\lambda} \ln \left[1 + \frac{\left(\frac{^{187}Os}{^{188}Os}\right)_{CHON} - \left(\frac{^{187}Os}{^{188}Os}\right)_{SMP}}{\left(\frac{^{187}Re}{^{188}Os}\right)_{CHON}} \right] \qquad \text{Eq. 3}$$

Essentially, in this equation the measured $^{187}Os/^{188}Os$ composition of the sample is considered constant up to the intersection with the mantle evolution line (Figure 1.4). As in the T_{MA} model age, the intersection is inferred to be the age of the sample. The T_{RDerup} model age is a hybrid of the T_{MA} and T_{RD} model ages, in this scenario it is assumed that any Re in the sample was added when the sample entrained within a melt and brought to the surface. It has been shown that when the melt brings the sample to the surface, there is an interaction between the melt and peridotite, and incompatible elements can be added to the peridotite in variable amounts (cf. Boyd 1989, Hawkesworth et al., 1990) Therefore, any in-growth of ^{187}Os is assumed to only have occurred since the time of eruption of the melt. The amount of ^{187}Os addition is calculated as in a T_{MA} model age, but only until the age of eruption.

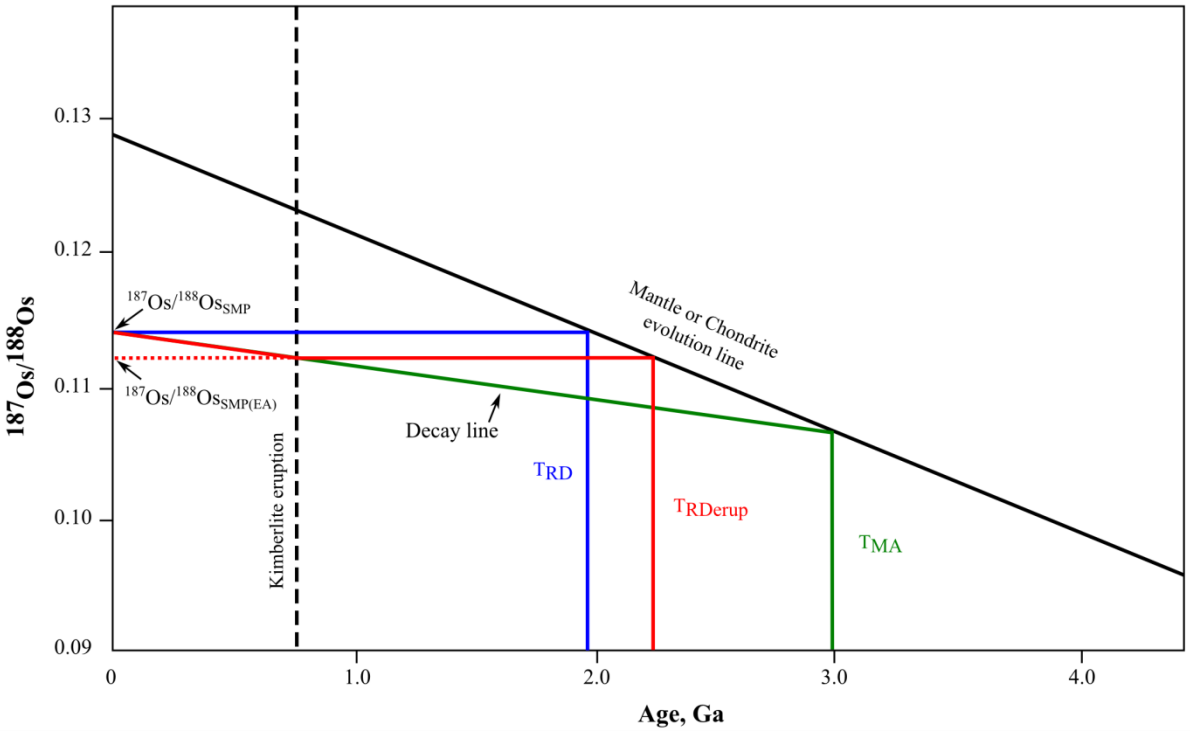

Figure 1.4. Schematic representation of the equations used for the calculation of Re-Os model ages, showing differences in age for the same sample using the three different model age methods. Black line is the chondrite or mantle evolution line (depending on which starting composition is utilised), blue line is calculation of T_{RD} (Rhenium depletion model age), red line is T_{RDerup} (rhenium depletion eruption model age) and green line is T_{MA} (Re-Os model age). Black dashed line represents age of fictional kimberlite eruption, used to calculate the T_{RDerup}. Red dotted line represents calculation of $^{187}Os/^{188}Os_{SMP(EA)}$ for calculation of T_{RDerup}.

Therefore, first a correction for the in-growth of $^{187}Os/^{188}Os$ since the time of eruption must be calculated, this is denoted the SMP(EA) (Eq. 4). This is then substituted into Eq. 3 for the $(^{187}Os/^{188}Os)_{SMP}$. After the slope is calculated for the in-growth the equation assumes a constant $^{187}Os/^{188}Os$ until the intersection with the mantle evolution line, as for the T_{RD} model age, and the age is determined (Figure 1.4).

$$\left[\frac{^{187}Os}{^{188}Os}\right]_{SMP(EA)} = \left[\frac{^{187}Os}{^{188}Os}\right]_{SMP} - \left[\frac{^{187}Re}{^{188}Os}\right]_{SMP} \times \left[e^{\lambda t} - 1\right] \qquad \text{Eq. 4}$$

The three different model ages provide a range of ages, of which the T_{MA} gives a maximum age and the T_{RD} a minimum age. Comparing how far apart the different ages are, can be useful for determining how robust the model ages are. When they span a rather narrow band (e.g. <500 m.y.) the ages are considered fairly well constrained and the T_{MA} is not a large over estimation and the T_{RD} is not a large underestimation. This signifies that the sample has not experienced a high degree of re-enrichment of Re. However, when the ages span a larger time frame (i.e. >500 m.y.) the sample has more than likely experienced a large

degree of re-enrichment of Re and it is therefore considered more appropriate to refer to the more conservative T_{RD} age estimate, which is always a minimum age.

A further constraint on the degree of re-enrichment of Re is by combining Re-Os model ages with highly siderophile element (HSE: Os, Ir, Ru, Pt, Pd, Re) concentration systematics. The HSE elements all behave as siderophile and chalcophile elements, but they have slightly different compatibilities during partial melting, with the compatibility in the residue of Os=Ir=Ru>Pt>Pd>Re (c. Lorand et al., 2013). When these concentrations are normalised to chondrite it is possible to obtain a depletion profile (Figure 1.5). For cratonic peridotitic rocks a negative slope from Ru to Re is expected, as the peridotite will have been highly depleted in these elements (Figure 1.5). Therefore, when a formerly-depleted peridotite has been re-enriched by a melt or fluid, the slope (pattern) will either be kinked upwards at the end, have become flat or even have a positive slope (Figure 1.5). When these patterns are identified at the whole-rock scale it can be used to infer that the Re-Os ages will have been disturbed by the addition of Re and other HSE at some point in the past, and that determined Re-Os ages may not be well constrained.

Due to the chemical affinities of both Re and Os, but specifically Os, the chronometer faces a number of difficulties. Osmium changes its chemical behaviour depending on what other elements are available. When S is still present, Os acts as a chalcophile element and will partition into sulphides. However, if the system is deficient in S, Os becomes siderophile and will partition into metal alloys or create its own alloys with the other HSE (most commonly Ir). These alloys are generally quite small and heterogeneously distributed throughout a rock and will be present in mantle samples as a minor/trace phase. Therefore, the Re-Os systematic of the sample is controlled by these single phases (sulphides and Os-bearing alloys) and a large amount of homogenised sample must be used to obtain reproducible results.

However, sulphides and alloys do not only form in the mantle due to partial melting, they can also be formed via a process called metasomatism. Metasomatism in the cratonic mantle is the process where a melt and/or fluid percolates through a prior depleted section of mantle and re-enriches the area in the incompatible elements, essentially partially undoing the effects of partial melting. The enrichment can be achieved in a number of ways: 1) The metasomatising agent can deposit new minerals that were not present in the rock e.g. in a clinopyroxene-free harzburgite the metasomatising agent can deposit clinopyroxene through enrichment in Ca. 2) The metasomatising agent may also cause a breakdown in the constituent minerals due to changing the redox conditions e.g. garnet + fluid = clinopyroxene

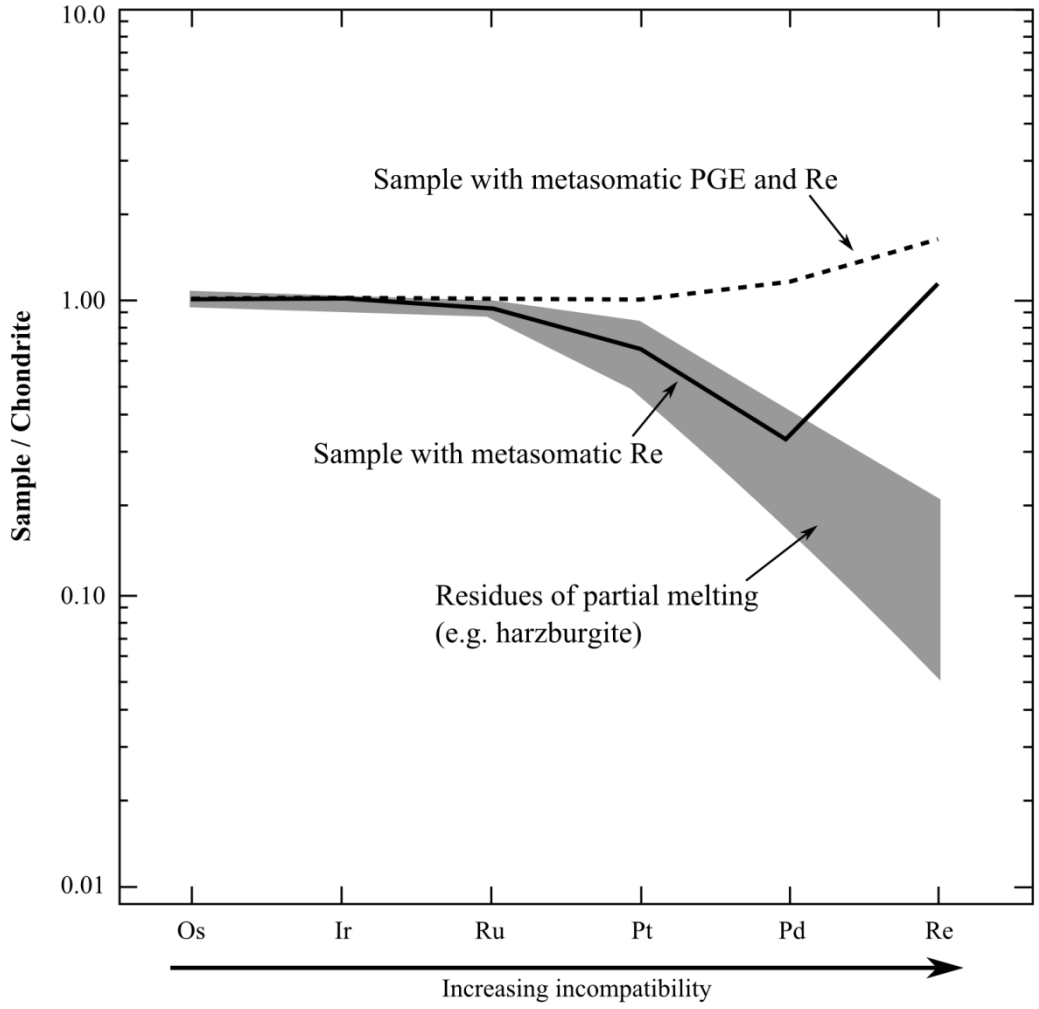

Figure 1.5. Systematics of the highly siderophile elements. Sample concentrations normalised to chondrite. Elements increase in incompatibility from Os to Re, therefore residues of partial melting will be depleted in Re over Os. Grey area represents expected pattern for residues of partial melting e.g. unaltered harzburgite. Black line represents a sample that has undergone metasomatism and Re-enrichment. Black dotted line is a sample that has experienced a high degree of re-enrichment in the PGE and Re.

+ phlogopite + spinel. The metasomatising agent may also deposit secondary sulphides and alloys, and due to the incompatibility of Re, it is likely that these secondary sulphides will be enriched in both Re and ^{187}Os. Therefore, when the whole-rock $^{187}Os/^{188}Os$ composition is measured in a sample that has experienced metasomatism, the composition is actually a mixture of the unradiogenic Os composition of the primary minerals and the radiogenic minerals formed from metasomatism. Therefore, the whole rock Re-Os systematics should be applied to samples with a detailed understanding of the metasomatic history.

More accurate and meaningful data can be obtained from single sulphide and alloy minerals. To date, the majority of Re-Os analyses in single minerals have been obtained through the use of laser ablation mass spectroscopy (LAMS; cf. Griffin et al., 2004). In this

technique, the mineral of interest is exposed in a section of the rock and then measured *in situ* by LAMS. In this thesis, I utilise a different technique that extracts the sulphide from the rock, the sulphide is subsequently dissolved so that Os can be extracted and analysed by more conventional means with a Thermal Ionisation Mass Spectrometer (TIMS). This technique was used due to a number of drawbacks with the LAMS technique, which are outlined below.

Firstly, within a single sulphide grain, multiple compositions can be present with various amounts of Fe-Ni-Cu. These different sulphide compositions all partition Re and Os differently, resulting in a heterogeneous $^{187}Os/^{188}Os$ composition across the sulphide. Therefore, when the LAMS method is used, only a part of the sulphide is analysed potentially resulting in a bias in the $^{187}Os/^{188}Os$ composition. It is therefore important to analyse as much of the sulphide as possible, preferably the entire grain. The extraction procedure used in this thesis also does not recover the entire sulphide, on average approximately 50% is removed and analysed. The second issue with the LAMS technique is that if the sulphide contains any Re, the amount of mass 187 measured will be mainly ^{187}Re, and a mass correction calculation needs to be used to accurately determine the amount of ^{187}Os. In samples with a high $^{187}Re/^{188}Os$ (i.e. > 0.5) this calculation will produce a large error so that the resulting $^{187}Os/^{188}Os$ composition can be over-corrected (Nowell et al, 2008). N-TIMS does not face this issue as Os and Re have been chemically separated prior to the analysis via micro-distillation of the Os (Pearson et al., 1998). Finally, the LAMS method requires a sulphide of at least 30 µm to enable a laser spot size of 15 µm diameter, which is unusual in cratonic peridotites as they have generally undergone >25% partial melting, which should extract all of the S from the residue (cf. Pearson et al., 2004). The sulphide extraction method does not have a size limit, with samples smaller than 1 µm analysed in this study.

1.3. Outline of this thesis

This thesis aims to add further constraints to the topics discussed in the previous two sections, this will be achieved through the utilisation of new and novel techniques as well as by adding new, critical, information to the already extensive database on Kalahari peridotites. In Chapter 1 a suite of 22 peridotites from the Kaapvaal Craton are analysed over a number of scales. Firstly, the combination of petrographic observations and whole-rock major and trace elements analysis are used to constrain the type and extent of depletion and enrichment the peridotites have undergone. The peridotites are also investigated for their whole-rock Re-Os and HSE systematic – this will be only the second study to combine these two parameters in the Kaapvaal Craton. The insights gained into the peridotites metasomatic history from the

major and trace elements enables a more complete understanding of the Re-Os and HSE systematics seen. Therefore, an accurate and geologically significant history can be detailed for these samples. The addition of analyses of single grain BMS for $^{187}Os/^{188}Os$ compositions adds a further constraint to the whole-rock information observed and provides a deeper understanding of the pervasive metasomatism that has affected these peridotites. This chapter concludes that the Re-Os systematics of the Kaapvaal peridotites has been systematically altered since an initial depletion event, and that as such, the Re-Os ages obtained are not indicative of partial melting events but rather of metasomatism of the Kaapvaal lithosphere.

Chapter 2 provides a further look at the Kaapvaal peridotites by investigating a single xenolith at the ultra-micron scale. Two separate BMS within a single Kaapvaal peridotite were found to host platinum-group mineral (PGM) inclusions. Similar inclusions have been documented in cratonic peridotites (Alard et al., 2000) but they have never been individually investigated for their Re-Os composition due to their sub-micron size. This study uses a new and novel technique that allows for the extraction of these minerals via focused-ion beam, the minerals are then investigated either via transmission electron microscopy or through digestion and analysis for $^{187}Os/^{188}Os$ and HSE compositions. The analysis of the PGM inclusions, the host BMS and the whole-rock provides a unique opportunity to investigate the source of these minerals as well as their impact on the Re-Os and HSE systematics at the mineral and whole-rock scale. The results of these analyses indicate that these sub-micron inclusions constitute a significant control on the whole-rock HSE systematics, and that the PGM inclusions, and therefore the BMS, are of a metasomatic origin that most likely formed in a silicate melt at least 3.1 Ga. This infers that the Kaapvaal peridotites had undergone extensive partial melting prior to 3.1 Ga, therefore the Kaapvaal lithosphere stabilisation age is much older than currently accepted.

The third and final chapter in this thesis investigates how extensive metasomatism impacts on the Re-Os of peridotites. This is achieved through the investigation of single grain BMS for $^{187}Os/^{188}Os$ compositions in peridotites from the Letlhakane kimberlite. The three peridotites used in this chapter show a steady increase from cryptic metasomatism (i.e. enrichment in the incompatible trace elements) to minor modal metasomatism (i.e. addition of minerals) to significant modal metasomatism. The degree of metasomatism is coupled with enrichment in the amount of BMS within the peridotite, as well as with increasing $^{187}Os/^{188}Os$ compositions. Twelve BMS from these peridotites are analysed for their Os compositions, the results show that even in the most pervasively metasomatised peridotite, highly depleted $^{187}Os/^{188}Os$ compositions are preserved that provide T_{RD} ages up to 2.5 Ga older than the

whole rock. This signifies that the Re-Os system is robust in the face of significant metasomatism and that peridotites that would not normally be investigated can still provide geologically relevant information. The oldest ages obtained within this study also push the age of initial stabilisation of the Zimbabwe Craton back towards the oldest crustal age, inferring that there is no crust-mantle decoupling in this region.

The scientific information obtained in this thesis show that the Re-Os and HSE systems can be pervasively altered at the whole-rock scale through the addition of metasomatic BMS and PGM. However, the combination of Re-Os and HSE systematics details how robust and geologically significant the geochronological information is. Most importantly, this study shows that the investigation of single grain Os-bearing minerals will provide information about the partial melting history and lithosphere stabilisation age of the craton, as well as the extent and type of metasomatism that has affected the host peridotites.

Chapter 2

Peridotite xenoliths from the Kaapvaal craton: Whole-rock Re-Os and HSE systematics

2.1. Introduction

The highly siderophile elements (HSE: Os, Ir, Pt, Pd, Re) are powerful tracers of melt depletion and metasomatic addition to mantle peridotites (Alard et al., 2000; 2002; Luguet et al., 2003; 2008b). When coupled with Re-Os geochronology the HSE provide a further insight into the meaning of the ages obtained and can be used to determine if the age is of geological significance (Alard et al., 2000; 2002; Luguet et al., 2003; Griffin et al., 2004; Pearson et al., 2004). It is well documented that base metal sulphides (BMS: Fe-Ni-Cu-sulphides) and platinum group minerals (PGM: e.g. laurite, osmiridium, Pt-alloy, tellurides, arsenides) control the bulk rock HSE systematics (cf. Handler and Bennett, 1999; Alard et al., 2000; 2002). As such, the addition of metasomatic BMS and PGM can be traced by whole-rock HSE analysis. This can be achieved due to the variation in the compatibility of the HSE during partial melting, where the compatibility in the residue is Os≈Ir>Pt>Pd>Re (cf. Lorand et al., 2013). As such, residues of high degrees of partial melting, such as cratonic peridotites, should be depleted in Pt, Pd and Re. If such residues show enrichment in Pt, Pd or Re then it can be determined if BMS or PGM have been added to the samples and potentially impacted on the whole-rock $^{187}Os/^{188}Os$ composition. Despite this powerful use, coupled HSE and Re-Os studies in cratonic peridotites are quite limited (Irvine et al., 2003; Pearson et al., 2004; Lorand et al., 2013). This is most notable in the Kaapvaal craton, where Re-Os model ages have been used to infer the age of stabilisation of the lithosphere and also used as evidence for the suturing of the craton (e.g. Carlson and Moore, 2004; Carlson et al., 1999; Pearson et al., 1995; Simon et al., 2003; 2007; Griffin et al., 2004; Schmitz et al., 2004). Yet only one coupled HSE and Re-Os study has been documented for the Kaapvaal Craton in which the robustness of the obtained ages is constrained (Pearson et al., 2004). As such, this study couples Re-Os and HSE systematics in peridotites from six localities across the Kaapvaal Craton in an attempt to further constrain the timing of stabilisation of the lithosphere.

The Kaapvaal Craton in southern Africa is composed of four different blocks, each formed separately during the Archean, prior to collision and suturing in the Paleo- to Mesoarchean (cf. James and Fouch, 2002; de Wit et al., 1992; Schmitz et al., 2004). In the north are the Pietersburg and Central terranes, within which the Bushveld igneous complex is

located, which led to the enrichment of the lithosphere in these terranes (cf. Grégoire et al., 2005). The south-western block is called the Kimberley terrane, this is where the most studied peridotites sampled by kimberlite have been studied (cf. Griffin et al., 2004). The eastern block is the south-eastern terrane and is host to the majority of Paleoarchean crustal rocks seen in the Kaapvaal (de Ronde and de Wit, 1994; Kröner et al., 1989; 1993; Armstrong et al., 1990). The western and south-eastern terranes are separated by the Colesburg lineament, which is interpreted to represent the suturing of the south-eastern and western terranes at 2.9 Ga (Schmitz et al., 2004). These two terranes have been interpreted as having formed at different times, as the 3.7 Ga ages from the south-eastern terrane are not seen in the western terrane, where ages of only 3.2 Ga are reported (cf. Schmitz et al., 2004). Assuming a crust-mantle genetic link, a similar dichotomy could be expected within the mantle ages, but so far has not been resolvable (Carlson and Moore, 2004).

Previous work on Kaapvaal cratonic peridotites has been quite extensive, with studies focusing on whole-rock major and trace elements, as well as Sm-Nd, Lu-Hf and Re-Os systematics (e.g. Erlank et al., 1987; Pearson et al., 1995; Irvine et al., 2001; Gibson et al., 2008). Recently, investigations into the Sm-Nd and Lu-Hf systematics of garnets and the Re-Os systematic in base metal sulphides (BMS: Fe-Ni-Cu-sulphides) have been conducted (e.g. Griffin et al., 2004; Lazarov et al., 2009a). Despite the numerous Re-Os studies there is only one coupled Re-Os and PGE investigation (Pearson et al., 2004), and no consensus on the timing and mechanism for the depletion and stabilisation of the Kaapvaal cratonic lithosphere.

The Kaapvaal cratonic kimberlites were broken into two distinct groups based on emplacement age and petrology by Smith (1983). The "Group 1" kimberlites are younger than 110 Ma, with the majority being <95 Ma. They are considered to be non-micaceous – in that there is no or little groundmass phlogopite (Smith, 1983). A study by Griffin et al. (2003) showed that peridotites entrained by the "Group 1" kimberlites (from >10 separate kimberlite pipes) were derived from a mantle with a well-defined geotherm of 700-1050°C close to the 40 mW/m^2 conductive model. The lithosphere shows a decrease in olivine Mg# (Mg# = (Mg / (Mg + Fe)) x 100) with depth, from a maximum Mg# of 93, with a sharp decrease below 150 km (Mg# of 88.5-92.2 over 30 km). This evidence suggests the cratonic lithosphere is strongly modified and the base of the lithosphere is at ca. 170km. "Group 2" kimberlites are all older than 110 Ma and have a phlogopite dominated groundmass (Smith, 1983). The Group 1 kimberlite peridotites (from 5 localities; Griffin et al., 2003) display a fairly constant olivine Mg# of ~93 with depth. The geotherm is closer to the lower conductive geotherm of

35 mW/m^2 with a temperature range of 800-1000°C (Griffin et al., 2003). The lithosphere appears to be only slightly stratified with a slight decrease in olivine Mg# at 150 km, but generally, the cratonic lithosphere appears to be unmodified (i.e. depleted) and extend to a depth of 220 km. Griffin et al. (2003) state that this difference in cratonic lithosphere between Group 1 and Group 2 kimberlite peridotites is due to a large scale mantle metasomatic event that occurred between the two emplacement ages, which led to a stratified cratonic lithosphere and the loss of ~50 km of cratonic root.

To add further constraints to the difference between Group 1 and Group 2 kimberlite peridotites, I determine Re-Os ages and HSE concentrations in peridotites from two Group 2 kimberlites, Finsch and Newlands, and five Group 1 kimberlites, Letseng, Monastery, Jagersfontein, Kimberley and Bultfontein (Figure 2.1). Due to the proximity of Kimberley and Bultfontein and their presence within the Kimberley kimberlite field, they will be considered as a single locality subsequently referred to as Kimberley. The selection of peridotite from multiple kimberlite localities will also enable me to further constrain any east-west dichotomy within the Kaapvaal Craton. This is achieved by the selection of peridotites from the South-Eastern Terrane (Monastery and Letseng), the Western Terrane (Kimberley, Newlands and Finsch) and from the Jagersfontein kimberlite which straddles the border of the two terranes (Figure 2.1). The peridotites were obtained from the collection of Kaapvaal peridotites housed at the Department of Geological Sciences, University of Cape Town, South Africa. Two peridotites analysed from Monastery have been previously investigated for Re-Os systematics at the whole-rock scale by Carlson and Moore (2004), from which Archean ages (T_{RD} of 2.8 Ga) were obtained.

2.2. Regional geology and peridotite description

The Kaapvaal peridotites are in general coarse and equigranular and either lherzolitic or harzburgitic in composition (Table 2.1). All of the peridotites have been serpentinised to some extent, with the Group 2 kimberlite peridotites displaying a greater extent of serpentinisation. Five peridotites display a protogranular texture that is due to a finer grained olivine (ol) and orthopyroxene (opx) matrix, with larger optically continuous ol and opx grains (Figure 2.2). Only one of these peridotites shows signs of deformation (09-LET-17) that can be seen at the whole-rock scale due to the alignment of the constituent minerals.

Seven peridotites display enrichment in modal orthopyroxene, with more orthopyroxene than olivine in a given thin section. Orthopyroxene enrichment in Kaapvaal peridotites is a well-documented phenomenon (cf. Boyd, 1989) for which three models have

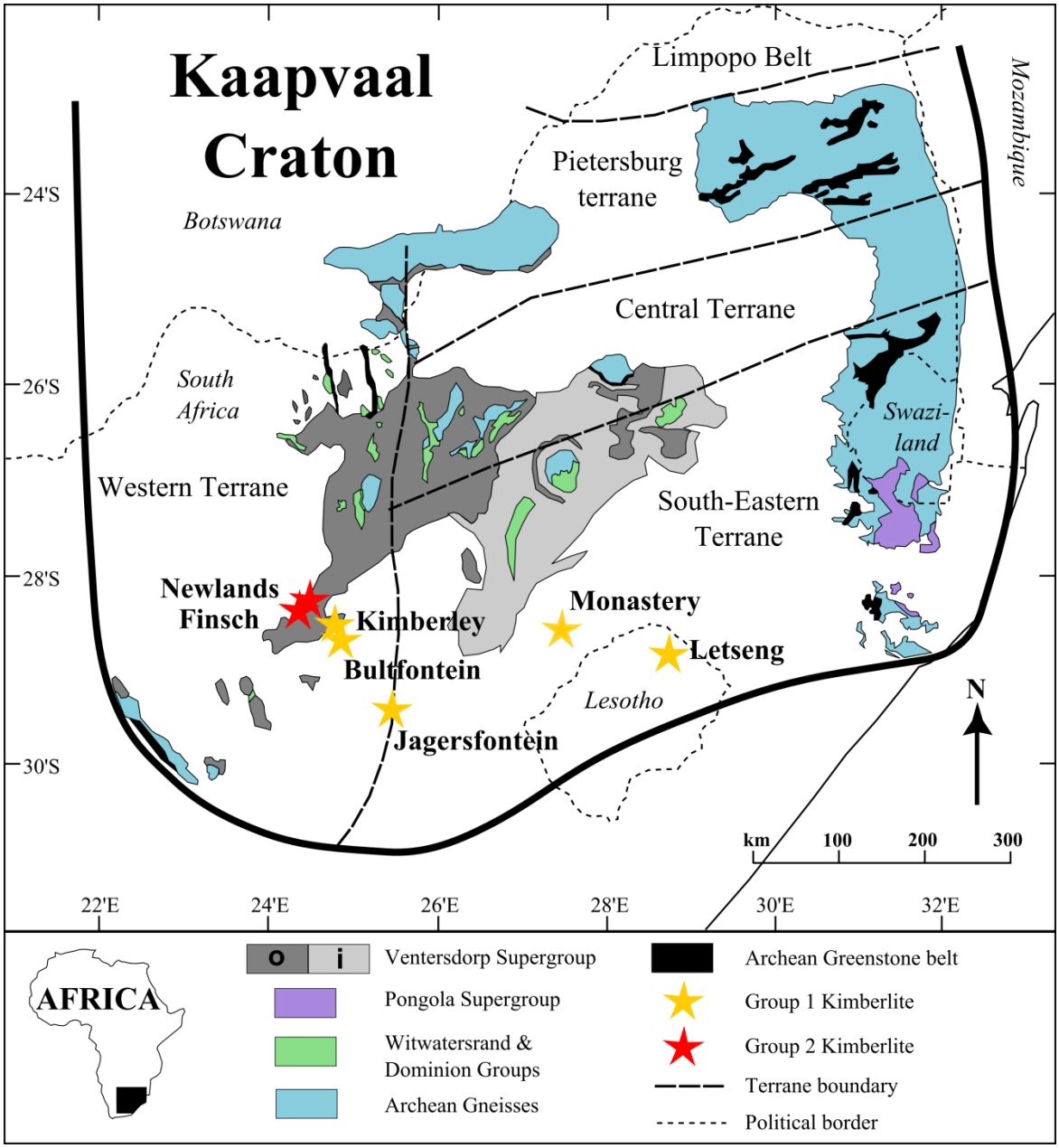

Figure 2.1. Sketch map of the Kaapvaal Craton, after Schmitz et al., 2004. Stars represent localities from which peridotites in this study are analysed. Thick black line is the known extent of the Kaapvaal Craton.

been proposed (cf. Walter, 1998): 1) melting due to metamorphic un-mixing of opx and ol rich layers (Boyd et al., 1997), 2) mixing with a opx-cumulate (Herzberg, 1999) or 3) the percolation of Si-rich fluids of melts (Kesson and Ringwood, 1989; Rudnick et al., 1994; Kelemen et al., 1998). Two peridotites ROM-207A and JAG12-133 contain orthopyroxene with spinel exsolutions

Garnet is more common in the Group 2 kimberlite peridotites, but is also found in Kimberley and Letseng (Table 2.1). The large (>1mm) garnets always display a kelyphite reaction rim that varies in size, from 2-50% of the entire garnet grain. In Finsch peridotites FIN12-004 and FIN12-011 the garnet hosts orthopyroxene and spinel inclusions close to the

Table 2.1 Petrographic description and classification of the Kaapvaal peridotites

Kimberlite Pipe	Peridotite	Description	Classification
Letseng	09-LET-17	Deformed, very fine grained ol, opx. With grt relics displaying reaction rims, some larger optically continuous ol and opx still evident (Figure 2.2). Sp interspersed with groundmass ol. Peridotite foliated with some very fine grained areas	Garnet Harzburgite
	09-LET-21	Coarse, equigranular. Ol very altered, significant serpentinisation. Reddy brown sp, all minerals have undulose extinction. More opx than ol in given thin section	Harzburgite
Monastery	ROM-69	Equigranular, coarse. Grt smaller than opx and ol, has reaction rim, ol has straight extinction, minor serpentinisation. Opx has sp exsolutions, small (<3 mm) cpx scattered through-out sample	Garnet-bearing Lherzolite
	ROM-207A	Semi-coarse ol, with a straight extinction, minor serpentinisation. Minor opx with sp exsolutions, cpx, very altered, lots of interstitial sp. Mix of smaller recrystallised ol with larger fractured ones, large resorbed porphyroblasts, that have high birefringence on the edge of the grain	Harzburgite
	BD-2224	Coarse, equigranular, very fresh, minor serpentinisation. Large grained ol and opx, phl laths. Ol and opx have undulose extinction. Two generations of phl that is associated to opx, one forms subhedral laths, the other is anhedral (Figure 2.2). Sp associated with phl and serpentinisation	Lherzolite
	BD-2227	Coarse, equigranular, very fresh, opx and ol with small phl laths. Opx has a straight extinction, ol is undulose. Cpx shows is mosaic of small (<2 mm) grains, phl is subhedral and appears to be resorbed (Figure 2.2). Opx have inclusions of sp and small grt. Serpentinisation veins associated with phl laths	Lherzolite
	BD-2267	Protogranular, lots of large opx, showing sp exsolutions, ol has undulose extinction. Ol and opx is intergranular, lots of interstitial chain grt	Harzburgite
Kimberley	04-KEN-38B	Coarse, granular. ~1 mm subhedral phl, which occur in clusters. Small sp distributed throughout. Moderately serpentinised.	Harzburgite
Bultfontein	04-BOS-46	Highly altered, large ol and opx that are fractured and serpentinised. Veins of sp associated with cpx and phl, which display mosaic texture (Figure 2.2)	Harzburgite
	09-BOS-05	Coarse, equigranular, minor serpentinisation. Grt have minor reaction rims. No sp, minor secondary cpx and phl	Garnet Harzburgite
	09-BOS-52	Moderately serpentinised, which obscures primary coarse texture. Altered grt, with reaction rim. Subhedral porphyroblasts of phl, 1-3 mm long, phl clustered. Minor sp porphyroblasts, 1 mm in diameter	Garnet Harzburgite

Jagersfontein	JAG12-79	Coarse, protogranular, opx larger than ol. Opx has sp exsolutions. Moderate serpentinisation. Minor sp, occasionally as a symplectite. Very small (<0.2 mm) grt in alteration veins.	Harzburgite
	JAG12- 133	Protogranular, ol and opx as large (>5mm) and small (<0.3 mm) crystals. Moderately serpentinised. Small (<0.05 mm) sp associated to cpx and phl, occurring in clusters	Harzburgite
	JAG12-146	Coarse protogranular, with small (<2mm) and large (>5mm) opx and ol. Minor serpentinisation. Minor cpx, phl and sp associated together along grain boundaries	Harzburgite
Newlands	JJG-4401	Coarse, equigranular, minor serpentinisation. Both grt and sp, sp appears as 1-2mm subhedral blasts that are being altered (Figure 2.2). Grt occurs as small (<2mm) grains, forming chains along grain boundaries (Figure 2.2). Both phl and amphibole (K-richterite) present along grain boundaries	Garnet-bearing Harzburgite
	JJG-4407	Coarse, equigranular. Minor serpentinisation. Minor sp, occurs as symplectite associated to secondary cpx and phl (Figure 2.2)	Harzburgite
Finsch	FIN12-002	Coarse, equigranular. Moderate serpentinisation. Large (>5 mm) garnet porphyroblasts, with small alteration rim. Larger garnets (>10 mm) contain opx inclusions. Ol and opx significantly fractured and altered, but show optical continuity	Garnet Harzburgite
	FIN12-003	Protogranular with two different ol, a fine grained <3mm matrix and larger >7mm fractured, optically continuous porphyroblasts (Figure 2.2), opx also >7mm and fractured, minor secondary cpx associated to alteration of ol and opx	Garnet Lherzolite
	FIN12-004	Coarse, equigranular, , opx and ol fractured, large optically continuous grains with undulose extinction, grt with reaction rims up to 50% of grain, grt occasionally have opx and sp inclusions (Figure 2.2) cpx occurs in small veinlets, minor opaques associated with grt	Garnet Harzburgite
	FIN12-006	Coarse, equigranular, large ol and opx displaying undulose extinction, fractured and minor serpentinisation. Grt is anhedral, with 10% kelyphite rims, minor cpx, sp and phl in serpentinisation veins	Garnet Harzburgite
	FIN12-011	Protogranular, moderate serpentinisation, <10% kelyphite rims on grt, opx inclusion in grt. Fine grained ol matrix, with some large optically continuous fractured grains. Large fractured opx. Significant cpx associated to matrix ol	Garnet Lherzolite
	FIN12-016	Coarse, equigranular, large fractured ol and opx displaying undulose extinction. Grt are anhedral with <10% kelyphite reaction rims	Garnet Harzburgite

core (Figure 2.2). Garnet also occurs as small (<0.5 mm) grains forming along grain boundaries like pearls on a string, this is most common in Newlands peridotite JJG-4401 and BD-2267 (Table 2.1; Figure 2.2)

Thirteen peridotites contain spinel. They are usually disseminated through-out the peridotite, but generally occur in clusters along the grain boundaries, and in association with phlogopite and clinopyroxene (Figure 2.2). In Newlands peridotite JJG-4401 the spinel occur as large (1 mm) subhedral grains that are being consumed by interstitial minerals (Figure 2.2), whereas the second Newlands peridotite JJG-4407 has spinel symplectites (Figure 2.2). Monastery peridotites BD-2227, BD-2267 and ROM-207A as well as Finsch peridotites FIN12-004 and FIN12-006 contain both spinel and garnet (Table 2.1). In the Monastery peridotites the garnet occurs as small (<1mm) grains located along grain boundaries, whilst the spinel is disseminated as larger (>1mm) grains through-out the peridotites. On the other hand, the Finsch samples contain large (>5mm) garnets, with small (<1mm) spinel grains disseminated along grain boundaries.

Clinopyroxene is present in 19 of the 22 peridotites, however in four of these it is a minor constituent and is located along grain boundaries. Only in peridotites FIN12-003, BD-2224, BD-2227 and BD-2267 does it occur as large (>3 mm) discrete phases (Table 2.1). In Kimberley peridotite 09-BOS-05 clinopyroxene occurs as large (3 mm) grains, but are quite sporadically disseminated through-out the peridotite, with only one grain per thin section. These large clinopyroxene grains are always associated to trace amounts of phlogopite occurring along the edge of the grain.

Through-out the Kaapvaal craton, mantle peridotites have been variably modally enriched in phlogopite and potassium-amphibole (Grégoire et al., 2003; Simon et al., 2003; Griffin et al., 2004; Bell et al., 2005; Lazarov et al., 2009b). This is reflected in the peridotites of this suite, where 13 of the peridotites contain secondary phlogopite and amphibole (Table 2.1). In general the Group 1 kimberlite peridotites host more phlogopite, with large (up to 1 mm) tabular laths present in four Monastery peridotites, however, smaller interstitial grains associated to secondary cpx are also present (Figure 2.2). The only amphibole is in Group 2 kimberlite peridotite JJG-4401 where it occurs interstitially to the modally major minerals.

2.3. Methods

2.3.1. Sample Preparation

Peridotite xenoliths varied in size from 10 cm to >100 cm in diameter, for the larger xenoliths a 10-20 cm wide slice was removed from the xenolith for analysis. All xenoliths

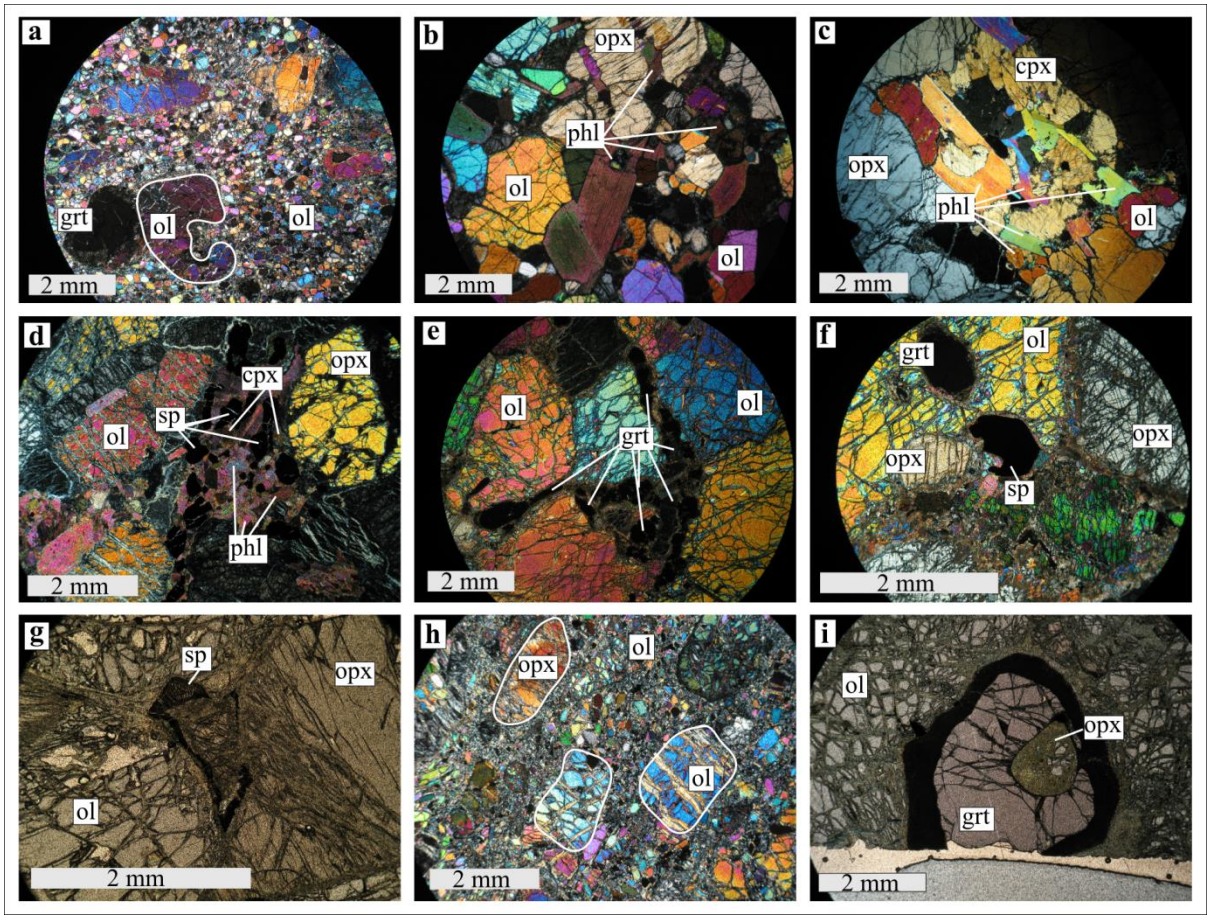

Figure 2.2. Transmitted light photomicrographs of a selection of the Kaapvaal peridotite displaying textures between modally major silicates and oxides. a) crossed-polarised light of 09-LET-17, showing occurrence of small ol crystals and larger optically continuous opx and ol. b) Crossed-polarised light image of BD-2224, detailing two different type of phlogopite. Large subhedral laths, and smaller interstitial anhedral grains. c) Crossed-polarised light of BD-2227, relationship between phl and cpx. d) Crossed-polarised light image of 04-BOS-46 displaying interstitial matrix phl and cpx. e) Crossed-polarised light image of JJG-4401 showing the occurrence of interstitial 'chain' garnet. f) Crossed-polarised light image of JJG-4401, displaying subhedral sp that is reacting to interstitial medium. g) Plain polarised light image of JJG-4407 displaying occurrence of sp symplectite. h) Crossed-polarised light image of FIN12-003 displaying matrix ol with larger ol and opx phorphyroblasts. i) Plain polarised light of FIN12-004 showing opx inclusion inside a grt grain.

had a reaction rim from interaction with the host kimberlite, which was removed by circular saw, only the dark inner core of the xenoliths were used to prepare rock powders. A section of the xenolith was retained and used for the preparation of thin sections and as a hand specimen, whilst the remaining section was crushed to chips before ca. 50% was powdered in an agate planetary mill.

2.3.2. Electron Microprobe major element mineral analyses

Silicates, spinels and BMS chemical compositions were obtained on a Jeol JXA-8200

electron probe at the Steinmann Institute, University of Bonn. All minerals were measured in wavelength dispersive (WDS) mode with a 15kV acceleration voltage, a 15 nA beam current and a 1 µm spot size. With the exceptions of the alkalis, all element calibrations were carried out by measuring their peak and background positions for 10 and 5 sec respectively, employing the ZAF matrix correction method. The alkalis (i.e. K_2O and Na_2O) were measured for 5 sec and 2.5 sec on the peak and background positions respectively, in order to avoid alkali migration and loss under the electron beam. For BMS, Fe and S were calibrated on a Canyon Diablo troilite, whereas Ni, Cu and Co were calibrated using pure alloys. Oxygen was measured using a LDE1 light element detector and calibrated by measuring the peak and background positions of its Kα x-ray line on a synthetic MgO standard. Oxygen calibrations were tested by measuring magnetite and ferro-chromite as a check for reproducibility. Major elements for the silicate minerals were calibrated using natural samples (e.g. San Carlos olivine; augite; natural pyrope and andradite; microcline), and a jadeite-diopside eutectic glass in the case of Na_2O.

2.3.3. Whole Rock Major and Trace Element Analyses

Major element analyses were carried out at the University of Bonn on glass beads by X-Ray Fluorescence. Trace elements concentrations were analysed at the Department of Geological Sciences, University of Cape Town, South Africa, with a Thermo X-Series 2 Quadrupole ICPMS. Peak-hopping mode was used, with a dwell time of 20 ms with 100 sweeps of selected masses per cycle and three measurement cycles per analysis. Analyses were performed on solutions. Intensities were corrected using ^{115}In, ^{187}Re and ^{209}Bi as internal standards (all spiked at 10 ppb). Intensities were converted to concentration values using calibration curves obtained from the measurement of 5 synthetic standards of varying concentrations, plus a blank. USGS international reference materials BIR-1, PCC-1 and AGV-1 were also analysed and yield average reproducibilities and precisions of 10% and 90% respectively (Table A.1).

2.3.4. Highly siderophile element and $^{187}Os/^{188}Os$ analytical techniques

For the determination of HSE concentrations and $^{187}Os/^{188}Os$ compositions in the whole-rocks, 1g of sample powder for each peridotite was weighed and spiked with a mixed HSE spike (^{185}Re, ^{106}Pd, ^{195}Pt, ^{191}Ir, ^{190}Os). They were then digested in 7.5ml of inverse aqua regia in 50 mL glass vials with an Anton Paar High Pressure Asher for 13.5 hours at 220°C

and ca. 120 bar. Following digestion the osmium was extracted using a $CHCl_3$ solution (7ml total) and then back extracted using HBr following the procedure described in Cohen and Waters (1996). The osmium was then further purified via micro-distillation, with the osmium-H_2SO_4-dichromite solution distilled into a 10 µL drop of 9N HBr at 80°C for 2 hours. The aqua regia containing the remaining HSE after osmium extraction was dried and desilicified with a concentrated HF-HNO_3 mixture at 120°C for 18 hours. This allows for the digestion of the silicate minerals and therefore a more efficient recovery of rhenium (Ishikawa et al., 2014). The samples were then equilibrated in 12N HCl to allow for HSE extraction via chromotography columns. A BioRad AG8 X1 (100-200 mesh) resin was used to separate the HSE from the matrix, following the procedure from Pearson and Woodland (2000) with extra HF-HCl steps prior to elution of the HSE to achieve a better HFSE-HSE (HFSE – high field strength elements, e.g. Zr, Hf) separation.

Base metal sulphides were extracted from thick sections (approximately 200 µm thick) following the procedure of Bragagni et al. (2013). In brief, after characterisation via electron microprobe (EMP) the BMS were isolated from the surrounding silicate with a Resonetics RESOlution M50-E 193nm Excimer Laser by ablating a path around the BMS. The ablated path was then further widened by hand using a diamond scribe under a binocular scope. The sulphide was then freed from the section and carefully moved to a containment vessel. Using these techniques enabled the extraction of the BMS with as little of the surrounding silicate as possible. However, even if silicates were incorporated the digestion procedure used would not dissolve it. BMS were then carefully weighed and those larger than 3 µg were spiked with a multi-element spike. Each BMS was weighed multiple times using a Mettler Ultra-micro scale to ensure accurate weighing data (weighing error is 0.2 µg). BMS that were too small to be weighed were run unspiked.

Osmium concentrations and $^{187}Os/^{188}Os$ compositions were obtained with a Thermo-Finnigan Triton N-TIMS at the NCIET (Northern Centre for Isotopic and Elemental Tracing), Earth Science Department, University of Durham, following the procedure detailed in Dale et al. (2008). The standard solution Durham Romil Osmium Standard (DROsS) with a load size of between 1.0-0.01 ng was analysed eleven times. A mean $^{187}Os/^{188}Os$ of 0.16083 with a 2σ error of 0.00055, this is in agreement with the values from Luguet et al. (2008a). Total procedural blanks (n = 5) are 1.00±0.42 pg Os for the whole rock and 20±5 fg Os (n = 2) for the BMS. International reference material UB-N (SARM-CRPG) was also analysed from which an $^{187}Os/^{188}Os$ of 0.1274±1 was obtained, this is in good agreement with previously published values (e.g. Fischer-Gödde et al., 2011). For the analysis of the BMS the ^{192}Os

beam ranged between 1210-141992 cps, with an ^{187}Os of 75-5124. These beam sizes result in absolute standard errors on the $^{187}Os/^{188}Os$ of between 0.0001-0.0007 with one outlier at 0.0018, which corresponds to 0.1-1.4% RSD.

The HSE were analysed at the Steinmann Institute, University of Bonn, with a Thermo Element XR ICP-MS. A cyclonic single pass boro-silicate glass spray chamber intake system was used, with whole-rock samples redissolved in 0.56N HNO_3. International reference material UB-N (SARM-CRPG) was analysed once to determine accuracy and precision, yielding concentrations of 3.27 ppb Os, 2.855 ppb Ir, 7.88 ppb Pt, 5.85 ppb Pd and 0.19 ppb Re; these values are in agreement with literature data (Meisel et al, 2003; Meisel and Moser, 2004; Fischer-Gödde et al., 2011; Luguet et al., submitted). The total average procedural blanks (n = 4) were 0.73±0.36 ppt Ir, 10.78±2.43 ppt Pt, 4.78±0.93 ppt Pd and 0.32±0.16 ppt Re.

2.4. Results

2.4.1 Major element compositions of the constituent minerals

The ol compositions across all seven localities are very similar, displaying high MgO contents with average Mg# (Mg# = Mg / (Mg + Fe) x 100) of 92.6 ± 0.8 (Table 2.2). Letseng peridotite 09-LET-17 has the lowest Mg# of 90.6, whilst the Monastery peridotites BD-2267, ROM-69 and ROM-207A all show variable Mg# (86.1-93.7) due to FeO enriched olivine rims (Table 2.2). The high Mg# are similar to previously reported data for the Kaapvaal Craton (cf. Boyd, 1989) and for the average cratonic mantle (median 92.1, Pearson et al., 2003). Concentrations of NiO in the ol range from 0.35-0.45 wt. % (average 0.40±0.03 wt. %; Table 2.2). These NiO contents are in good agreement with previously reported data from Kaapvaal peridotites (cf. Boyd, 1989; Simon et al., 2007; Gibson et al., 2008).

The opx in the Kaapvaal peridotites is enstatite in composition with an average En (En=Mg / (Mg + Fe + Ca) x 100) of 92.8 ± 1.0 (Table 2.2), typical of cratonic peridotites (cf. Pearson et al., 2003). The opx compositions are relatively homogeneous between all of the localities, and within a given peridotite. In three peridotites from different localities – 09-LET-17, ROM-207A and FIN12-006 – a high Al orthopyroxene is present with average Al_2O_3 in each peridotite between 8.92-11.15 wt. % (Table 2.2). This Al-opx is less magnesian and Ca-richer (1.68-2.01 wt. %) than the modally major opx, which results in an average En of 83.33-86.04, (Table 2.2).

Of the 22 Kaapvaal peridotites, 19 contain clinopyroxene (cpx) of a diopside composition, with variable Wo (Wo=Ca / (Ca + Fe + Mg) x 100) of 37.1-48.6. They also

contain variable Na_2O between 0.59-2.94 wt. % and TiO_2 of 0.01-0.59 wt. % (Table 2.2). There is no correlation with locality and Wo, with a wide range in composition seen within a given locality (Table 2.2). In combination with diopside three Monastery peridotites contain high-Al pyroxenes. ROM-207A contains an Al-rich clinopyroxene (Al_2O_3 of 13.17 wt. %), with a Wo of 46.07 (Table 2.2). Whilst peridotites BD-2224 and BD-2227 contain high-Al pigeonite with a Wo of 20.0-24.0 (Al_2O_3 of 9.5 wt. %; Table 2.2).

The garnet (grt) compositions across the 12 garnet bearing peridotites vary significantly, but are all pyrope garnet and are internally homogeneous. CaO contents range between 4.47-5.52 wt. % with a large range in Cr# (Cr# = Cr / (Cr + Al) x 100) of 3.6-17.2, except in FIN12-002 which has a Cr# of 28.69. The Cr# varies within each locality, with no correlation between locality and composition. In agreement with the lack of modal clinopyroxene FIN12-002 is the only peridotite where the garnet composition plots in the harzburgite field of a CaO-Cr_2O_3 diagram, all other garnets are lherzolitic (Figure 2.3). The TiO_2 are generally <0.2 wt. % except in four peridotites from Finsch and Letseng where it ranges between 0.28-0.91 wt. %. Garnets of these variable compositions have been previously reported in the Kaapvaal Craton (cf. Simon et al., 2003; Lazarov et al., 2009a; 2009b).

Spinel (sp) compositions vary widely, with four different compositions seen based on Al_2O_3 content. The most predominate composition has a Cr# between 70.72-76.62 and is found in Monastery, Jagersfontein and Bultfontein peridotites. Spinel from these peridotites has a fairly constant Al_2O_3 content of 11.88-14.78 wt. % (Table 2.2). Peridotite 09-KEN-38B hosts the most Cr rich sp, with a Cr# of 9.58 (Table 2.2), this sp has a very low Al_2O_3 of 1.35 wt. % with a relatively high TiO_2 of 2.46 wt. %. The third sp composition is located in Letseng, Newlands, Finsch and Monastery peridotite ROM-207A and has a Cr# of between 43.34-61.60. Spinel of this composition is highly variable in Al_2O_3 (19.85-32.89 wt. %) but relatively homogeneous in Cr_2O_3 content (37.50-45.89 wt. %). The fourth and final sp composition is an Al-rich variety, this spinel only occurs in Finsch and Monastery peridotite ROM-207A. In the Monastery peridotite and FIN12-006 an Al-rich and Cr-rich spinel is present, whilst in FIN12-004 there is only Al-rich spinel. In the Finsch peridotites the Al-rich sp is fairly homogeneous with Al_2O_3 between 50.78-52.64 wt. % and Cr_2O_3 16.91-18.08 wt. %. Whilst the Al-rich sp in ROM-207A has a higher Al_2O_3 content of 64.35 wt. % and a very low Cr_2O_3 of 4.33 wt. %.

Phlogopite (phl) is present in 13 peridotites. In six peridotites (BD-2224, BD-2227, BD-2267, 09-BOS-52, 09-KEN-38B and JAG12-79) from Group 1 peridotites it forms

Table 2.2 Major element compositions of the modally major consituent minerals

Olivine	**Group 1 Kimberlites**												
Kimberlite:	**Letseng**		**Monastery**									**Kimberley**	**Bultfontein**
Xenolith:	**09-LET-17**	**09-LET-21**	**BD-2224**	**BD-2227**		**BD-2267**		**ROM-69**		**ROM-207A**		**09-KEN-38B**	**04-BOS-46**
	average	average	average	average	average	rim	core	average	average	lowest	highest	average	average
	n=19	n=21	n-18	n=56	n=54	n=11	n=11	n=16	n=42	Mg#	Mg#	n=43	n=34
SiO_2	40.97	41.36	41.05	41.08	41.04	40.62	41.09	41.29	41.35	40.12	41.71	41.02	41.29
TiO_2	0.04	0.01	0.02	0.01	0.02	0.03	0.01	0.01	0.02	0.05	0.03	0.03	0.02
Al_2O_3	0.02	0.01	0.01	0.01	0.01	0.01	0.01	0.01	0.02	0.07	0.01	0.01	0.01
Cr_2O_3	0.04	0.01	0.01	0.01	0.01	0.01	0.01	0.02	0.02	0.10	0.00	0.01	0.02
FeO_T	9.20	6.61	7.30	6.87	8.64	10.60	7.96	6.86	7.71	11.84	6.83	8.22	6.88
MnO	0.10	0.09	0.13	0.09	0.10	0.12	0.09	0.10	0.13	0.58	0.12	0.10	0.09
MgO	49.98	52.17	51.31	51.63	50.59	49.03	51.21	52.21	51.45	47.34	52.08	50.32	51.41
CaO	0.07	0.02	0.05	0.02	0.03	0.05	0.03	0.02	0.02	0.14	0.01	0.02	0.03
Na_2O	0.03	0.02	0.02	0.01	0.01	0.01	0.02	0.01	0.01	0.03	0.01	0.01	0.02
K_2O	0.00	0.00	0.02	0.00	0.00	0.00	0.01	0.00	0.01	0.00	0.00	0.00	0.00
NiO	0.36	0.45	0.35	0.42	0.40	0.34	0.41	0.41	0.39	0.10	0.43	0.36	0.40
Total	100.81	100.76	100.27	100.17	100.87	100.84	100.85	100.92	101.12	100.37	101.23	100.10	100.18
Mg#	90.64	93.40	92.61	93.05	91.23	89.16	91.96	93.12	92.12	87.70	93.15	91.61	93.01
			Group 2 Kimberlites										
Kimberlite:	**Bultfontein**		**Jagersfontein**			**Newlands**		**Finsch**					
Xenolith:	**09-BOS-05**	**09-BOS-52**	**JAG12-79**	**JAG12-133**	**JAG12-146**	**JJG-4401**	**JJG-4407**	**FIN12-002**	**FIN12-003**	**FIN12-004**	**FIN12-006**	**FIN12-011**	**FIN12-016**
	average	average	average	average	average	average	average	average	average	average	average	average	average
	n=18	n=33	n=25	n=16	n=18	n=22	n=34	n=58	n=28	n=20	n=32	n=35	n=68
SiO_2	40.88	41.27	41.30	41.41	41.60	41.40	41.09	41.20	40.94	41.02	41.13	41.19	41.23
TiO_2	0.01	0.02	0.02	0.01	0.02	0.01	0.01	0.02	0.02	0.03	0.02	0.01	0.02
Al_2O_3	0.01	0.02	0.01	0.01	0.01	0.01	0.01	0.01	0.02	0.01	0.01	0.02	0.02
Cr_2O_3	0.03	0.02	0.02	0.02	0.01	0.02	0.01	0.07	0.03	0.03	0.04	0.04	0.07
FeO_T	6.84	6.63	6.65	6.79	7.12	6.45	7.17	6.58	8.26	7.90	7.81	7.55	6.90
MnO	0.07	0.10	0.08	0.09	0.10	0.09	0.10	0.08	0.11	0.08	0.10	0.11	0.09
MgO	50.85	51.54	52.01	51.67	52.02	51.73	51.32	51.37	50.36	50.57	50.69	51.08	51.70
CaO	0.02	0.03	0.01	0.02	0.01	0.02	0.02	0.03	0.05	0.04	0.05	0.05	0.03
Na_2O	0.02	0.03	0.01	0.01	0.01	0.01	0.02	0.02	0.01	0.02	0.02	0.02	0.02
K_2O	0.00	0.01	0.00	0.01	0.01	0.00	0.01	0.00	0.01	0.01	0.01	0.01	0.01
NiO	0.42	0.41	0.43	0.42	0.44	0.40	0.39	0.36	0.38	0.38	0.39	0.37	0.38
Total	99.15	100.07	100.53	100.45	101.36	100.16	100.15	99.74	100.19	100.10	100.28	100.45	100.45
Mg#	92.98	93.27	93.31	93.13	92.86	93.46	92.73	93.30	91.57	91.94	92.05	92.35	93.04

Table 2.2 cont.

Orthopyroxene	**Group 1 Kimberlites**												
Kimberlite:	**Letseng**			**Monastery**						**Bultfontein**			**Kimberley**
Xenolith:	**09-LET-17**		**09-LET-21**	**BD-2224**	**BD-2227**	**BD-2267**	**ROM-69**	**ROM-207A**		**04-BOS-46**	**09-BOS-05**	**09-BOS-52**	**09-KEN-38B**
	average	Al-rich	average	average	average	average	average	average	Al-rich	average	average	average	average
	n=15	n=3	n=14	n=50	n=14	n=24	n=10	n=22	n=13	n=21	n=14	n=19	n=25
SiO_2	56.72	51.20	57.19	57.66	57.62	58.12	57.83	57.82	50.08	55.31	57.70	58.00	58.07
TiO_2	0.24	0.75	0.01	0.04	0.02	0.01	0.01	0.01	0.04	0.03	0.01	0.07	0.08
Al_2O_3	1.03	9.41	1.73	0.87	0.82	0.89	0.88	0.99	11.15	0.76	0.82	0.66	0.07
Cr_2O_3	0.27	0.49	0.36	0.27	0.26	0.27	0.30	0.19	1.07	0.30	0.34	0.36	0.14
FeO_T	5.55	7.30	4.26	4.58	4.22	4.15	4.26	4.59	7.89	4.35	4.18	4.08	5.23
MnO	0.11	0.31	0.11	0.13	0.11	0.09	0.10	0.11	0.60	0.12	0.10	0.11	0.13
MgO	34.04	29.59	35.97	36.46	36.20	36.56	36.40	36.34	28.24	35.93	35.92	36.09	35.83
CaO	1.17	2.01	0.33	0.24	0.24	0.28	0.25	0.17	1.70	0.26	0.43	0.35	0.34
Na_2O	0.21	0.08	0.03	0.11	0.06	0.06	0.09	0.01	0.05	0.09	0.12	0.11	0.07
K_2O	0.01	0.01	0.01	0.01	0.01	0.01	0.00	0.00	0.01	0.00	0.00	0.01	0.01
NiO	0.11	0.19	0.10	0.10	0.09	0.09	0.09	0.06	0.04	0.12	0.11	0.10	0.09
Total	99.46	101.33	100.10	100.45	99.65	100.52	100.21	100.30	100.88	97.28	99.73	99.93	100.04
En%	89.58	84.25	93.19	93.01	93.44	93.53	93.41	93.28	83.33	93.20	93.12	93.43	91.86

	Group 2 Kimberlites											
Kimberlite:	**Jagersfontein**			**Newlands**		**Finsch**						
Xenolith:	**JAG12-79**	**JAG12-133**	**JAG12-146**	**JJG-4401**	**JJG-4407**	**FIN12-002**	**FIN12-003**	**FIN12-004**	**FIN12-006**		**FIN12-011**	**FIN12-016**
	average	average	average	average	average	average	average	average	average	Al-rich	average	average
	n=21	n=27	n=13	n=20	n=13	n=32	n=30	n=13	n=9	n=3	n=15	n=11
SiO_2	57.16	58.19	57.92	58.12	55.27	57.68	57.67	57.64	57.92	51.22	57.71	57.73
TiO_2	0.01	0.03	0.01	0.01	0.01	0.03	0.09	0.04	0.09	0.23	0.03	0.04
Al_2O_3	1.25	0.67	0.60	0.59	4.19	0.57	0.67	0.61	0.64	8.92	0.64	0.58
Cr_2O_3	0.35	0.24	0.22	0.25	0.82	0.46	0.24	0.25	0.30	2.01	0.35	0.49
FeO_T	4.21	4.28	4.53	3.84	4.49	3.94	5.01	4.74	4.60	6.34	4.50	4.13
MnO	0.11	0.10	0.11	0.11	0.12	0.09	0.12	0.10	0.10	0.29	0.11	0.09
MgO	35.92	36.18	36.37	36.56	34.10	35.95	35.16	35.36	35.17	29.39	35.56	36.32
CaO	0.22	0.31	0.27	0.24	0.67	0.44	0.72	0.69	0.65	1.68	0.72	0.40
Na_2O	0.02	0.05	0.04	0.03	0.05	0.12	0.15	0.15	0.16	0.11	0.13	0.11
K_2O	0.00	0.01	0.00	0.00	0.00	0.01	0.04	0.01	0.00	0.01	0.01	0.00
NiO	0.07	0.11	0.10	0.10	0.08	0.10	0.12	0.13	0.10	0.03	0.11	0.13
Total	99.33	100.15	100.17	99.84	99.81	99.39	99.98	99.71	99.75	100.23	99.86	100.03
En%	93.43	93.22	93.01	94.02	91.91	93.44	91.34	91.81	92.02	86.04	92.12	93.31

Table 2.2 cont.

Clinopyroxene	**Group 1 Kimberlites**												
Kimberlite:	**Letseng**	**Monastery**								**Bultfontein**			**Kimberley**
Xenolith:	**09-LET-17**	**BD-2224**		**BD-2227**		**BD-2267**	**ROM-69**	**ROM-207A**		**04-BOS-46**	**09-BOS-05**	**09-BOS-52**	**09-KEN-38B**
	average	average	Al-rich pigeonite	average	Al-rich pigeonite	average	average	average	Al-rich	average	average	average	average
	n=14	n=14	n=39	n=9	n=9	n=3	n=15	n=16	n=2	n=11	n=9	n=9	n=19
SiO_2	54.04	53.97	46.27	53.50	47.84	54.28	55.31	49.76	46.50	54.54	54.28	54.43	54.56
TiO_2	0.44	0.18	0.31	0.15	0.12	0.01	0.05	0.53	0.08	0.20	0.14	0.33	0.59
Al_2O_3	2.71	2.38	9.50	2.26	9.45	2.48	2.68	6.20	13.17	2.99	2.19	1.90	1.10
Cr_2O_3	0.93	2.66	1.97	2.55	2.03	1.76	2.34	0.89	1.88	2.55	1.57	2.64	1.26
FeO_T	3.51	2.37	2.81	2.47	2.45	1.63	2.03	3.94	4.90	2.19	2.10	2.33	3.12
MnO	0.11	0.08	0.07	0.10	0.06	0.06	0.05	0.34	0.60	0.09	0.08	0.09	0.10
MgO	18.82	16.20	19.31	16.14	20.07	16.05	15.94	16.84	13.72	15.50	16.97	16.32	17.89
CaO	17.05	19.84	7.25	19.95	9.41	21.67	19.79	20.16	19.57	18.68	20.32	19.04	19.63
Na_2O	1.55	2.06	5.05	1.87	4.11	1.80	2.42	0.59	0.39	2.94	1.66	2.32	1.44
K_2O	0.04	0.04	0.82	0.03	1.36	0.00	0.01	0.01	0.02	0.02	0.02	0.02	0.01
NiO	0.06	0.05	0.12	0.06	0.11	0.07	0.04	0.05	0.02	0.04	0.13	0.03	0.08
Total	99.24	99.83	93.47	99.07	97.01	99.80	100.67	99.33	100.85	99.75	99.47	99.46	99.78
Wo%	37.11	44.80	20.00	44.98	23.98	47.87	44.85	43.10	46.07	44.57	44.60	43.82	41.82

	Group 2 Kimberlites								
Kimberlite:	**Jagersfontein**			**Newlands**		**Finsch**			
Xenolith:	**JAG12-79**	**JAG12-133**	**JAG12-146**	**JJG-4401**	**JJG-4407**	**FIN12-003**	**FIN12-004**	**FIN12-006**	**FIN12-011**
	average	average	average	average	average	average	average	average	average
	n=4	n=12	n=13	n=2	n=10	n=30	n=12	n=16	n=24
SiO_2	51.55	54.33	54.38	54.66	53.23	54.87	53.92	53.73	54.27
TiO_2	0.45	0.17	0.21	0.46	0.02	0.14	0.16	0.18	0.09
Al_2O_3	4.99	1.80	1.91	0.18	4.26	2.02	1.90	3.08	1.98
Cr_2O_3	1.12	1.25	1.56	0.98	1.28	1.22	1.52	1.75	1.67
FeO_T	3.82	2.29	2.09	2.70	1.33	2.72	2.60	2.60	2.47
MnO	0.26	0.12	0.10	0.13	0.08	0.09	0.11	0.12	0.11
MgO	17.33	17.74	17.20	19.09	16.10	18.02	17.93	17.38	18.08
CaO	18.58	21.00	20.84	20.60	22.18	18.78	19.81	19.30	19.91
Na_2O	1.06	1.13	1.44	0.69	1.25	1.63	1.20	1.45	1.19
K_2O	0.02	0.02	0.01	0.01	0.01	0.04	0.06	0.03	0.10
NiO	0.03	0.05	0.04	0.04	0.03	0.06	0.05	0.04	0.06
Total	99.21	99.90	99.78	99.53	99.75	99.59	99.26	99.66	99.93
Wo%	40.79	44.24	44.92	41.81	48.64	40.85	42.32	42.39	42.37

Table 2.2 cont.

Garnet	Group 1 Kimberlites							Group 2 Kimberlites					
Kimberlite:	**Letseng**	**Monastery**				**Bultfontein**	**Jagersfontein**	**Newlands**	**Finsch**				
Xenolith:	**09-LET-17**	**BD-2227**	**BD-2267**	**ROM-69**	**ROM-207A**	**09-BOS-05**	**JAG12-79**	**JJG-4401**	**FIN12-002**	**FIN12-003**	**FIN12-004**	**FIN12-006**	**FIN12-011**
	average n=9	average n=5	average n=25	average n=17	average n=7	average n=8	average n=3	average n=14	average n=7	average n=17	average n=7	average n=7	average n=11
SiO_2	41.94	41.98	42.27	42.63	42.43	42.11	42.19	42.35	41.19	42.14	42.16	42.13	41.35
TiO_2	0.91	0.00	0.14	0.01	0.03	0.03	0.01	0.02	0.07	0.39	0.28	0.36	0.18
Al_2O_3	20.22	22.47	22.57	21.70	24.00	21.17	23.65	21.41	16.57	21.43	20.63	20.55	19.36
Cr_2O_3	3.45	2.89	2.72	3.13	1.32	4.46	1.64	4.59	9.94	3.41	4.66	4.78	5.99
FeO_T	7.36	6.85	6.89	7.08	8.22	6.39	8.00	6.57	5.87	7.14	6.63	6.75	6.56
MnO	0.28	0.44	0.40	0.41	0.63	0.34	0.50	0.40	0.30	0.29	0.35	0.33	0.33
MgO	21.27	21.58	20.98	21.64	19.91	21.15	20.18	20.90	21.11	21.34	21.11	21.22	21.07
CaO	5.05	4.73	4.75	4.64	5.52	5.10	5.11	5.10	4.47	4.74	4.93	4.91	5.50
Na_2O	0.09	0.02	0.03	0.02	0.02	0.03	0.01	0.01	0.01	0.05	0.03	0.04	0.04
K_2O	0.00	0.01	0.28	0.01	0.01	0.00	0.01	0.01	0.00	0.00	0.00	0.01	0.01
NiO	0.02	0.02	0.01	0.03	0.01	0.02	0.01	0.02	0.01	0.02	0.01	0.02	0.02
Total	100.57	100.98	101.04	101.30	102.09	100.81	101.30	101.37	99.54	100.96	100.79	101.11	100.42
Cr#	10.27	7.95	7.50	8.83	3.56	12.39	4.44	12.56	28.69	9.65	13.15	13.51	17.20

Spinel	Group 1 Kimberlites											Group 2 Kimberlites			
Kimberlite:	**Letseng**	**Monastery**					**Bultfontein**		**Kimberley**	**Jagersfontein**		**Newlands**	**Finsch**		
Xenolith:	**09-LET-21**	**BD-2224**	**BD-2227**	**BD-2267**	**ROM-207A**		**04-BOS-46**	**09-BOS-52**	**09-KEN-38B**	**JAG12-133**	**JAG12-146**	**JJG-4407**	**FIN12-004**	**FIN12-006**	
	average n=7	average n=8	average n=3	average n=12	Cr-rich n=22	Al-rich n=9	average n=9	average n=3	average n=13	average n=11	average n=6	average n=3	average n=3	Cr-rich n=2	Al-rich n=2
SiO_2	0.04	0.78	0.03	0.03	0.05	0.45	0.04	0.05	0.02	1.27	0.03	0.04	0.08	0.13	0.12
TiO_2	0.06	0.49	0.12	0.32	0.03	0.02	0.75	1.51	2.46	0.80	1.01	0.03	0.17	0.96	0.18
Al_2O_3	28.61	13.48	13.26	14.88	19.98	64.35	14.78	11.88	1.35	14.37	11.34	32.89	50.78	19.85	52.64
Cr_2O_3	40.89	50.34	53.38	52.09	43.87	4.33	51.14	52.56	56.91	50.52	54.58	37.50	18.08	45.89	16.91
FeO_T	11.31	19.81	18.88	18.59	21.79	11.23	18.38	17.49	27.11	16.44	18.28	12.40	11.55	16.33	11.25
MnO	0.14	0.29	0.27	0.24	0.28	0.40	0.25	0.24	0.30	0.27	0.29	0.21	0.24	0.31	0.30
MgO	17.79	12.68	12.60	12.50	12.55	20.48	13.40	0.02	9.06	13.76	12.43	15.39	18.99	14.98	19.12
CaO	0.01	0.03	0.00	0.01	0.03	0.06	0.02	0.02	0.01	0.08	0.06	0.28	0.05	0.03	0.10
Na_2O	0.01	0.02	0.01	0.01	0.02	0.00	0.01	14.08	0.02	0.01	0.08	0.02	0.00	0.01	0.01
K_2O	0.00	0.01	0.00	0.01	0.01	0.02	0.01	0.01	0.01	0.02	0.01	0.01	0.01	0.04	0.01
NiO	0.18	0.10	0.09	0.10	0.18	0.31	0.14	0.15	0.13	0.14	0.10	0.09	0.11	0.17	0.08
Total	99.02	98.03	98.64	98.76	98.78	101.67	98.90	98.00	97.38	97.69	98.21	98.85	100.06	98.69	100.71
Cr#	49.08	71.48	72.99	70.16	59.55	4.33	76.21	75.09	96.58	70.72	76.62	43.34	19.30	61.60	17.82

Table 2.2 cont.

Phlogopite	**Group 1 Kimberlites**										**Group 2 Kimberlites**		
Kimberlite:	**Monastery**				**Bultfontein**		**Kimberley**	**Jagersfontein**			**Newlands**	**Finsch**	
Xenolith:	**BD-2224**	**BD-2227**	**BD-2267**	**ROM-207A**	**04-BOS-46**	**09-BOS-52**	**09-KEN-38B**	**JAG12-79**	**JAG12-133**	**JAG12-146**	**JJG-4401**	**FIN12-006**	**FIN12-016**
	average	average	average	average	average	average	average	average	average	average	average	average	average
	n=39	n=27	n=11	n=6	n=8	n=15	n=29	n=6	n=11	n=5	n=5	n=7	n=3
SiO_2	40.90	41.56	40.07	39.43	41.88	42.37	43.27	39.93	41.19	39.64	40.91	41.14	41.16
TiO_2	0.37	0.33	1.50	1.82	0.37	0.51	0.77	3.02	1.79	2.88	0.57	1.57	1.48
Al_2O_3	13.99	13.75	15.78	16.60	13.82	12.58	11.66	13.92	13.91	15.19	14.08	14.37	13.57
Cr_2O_3	0.98	0.95	1.46	1.23	1.03	0.90	0.47	1.36	1.22	1.95	1.76	2.31	1.58
FeO_T	2.66	2.92	3.90	4.28	2.39	2.53	3.42	3.61	4.31	3.43	2.97	3.66	3.90
MnO	0.03	0.03	0.04	0.07	0.01	0.03	0.02	0.05	0.09	0.03	0.04	0.07	0.06
MgO	25.44	25.46	22.88	21.83	25.45	25.74	25.74	22.68	23.15	21.89	24.14	22.79	23.33
CaO	0.02	0.01	0.02	0.60	0.00	0.00	0.01	0.00	0.06	0.01	0.00	0.02	0.00
Na_2O	1.20	0.77	0.59	0.51	0.66	0.30	0.18	0.37	0.55	0.65	0.24	0.21	0.21
K_2O	8.55	9.02	9.61	9.77	9.87	10.02	10.84	10.20	9.55	9.91	10.34	10.04	10.44
NiO	0.19	0.24	0.19	0.10	0.21	0.21	0.22	0.21	0.10	0.15	0.12	0.19	0.30
F	0.11	0.12	0.27	0.52	0.06	0.17	0.29	0.55	0.26	0.30	0.18	0.10	0.12
Total	94.33	95.04	96.04	96.24	95.69	95.19	96.59	95.34	95.92	95.71	95.37	96.47	96.15
Mg#	94.47	94.04	91.15	90.07	95.00	94.78	93.07	91.80	90.58	91.93	93.54	91.74	91.44

Amphibole	**Group 2**
Kimberlite:	**Newlands**
Xenolith:	**JJG-4401**
	average
	n=5
SiO_2	55.48
TiO_2	0.65
Al_2O_3	0.55
Cr_2O_3	0.38
FeO_T	1.78
MnO	0.06
MgO	22.42
CaO	7.02
Na_2O	3.51
K_2O	4.63
NiO	0.05
Total	96.53

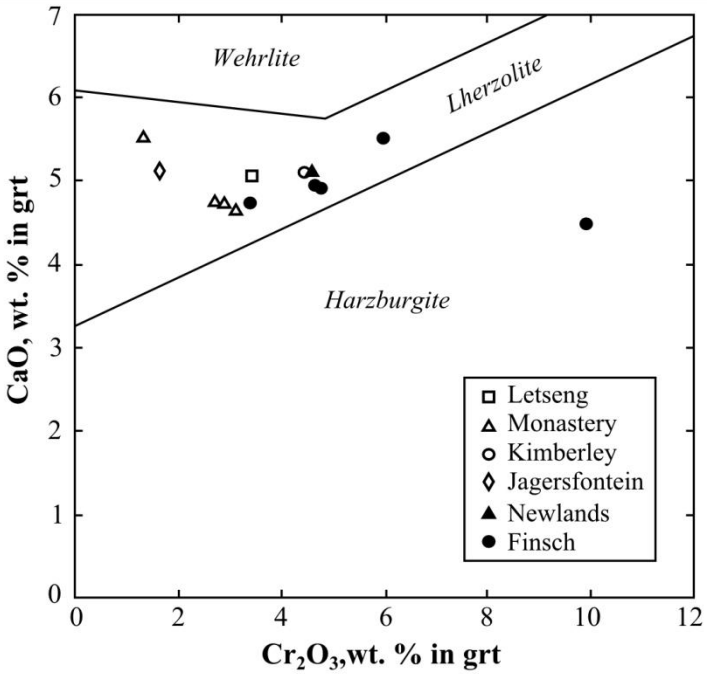

Figure 2.3. CaO vs. Cr_2O_3 in garnets of the Kaapvaal peridotites. All garnets are of the Lherzolite type, except FIN12-002 which is harzburgitic. Fields boundaries are from Dawson and Stephens, (1976) and Grütter et al., (2006)

tabular crystals up to 5 mm x 2 mm (Figure 2.2). In the other peridotites it is present as small grains and is found interstitially to the modally major silicates. Mg# ranges from 90.07-95.0 and TiO_2 between 0.33-3.02 wt. % (Table 2.2), and does not correlate with the size or habit of the phlogopite or with the peridotite location. Amphibole is present in Newlands peridotite JJG-4401, it is a potassium-richterite variety and occurs as an interstitial mineral. The amphibole has average K_2O of 4.63 wt. %, Na_2O of 3.51 wt. % and CaO of 7.02 wt. % (Table 2.2).

2.4.2. Pressure and temperature conditions at last equilibration

The pressure and temperature of equilibration have been calculated iteratively for the garnet and clinopyroxene bearing peridotites using four different pressure and temperature pairs. Nimis and Grütter, (2010) recommended the combination of the TA98 (opx-cpx solvus; Taylor, 1998) thermometer with the barometer NG85 (Al-in-opx; Nickel and Green, 1985). For the Kaapvaal peridotites this combination gives temperatures between 870-1370°C and pressures of 3.4-6.2 GPa, with one outlier at 2.3 GPa (Table 2.3). These data plot between the 40 mW/m^2 and 42 mW/m^2 geotherms (Figure 2.4) and fit well with previous estimates (Rudnick and Nyblade, 1999; Simon et al., 2007; Gibson et al, 2008; Lazarov et al., 2009b).

Table 2.3 Pressure and temperature estimates for the Kaapvaal peridotites

	T, °C opx-cpx TA98	P, Gpa Al-opx NG85	T, °C opx-cpx solvus BK90	P, Gpa Al-opx BK90	T, °C opx-grt NG09	P, Gpa Al-opx NG85	T, °C cpx NT00	P, Gpa cpx NT00
Letseng								
09-LET-17	1345	5.80	1359	6.97	1373	5.95	1240	4.47
09-LET-21	n.a.	n.a.	n.a.	n.a.	n.a.	n.a.	n.a.	n.a.
Monastery								
ROM-69	1051	4.35	979	4.40	836	3.19	867	3.65
ROM-207A	1248	5.32	1245	6.36	674	2.16	1081	1.78
BD-2224	n.a.	n.a.	n.a.	n.a.	n.a.	n.a.	906	3.57
BD-2227	1091	4.72	1027	4.89	909	3.71	915	3.56
BD-2267	870	3.38	710	3.01	801	3.00	642	2.67
Jagersfontein								
JAG12-79	1301	5.32	1311	6.22	599	1.60	1153	2.56
JAG12-133	n.a.	n.a.	n.a.	n.a.	n.a.	n.a.	1019	4.00
JAG12-146	n.a.	n.a.	n.a.	n.a.	n.a.	n.a.	961	3.92
Kimberley								
09-KEN-38B	n.a.	n.a.	n.a.	n.a.	n.a.	n.a.	1200	9.91
Bultfontein								
04-BOS-46	n.a.	n.a.	n.a.	n.a.	n.a.	n.a.	836	3.80
09-BOS-05	1127	4.73	1045	4.74	973	3.94	963	3.90
09-BOS-52	n.a.	n.a.	n.a.	n.a.	n.a.	n.a.	964	4.70
Newlands								
JJG-4401	1249	6.22	1217	6.75	912	4.30	n.a.	n.a.
JJG-4407	n.a.	n.a.	n.a.	n.a.	n.a.	n.a.	764	1.74
Finsch								
FIN12-002	n.a.	n.a.	n.a.	n.a.	1158	5.65	n.a.	n.a.
FIN12-003	1264	5.87	1246	6.67	1238	5.72	1158	5.07
FIN12-004	1242	5.67	1194	6.08	1241	5.67	1110	4.20
FIN12-006	n.a.	n.a.	1220	6.34	1179	5.42	1101	3.44
FIN12-011	1363	2.25	1090	1.76	1401	2.35	1112	4.11
FIN12-016	n.a.	n.a.	n.a.	n.a.	n.a.	n.a.	n.a.	n.a.

TA98: Taylor, 1998; NG88: Nickel and Green, 1985; BK90: Brey and Köhler 1990; NG09: Nimis and Grütter, 2009; NT00: Nimis and Taylor, 2000

The coupled thermometer and barometer of Brey and Köhler (1990; BK90, Al-in-opx barometer and opx-cpx solvus thermometer) also results in a wide spread with temperatures of 700-1360°C and pressures of 3.0-7.0 GPa, with one outlier at 1.8 GPa (Table 2.3). This data creates a distinct array, below the 40 mW/m^2 geotherm, however two peridotites sit between the 40-42 mW/m^2 geotherms (Figure 2.4). The thermometer NG09 (Mg-Fe in opx-grt; Nimis and Grütter, 2010) coupled with the barometer NG85 is recommended in garnet

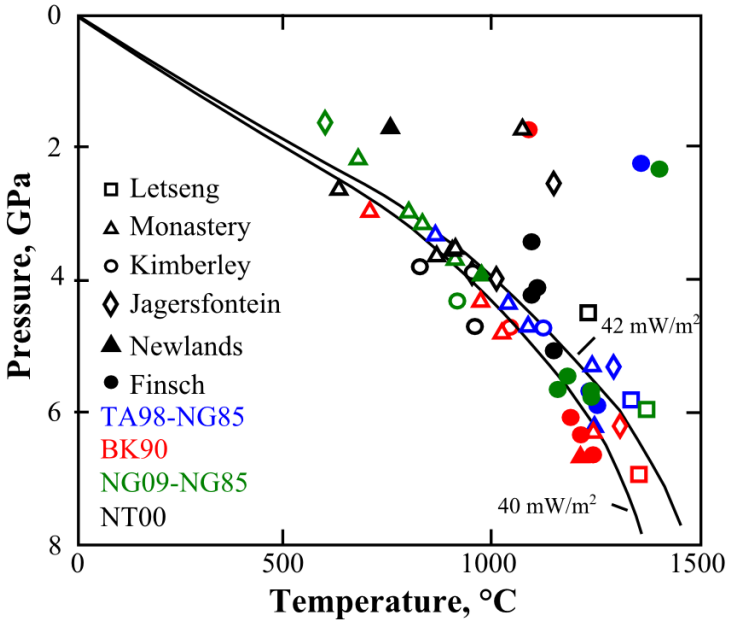

Figure 2.4. Pressure and temperature estimates for the Kaapvaal Peridotites, using four different thermometer and barometer calculations. All pairs were calculated iteratively. Paleogeotherms of 40mW/m2 and 42mW/m2 are indicated, after Chapman and Pollack (1977). TA98: Taylor, 1998; BK90: Brey and Köhler, 1990; NG85: Nickel and Green, 1985; NG09: Nimis and Grütter, 2010; NT00: Nimis and Taylor, 2000

peridotites with no clinopyroxene. Nevertheless, for completeness it was calculated for all garnet bearing peridotites. The results match well with the other thermobarometer combinations, with temperatures between 600-1380°C and pressures of 1.6-6.0 GPa. The majority of peridotites plot between the 40-42 mW/m^2 geotherms (Figure 2.4), however, the NG09-NG85 calculation does generally give lower temperatures and pressures. Finally, the clinopyroxene thermometer (enstatite-in-cpx) and barometer (Cr-in-cpx) NT00 (Nimis and Taylor, 2000) was used to also calculate temperature and pressure for peridotites containing no modal garnet. For further comparison the NT00 thermobarometer was also used for the garnet-bearing peridotites. From this calculation ten peridotites plot in the vicinity of the 40-42 mW/m^2 geotherms (Figure 2.4) with temperatures of 1080-1160 °C and pressures of 1.8-5.1 GPa (Table 2.3). While the other seven peridotites lie off the geotherms with temperatures up to 1240 °C and one peridotite with a significantly over estimated pressure (09-KEN-38B – 9.9 GPa; Table 2.3). The Monastery, Kimberley and Finsch peridotites are quite reproducible, with similar pressures and temperatures determined by each geothermobarometer combination (Table 2.3). Based off these calculations the depth of the lithosphere beneath the Group 1 and Group 2 kimberlites is between 150-180 km, except for Group 1 kimberlite Jagersfontein where it is only 140 km.

2.4.3. Whole-rock major and trace element compositions

The Kaapvaal peridotites are highly depleted in incompatible elements CaO (<1.4 wt. %) and Al_2O_3 (<2.1 wt. %) compared to the primitive mantle estimate (McDonough and Sun, 1995) and have high MgO contents of 38.69-44.43 wt. % (Table 2.4). MgO shows a negative correlation with CaO and Al_2O_3 as expected from residues of partial melting. There is a large range in Cr of 794-3027 ppm (Table 2.4), which shows a positive correlation with Al_2O_3. However, peridotites FIN12-002, FIN12-006 and FIN12-011 lie off this trend (Figure 2.5b). Due to the high SiO_2 contents (>39 wt. %), Mg/Si ratios are low <1.2 (Figure 2.5a) and plot well above the oceanic trend of Boyd (1989).

Primitive mantle normalised patterns generally show an enrichment over primitive mantle in the most incompatible elements, most notably in Rb_{PM} (0.7-61; sub-script PM denotes concentration normalised to primitive mantle), Ba_{PM} (3-92), U_{PM} (0.7-23; Figure 2.6). However, they are depleted in the most compatible elements such as Gd_{PM} (0.1-1.1) and Yb_{PM} (0.01-0.32). The Jagersfontein peridotites are all fairly reproducible with similar enrichment and depletion profiles. For the Monastery peridotites the general profile of the slope is the same across the five peridotites. However, they have slightly different enrichment degrees, most notably in the most compatible elements. In the compatible elements the peridotites can be defined by two groups with primitive mantle values of either ca. 0.5 or ca. 0.1 (Figure 2.6). All of the other localities display diverse enrichment profiles and slopes for each peridotite. The CI-chondrite (CI-chondrite from Anders and Grevesse, 1989) normalised rare earth element (REE) diagrams show a similar trend, with enrichment in the light-REE and generally a depletion of the heavy-REE (Lu_N of 0.06-1.01, sub-script N denotes concentration normalised to CI-chondrite; Figure 2.7). A number of peridotites, such as 09-LET-17 and FIN12-003, show a very limited depletion of the heavy-REE with chondrite normalised values close to one (Figure 2.7). La_N/Yb_N values vary significantly (2.3-162.8; Table 2.4) across the peridotites reflecting the large range in heavy-REE and light-REE fractionation. These variations in incompatible element show no correlation with either the kimberlite type or the terrane locality of the kimberlite, with distinct enrichment profiles seen across all localities.

2.4.4. Textural habit and major element composition of base metal sulphides

Base metal sulphides were found in 17 of the peridotites, with samples 09-LET-21, JAG12-79, JAG12-146, JJG-4407 and FIN12-002 being BMS free. Up to 60% of the BMS found in the Kaapvaal peridotites are found as small (<100 µm) interstitial grains. Inclusions

Table 2.4 Whole-rock major and trace elements of the Kaapvaal Peridotites

Group 1	**Letseng**		**Monastery**				
East	**09-LET-17**	**09-LET-21**	**ROM-69**	**ROM-207A**	**BD-2224**	**BD-2227**	**BD-2267**
SiO_2	41.77	44.67	43.06	43.61	46.64	45.37	44.86
Al_2O_3	1.64	0.81	1.05	1.72	2.08	1.07	1.32
Fe_2O_3	8.93	6.26	6.93	7.50	6.33	6.58	7.19
MnO	0.12	0.10	0.10	0.13	0.11	0.10	0.11
MgO	40.49	42.33	42.68	43.67	39.32	43.23	42.17
CaO	1.32	0.30	0.93	0.69	0.85	0.74	0.82
Na_2O	0.16	0.06	0.20	0.11	0.57	0.23	0.17
K_2O	0.01	0.00	0.15	0.19	0.86	0.21	0.32
TiO_2	0.16	0.01	0.05	0.06	0.08	0.03	0.10
P_2O_5	0.00	0.00	0.00	0.01	0.01	0.02	0.02
SO_3	0.06	0.07	0.03	0.00	0.05	0.02	0.01
L.O.I.	4.70	4.70	4.04	1.38	1.82	1.41	2.22
Total	99.36	99.31	99.22	99.07	98.72	99.01	99.31
Sc	20.5	9.8	12.2	30.6	20.1	11.6	11.0
V	40	16	25	19	49	20	27
Cr	2538	1260	1952	2295	2677	1704	1788
Co	127	113	123	113	93	115	110
Ni	1962	2010	2124	1869	1624	2106	1937
Cu	12	1	4	7	4	3	5
Zn	56.88	20.89	32.46	33.04	32.38	48.37	29.04
Rb	0.61	0.46	11.59	12.58	26.17	8.56	15.48
Ba	35.97	131.17	28.76	61.12	610.66	37.54	84.00
Nb	0.73	1.02	7.11	6.56	25.40	7.99	6.91
La	0.55	1.99	3.21	2.97	5.17	3.23	3.91
Ce	1.33	4.36	7.22	5.99	12.74	6.87	7.79
Pr	0.19	0.48	0.93	0.71	1.61	0.80	0.87
Sr	9.73	12.83	44.41	60.99	95.62	36.19	46.57
Nd	0.91	1.56	3.36	2.63	5.95	3.13	3.08
Sm	0.26	0.15	0.50	0.45	0.88	0.50	0.47
Zr	7.83	1.73	13.17	12.43	11.52	11.92	15.58
Eu	0.09	0.03	0.13	0.13	0.22	0.14	0.12
Ti	1071	22	303	345	550	183	682
Gd	0.28	0.09	0.34	0.36	0.60	0.35	0.32
Tb	0.05	0.01	0.04	0.05	0.07	0.04	0.04
Dy	0.26	0.04	0.17	0.26	0.34	0.20	0.16
Y	1.55	0.18	0.73	1.55	1.71	0.82	0.70
Ho	0.05	0.01	0.03	0.05	0.06	0.03	0.03
Er	0.15	0.01	0.05	0.14	0.14	0.07	0.06
Th	*54.02*	*169.86*	*347.87*	*379.08*	*1017.82*	*391.64*	*610.49*
U	*15.20*	*41.37*	*125.72*	*90.30*	*189.00*	*100.60*	*143.12*
Pb	*870.15*	*268.71*	*353.92*	*224.97*	*427.01*	*621.33*	*337.73*
Hf	*204.74*	*32.43*	*312.97*	*310.92*	*235.62*	*281.52*	*380.46*
Tm	*21.15*	*1.49*	*6.19*	*18.35*	*18.35*	*7.64*	*6.78*
Yb	*138.52*	*8.46*	*33.93*	*141.87*	*115.16*	*44.78*	*41.59*
Lu	*20.29*	*1.49*	*4.64*	*24.60*	*16.43*	*5.98*	*5.82*
La_N/Yb_N	2.77	162.79	31.06	49.94	65.03	65.54	14.48

major element oxides in wt. %, trace elements in ppm, except those in italics which are ppb

Table 2.4 cont.

Group 1	Kimberley	Bultfontein			Jagersfontein		
West	09-KEN-38B	04-BOS-46	09-BOS-05	09-BOS-52	JAG12-79	JAG12-133	JAG12-146
SiO_2	43.62	42.48	43.81	40.22	43.82	43.60	43.85
Al_2O_3	0.97	1.04	1.35	0.37	1.10	0.92	0.71
Fe_2O_3	7.68	6.24	6.47	6.74	6.33	6.38	6.53
MnO	0.11	0.09	0.10	0.09	0.10	0.10	0.10
MgO	39.91	40.87	42.46	44.43	41.42	42.39	41.59
CaO	1.25	0.64	0.61	0.30	0.62	0.57	0.54
Na_2O	0.19	0.20	0.12	0.12	0.10	0.19	0.09
K_2O	0.71	0.41	0.05	0.21	0.21	0.36	0.17
TiO_2	0.20	0.05	0.02	0.07	0.08	0.10	0.07
P_2O_5	0.03	0.03	0.01	0.04	0.01	0.03	0.02
SO_3	0.16	0.17	0.00	0.26	0.00	0.01	0.00
L.O.I.	4.54	7.57	4.50	7.23	5.55	4.75	5.51
Total	99.37	99.79	99.50	100.08	99.34	99.40	99.18
Sc	11.6	12.2	13.5	6.5	12.4	9.2	8.9
V	27	20	23	12	25	21	19
Cr	1407	1800	2563	794	2483	1497	1548
Co	103	105	113	134	115	110	115
Ni	1770	1862	1979	2692	2014	2002	1971
Cu	13.86	5.22	1.36	4.04	3.44	7.06	3.64
Zn	53.38	23.22	47.59	48.94	24.72	31.99	31.96
Rb	36.82	15.16	3.08	7.85	14.64	16.38	8.03
Ba	77.08	164.21	18.62	103.13	45.40	90.55	58.60
Nb	5.62	4.57	2.84	7.20	6.07	8.54	6.14
La	4.70	3.64	2.20	5.52	3.83	5.40	3.84
Ce	8.90	7.82	4.43	10.88	7.30	10.00	7.08
Pr	0.99	0.96	0.52	1.21	0.81	1.09	0.77
Sr	62.40	49.74	25.29	39.64	44.90	65.91	35.27
Nd	3.57	3.73	1.99	4.31	2.87	3.77	2.74
Sm	0.59	0.62	0.40	0.65	0.44	0.54	0.41
Zr	39.26	11.23	12.56	15.51	8.36	10.14	7.27
Eu	0.15	0.16	0.11	0.17	0.11	0.14	0.10
Ti	1322	344	99	519	560	676	447
Gd	0.39	0.45	0.33	0.42	0.27	0.33	0.25
Tb	0.05	0.05	0.04	0.05	0.03	0.04	0.03
Dy	0.21	0.22	0.17	0.19	0.13	0.15	0.12
Y	0.83	0.88	0.62	0.74	0.55	0.61	0.58
Ho	0.03	0.03	0.02	0.03	0.02	0.02	0.02
Er	0.07	0.07	0.04	0.05	0.04	0.05	0.05
Th	*567.45*	*408.21*	*257.91*	*647.93*	*406.90*	*607.45*	*504.78*
U	*169.48*	*117.39*	*79.37*	*159.43*	*73.39*	*108.33*	*77.23*
Pb	*533.54*	*418.80*	*219.16*	*528.59*	*297.14*	*645.85*	*504.39*
Hf	*1142.27*	*271.32*	*265.20*	*332.85*	*182.06*	*218.87*	*154.21*
Tm	*7.37*	*8.30*	*5.28*	*4.92*	*5.60*	*5.96*	*6.39*
Yb	*49.70*	*44.78*	*35.19*	*32.86*	*35.11*	*28.91*	*34.07*
Lu	*5.30*	*5.85*	*5.41*	*3.64*	*4.85*	*4.23*	*6.04*
La_N/Yb_N	65.42	56.23	43.29	116.23	75.60	129.38	77.95

major element oxides in wt. %, trace elements in ppm, except those in italics which are ppb

Table 2.4 cont.

Group 2	Newlands		Finch					
West	**JJG-4401**	**JJG-4407**	**FIN12-002**	**FIN12-003**	**FIN12-004**	**FIN12-006**	**FIN12-011**	**FIN12-016**
SiO_2	45.20	44.17	39.88	40.93	39.79	39.44	40.54	39.03
Al_2O_3	0.86	1.44	0.51	2.26	1.19	1.15	0.97	0.38
Fe_2O_3	5.84	6.77	6.40	7.75	7.83	7.56	7.04	6.63
MnO	0.10	0.10	0.09	0.12	0.11	0.10	0.11	0.09
MgO	42.72	42.40	43.50	38.69	42.04	41.38	41.14	43.88
CaO	0.60	0.81	0.23	1.36	0.61	0.53	0.60	0.24
Na_2O	0.13	0.10	0.07	0.14	0.09	0.09	0.09	0.07
K_2O	0.41	0.12	0.04	0.03	0.08	0.14	0.03	0.04
TiO_2	0.04	0.01	0.02	0.07	0.05	0.05	0.04	0.03
P_2O_5	0.03	0.00	0.00	0.00	0.00	0.00	0.01	0.00
SO_3	0.00	0.06	0.07	0.12	0.12	0.16	0.24	0.00
L.O.I.	2.77	3.17	8.74	7.24	7.76	9.05	8.38	8.86
Total	98.70	99.15	99.55	98.71	99.67	99.65	99.19	99.25
Sc	11.1	11.2	12.2	23.8	17.3	14.0	16.6	12.1
V	20	24	17	41	26	28	28	15
Cr	1631	2191	2806	3027	2473	2282	2815	2508
Co	107	108	121	120	125	123	118	129
Ni	1938	1961	2074	1897	2007	2005	1906	2204
Cu	3.04	2.74	3.67	18.89	10.06	12.45	4.35	5.47
Zn	23.26	19.83	31.91	44.78	91.26	38.35	34.35	33.46
Rb	19.61	4.75	1.68	1.43	3.43	4.87	1.46	1.53
Ba	168.10	53.90	25.42	17.60	46.98	33.06	51.17	15.44
Nb	5.83	2.03	0.93	0.45	0.98	1.12	1.53	0.81
La	6.04	3.00	1.04	0.35	1.37	1.35	1.97	0.76
Ce	10.66	5.13	2.09	0.75	2.83	2.65	3.91	1.52
Pr	1.10	0.51	0.24	0.10	0.32	0.30	0.46	0.18
Sr	91.01	29.50	4.64	6.04	10.99	7.98	19.39	6.63
Nd	3.46	1.62	0.85	0.46	1.16	1.10	1.56	0.68
Sm	0.35	0.16	0.13	0.14	0.18	0.18	0.23	0.11
Zr	5.81	3.62	3.91	3.54	5.93	5.97	9.73	3.38
Eu	0.07	0.03	0.03	0.05	0.05	0.05	0.05	0.02
Ti	213	48	94	407	332	317	243	214
Gd	0.18	0.09	0.08	0.16	0.15	0.15	0.16	0.06
Tb	0.02	0.01	0.01	0.03	0.02	0.03	0.02	0.01
Dy	0.08	0.04	0.03	0.17	0.13	0.14	0.10	0.04
Y	0.43	0.26	0.15	1.06	0.82	0.84	0.47	0.19
Ho	0.02	0.01	0.01	0.04	0.03	0.03	0.02	0.01
Er	0.04	0.03	0.01	0.11	0.09	0.08	0.04	0.02
Th	*653.74*	*635.64*	*132.65*	*46.51*	*164.01*	*281.83*	*206.21*	*93.95*
U	*127.25*	*83.23*	*47.60*	*11.46*	*41.90*	*477.21*	*48.58*	*34.20*
Pb	*1052.12*	*557.17*	*1031.15*	*73.07*	*546.09*	*381.41*	*323.63*	*251.63*
Hf	*131.32*	*66.66*	*88.02*	*95.10*	*158.84*	*139.62*	*238.18*	*88.18*
Tm	*4.99*	*4.74*	*1.75*	*16.87*	*13.00*	*11.78*	*6.00*	*2.50*
Yb	*33.04*	*34.07*	*12.72*	*105.99*	*85.85*	*79.49*	*39.13*	*15.86*
Lu	*4.35*	*5.32*	*2.14*	*17.49*	*13.99*	*13.00*	*6.72*	*2.74*
La_N/Yb_N	126.53	60.87	56.87	2.30	11.07	11.72	34.85	33.15

major element oxides in wt. %, trace elements in ppm, except those in italics which are ppb

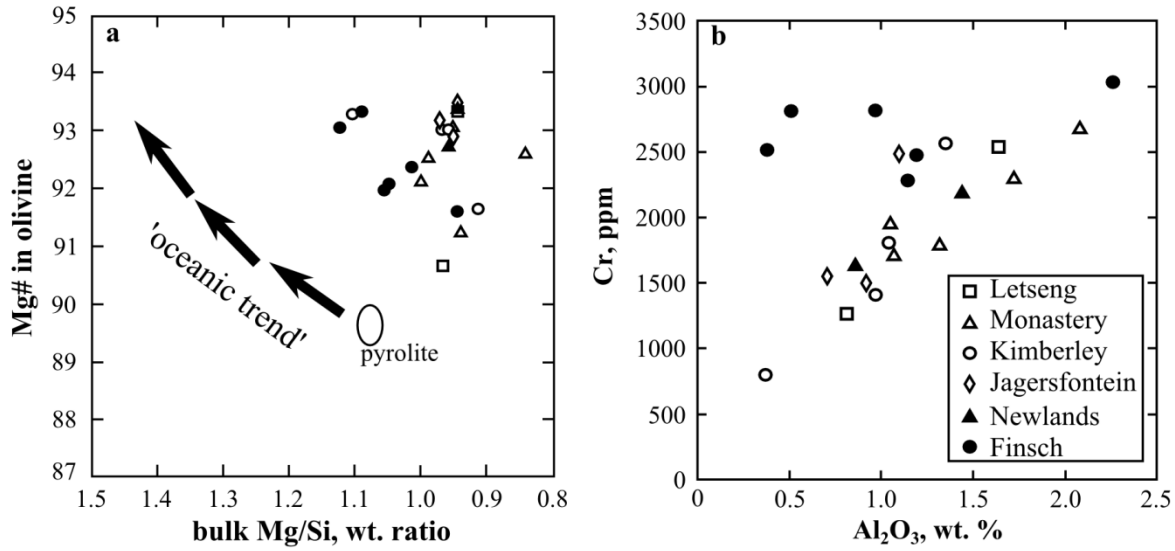

Figure 2.5. a) Mg# in olivine vs bulk Mg/Si ratio, the Kaapvaal peridotite samples plot well above the oceanic trend of Boyd (1989), large open circle is pyrolite composition (Ringwood, 1975)

in silicates are generally very small (<50 µm) and compose 19% of the BMS found. The final habit of the BMS accounts for 21% of all BMS and will be referred to as "pseudo-inclusions". This habit describes BMS that exhibit pseudo-rounded morphology, are generally between 50-100 µm and are contained within an optically continuous silicate that is sometimes serpentinised, such that the BMS pseudo-inclusions are in contact with the interstitial medium (see Figure 2.13). As such, pseudo-inclusion BMS could once have been isolated as an inclusion within the silicate. Peridotite BD-2224 is an unusual sample as it contains BMS of up to 1 mm x 0.5 mm that form as large tabular grains, and therefore cannot be described by the habits detailed above.

Pentlandite is the main BMS composition across all of the peridotites, with heazlewoodite (Letseng, Monastery, Kimberley, Jagersfontein) and monosulphide solid solution (mss; Monastery, Newlands) also present in minor quantities. Chalcocite is the most common Cu-mineral, present in peridotites ROM-207A, FIN12-003 and FIN12-004. Minor amounts of chalcopyrite are located in 09-LET-17 and 04-BOS-46, whilst JAG12-133 contains native copper.

Pentlandite has a range of compositions with Ni and Fe contents varying (25.80-41.80 wt. % Fe, 25.29-43.29 wt. % Ni, Table 2.5). Pentlandite is the only BMS composition that is present in each of the three textural habits. The composition of the pentlandite varies independently of the textural habit, with every habit hosting pentlandite of variable composition. Every locality has both Fe and Ni-rich pentlandite, however, Ni-rich pentlandite are predominantly located in peridotites from Finsch (Table 2.5). The compositions of Finsch

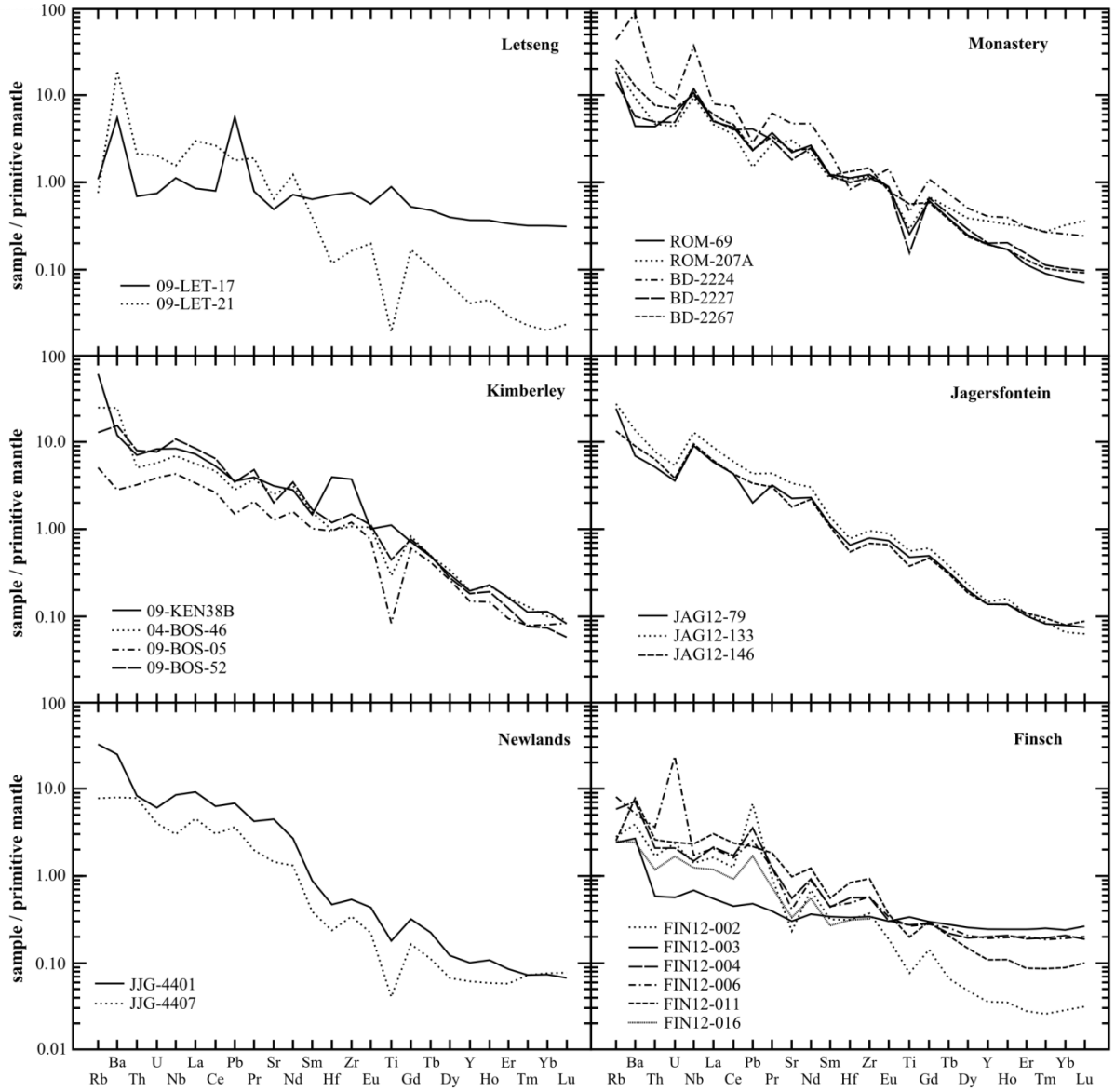

Figure 2.6. Primitive mantle normalised incompatible trace element plots for the Kaapvaal peridotites. All samples display enrichment in the most incompatible elements. Primitive mantle after McDonough and Sun (1995)

pentlandite have a (M:S = (Fe + Ni + Cu) / S) ranging from 1.08-1.11, with Ni contents between 35.93-41.57 wt. %. Monastery and Kimberley are dominated by pentlandite with Ni:Fe close to 1, with a broad range in Ni contents of 30.77-41.55 wt. % (most <36 wt. %).

Heazlewoodite is predominantly interstitial and generally occurs in multi-phase BMS with pentlandite. In one interstitial BMS the heazlewoodite is associated to chalcocite. There are two instances of heazlewoodite present in a pseudo-inclusion habit, where it is associated to pentlandite or a Cu-Ni-Fe-sulphide (Table 2.5). The heazlewoodite is fairly homogeneous in composition with an average Ni content of 69.71 ± 3.5 wt. % (1-s.d.), Fe is generally low (<3 wt. %). The composition of the heazlewoodite does not vary based on habit or mineral

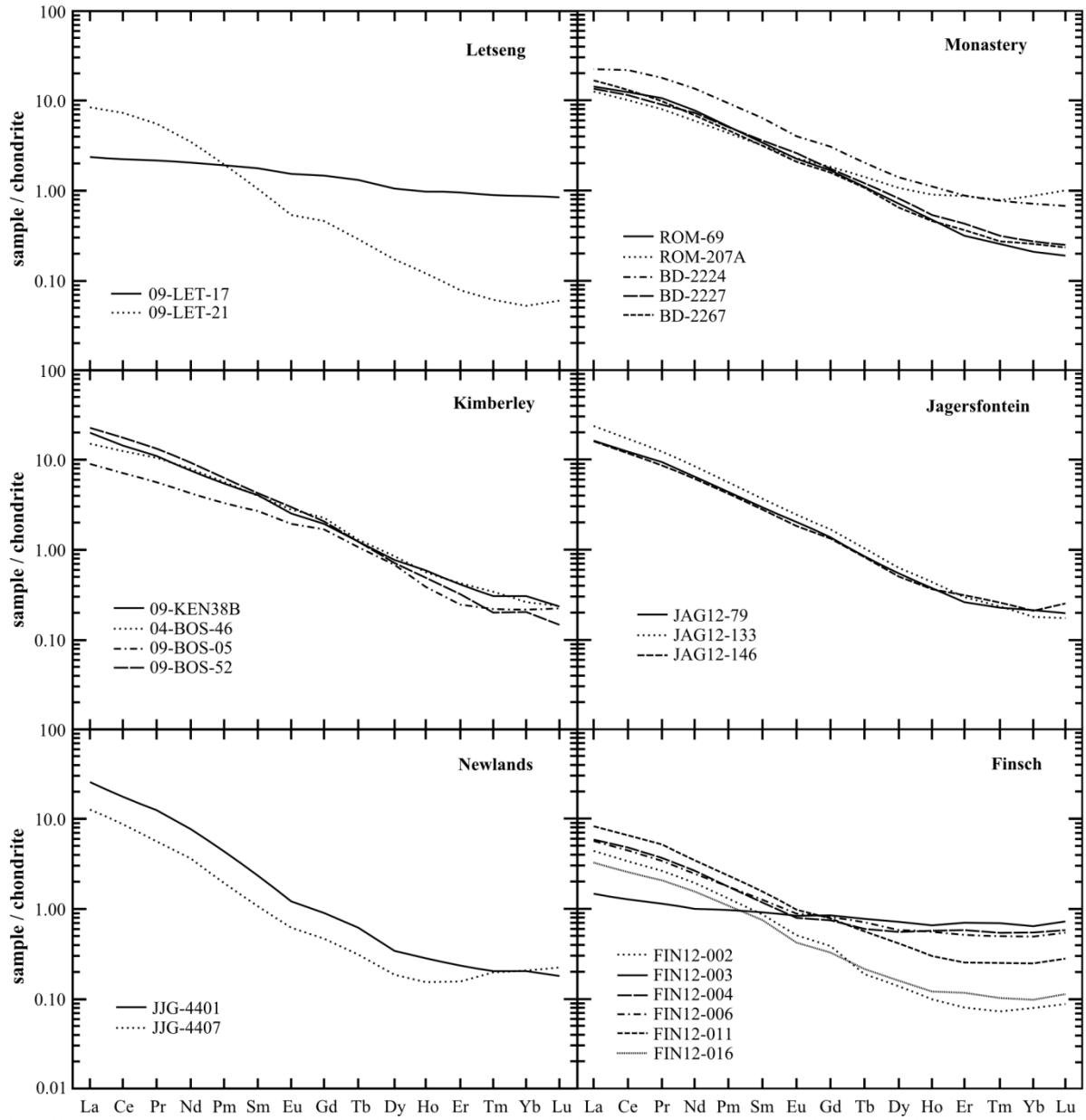

Figure 2.7. CI-chondrite normalised rare earth element (REE) plot for the Kaapvaal peridotites. Samples show a variable range in enrichment of the light-REE and depletion in heavy-REE. CI-chondrite from Anders and Grevesse, (1989).

associations; heazlewoodite present with Ni-rich pentlandite has both high and low Ni contents.

Monosulphide solid solution occurs as an isolated inclusion associated to pentlandite in two peridotites (BD-2227 and JJG-4401). The two mss have very different compositions, the version in Monastery is significantly Ni rich (24.48 wt. %) with no Cu and an Fe of 35.66 wt. % (M:S 0.9; Table 2.5). Whereas the mss in Newlands is Fe rich (53.91 wt. %) and Ni poor (7.81 wt. %) with a high M:S of 0.96 (Table 2.5).

Table 2.5. Single grain BMS electron microprobe and $^{187}Os/^{188}Os$ results

Xenolith	BMS	Habit	O	S	Fe	Ni	Cu	Co	Total	M:S	Mineral	Os, ppb	$^{187}Os/^{188}Os$	2-s.d.	T_{RD}, Ga	2-s.e.
Letseng																
09-LET-17	*n.a.*	*interstitial*	*0.29*	*34.14*	*38.15*	*27.57*	*0.00*	*0.12*	*100.26*	*1.08*	*pentlandite*	*n.a.*	*n.a.*	*n.a.*	*n.a.*	*n.a.*
			0.15	*26.24*	*2.70*	*69.41*	*0.00*	*0.89*	*99.38*	*1.50*	*heazlewoodite*					
09-LET-17	*n.a.*	*interstitial*	*0.02*	*32.88*	*27.67*	*39.27*	*0.00*	*0.28*	*100.11*	*1.14*	*pentlandite*	*n.a.*	*n.a.*	*n.a.*	*n.a.*	*n.a.*
			0.08	*33.96*	*31.66*	*0.38*	*32.32*	*0.00*	*98.40*	*1.02*	*chalcopyrite*					
Monastery																
BD-2224	**Mon-7**	inclusion	0.06	33.04	34.09	32.25	0.00	1.09	100.53	1.13	pentlandite	n.a.	0.13580	0.00183	-8.62	0.51
BD-2227	*n.a.*	*interstitial*	*0.33*	*27.17*	*0.60*	*71.41*	*0.00*	*0.58*	*100.10*	*1.45*	*heazlewoodite*	*n.a.*	*n.a.*	*n.a.*	*n.a.*	*n.a.*
BD-2227	*n.a.*	*inclusion*	*0.19*	*37.39*	*35.66*	*24.48*	*0.00*	*0.41*	*98.13*	*0.90*	*mss*	*n.a.*	*n.a.*	*n.a.*	*n.a.*	*n.a.*
			0.60	*32.06*	*26.81*	*37.26*	*0.00*	*0.71*	*97.42*	*1.11*	*pentlandite*					
ROM-207A	*n.a.*	*interstitial*	*0.07*	*26.93*	*0.35*	*73.38*	*0.00*	*0.07*	*100.79*	*1.50*	*heazlewoodite*	*n.a.*	*n.a.*	*n.a.*	*n.a.*	*n.a.*
			0.05	*20.22*	*0.44*	*3.71*	*75.47*	*0.07*	*99.97*	*2.00*	*chalcocite*					
Bultfontein																
09-BOS-05	**Bult-3**	pseudo	0.24	32.11	30.49	36.12	0.00	0.80	99.76	1.16	pentlandite	n.a.	0.10840	0.00062	2.86	0.16
			18.66	13.45	51.75	14.70	0.05	0.16	98.76	2.81	oxidised					
09-BOS-05	**Bult-4**	inclusion	0.05	31.67	25.78	41.55	0.00	0.79	99.84	1.18	pentlandite	n.a.	0.10659	0.00032	3.09	0.85
09-BOS-52	**Bult-5**	pseudo	1.08	26.52	2.38	70.03	0.00	0.01	100.02	1.49	heazlewoodite	n.a.	0.10565	0.00023	3.22	0.63
			22.45	4.87	61.34	7.02	0.06	0.08	95.82	-	magnetite					
			4.25	17.89	9.46	7.32	56.02	0.13	95.08	2.11	Cu-Fe-Ni-S					
Kimberley																
09-KEN38B	*n.a.*	*interstitial*	*0.21*	*32.35*	*39.06*	*28.78*	*0.00*	*0.30*	*100.69*	*1.18*	*pentlandite*	*n.a.*	*n.a.*	*n.a.*	*n.a.*	*n.a.*
Jagersfontein																
JAG12-133	**Jag-1**	interstitial	0.05	26.04	1.06	72.39	0.00	0.07	99.60	1.54	heazlewoodite	1258	0.21899	0.00044	-1.38	0.16
			11.11	0.35	1.49	3.62	83.48	0.06	100.10	-	Copper					
			0.63	0.06	4.39	0.50	94.47	0.08	100.12	-	Copper					
Newlands																
JJG-4401	*n.a.*	*inclusion*	*0.20*	*36.74*	*53.91*	*7.81*	*0.00*	*0.21*	*98.88*	*0.96*	*mss*	*n.a.*	*n.a.*	*n.a.*	*n.a.*	*n.a.*
			0.27	*32.47*	*28.93*	*37.08*	*0.00*	*0.15*	*98.91*	*1.14*	*pentlandite*					
Finsch																
FIN12-003	**Fin-2**	interstitial	0.28	33.00	26.49	39.26	0.00	1.00	100.04	1.11	pentlandite	n.a.	0.13915	0.00052	-1.33	0.15
FIN12-003	**Fin-3**	pseudo	0.187	33.48	26.08	40.27	0.00	0.88	100.91	1.10	pentlandite	343	0.13906	0.00030	-1.32	0.08
			0.533	32.89	25.43	31.09	8.13	0.72	98.79	1.08	Cu-pentlandite					
FIN12-006	**Fin-4**	interstitial	0.00	33.33	32.66	33.11	0.00	0.79	99.88	1.10	pentlandite	3637	0.11338	0.00073	2.20	0.19
FIN12-006	**Fin-5**	interstitial	0.00	33.54	26.82	39.89	0.00	0.89	101.13	1.11	pentlandite	1276	0.14434	0.00193	-2.07	0.55
			0.00	26.32	12.54	0.11	61.19	0.00	100.16	1.45	Fe-chalcocite					
FIN12-011	**Fin-6**	pseudo	0.43	33.375	36.08	30.13	0.00	0.53	100.54	1.11	pentlandite	n.a.	0.11094	0.00010	2.52	0.03
			27.70	0.08	70.10	0.11	0.02	0.03	98.04	-	magnetite					
FIN12-016	**Fin-7**	pseudo	14.48	14.686	34.19	34.74	0.00	0.31	98.43	2.63	oxidised	16849	0.10835	0.00012	2.86	0.03
			15.17	14.468	39.91	26.25	0.28	2.18	98.26	2.58	oxidised					
FIN12-003	*n.a.*	*interstitial*	*0.81*	*21.87*	*3.91*	*0.17*	*74.74*	*0.00*	*101.49*	*1.83*	*chalcocite*	*n.a.*	*n.a.*	*n.a.*	*n.a.*	*n.a.*
			0.07	*33.29*	*25.80*	*40.64*	*0.00*	*0.52*	*100.31*	*1.11*	*pentlandite*					
FIN12-004	*n.a.*	*interstitial*	*0.47*	*21.29*	*2.73*	*0.27*	*75.45*	*0.06*	*100.31*	*1.87*	*chalcocite*	*n.a.*	*n.a.*	*n.a.*	*n.a.*	*n.a.*
			0.76	*32.82*	*25.56*	*39.99*	*0.00*	*0.73*	*99.88*	*1.11*	*pentlandite*					

Model ages calculated using present-day primitive mantle $^{187}Os/^{188}Os$ of 0.1296 and a $^{187}Re/^{188}Os$ of 0.435 (Becker et al., 2006). Sub-script N denotes value normalised to CI-chondrite (CI-chondrite values from Anders and Grevesse, 1989). Bold for BMS analysed for $^{187}Os/^{188}Os$ compositions, italtics for representative BMS. See Section 2.4.4 for habit descriptions

Chalcopyrite is present twice and is always associated to pentlandite. In 09-LET-17 it occurs as an interstitial BMS, whilst in 04-BOS-46 it is an isolated inclusion. Despite the different localities and habits, the chalcopyrite has very similar composition with a Cu content of 32.3 wt. %, Ni of 0.37 wt. %, Fe of 31.67-32.34 wt. % and S between 33.09-33.96 wt. % (Table 2.5).

Chalcocite is always interstitial, in the Finsch peridotites it is associated to pentlandite whilst in Monastery peridotite ROM-207A it is associated to heazlewoodite. In the Finsch peridotites the chalcocite is fairly homogeneous with Cu content of 73.21-75.45 wt. %, Ni is always <0.36 wt. %, with Fe between 2.38-5.13 wt. % (Table 2.5). The chalcocite in Monastery has a similar Cu content (75.47 wt. %), however the Fe is low (0.44 wt. %) with high Ni (3.71 wt. %; Table 2.5).

Native copper in JAG12-133 is also always interstitial and associated to either pentlandite or heazlewoodite, with Cu contents >95 wt. %, except in one heazlewoodite-native Cu BMS (Jag-1; Figure 2.13), where the Cu is oxidised and has a Cu of 83.48 wt. % (O of 11.11 wt. %; Table 2.5).

2.4.5. HSE concentrations and systematics, and major element-HSE correlations

The HSE concentrations are highly variable through-out the peridotite localities analysed. Compared to the primitive upper mantle estimate (PUM: from Becker et al., 2006) the majority of samples are depleted in Os and Ir, but the Os/Ir follows the trend of the PUM. Three Monastery peridotites, one Kimberley and one Finsch peridotite are enriched in Os and sometimes Ir over PUM (Figure 2.8; Table 2.6). Three peridotites lie significantly above the PUM Os/Ir trend, with one of these peridotites (09-LET-21) having an Os concentration lower than PUM (3.68 ppb), but a significantly lower Ir (1.25 ppb; Table 2.6). Kimberley peridotite (04-BOS-46) is the only peridotite enriched in Pt compared to PUM, with a Pt concentration of 9.24 ppb. These variations compared to PUM are similar to previously reported data from Kaapvaal (Pearson et al., 2004).

The HSE show some correlations with one-another, a broad positive correlation is seen between Os-Ir (Figure 2.8), Pt-Pd and Pt-Re (Figure 2.9). The Os-Ir correlation is well defined and follows the $(Os/Ir)_{PUM}$. The correlation is reflected in all peridotites except 09-LET-21, BD-2227 and BD-2267 (Figure 2.8). The correlations between Pt-Pd and Pt-Re are scattered but show a general positive trend (Figure 2.9), which for Pt-Re generally mimics the PUM Pt/Re trend. No correlation is seen between the HSE and melt depletion parameters such as Al_2O_3 and MgO.

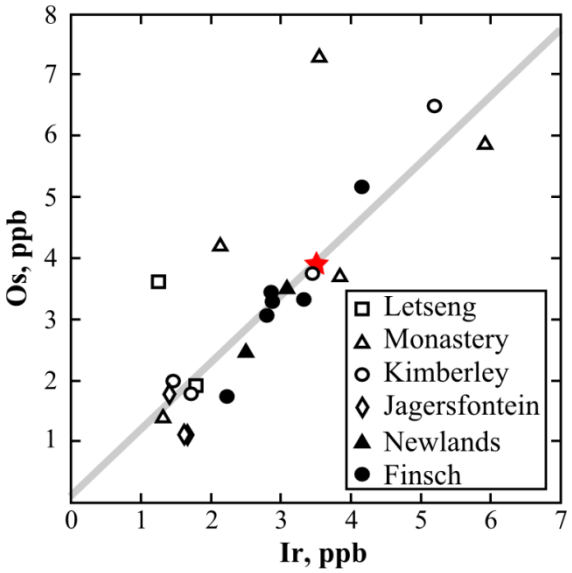

Figure 2.8. Os vs Ir bivariate plot for the Kaapvaal peridotites. Red star is PUM composition and grey line is the trend of PUM Os/Ir (PUM from Becker et al., 2006).

The high variability of the HSE concentrations is reflected in CI-chondrite normalised diagrams (Figure 2.10). These patterns show a range of depletion profiles, from peridotite JJG-4401 displaying the largest depletion in Pt and Pd (Pt_N/Ir_N 0.05, Pd_N/Pt_N 0.01), toperidotite FIN12-003 and 09-LET-17 exhibiting a positive slope from Ir to Pd and the highest enrichment in Pt and Pd (Pt_N/Ir_N 1.29-1.61, Pd_N/Pt_N 0.67-1.49). Os_N/Ir_N also shows high variability, nine peridotites have a range of 0.96-1.08 whilst the other 15 range between 0.66-2.85 (average 1.28±0.64; Table 2.6). The Re is also highly variably with Re_N/Pd_N of between 0.26-9.88. As with the other geochemical systematics, the HSE show no correlation between enrichment/depletion and the localities and kimberlite types.

2.4.6. Whole-rock Re-Os systematics and model ages

As with all of the other parameters the $^{187}Os/^{188}Os$ composition varies significantly between the localities and within each locality. Overall the Kaapvaal peridotites have unradiogenic $^{187}Os/^{188}Os$ of between 0.10511-0.12079 (Table 2.6). The $^{187}Os/^{188}Os$ compositions show no correlations with 1/Os (Figure 2.11a), either across the peridotite suite or within a locality, suggesting the control on Os composition is not a simple two-component mixing. There is also no correlation between $^{187}Os/^{188}Os$ and Al_2O_3 (Figure 2.11b) therefore, the variation in the Os signature is not partial melting related. However, $^{187}Os/^{188}Os$ shows a broad positive correlation with Pd_N/Ir_N (Figure 2.11c).

Despite the large range in $^{187}Os/^{188}Os$ and $^{187}Re/^{188}Os$ compositions, no isochron can be formed either with the whole peridotite suite or within a locality. Therefore Re-Os model

Table 2.6 $^{187}Os/^{188}Os$ compositions, model ages and HSE concentrations and inter-element ratios for the Kaapvaal peridotites

Xenolith	Os, ppb	Ir, ppb	Pt, ppb	Pd, pbb	Re, ppb	Os_N/Ir_N	Pt_N/Ir_N	Pd_N/Ir_N	Pd_N/Pt_N	Re_N/Pd_N	$^{187}Re/^{188}Os$	$^{187}Os/^{188}Os$	2-s.d.	T_{MA}, Ga	T_{RD}, Ga	T_{RDerup}, Ga
Letseng																
09-LET-17	1.95	1.80	5.96	4.00	0.066	1.05	1.61	1.91	0.67	0.26	0.17	0.11963	0.00010	2.20	1.36	1.40
09-LET-21	3.68	1.25	0.57	0.03	0.019	2.85	0.22	0.02	0.05	9.88	0.03	0.10942	0.00012	2.88	2.72	2.73
Monastery																
ROM-69	3.79	3.84	1.30	0.20	0.033	0.96	0.16	0.04	0.15	2.63	0.04	0.10880	0.00019	3.11	2.80	2.81
ROM-207A	1.44	1.32	1.09	0.03	0.011	1.06	0.40	0.02	0.02	6.35	0.04	0.10907	0.00038	3.03	2.77	2.77
BD-2224	5.99	5.91	0.25	1.15	0.095	0.98	0.02	0.17	4.55	1.26	0.08	0.11200	0.00054	2.88	2.38	2.40
BD-2227	7.45	3.54	1.71	0.16	0.054	2.04	0.23	0.04	0.10	5.02	0.04	0.11002	0.00019	2.87	2.64	2.65
BD-2267	4.31	2.13	1.22	0.39	0.091	1.96	0.28	0.16	0.32	3.63	0.10	0.11260	0.00021	3.00	2.30	2.32
Kimberley																
09-KEN-38B	2.01	1.46	1.55	0.87	0.043	1.33	0.52	0.51	0.56	0.76	0.10	0.11100	0.00024	3.29	2.51	2.53
Bultfontein																
04-BOS-46	6.47	5.21	9.24	4.55	0.098	1.23	0.86	0.75	0.49	0.33	0.07	0.11239	0.00010	2.79	2.33	2.34
09-BOS-05	3.83	3.44	3.29	0.97	0.059	1.08	0.46	0.24	0.30	0.93	0.08	0.10893	0.00043	3.36	2.79	2.80
09-BOS-52	1.82	1.71	0.35	0.08	0.015	1.04	0.10	0.04	0.22	2.94	0.04	0.10511	0.00034	3.61	3.29	3.30
Jagersfontein																
JAG12-79	1.15	1.62	1.02	0.09	0.005	0.69	0.31	0.05	0.09	0.82	0.02	0.10735	0.00078	3.14	2.99	3.00
JAG12-133	1.82	1.39	1.21	0.55	0.080	1.27	0.42	0.34	0.45	2.25	0.22	0.11868	0.00021	2.93	1.49	1.53
JAG12-146	1.13	1.67	1.01	0.09	0.026	0.66	0.29	0.04	0.08	4.76	0.11	0.10698	0.00053	4.09	3.04	3.06
Newlands																
JJG-4401	2.51	2.49	0.26	0.04	0.008	0.98	0.05	0.01	0.16	2.93	0.01	0.10706	0.00046	3.14	3.03	3.04
JJG-4407	3.59	3.09	2.41	1.81	0.085	1.13	0.38	0.50	0.75	0.72	0.12	0.11046	0.00054	3.50	2.58	2.61
Finch																
FIN12-002	3.35	2.87	1.63	0.54	0.070	1.13	0.28	0.16	0.33	1.99	0.10	0.10839	0.00101	3.71	2.86	2.88
FIN12-003	1.78	2.23	5.91	3.88	0.189	0.77	1.29	1.49	0.66	0.75	0.52	0.12079	0.00015	-6.48	1.20	1.34
FIN12-004	3.11	2.79	3.12	1.65	0.108	1.08	0.54	0.51	0.53	1.01	0.17	0.11428	0.00010	3.38	2.08	2.12
FIN12-006	3.39	3.32	4.02	2.11	0.156	0.99	0.59	0.55	0.52	1.14	0.23	0.11318	0.00021	4.55	2.22	2.28
FIN12-011	5.28	4.16	2.47	0.39	0.009	1.23	0.29	0.08	0.16	0.37	0.01	0.11243	0.00059	2.37	2.32	2.33
FIN12-016	3.49	2.84	1.69	1.46	0.160	1.19	0.29	0.44	0.86	1.68	0.22	0.11129	0.00036	5.01	2.47	2.53

Model ages calculated using present-day primitive mantle $^{187}Os/^{188}Os$ of 0.1296 and a $^{187}Re/^{188}Os$ of 0.435 (Becker et al., 2006). Sub-script N denotes value normalised to CI-chondrite (CI-chondrite values from Anders and Grevesse, 1989)

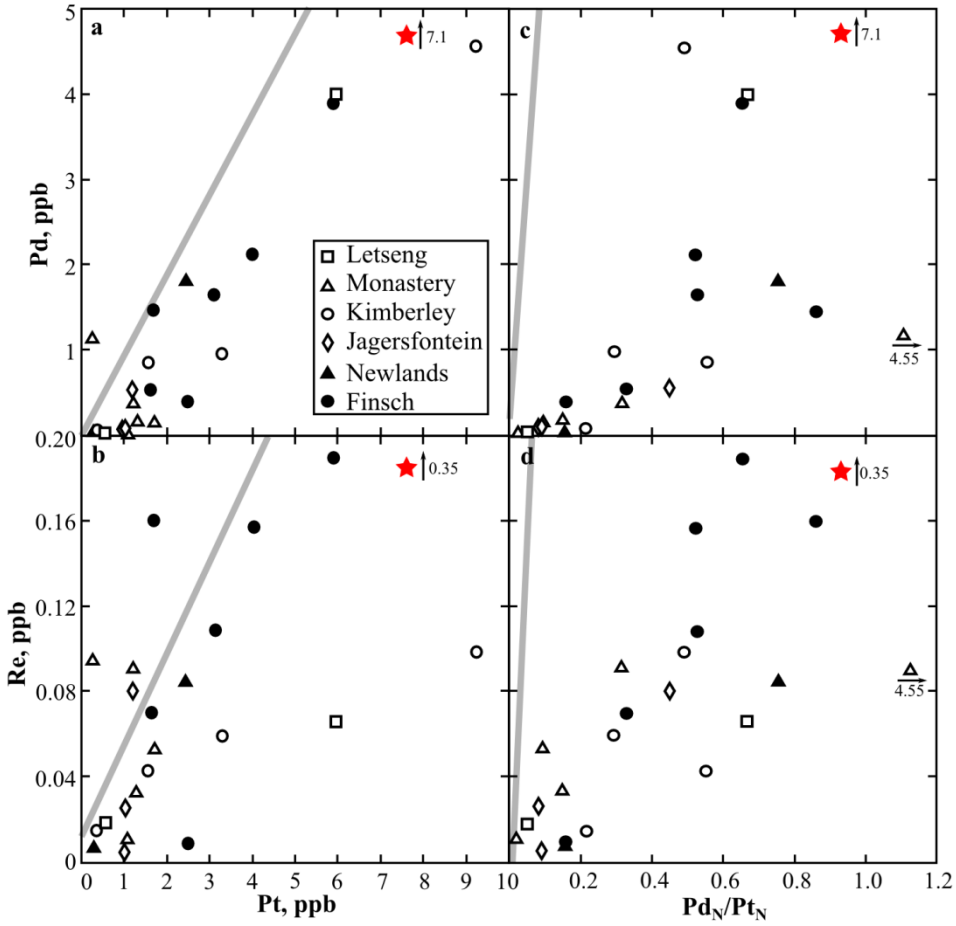

Figure 2.9. Bivariate diagrams for the highly siderophile elements (HSE) for the Kaapvaal peridotites. a) Whole-rock Pd concentration vs. Pt concentration, b) whole-rock Re concentration vs. Pd concentration, c) whole-rock Pd concentration vs. Pd_N/Pt_N, d) whole-rock Re concentration vs. Pd_N/Pt_N Red star is PUM composition and grey line is the trend of PUM inter-element ratio (PUM from Becker et al., 2006).

ages were calculated, with T_{RD} ages spanning 1.20-3.29 Ga (Table 2.6) and a broad range of T_{MA} ages from future ages to older than the Earth. The realistically possible T_{MA} ages span 2.20-4.09 Ga (Figure 2.12). Both Monastery and Newlands show a limited range in both T_{RD} and T_{MA} ages, with all other localities displaying a broad range in ages (Figure 2.12).

2.4.7. Single grain sulphide $^{187}Os/^{188}Os$ compositions and T_{RD} ages

The eleven BMS analysed for osmium compositions have highly variable compositions from radiogenic ($^{187}Os/^{188}Os$ = 0.2190) to unradiogenic ($^{187}Os/^{188}Os$ = 0.1057). There is no systematic relationship between the BMS Fe-Ni composition and the Os composition, however, three of the four BMS containing Cu give radiogenic $^{187}Os/^{188}Os$ compositions (Table 2.5). There is also a general trend with textural habit, where the interstitial BMS give the most radiogenic compositions (0.13915-0.21899, and one

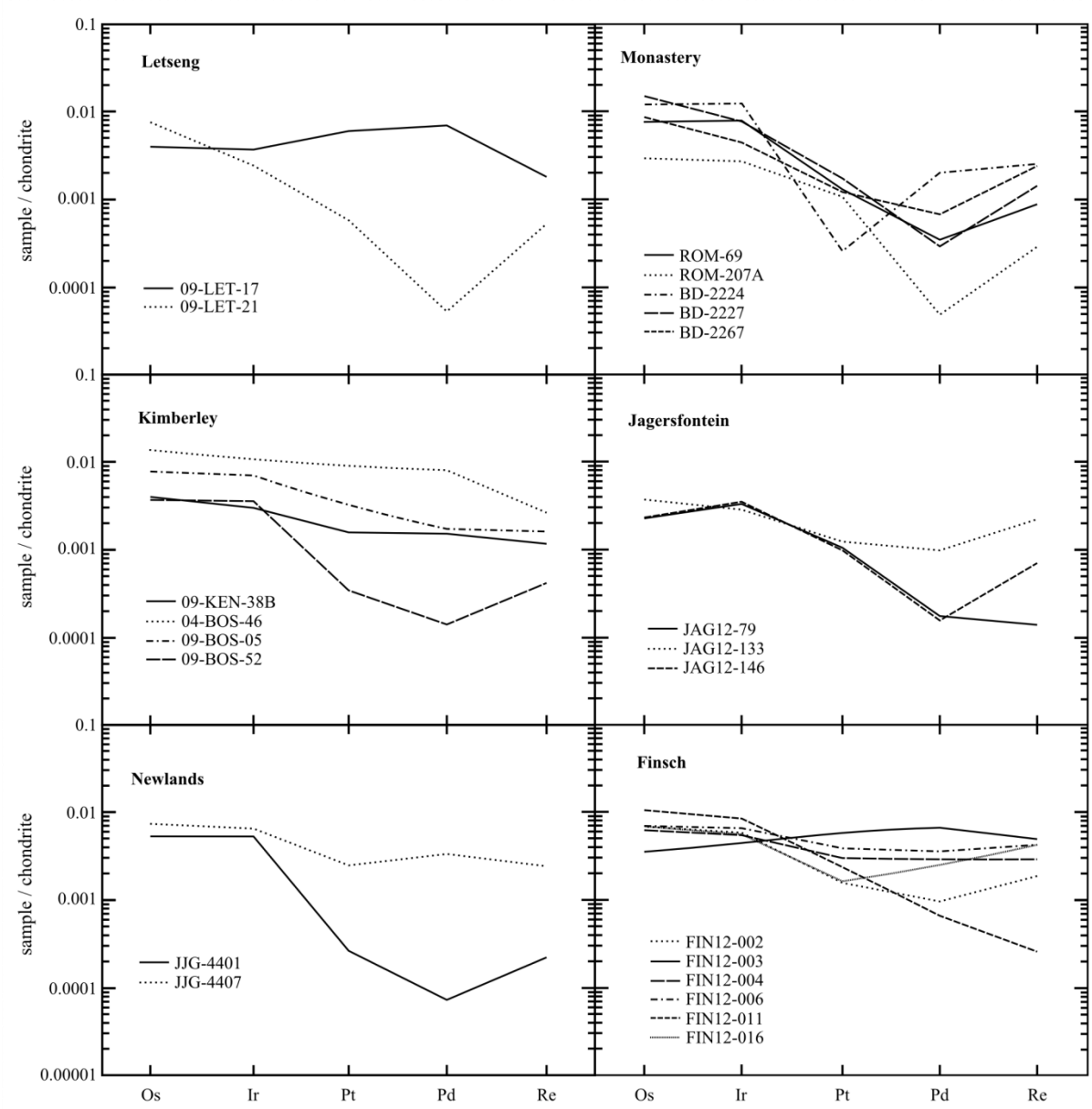

Figure 2.10. CI-chondrite normalised highly siderophile element (HSE) plots for the Kaapvaal peridotites (CI-chondrite from Anders and Grevesse, 1995). Each locality within the sample suite shows a wide range in HSE systematics.

unradiogenic 0.11338) whilst the pseudo-inclusions are generally unradiogenic (0.10565-0.11094, one radiogenic 0.13906; Table 2.5).

From the Monastery peridotite BD-2224, a pentlandite inclusion in phlogopite, Mon-7 (Figure 2.13a), gives a radiogenic $^{187}Os/^{188}Os$ of 0.1358±18. Despite different compositions and habits the three BMS from Bultfontein give similar compositions. The pseudo-inclusions in olivine have $^{187}Os/^{188}Os$ of 0.1084±6 for the pentlandite Bult-3 (09-BOS-05; Figure 2.13b) and 0.1057±2 for the heazlewoodite Bult-5 (09-BOS-52; Figure 2.13d). Whilst the pentlandite inclusion in clinopyroxene, Bult-4 (09-BOS-05; Figure 2.13c) has a $^{187}Os/^{188}Os$

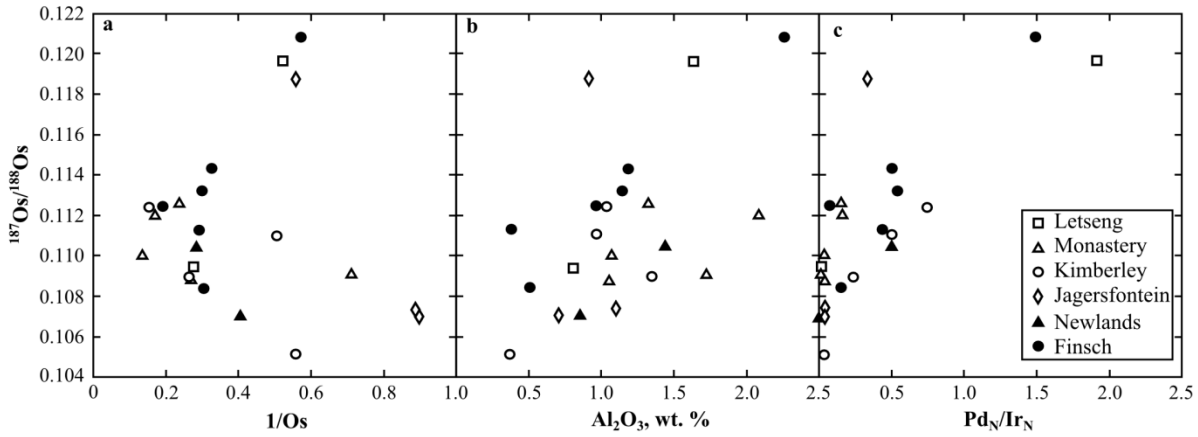

Figure 2.11. $^{187}Os/^{188}Os$ vs. a) 1/Os, b) Al_2O_3 in wt. % and c) Pd_N/Ir_N. A broad positive correlation is seen between $^{187}Os/^{188}Os$ and Pd_N/Ir_N, indicating that high Pd abundances are coupled with more radiogenic signatures.

composition of 0.1066±3. From the Jagersfontein peridotite JAG12-133, a heazlewoodite interstitial to orthopyroxene and clinopyroxene, Jag-1 (Figure 2.13e), has a radiogenic $^{187}Os/^{188}Os$ of 0.2190±4 and an Os concentration of 1,258 ppb. Finally, the six BMS from Finsch show a wide range in $^{187}Os/^{188}Os$ compositions. The pentlandite pseudo-inclusions Fin-3 (FIN12-003; Figure 2.13g), Fin-6 (FIN12-011; Figure 2.13j) and Fin-7 (FIN12-016; Figure 2.13k) display radiogenic and unradiogenic $^{187}Os/^{188}Os$ compositions of 0.1391±3, 0.1109±1 and 0.1084±1, respectively. Osmium concentrations were also obtained for Fin-3 of 343 ppb and Fin-7 of 16,849 ppb. Whilst the interstitial pentlandite have $^{187}Os/^{188}Os$ compositions of 0.1392±5 for Fin-2 (FIN12-003; Figure 2.13f), 0.1134±7 for Fin-4 (FIN12-006, Figure 2.13h) and 0.1443±19 for Fin-5 (FIN12-006; Figure 2.13i). Osmium concentrations of 3,637 ppb for Fin-4 and 1,276 ppb for Fin-5 were obtained.

As Re concentrations could not be determined, only T_{RD} ages are calculated for all BMS. T_{RD} model ages will always provide a minimum age as they do not correct for the ingrowth of ^{187}Os due to Re decay. The T_{RD} ages span a wide range from future (Mon-7, Jag-1, Fin-2, Fin-3 and Fin-5) to Archean (i.e. 3.22 Ga for grain Bult-5; see Table 2.5). For the BMS with non-future ages the corresponding whole-rock T_{RD} age is within 500 m.y.

2.5. Discussion

2.5.1. Melt depletion and re-enrichment history of the Kaapvaal peridotites

The Kaapvaal peridotites have the trade mark signatures of residues of partial melting, their whole-rock major elements are extremely depleted in fertile components and are typical for cratonic peridotites (cf. Boyd, 1989; Hawkesworth et al., 1990). This is evident by the high Mg# in olivines and the low CaO and Al_2O_3 contents (cf. Simon et al., 2007; Pearson

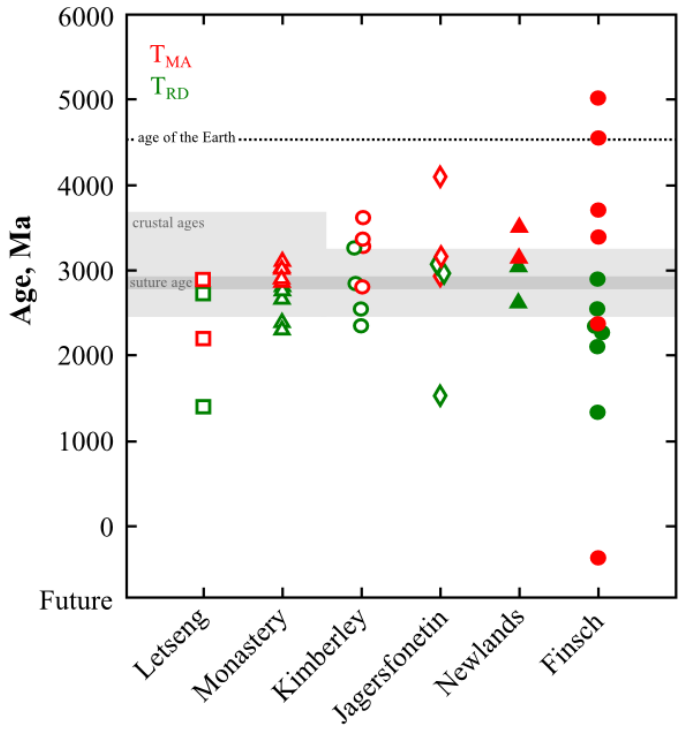

Figure 2.12. Whole-rock Re-Os model ages for the Kaapvaal peridotites. Symbols as in Figure 2.9. Green colour is the T_{RD} model age calculations and red is for T_{MA} ages. Each locality shows a wide range in calculated ages, in both T_{RD} and T_{MA} calculations. Dotted line is the age of the Earth. Light grey areas denote crustal ages for the terrane of the kimberlite locality, dark grey is the age of suturing of the eastern and western Kaapvaal (Schmitz et al., 2004).

and Wittig, 2008; Wittig et al., 2008). However, most of the peridotites have experienced orthopyroxene enrichment as is reflected in the abundance of orthopyroxene and the high SiO_2 contents (i.e. >39 wt. %), this is a common feature of Kaapvaal peridotites (cf. Boyd 1989; Canil 1992). This orthopyroxene enrichment will disturb the FeO, Al_2O_3 and CaO content, therefore, estimates on the depth and degree of partial melting cannot be accurately calculated through standard calculations (i.e. FeO vs MgO; Herzberg, 2004). Nevertheless, an estimate on the pressure and degree of partial melting can be inferred from whole-rock Yb and Lu concentrations and the Mg# in olivine (Figure 2.14; Pearson and Wittig, 2008; Wittig et al., 2008). As Yb and Lu are compatible in garnet during partial melting, they provide a unique insight into the pressure at which partial melting occurred (Wittig et al., 2008). As such, for the Kaapvaal peridotites they allow an estimate on the pressure of melt extraction (Figure 2.14a). This estimate shows that for the majority of the Kaapvaal peridotites a shallow pressure of 3 GPa is required, whilst for peridotites 09-LET-17, 09-LET-21, BD-2224, 09-KEN-38B, 09-BOS-52 and JAG12-79 a lower pressure of 2 GPa is required. These low pressures are typical of the Kaapvaal craton, with partial melting in the spinel stability

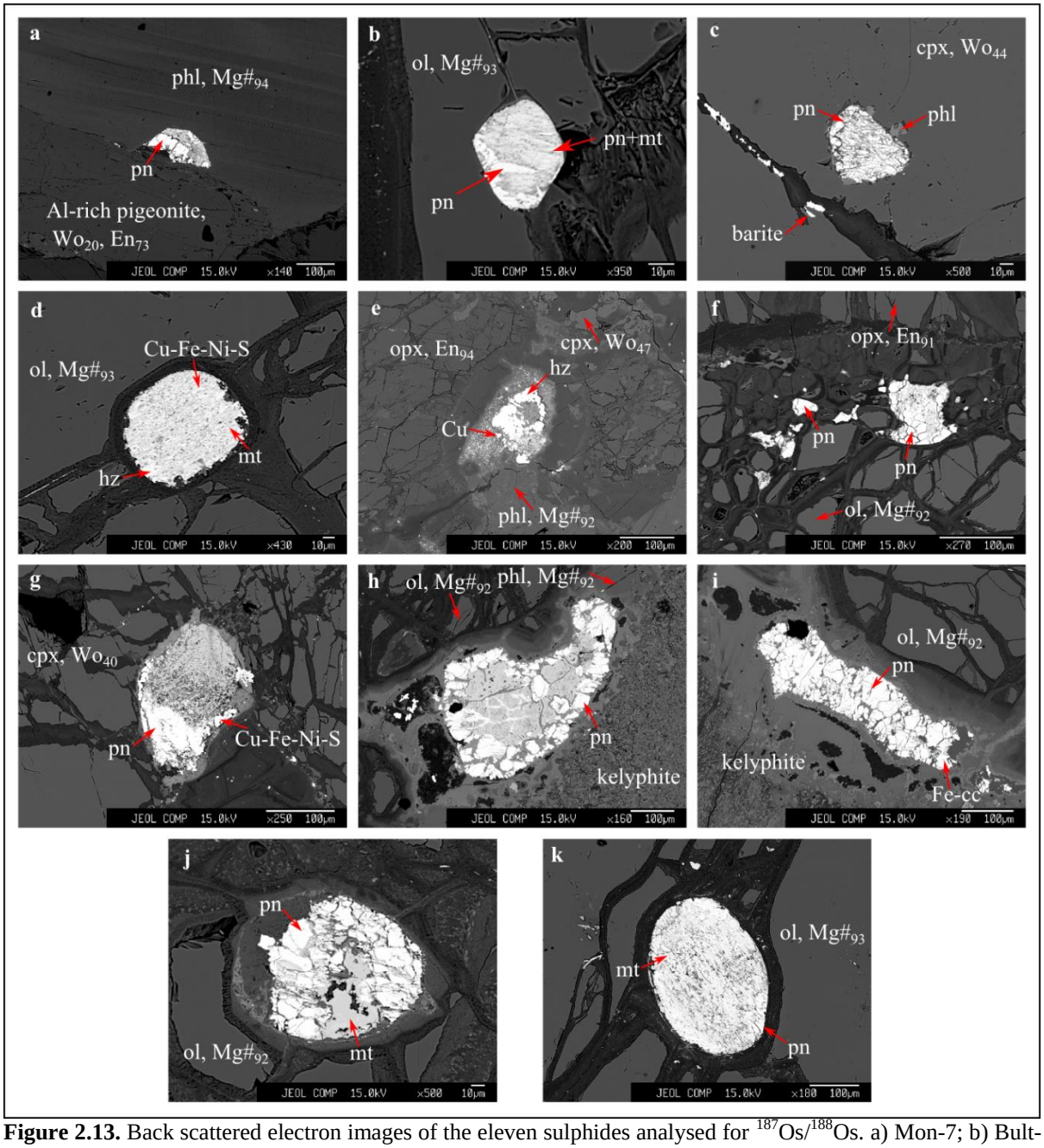

Figure 2.13. Back scattered electron images of the eleven sulphides analysed for $^{187}Os/^{188}Os$. a) Mon-7; b) Bult-3; c) Bult-4; d) Bult-5; e) Jag-1; f) Fin-2; g) Fin-3; h) Fin-4; i) Fin-5; j) Fin-6; k) Fin-7. *Ol* – olivine, *opx* – orthopyroxene, *cpx* – clinopyroxene, *phl* – phlogopite, *pn* – pentlandite, *hz* – heazlewoodite, *cc* – chalcocite, *mt* – magnetite.

field seen in wide variety of peridotites (Kelemen et al., 1998; Simon et al, 2003; Canil, 2004; Gibson et al., 2005) Combining these pressures with experimental data on the amount of melt extraction required to obtain high Mg# in olivine (Baker and Stolper, 1994), allows for an estimation on the extent of partial melting experienced by the Kaapvaal peridotites (Figure 2.14b). However, these experiments were only calculated for pressures of 3 and 7 GPa, as such, a pressure of 3 GPa is assumed for all Kaapvaal peridotites (Figure 2.14b). These calculations indicate that all of the Kaapvaal peridotites experienced >20% melt

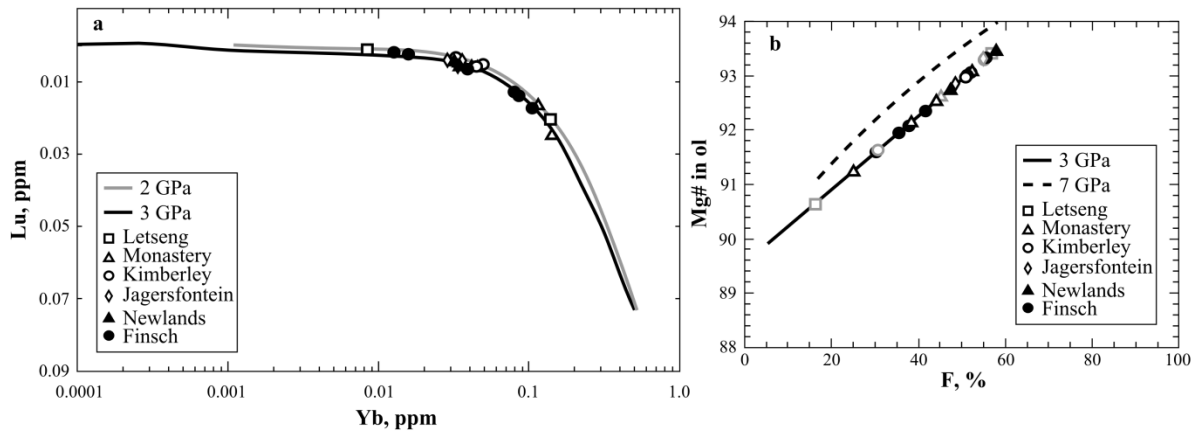

Figure 2.14. Modelling for the depth and degree of partial melting of the Kaapvaal peridotite. A) estimate of depth of partial melting based off whole-rock Yb and Lu concentrations (after Wittig et al., 2008). B) Estimate on degree of partial melting (F%) based on experiments on Mg# in olivine (Baker and Stolper, 1994; image after Pearson and Wittig, 2008).

extraction, with only four peridotites (09-LET-17, BD-2267, 09-KEN-38B and FIN12-003) with <35% melt extraction. These estimates of partial melting are typical for cratonic peridotites and indicate that the peridotites are residues of large degrees of partial melting at shallow pressure. The depletion in the heavy-REE in the Kaapvaal peridotites adds further evidence for depletion at shallow pressures. With the low abundance of garnet hosted trace elements, e.g. Sc < 24 ppm, Cr < 3000 ppm, Lu < 25 ppb and Yb <145 ppb, indicating that a large degree of partial melting occurred within the spinel stability field (cf. Tainton and McKenzie, 1991; Kelemen et al., 1998; Simon et al, 2003; Canil, 2004; Gibson et al., 2005; Pearson and Wittig, 2008).

Despite the large degree of melt extraction the Kaapvaal peridotites are characterised by variable enrichment in the incompatible trace elements. Most notably the HFSE (high field strength elements; Zr and Hf), LILE (large ion lithophile elements; K, Rb, Sr, Ba) and LREE (light rare earth elements; La-Sm; Figure 2.6 and 2.7), this enrichment is indicative of cryptic metasomatism. The enrichment in incompatible trace elements is a common feature of kimberlite derived peridotites, and is attributed to interaction with the kimberlite melt during ascent to the surface (c.f. Hawksworth et al., 1983; Simon et al., 2007). This contribution from the kimberlite can account for greater than 90% of the whole-rock budget for the most highly incompatible elements (e.g. Ba, Rb, Nb, Nd, Hf; Grégoire et al., 2003). The metasomatism of the Kaapvaal peridotites is also evidenced by the addition of hydrous minerals such as phlogopite and amphibole. These minerals would not be expected to reside in residues of high degrees of partial melting and can be used as indicators for kimberlite metasomatism (Grégoire et al., 2003). Potassium-rich amphibole and phlogopite with low

Mg# (<92), such as those in peridotites JJG-4401, ROM-207A and JAG12-133, are considered to be crystallising products involving the Group 2 kimberlite melts (Grégoire et al., 2003). Phlogopite with much higher Mg#, such as those in BD-2224, BD-2227 and 09-BOS-52, is indicative of crystallisation involving the Group 1 kimberlite melt (Grégoire et al., 2003). The presence of phlogopite with high Mg# in peridotites from both Group 1 and Group 2 kimberlites indicates the possibility that the earlier Group 2 kimberlite melt pervasively metasomatised the lithosphere in sections it did not directly sample. This further highlights the complex metasomatic history that has affected these peridotites.

2.5.2. Origin of the whole-rock HSE and $^{187}Os/^{188}Os$ signatures

During partial melting of fertile mantle, BMS will melt incongruently and produce a Cu-Ni-rich sulphide melt that partitions Pt and Pd, and a monosulphide solid solution (mss) that partitions Os, Ir and Ru. The Cu-Ni-rich sulphide melt fractionates away from the residue with the basaltic melt, whilst the mss is left in the residue (Alard et al., 2000; Luguet et al., 2003; Bockrath et al., 2004), this results in a fractionation of the P-PGE from the I-PGE during partial melting. As the HSE are controlled by BMS in fertile peridotites (i.e. before the complete extraction of S; cf. Alard et al., 2000; Lorand et al., 2013 and ref. therein) the fractionation of the HSE results in a very distinct HSE pattern in the peridotites (Figure 2.15). This pattern shows subchondritic Pt_N/Ir_N and Pd_N/Ir_N, with a Pt_N/Pd_N of 1 (Figure 2.15) and a Re_N/Ir_N of 1 (Fleet et al, 1993; Bockrath et al., 2004; Ballhaus et al., 2006). The CI-chondrite normalised HSE patterns of the Kaapvaal peridotites do not show a similar trend to the calculated partial melting signature (Figure 2.15). The majority of peridotites display enrichment in Pt and Pd with no correlation between Pd (or Pt) and Ir, coupled with a depletion in Re, despite the large extents of partial melting seen. There are a few peridotites that display depleted Pt and Pd and Os_N/Ir_N of ~1, i.e. ROM-207A, 09-BOS-52, JJG-4407 and FIN12-002. However, Pd is always depleted over Pt compared to what is expected by the partition coefficients of the HSE during partial melting (Figure 2.15). This can be explained by experimental work of Peregoedova et al. (2004) that show that during partial melting of a sulphide melt Pt-alloys can become stable within the residue, allowing for the fractionation of Pt from Pd. This would explain the Pt and Pd depletions of the HSE patterns for ROM-207A, 09-BOS-52, JJG-4407 and FIN12-002. However, all of these peridotites also display a depletion in Re that cannot be explained by partial melting of a sulphide melt. This can be resolved by the high incompatibility of Re, and its lithophile affinities (McDonough, 1994; Reisberg and Lorand, 1995). Unlike the other HSE, Re is not purely chalcophile and during

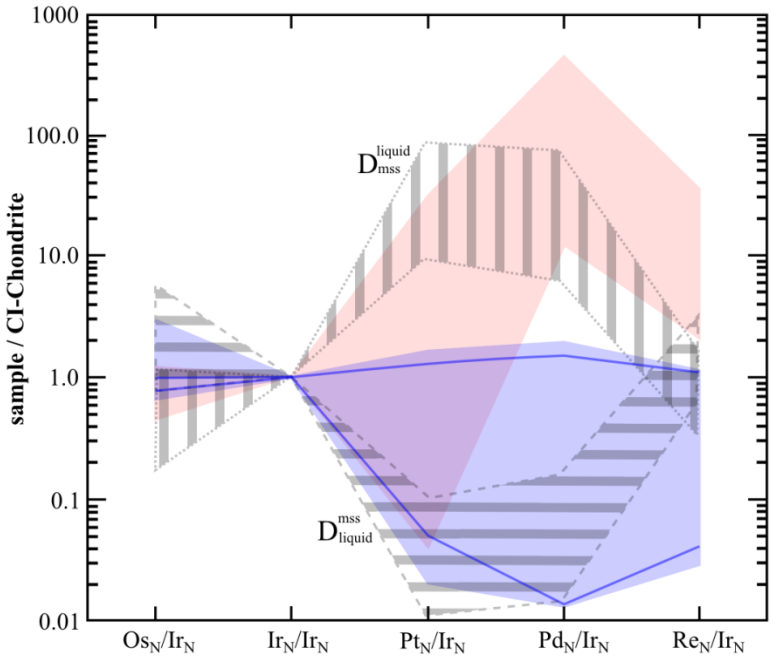

Figure 2.15. CI-chondrite and Ir normalised HSE diagrams. Grey region represents the Kaapvaal peridotites of this study, dark grey lines are samples FIN12-003 (enriched Pd) and JJG-4401 (depleted Pd) for comparison. Pink field is Type-2 metasomatic pentlandites from Alard et al. (2005), whilst the grey stripped areas are the fields for partition coefficients (D) of the PGE between Ni-Cu-rich sulphide melt and mss. Vertical stripes are the D for PGE during melting of sulphide (mss+iss), horizontal stripes are the D for the PGE in the mss over the Ni-Cu-liquid. i.e. vertical = melt, horizontal = residue (Fleet et al., 1993, Bockrath et al., 2005; Ballhaus et al., 2006).

partial melting of a peridotite will behave as a moderately lithophile element. Experiments suggest that >20% partial melting will completely deplete the residue of Re (Fonseca et al., 2011). This has been reflected in natural lherzolite and harzburgite where between 35-100% of the whole-rock Re is hosted by silicates (Handler and Bennett, 1999; Burton et al., 1999; Luguet et al., 2007). As such, the Kaapvaal peridotites do not have depleted Re, but rather are enriched in Re. Therefore, due to the variable enrichment in Pt-Pd-Re none of the Kaapvaal peridotites can be explained purely by partial melting and require secondary processes to explain.

Nevertheless, the HSE systematics of the Kaapvaal peridotites retain some indications of partial melting. The variable supra- to sub-chondritic Os_N/Ir_N of a number of peridotites is evidence for the potential stabilisation of refractory alloys due to the exhaustion of S from the residue. The shallow pressures and extent of partial melting experienced by the peridotites implies that they should be S free. As with an assumed S solubility in basaltic melts of 1000 ppm at 2 GPa (Mavrogene and O'Neill, 1999), with a primitive upper mantle S content of 250 ppm, partial melting of >25% will completely deplete the residue of S (cf. Lorand et al., 1999; Fonseca et al., 2011). This would create a BMS free residue with the PGE hosted by

refractory alloys. Despite Os and Ir having very similar compatibilities during partial melting, when refractory alloys become stable Os and Ir will partition into different minerals. Osmium will form Os-Ru-rich minerals such as laurite and erlichmanite, whilst the Ir potentially forms Pt-Ir-alloys (cf. Lorand et al., 2013 and ref, therein). Due to the high concentration of the PGE within these minerals, and their low abundance in the peridotite, the minerals formed will be small and most likely heterogeneously distributed (Luguet et al., 2004; 2007; Lorand et al., 2004; 2013). This can create a sampling bias due to a 'nugget-effect' during digestion of the peridotites, and could artificially fractionate the Os from the Ir. Duplicate analysis of a peridotite can resolve whether the nugget-effect has occurred, or if the Os_N/Ir_N values seen are representative of the peridotite (Luguet et al., 2004; Lorand et al., 2013).

Nearly all of the Kaapvaal peridotites within this suite contain BMS, only peridotites 09-LET-21, JAG12-79, JAG12-146, JJG-4407 and FIN12-002 are BMS free. However, as only two thin sections were investigated for these peridotites, it is not possible to sate unequivocally that the peridotites are BMS free. As up to six thin sections can be required to accurately detail the presence and assemblage of BMS in peridotite (Lorand and Grégoire, 2006). The presence of BMS within the majority of Kaapvaal peridotites is unexpected, as S should have been completely extracted due to the degree of partial melting experienced at low pressures. Essentially, the BMS within the Kaapvaal peridotites must be metasomatic and therefore, possibly account for the variability in the HSE patterns.

As the HSE systematics of the Kaapvaal peridotites cannot be solely attributed to partial melting, they require a secondary process such as metasomatism. The presence of BMS within such depleted peridotites is the most obvious sign of metasomatic addition of BMS (Pearson et al., 2004). Moreover, the habit and composition of the BMS also attest to their secondary nature. The majority of the BMS contained within the Kaapvaal peridotites is of a Ni-rich nature, yet has no complementary Fe-rich BMS. This attests to their formation via a Ni-Cu-rich sulphide melt, rather than due to the sub-solidus re-equilibration of high temperature mss + iss (iss: intermediate solid solution) assemblages considered to represent the primary mantle BMS (cf. Lorand and Grégoire, 2006). Such Ni-Cu-rich sulphide melts formed after extraction during partial melting of a fertile peridotite during the incongruent melting of the original BMS (mss + iss). These Ni-Cu-rich sulphide melts form after extraction within the partial melts and are the source of metasomatic BMS (Lorand and Grégoire, 2006). Most of the BMS in the Kaapvaal peridotites are also found as interstitial grains and associated to secondary minerals such as clinopyroxene and phlogopite, further attesting to their secondary nature.

The degree and style of enrichment in the HSE varies markedly within a locality as well as between localities. Therefore, different metasomatic processes in terms of metasomatic melt composition, genesis and the dynamics of rock/melt interaction, must be involved. Ultimately two processes can be distinguished in the inter-element ratios of the Kaapvaal peridotites that cannot be accounted for by partial melting, 1) variably enriched Pd to suprachondritic Pd_N/Ir_N and 2) variably enriched Pt and suprachondritic Pd_N/Pt_N. These enrichments are either due to the same process but different mineral hosts or caused by different metasomatic processes, as the enrichment in Pt and Pd is not always coupled (Figure 2.9). The addition of metasomatic BMS is a possible mechanism for the variability seen in the HSE, as BMS control the whole-rock HSE (Alard et al., 2002; Griffin et al., 2004). As discussed previously, a Ni-Cu-rich sulphide melt will readily partition Pt and Pd. As such, the percolation of such a melt through the depleted Kaapvaal peridotites could precipitate Pt-Pd-rich BMS, such as those seen in ophiolitic peridotites, abyssal peridotites and alkali basalt borne peridotites (Alard et al., 2000; Lorand et al., 2004; Luguet et al., 2001; 2004). This addition of metasomatic Pt-Pd-rich BMS to a prior extensively depleted peridotite could account for the enrichments of Pt and Pd. This is shown in Figure 2.15, where the HSE systematic of metasomatic BMS (Alard et al., 2005) is compared to the Kaapvaal whole-rock peridotite. The variable addition of such BMS would increase the whole-rock Pt and Pd to the enrichments seen at the whole-rock scale. The variability in the Pt_N/Pd_N can be accounted for by the mineralogical controls on Pt and Pd. Whilst both Pt and Pd are compatible in high-temperature Ni-rich sulphide melt, the sub-solidus re-equilibration products of this melt i.e. pentlandite, does not readily retain Pt (Makovicky et al., 1986; Ballhaus and Ryan, 1995). As such, upon cooling the Pt will exsolve from the pentlandite structure and form separate minerals, such as Pt-Fe-alloys, Pt-tellurides or Pt-arsenides (Barnes et al., 2008; Lorand et al., 2008; 2013). The heterogeneous distribution of these minerals can create a ‘nugget-effect’ as was described for the Os-Ir systematics. Accordingly, the variability of the HSE systematics in the Kaapvaal peridotites attests to the existence of residual PGM and metasomatic BMS and PGM.

Significantly, the variations in the whole-rock HSE and incompatible trace element data do not correlate. The peridotites displaying the lowest Pd_N/Ir_N and Pt_N/Ir_N, in a given locality, have experienced a higher degree of incompatible trace element enrichment (see Figures 2.6 and 2.11). This signifies that the processes that produced the metasomatic enrichment of the HSE and the incompatible trace elements are not related. This observation

is evidence for multiple metasomatic events affecting the Kaapvaal peridotites and infers the peridotites have a complex petrological history.

As almost all of the Kaapvaal peridotites have undergone Re addition, the T_{MA} ages will overestimate the timing of partial melting. As such, only the T_{RD} age provides a minimum for the timing of melt depletion and lithosphere stabilisation. However, the control of the whole-rock $^{187}Os/^{188}Os$ composition by Os-bearing BMS and PGM results in a mixed composition between unradiogenic residual PGM and radiogenic metasomatic BMS-PGM (cf. Alard et al., 2002; Griffin et al., 2004; Pearson et al., 2004). Therefore, a T_{RD} model age calculated from the whole-rock does not provide an age of partial melting but rather an integration of these multiple populations (cf. Pearson et al., 2004). This is highlighted by the variability in the T_{RD} ages obtained for the Kaapvaal peridotites, with the peridotites showing the lowest Pt_N/Ir_N and Pd_N/Ir_N having Archean T_{RD} ages, whilst peridotites with enriched Pt and Pd give Proterozoic ages (Table 2.6; Figure 2.13). Similar enrichments in whole-rock $^{187}Os/^{188}Os$ compositions due to metasomatic BMS have been reported in the past (Alard et al., 2002; Griffin et al., 2004). Accordingly, the T_{RD} ages of BMS-rich highly depleted peridotites are not geologically significant. Nevertheless, the investigation of the Re-Os compositions of BMS hosted within the peridotites can provide further insight into the metasomatic and melt depletion history of the peridotites (cf. Griffin et al., 2004).

2.5.3. Single grain BMS and their importance for the whole-rock $^{187}Os/^{188}Os$ compositions

Previous work on peridotites have shown that at the BMS scale, the $^{187}Os/^{188}Os$ significantly varies (cf. Alard et al., 2002; Aulbach et al., 2004; Griffin et al., 2004;), and that the presence of metasomatic BMS have an impact on the whole-rock compositions. This has also been reflected in the $^{187}Os/^{188}Os$ compositions of the BMS studied from this Kaapvaal suite, with radiogenic and un-radiogenic compositions documented. The BMS T_{RD} ages obtained from four different localities display no correlation with the T_{RD} ages obtained for the whole-rock (Figure 2.16) nor with the whole-rock HSE systematics. Peridotites that have enriched Pt-Pd have BMS ages that are both older (09-BOS-05) and younger (JAG12-133) than the whole-rock. BMS younger and older than the whole-rock are also observed in the peridotites with depleted Pt-Pd (i.e. 09-BOS-52 and FIN12-011). This signifies that the level of depletion of the P-PGE (see Figure 2.15) does not rule out the presence of secondary BMS with radiogenic $^{187}Os/^{188}Os$ compositions. Three BMS have T_{RD} ages up to 500 m.y. older than the whole-rock $T_{RD,}$ further signifying that the whole rock T_{RD} ages are a mixture of different Os-bearing minerals and as such do not reflect the age of partial melting.

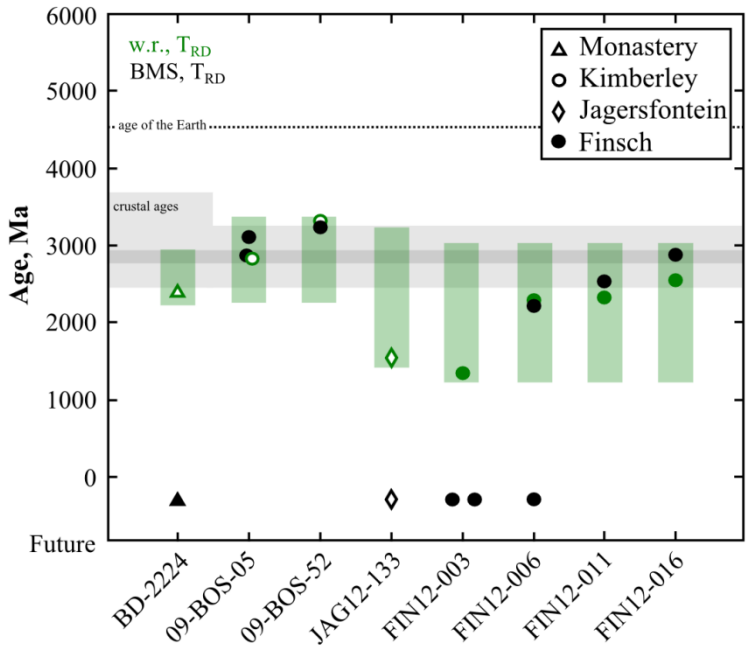

Figure 2.16. Re-Os T_{RD} ages for single grain BMS vs whole rock. Black symbols are the BMS, green are the whole-rock peridotite. Green field represents the T_{RD} age for the entire locality. Dotted line is age of the Earth. Light grey is the age of the crustal rocks in the given terrane, dark grey is age of the suturing of the eastern and western Kaapvaal (Schmitz et al., 2004).

2.5.4. Relationships between kimberlite localities and type and the implications for formation of the Kaapvaal Craton

The peridotites analysed in this suite show no discernible differences between Group 1 and Group 2 kimberlite peridotites. The variation in Mg# of olivine with depth seen by Griffin et al. (2003) has not been completely reproduced (Figure 2.17), with the Group 1 kimberlite peridotites broadly following the trend whilst the Group 2 kimberlite peridotites plot completely off the Group 2 trend. This may be as a result of the different methods used to calculate the depths and Mg# in olivine. Griffin et al. (2003) used the Ni-in-grt barometer to infer the depth and utilised the garnet compositions to calculate Mg# in co-existing olivine. Therefore, it is most likely that the differences between the calculations used for the pressures and olivine Mg# account for some of the discrepancies. For the calculation of the trends with depth, Griffin et al. (2003) used multiple kimberlite pipes, of these localities, only Kimberley, Finsch and Newlands were investigated by this study. Interestingly, it is the Finsch and Newlands peridotites that do not follow the Group 2 trend. It is therefore possible, that the calculated olivine Mg# from Griffin et al (2003) do not reflect those of natural olivine with co-existing garnet in Finsch and Newlands. Otherwise, the peridotites investigated within this study may not have experienced the same processes that affected those of Griffin et al.

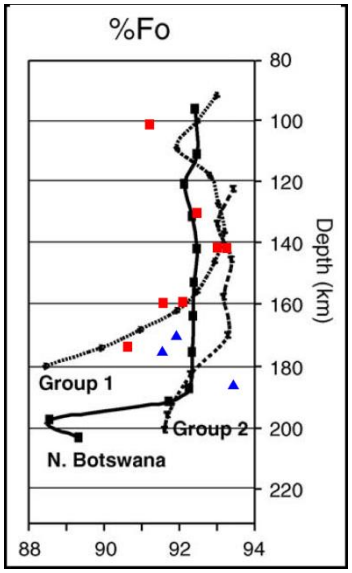

Figure 2.17. Variation in Forsterite content (Mg#) with depth., after Griffin et al., 2003. Red squares are Group 1 peridotites from this study, blue triangles are Group 2 peridotites from this study. The Group 1 peridotites mimic the general trend seen by Griffin et al. (2003), however the Group 2 peridotites are quite different, lying on either side of the observed trend.

(2003), which infers that the lithosphere beneath the Kaapvaal Craton is extremely heterogeneous.

There are also no systematic differences between the Group 1 and Group 2 peridotites based on their major elements, incompatible trace elements or even HSE systematics. The variations seen in these systems (e.g. enriched Pt-Pd-Re-Ba-Rb-LREE) are equally variable between and within the two different populations. As such, any difference between the lithosphere at the different times of eruption of the Group 1 and Group 2 kimberlites cannot be determined.

The south-eastern terrane of the Kaapvaal Craton has been interpreted to have formed earlier than the western terrane due to the abundance of older crustal ages (Kröner et al., 1989; 1993; Armstrong et al., 1990; Drennen et al., 1990; de Ronde and de Wit, 1994; Schmitz et al., 2004). This dichotomy has been partially reproduced in mantle ages (Carlson and Moore, 2004), with the average Re-Os T_{MA} ages from Monastery (east) older than Kimberley (west), yet they are still within error of each other. The results obtained from the peridotites in my study show a similarity in T_{RD} ages regardless of the terrane, and those from the South Eastern Terrane, Monastery and Letseng, actually display some of the lowest T_{RD} ages. This is also true when T_{MA} ages are taken into account, despite the lower Re contents of the eastern peridotites, the T_{MA} ages are younger than the majority of the western ages and are actually younger than the oldest T_{RD} age from Kimberley. As the whole-rock ages have been shown to be related to a mixing of metasomatic BMS with residual PGM it is not

surprising that the ages obtained do not reflect the ages of crustal growth. However, even when the ages of the BMS are taken in to account, the range in T_{RD} age of the BMS from Monastery (future-3.2 Ga) are indistinguishable from BMS T_{RD} ages from Kimberley (future-3.2 Ga; this study; Griffin et al., 2004). Therefore, no resolvable time difference can be distinguished between the lithosphere of the eastern and western Kaapvaal craton.

In comparison to previous Re-Os studies on Kaapvaal peridotites, the peridotites from this study provide similar results. The Letseng and Kimberley localities have been the most heavily investigated, with T_{RD} ages ranging from 1.0-3.0 Ga in Letseng and 1.7- 3.0 Ga in Kimberley (Carlson et al, 1999; Irvine et al., 2001; Simon et al., 2003; 2007: Griffin et al., 2004). All of the Kimberley and Letseng peridotites within this study fall within these ranges, expect for Kimberley peridotite 09-BOS-52 which gives an older T_{RD} age of 3.3 Ga. The same can be said for the peridotites from Finsch (range 1.0-2.8 Ga; Griffin et al., 2004; Pearson et al., 1995) and Newlands (range: future-3.18 Ga; Menzies et al., 1999). Whilst the Jagersfontein peridotites from this study give much older T_{RD} ages then those previously reported, with Pearson et al. (1995) finding no age older than 2.2 Ga, whereas peridotites JAG12-79 and JAG12-146 have T_{RD} ages of 3.0 Ga. This variability highlights the need for statistically robust numbers of samples to be investigated to be able to obtain a complete overview of the lithosphere.

The peridotites from the Monastery kimberlite are quite interesting when compared to previously published data. The T_{RD} ages obtained by this study fall within the range of 1.4-3.02 Ga from Carlson and Moore (2004). However, the analysis of the same peridotite, BD-2227 is different. In the Carlson and Moore (2004) study, peridotite BD-2227 has an $^{187}Os/^{188}Os$ of 0.10883, whilst in this study a composition of 0.11002 was obtained. This is coupled with a much lower Os concentration in the Carlson and Moore (2004) study of 3.20 ppb compared to 7.45 ppb (similar Re of 0.054 ppb and 0.041 ppb, respectively) This discrepancy can be explained by the different methods used for the digestion of the peridotite, as the peridotites from Carlson and Moore (2004) were digested with Carius Tubes, whilst those of this study were digested in a high pressure Asher. The difference between the two digestion techniques has been shown to have an impact on samples containing refractory minerals (e.g. alloys), as the higher pressure of the Asher digestion is able to dissolve these minerals whilst the Carius Tubes cannot (cf. Reisberg and Meisel, 2002; Ishikawa et al., 2014). As the aliquot that was digested at high pressure results in a lower $^{187}Os/^{188}Os$ composition the alloys in this peridotite are of a metasomatic origin and not formed due to partial melting. As the Carlson and Moore (2004) study did not include the other HSE in the

study, it is impossible to tell what other affects the digestion of the alloys had on the HSE systematics of this peridotite, and exactly what type of alloy might be located within this peridotite. The difference in compositions could also be due to the 'nugget-effect' of either BMS or PGM. As these minerals are generally small and heterogeneously distributed they may not always be representatively sampled during a digestion (Luguet et al., 2004; Lorand et al., 2013). The lower $^{187}Os/^{188}Os$ composition of the analyses in this study could be explained if the aliquot digestion was a portion with a higher proportion of metasomatic BMS. As it is also notable that Carlson and Moore (2004) define BD-2227 as an amphibole-bearing garnet harzburgite, whereas in this study phlogopite was observed and no amphibole. The lack of amphibole and the potential nugget-effect of the BMS (and PGM) infers that this xenolith is highly heterogeneous in mineralogy at the hand sample size, which may explain the contrasting Re-Os systematic seen.

The ages obtained from BMS within this study are also within the range of those from previous studies on Finsch, Kimberley and Jagersfontein (i.e. future – 3.2 Ga; Griffin et al., 2004). As all of the BMS within these peridotites were formed due to the metasomatism of a prior extremely depleted lithosphere, the oldest BMS ages (~3.2 Ga) found thus far may represent the oldest influx of metasomatic BMS within the Kaapvaal cratonic lithosphere, rather than reflecting the age of stabilisation of the lithosphere. Therefore, they provide a minimum age for the enrichment of the lithosphere in HSE via BMS metasomatism, which infers that the lithosphere was already highly depleted at 3.2 Ga and that the stabilisation age for the Kaapvaal lithosphere is much older than currently accepted.

2.6. Conclusion

The Kaapvaal peridotites have experienced high degrees of partial melting, as evidenced by their low Al_2O_3 and CaO contents. The Mg# in olivine indicates that the peridotites have experienced at least 20% partial melting, with the majority having experienced >35%. Despite this level of depletion the incompatible trace elements are enriched, most notably in Rb, Ba, U and the light-REE. The heavy-REE elements are also variably depleted, high-lighting that the Kaapvaal peridotites experienced partial melting at shallow pressures, within the spinel stability field. Nevertheless, over half of the peridotites contain modal garnet, indicating that the Kaapvaal peridotites have experienced a complicated history. The modification of the highly depleted residues is also evident by the presence of hydrous metasomatic minerals such as phlogopite and amphibole. Therefore, the Kaapvaal peridotites have also experienced variable degrees of pervasive metasomatism.

The highly siderophile element systematics are highly variable, and show no systematic with the locality of the kimberlite pipe. Only two peridotites display the low Pt_N/Ir_N, Pd_N/Ir_N and suprachondritic Os_N/Ir_N expected of residues of high degrees of partial melting, and indicative of the presence of refractory Os-bearing alloys. All of the remaining xenoliths are variably enriched in Pt and Pd, but they do not display constant Pd_N/Pt_N. Furthermore, all of the Kaapvaal peridotites have experienced Re addition as evidenced by predominantly suprachondritic Re_N/Pd_N. The variability in the Pt-Pd-Re systematics can be explained by the addition of metasomatic BMS. This is supported by the presence of BMS in these peridotites, which due to the high degrees of partial melting experienced at shallow pressures, would not be expected. However, the variability in Pt_N/Ir_N and Pd_N/Ir_N do not correlate with the enrichment in the incompatible trace elements, indicating that the metasomatic events that led to incompatible trace element enrichment and precipitation of BMS are unrelated.

Due to the control BMS have on whole-rock Os compositions, the formation of the metasomatic BMS has obscured with primary $^{187}Os/^{188}Os$ composition of these peridotites. As such, the model age calculations are an integration of the original residual PGM and metasomatic BMS Os signatures. Model ages determined in the BMS support this observation, with the majority of ages obtained mimicking those of the whole-rock. Accordingly, the $^{187}Os/^{188}Os$ composition of the Kaapvaal peridotites is dominated by the metasomatic BMS. This is further supported by the correlation of Archean T_{RD} ages with low Pt_N/Ir_N and Pd_N/Ir_N, whilst peridotites with Proterozoic T_{RD} ages have higher Pt_N/Ir_N, Pd_N/Ir_N. Moreover, the Archean ages obtained for the whole-rock and BMS indicate that the metasomatic addition of BMS occurred at least 3.2 b.y.a.

The Re-Os ages and HSE systematics obtained in this study show that there is no resolvable difference between the eastern and western Kaapvaal peridotites or between Group 1 and Group 2 kimberlite borne peridotites. As such, any differences between the timing of stabilisation of the lithosphere cannot be resolved. However, the results indicate that the Kaapvaal lithosphere, across the entire extent, shows highly variable and heterogeneous enrichment in HSE that has occurred due to multiple metasomatic events. These metasomatic events were most likely caused by the percolation of small degrees of melt that have occurred since at least 3.2 Ga, implying that the lithosphere was already highly depleted at the beginning of the Mesoarchean.

Chapter 3

Peridotite xenoliths from the Kaapvaal craton: Re-Os and HSE systematics of Platinum-Alloys

3.1. Introduction

It is well documented that micro-metric platinum group minerals (PGM) and base metal sulphides (BMS: Fe-Ni-Cu-sulphides) within peridotites control the whole-rock highly siderophile element (HSE: Os, Ir, Pt, Pd, Re) and Re-Os signatures (Luguet et al., 2001; 2004; Alard et al., 2002; Griffin et al., 2004). As such, they are important archives for the partial melting and metasomatic history of the peridotites. Developments in laser-ablation mass spectroscopy in the last 14 years (cf. Alard et al., 2000) has enabled the Re-Os and HSE signatures of BMS from cratonic peridotites to be obtained (cf. Griffin et al., 2004). However, due to the sub-micron size of PGM in cratonic peridotites, their analysis for Re-Os and HSE signatures has thus far remained elusive.

Platinum group minerals are found in a variety of locations from platinum group element (PGE) ore deposits to chromite layers in ophiolites. These PGM are well constrained with a high temperature (residual) or a low temperature (metasomatic) origin (cf. Hattori and Cabri, 1992; Farrow and Watkinson, 1997; Malitch and Thalhammer, 2002). A low-temperature, S-undersaturated hydrothermal fluid has been proposed as the mechanism for formation of Pt-Pd-alloys at the Stillwater Complex, Montana (Li and Ripley, 2006). Whereas PGM in the Merensky Reef of the Bushveld Complex, South Africa, have been proposed to form at high temperature, due to the percolation of S-undersaturated silicate melt (Ballhaus and Sylvester, 2000; Holwell and McDonald, 2010). Ophiolitic PGM have been proposed to have formed due to partial melting in the supra-subduction zone with large differences in interfacial energy causing the accumulation of the PGM within chromites (Brenker et al., 2003). PGM formed via these contrasting processes result in different textural features as well as contrasting mineral associations, i.e. included within chromite or BMS.

PGM minerals are also known to occur within cratonic peridotite, where their mechanism for formation has been inferred from major element compositions and textural observation (cf. Lorand et al., 2013). As such, the formation of PGM in cratonic peridotites have been interpreted in a number of ways, 1) as residues of partial melting, similar to the PGM in ophiolites, 2) from the percolation of S-undersaturated fluid/melt causing desulphurisation, either at high or low temperature or 3) from sub-solidus re-equilibration of

BMS. This third mechanism has been proposed to explain the occurrence of small Pt-nuggets seen during time-resolved laser-ablation of BMS (cf. Alard et al., 2005). The sub-solidus re-equilibration of pentlandite affects Pt, as only trace amounts of Pt can be accommodated in pentlandite, compared to a few per cent of Ru-Pd (Makovicky et al., 1986; Ballhaus and Ryan, 1995). Due to their sub-micron size, Pt-nugget inclusions in BMS of cratonic origin have never been investigated for their HSE and Re-Os compositions, therefore, their impact on the whole-rock and host BMS HSE and Re-Os systematics is unknown. This lack of information also implies that the mechanism for their formation is not accurately constrained and is based purely from experiments and textural observation.

To further our understanding of micrometric PGM from cratonic peridotite this study investigates the HSE and $^{187}Os/^{188}Os$ compositions of PGM inclusions in sulphide from the Bultfontein kimberlite, South Africa. This is achieved through a new and novel technique for the extraction of sub-micron PGM via a focused ion beam (FIB). Through the combination of petrology and geochronology I assess the significance of PGM inclusions on the Re-Os and HSE systems at both the whole-rock and single grain BMS scale.

3.2. Materials and methods

3.2.1. Sample description

This study focuses on two pentlandite BMS and PGM from a single peridotite xenolith from the Bultfontein kimberlite, South Africa. The Bultfontein kimberlite is a Group 1 kimberlite and is located within the Kimberley kimberlite field and has been dated at 84 Ma (Allsopp and Barrett, 1975). The xenolith investigated here, 09-BOS-05, is a garnet harzburgite, that has experienced high degrees of partial melting evidenced by highly depleted Al_2O_3 (1.35 wt. %) CaO (0.61 wt. %) and Lu_{PM} (0.08; Lu_{PM} = primitive mantle normalised Lu) and high Mg# (Mg# = (Mg / (Mg + Fe) x 100) in olivine (93.0). No evidence of major element metasomatism is observed with constant Mg# in olivine and orthopyroxene, however, cryptic metasomatism is evidenced by the positive slope of the incompatible trace elements. Modal metasomatism also occurs within the peridotite, through the addition of minor clinopyroxene and phlogopite. Two BMS were observed over the two thin sections, within 1.5 cm of each other. Both of these BMS also contained small (<1 μm) PGM inclusions.

3.2.2. Sample preparation and petrological investigation

The peridotite was a 20cm x 15cm x 10cm sawed section of a larger xenolith,

displaying a small altered rim caused by the reaction with the kimberlitic lava. This rim was carefully removed and discarded prior to processing the peridotite. A small block was cut, from which a representative thin (~30 µm) and thick (~200 µm) sections were cut. A small section was retained as a hand specimen and approximately 70% of the remaining sample was then crushed in a steel jaw-crusher. Of this crush ca. 50% was then further crushed to a fine powder in an agate planetary mill.

One thin and one thick section were then subsequently investigated with transmitted and reflected light microscopy to determine mineral constituents and to characterise BMS and PGM petrography. All minerals (silicate, oxide, BMS) were then analysed with a JEOL JXA 8200 electron microprobe (EMP) at the Steinmann-Institute University of Bonn, Germany. They were analysed in WDS mode with an operating voltage of 20 kV, and beam current of 20 nA and a spot size of 1 µm. All element calibrations were carried out by measuring their peak and background positions for 10 and 5 sec. respectively, employing the ZAF matrix correction method. For sulphides, Fe and S were calibrated on a Canyon Diablo troilite, whereas Ni, Cu and Co were calibrated using pure alloys. Oxygen was measured using a LDE1 light element detector and calibrated by measuring the peak and background positions of its Kα x-ray line on a synthetic MgO standard. Oxygen calibrations were tested by measuring magnetite and ferro-chromite as a check for reproducibility.

The occurrence of PGM were investigated by a Tescan VEGA II LSU scanning electron microscope (SEM) at the Institut de Minéralogie, de Physique des Matériaux et de Cosmochimie, Muséum National d'Histoire Naturelle, Paris, France. This instrument is equipped with a Bruker XFlash SDD detector in EDS (energy dispersive x-ray spectrometry) mode, with a resolution of 133 eV. The instrument was used with a 20 kV accelerating voltage. The SEM has a high resolution of 50 nm for the HSE elements in back scattered electron (BSE) imaging and an EDS detection limit of between 500-1000 ppm.

The five largest PGMs were extracted through the combination of a FIB and the lift-out technique (cf. Wirth et al., 2013 for detailed explanation). In brief, the FIB is a site-specific technique that allows for thin (<1 µm) electron transparent membranes (or foils) to be cut and extracted from the sample. This is achieved by sputtering the sample by accelerating Ga ions to 30 keV at the specific site on a thin section or mount. Two PGM were extracted for HR-TEM (high resolution transmission electron microscope) analysis and the remaining three were used to determine the $^{187}Os/^{188}Os$ isotopic composition and HSE systematics. The two TEM foils were sputtered in a cross-section including the PGM and the

BMS to enable compositional changes from the host BMS and the PGM inclusion to be detected. These samples were cut with the dimension 15 x 10 x 0.15 µm. The three PGM for HSE analysis were sputtered in a way to ensure that the whole alloy grain was sampled with as little BMS as possible, as such they were sputtered thicker and smaller (6.9 x 6.0 x 1.6 µm; 10 x 6.0 x 1.5 µm; 7.0 x 6.0 x 1.2 µm).

The TEM foils were analysed with a FEI F20 X-Twin transmission election microscope at the GeoForschungs Zentrum (GFZ) Potsdam, Germany. The instrument is equipped with a Gatan Tridiem imaging filter, a Fishione high-angle annular dark-field detector and an EDAX X-ray analyser with an ultra-thin window. These allow for bright field, dark field and HR-TEM images to be obtained. Crystallographic data can be obtained from convergent and single beam electron diffraction patterns, which are compared to parameters from the literature to allow for crystal identification. Detection limits for the HSE vary between 700-1000 ppm (Wirth et al., 2013).

3.2.3 HSE and $^{187}Os/^{188}Os$ analytical techniques

The whole-rock HSE and ^{187}Os isotope signatures were determined for aliquots of 0.25, 0.5 and 1 g (two of each). Each aliquot was spiked with a mixed HSE spike (^{185}Re, ^{106}Pd, ^{195}Pt, ^{191}Ir and ^{190}Os) and digested in 7.5 mL of reverse aqua regia in 50 mL glass vials in an Anton Paar HP-Asher (HPA) at 220°C and ca. 120 bar for 13.5 hours. Following digestion the osmium was extracted via 7 mL of $CHCl_3$ and then back-extracted into HBr following the procedure described in Cohen and Waters (1996). The osmium was then purified via micro-distillation, with the osmium-H_2SO_4-dichromate solution distilled into a 10 µL drop of 9N HBr at 80°C for 2 hours. The aqua regia fraction left over from the Os extraction was then dried down and desilicified using a HF-HNO_3 mix overnight. This allows for complete digestion of the silicates and more efficient recovery of Re (cf. Ishikawa et al., 2014). The samples were then equilibrated with HCl and the HSE were separated from the matrix with anion resin (BioRad AG8 X1, 100-200 mesh) chromatography columns. The separation technique of Pearson and Woodland (2000) was followed, with additional HF-HCl steps prior to elution of the HSE to achieve a better HFSE-HSE (HFSE – high field strength elements) separation.

PGM were digested in a similar fashion to the whole rock with the following changes. Smaller HPA vials (15 mL) were used due to the much smaller sample size; therefore only 3ml of reverse aqua regia (2:1 HNO_3-HCl) was used. The samples were also digested unspiked as accurate weighing and spiking of such small grains could not be performed.

Following digestion the aqua regia was gravimetrically aliquoted into 80% and 20% fractions. The 20% aliquot was then spiked and placed on a rocking plate at room temperature for 24 hours to allow for spike-sample equilibration, after which point it was processed for Os and HSE. The remaining 80% unspiked aliquot was processed immediately for Os and the HSE. For both aliquots only 3 mL of $CHCl_3$ and HBr were utilised in the Os extraction procedure. The HSE portion were not desilicified or processed over columns, due to the small amount of high field strength element interferences present in the alloys.

Base metal sulphides were extracted from thick sections following the procedure of Bragagni et al. (2013). In brief, after characterisation with EMP, BMS were isolated from surrounding silicate minerals via laser ablation (Resonetics M50-E 193 nm ATL Excimer laser system). The laser path was then widened using a diamond scribe and the BMS was carefully extracted from the section. The BMS was then digested via micro-distillation following the procedure of Pearson, et al. (1998), due to their small size the BMS could not be weighed and spiked, so were run unspiked for $^{187}Os/^{188}Os$ composition only, following the procedure previously described for the PGM analysis.

Osmium concentrations and isotopic composition was determined with a Thermo-Finnigan Triton N-TIMS at the NCIET (Northern Centre for Isotopic and Elemental Tracing), Earth Science department, University of Durham, UK. Samples were run on Pt-wire following the procedures described in Dale et al. (2008). Replicate analysis of the standard solution Durham Romil Osmium Standard (DRosS) with load sizes between 10-1000 ng was run 11 times, producing a mean $^{187}Os/^{188}Os$ of 0.16083±0.00055 which is in good agreement with values obtained by Luguet et al. (2008). Total procedural blanks (n = 5) of 1.00±0.42 pg for the whole rock and PGM and 20±5 fg (n = 2) for the BMS were obtained. International reference material UB-N (SARM-CRPG) was analysed once where an $^{187}Os/^{188}Os$ of 0.1274±1 was obtained, similar to published values (e.g. Fischer-Gödde et al., 2011). For the PGM analyses ^{192}Os signal was between 1437-4354 cps, the ^{187}Os was 70-190 cps (240/233 ratio of 276-1047). This led to high 1-s.d. abs. err. range of 0.001-0.002 on the $^{187}Os/^{188}Os$ composition. For the BMS the ^{192}Os signal was between 2728-6627 cps, whilst the ^{187}Os was 98-236 cps (240/233 ratio of 18815-2391). This produced a 1-s.d. abs. err. range of 0.0003-0.0006 on the $^{187}Os/^{188}Os$ composition.

The HSE were analysed by a Thermo Element XR ICP-MS at the Steinmann Institute, University of Bonn, Germany. A double pass boro-silicate glass spray chamber intake system with 0.56M HNO_3 was utilised. International reference material UB-N (SARM-CRPG) was analysed once to determine accuracy and precision, yielding concentrations of 3.27 ppb Os,

2.86 ppb Ir, 7.88 ppb Pt, 5.85 ppb Pd and 0.19 ppb Re; these values are in agreement with literature data (Meisel et al, 2003; Meisel and Moser, 2004; Fischer-Gödde et al., 2011; Luguet et al., submitted). The total average procedural blanks (n = 4) were 0.73±0.36 ppt Ir, 10.78±2.43 ppt Pt, 4.78±0.93 ppt Pd and 0.32±0.16 ppt Re.

3.3. Results

3.3.1. Whole-rock HSE and osmium systematics

Whole-rock HSE systematics varies independently of the quantity of sample digested (Figure 3.1), with variations seen in Os, Ir and Pt contents. Concentrations average 4.12±0.9 (1-s.d.) ppb Os, 3.32±0.53 ppb Ir, 2.51±0.1 ppb Pt for five runs with one outlier at 3.29 ppb (Figure 3.1), whilst Pd and Re concentration are highly reproducible at 0.92±4 ppb and 0.06 ppb respectively (Table 3.1). The variation in concentration does not systematically change with the aliquot size, with replicate analyses of the same mass aliquot showing large differences (e.g. in 0.5 g aliquots, Os concentration varies between 2.84 and 4.31 ppb; Figure 3.1). The variable concentrations in Os, Pt, Pd and Re also show no systematic correlation with Ir concentration, indicating that they are not controlled by the same phases (Figure 3.1).

In general, the HSE display typical CI-Chondrite (Anders and Grevesse, 1989) normalised patterns expected for residues of high degrees of partial melting (Figure 3.2a), with slightly suprachondritic Os_N/Ir_N (subscript N denotes concentration normalised to CI-chondrite) of 1.07-1.36 and sub-chondritic Pt_N/Ir_N of 0.30-0.46 and Pd_N/Pt_N of 0.52-0.66. The Pd_N/Ir_N is highly sub-chondritic ranging between 0.19-0.28, whilst Re_N/Pd_N ratios are close to chondritic (0.93-1.06).

Despite the high variability of the Os concentration the $^{187}Os/^{188}Os$ ratio does not significantly vary based on the quantity of sample digested, with ratios between 0.10893-0.10965. The variability in the $^{187}Os/^{188}Os$ with Ir shows no correlation with all of the aliquots, $^{187}Os/^{188}Os$ also does not vary with 1/Os concentration (Figure 3.3). The $^{187}Re/^{188}Os$ varies between 0.051-0.099, however, as there is no correlation with $^{187}Os/^{188}Os$ no isochron can be produced. Despite the minor variation in $^{187}Os/^{188}Os$ ratios, the model age calculations show a significant range due to the variability in the Os and Re concentrations. Therefore, both rhenium depletion model ages (T_{RD}) and mantle model ages (T_{MA}) were calculated. The T_{RD} ages show a limited range of 2.69-2.79 Ga whilst the T_{MA} ranges significantly wider and to higher values, between 3.09-3.48 Ga (Table 3.1).

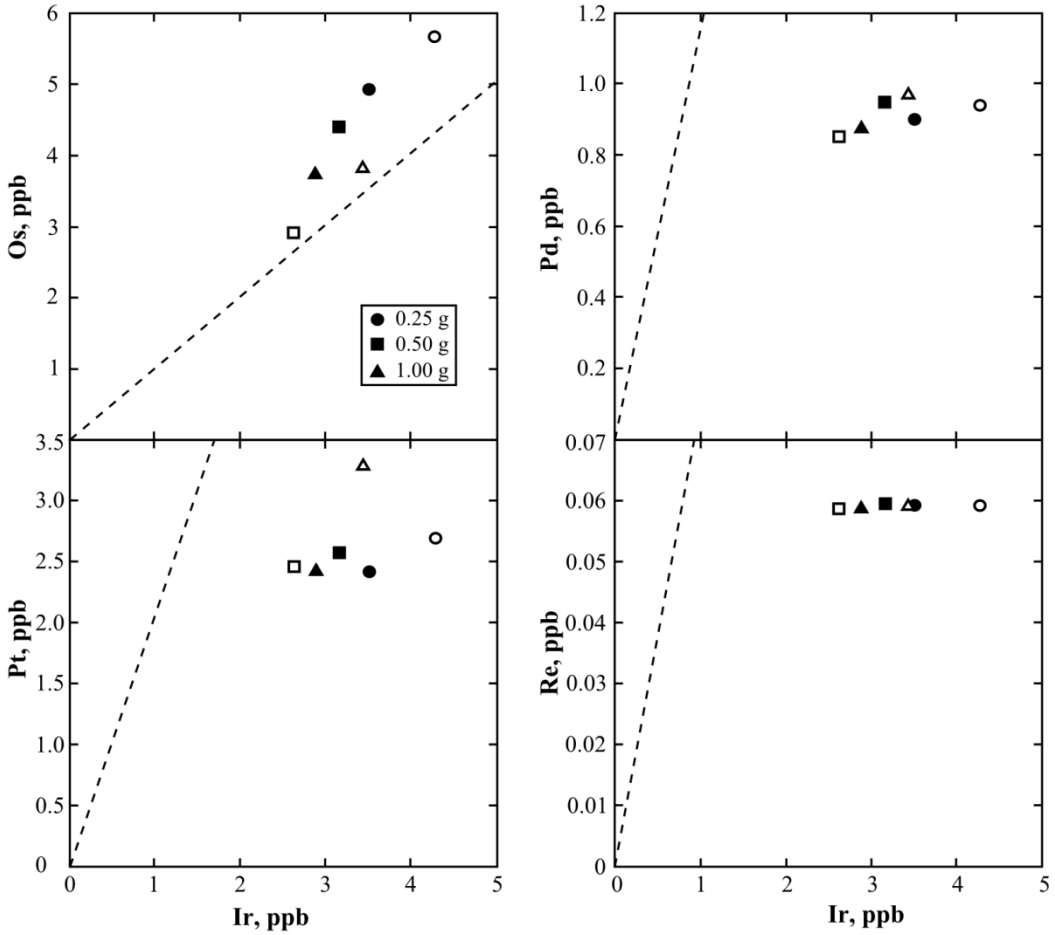

Figure 3.1. Bivariate HSE concentrations for the multiple whole-rock aliquots. Open and closed shapes refer to the same size aliquot, i.e. both triangles are 0.25g. The plots show a correlation between Ir and Os, Pt, Pd for the majority of digestions, however at least one digestion always plots as an outlier. This infers there are multiple controls on the whole-rock HSE systematic.

3.3.2. BMS and PGM major element compositions and osmium systematics

Two BMS located within one thin section ca 1.5 cm apart were analysed for their major element and osmium compositions (Figure 3.4b). The first BMS, Bult-3, is 40 µm in diameter and is partly included in an olivine (Mg# 93) but is in contact with the interstitial serpentinised medium (Figure 3.4a). The second BMS, Bult-4, is also 40 µm in diameter and is an isolated inclusion within a secondary clinopyroxene grain (cf. Chapter 2.4.3). Small interstitial grains of phlogopite (<10 µm) are found in contact with the BMS Bult-4. Within 30 µm of the BMS edge is a serpentinisation vein transecting the clinopyroxene, within which barite minerals are recognised (Figure 3.4c).

The BMS Bult-3 is homogeneous in composition, with up to 70% of the grain containing variable amounts of O. Due to the low solubility of O in Ni-rich sulphide mattes (cf. Fonseca et al., 2008; Wohlgemuth-Ueberwasser et al., 2013), this is most likely not a primary feature and represents the alteration of the BMS into magnetite. The O-free parts are

Table 3.1. Whole-rock $^{187}Os/^{188}Os$ and HSE systematics of 09-BOS-05 with varying sample amounts digested

Weight, g	Os, ppb	Ir, ppb	Pt, ppb	Pd, ppb	Re, ppb	Os_N/Ir_N	Os_N/Pt_N	Pt_N/Ir_N	Pd_N/Ir_N	Pd_N/Pt_N	Re_N/Pd_N	$^{187}Os/^{188}Os_{corr}$	2-sigma error	$^{187}Re/^{188}Os$	T_{MA}, Ga	T_{RD}, Ga
0.25	4.837	3.515	2.411	0.9	0.059	1.36	4.09	0.33	0.16	0.22	1.01	0.10939	0.00019	0.059	3.14	2.73
0.25	5.560	4.284	2.684	0.94	0.059	1.28	4.22	0.30	0.15	0.19	0.96	0.10929	0.00007	0.051	3.09	2.74
0.5	4.312	3.164	2.562	0.949	0.059	1.35	3.43	0.39	0.19	0.26	0.96	0.10965	0.00010	0.066	3.16	2.69
0.5	2.845	2.627	2.452	0.849	0.058	1.07	2.36	0.45	0.26	0.28	1.06	0.10955	0.00012	0.099	3.48	2.71
1.0	3.753	3.444	3.287	0.973	0.059	1.08	2.33	0.46	0.22	0.24	0.93	0.10893	0.00043	0.076	3.36	2.79
1.0	3.403	2.888	2.424	0.877	0.059	1.17	2.86	0.41	0.22	0.26	1.03	0.10951	0.00006	0.083	3.33	2.71

Table 3.2. Single grain BMS and PGM electron microprobe results, $^{187}Os/^{188}Os$ systematics and inter-elemental HSE ratios

	EMP, wt. %														Isotope Dilution					
Sample	O	S	Fe	Ni	Cu	Co	Pt	Os	Ir	Ru	Total	M/S	$^{187}Os/^{188}Os_{corr}$	2-sigma error	T_{RD}, Ga	Pt/Ir	Pd/Ir	Re/Ir	Pt_N/Ir_N	Pd_N/Ir_N	Re_N/Ir_N
Bult-3	0.24	32.11	30.49	36.12	0	0.80	n.d.	n.d.	n.d.	n.d.	99.76	1.16	0.1084	0.0006	2.86	n.a.	n.a.	n.a.	n.a.	n.a.	n.a.
Bult-4	0.05	31.67	25.78	41.55	0	0.79	n.d.	n.d.	n.d.	n.d.	99.84	1.18	0.1066	0.0003	3.09	n.a.	n.a.	n.a.	n.a.	n.a.	n.a.
foil-3	n.a.	n.a.	n.a.	n.a.	n.a.	n.a.	n.a.	n.a.	n.a.	n.a.	n.a.	n.a.	0.1294	0.0012	0.003	27.04	0.99	0.88	13.14	0.85	11.64
foil-5	n.a.	n.a.	n.a.	n.a.	n.a.	n.a.	n.a.	n.a.	n.a.	n.a.	n.a.	n.a.	0.1342	0.0019	-0.64	5.18	0.39	1.10	2.52	0.34	14.48

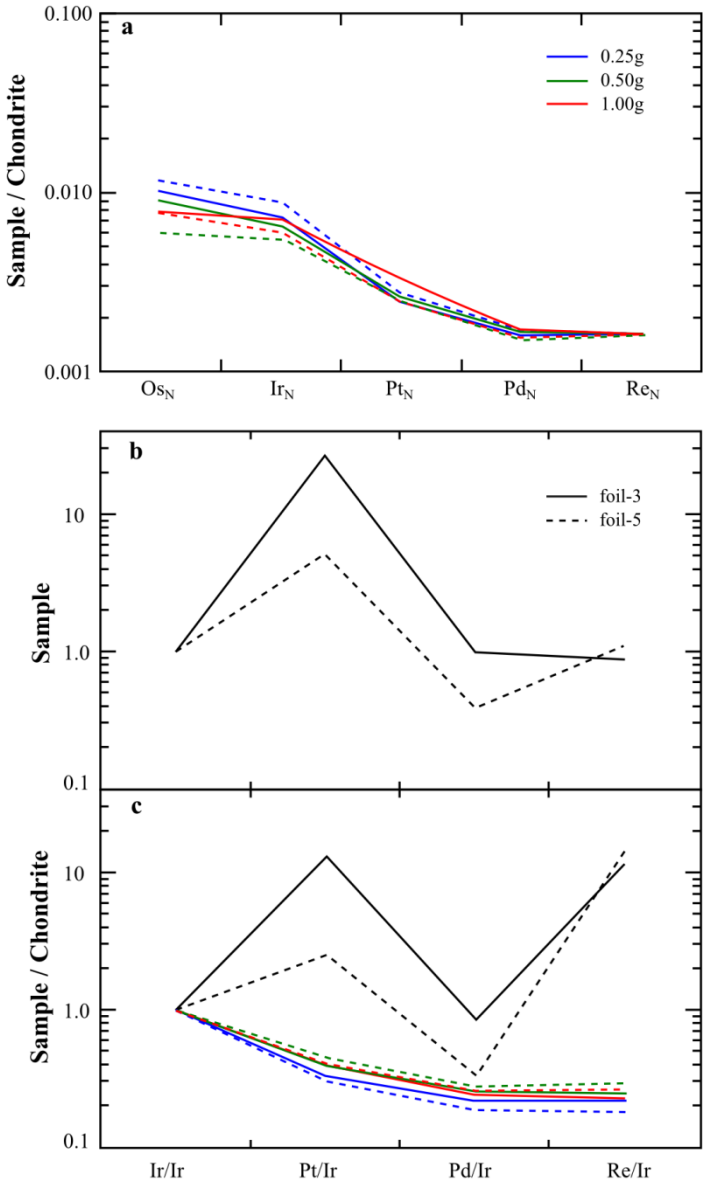

Figure 3.2. HSE concentration patterns for the whole-rock and Pt-alloys. a) CI-chondrite normalised HSE pattern for the multiple whole-rock aliquots. Dotted lines is secondary analysis of the same aliquot size. CI-chondrite values from Anders and Grevesse (1989). The patterns display highly variable Os-Ir-Pt that varies regardless of aliquot size, which is due to the highly heterogeneous distribution of PGM within the whole-rock. b) HSE composition of the two Pt-alloys analysed. Due to the inability to accurately spike the samples absolute concentrations were not obtained, therefore, only ratios with Ir are shown. Both alloys display similar enrichments in Pt over Ir, with variable Pd and Re. c) Comparison of whole-rock, Pt-alloy and CI-chondrite (Anders and Grevesse, 1989) normalised HSE compositions. As in b, all concentrations normalised to Ir, symbols as in a and b.

pentlandite with a metal/sulphur (M/S = (Fe + Ni + Cu + Co) / S) ratio of 1.15, with Fe and Ni contents of 30.5 and 36.1 wt. % respectively (Table 3.2). The oxidised sections contain up to 18.7 wt. % O, this oxidation is coupled with a decrease in S (13.4 wt. %) and Ni (14.7 wt. %) content and an increase in Fe (51.7), signifying the transition of the pentlandite into

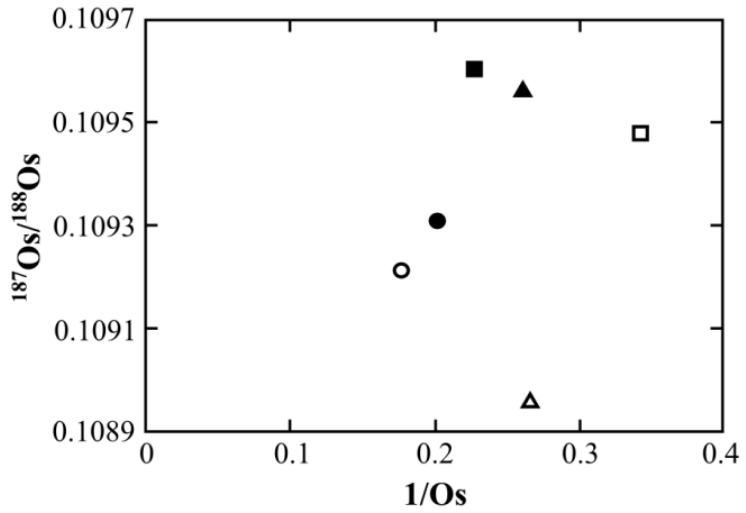

Figure 3.3. $^{187}Os/^{188}Os$ versus 1/Os mixing diagram, symbols as in Figure 3.1. No correlation between the Os concentration and composition is seen, inferring that the control of the $^{187}Os/^{188}Os$ at the whole-rock scale is not due to simple two-component mixing.

magnetite. Bult-4 is also a pentlandite with a M/S ratio of 1.17, which is coupled with a much higher Ni content of 41.8 wt. % and a significantly lower Fe content of 24.1 wt. % (Table 3.2). Bult-4 shows no variability in composition, however small (~2 µm) cracks transect the grain (Figure 3.4d).

Platinum group minerals were found in each pentlandite, with the SEM revealing >15 PGM within Bult-3 and two within Bult-4. The alloys in Bult-3 have similar morphology, formed as long (1-5 µm), thin (≪ 1 µm) inclusions. Whilst the two from Bult-4 are discrete minerals and have dimensions of 1 µm x 1 µm and 2 µm x 4 µm. The alloys in Bult-3 are clearly orientated parallel to one another, while in Bult-4 the alloys are found along the rim of the BMS grain (Figure 3.4).

The five largest alloys were extracted from the BMS, three grains from Bult-3 (foil-1, foil-2, and foil-3) and the two from Bult-4 (foil-4 and foil-5; Figure 3.4). Foil-2 and foil-4 were extracted for analysis with the HR-TEM whilst the remaining three were used for Os isotope compositions and HSE concentrations. The HR-TEM images revealed that in foil-2 (from Bult-3) five distinct grains can be identified (Figure 3.5a). Each PGM varies in length from 1 µm to 4 µm, but are of a somewhat uniform thickness ~75 nm and lie parallel to one-another. In contrast, foil-4 from Bult-4 contains one PGM as a single discreet phase and is the only PGM seen in the foil (Figure 3.5d). This PGM measures approximately 900 x 300 nm and has a "Chinese script" lamellae texture. EDX scans across the PGM from both samples indicate that the PGM are composed of Pt-Fe, with the PGM in foil-2 also containing Ir and Rh (Figure 3.5). Platinum and iron ratios vary in two separate PGM from foil-2, with the

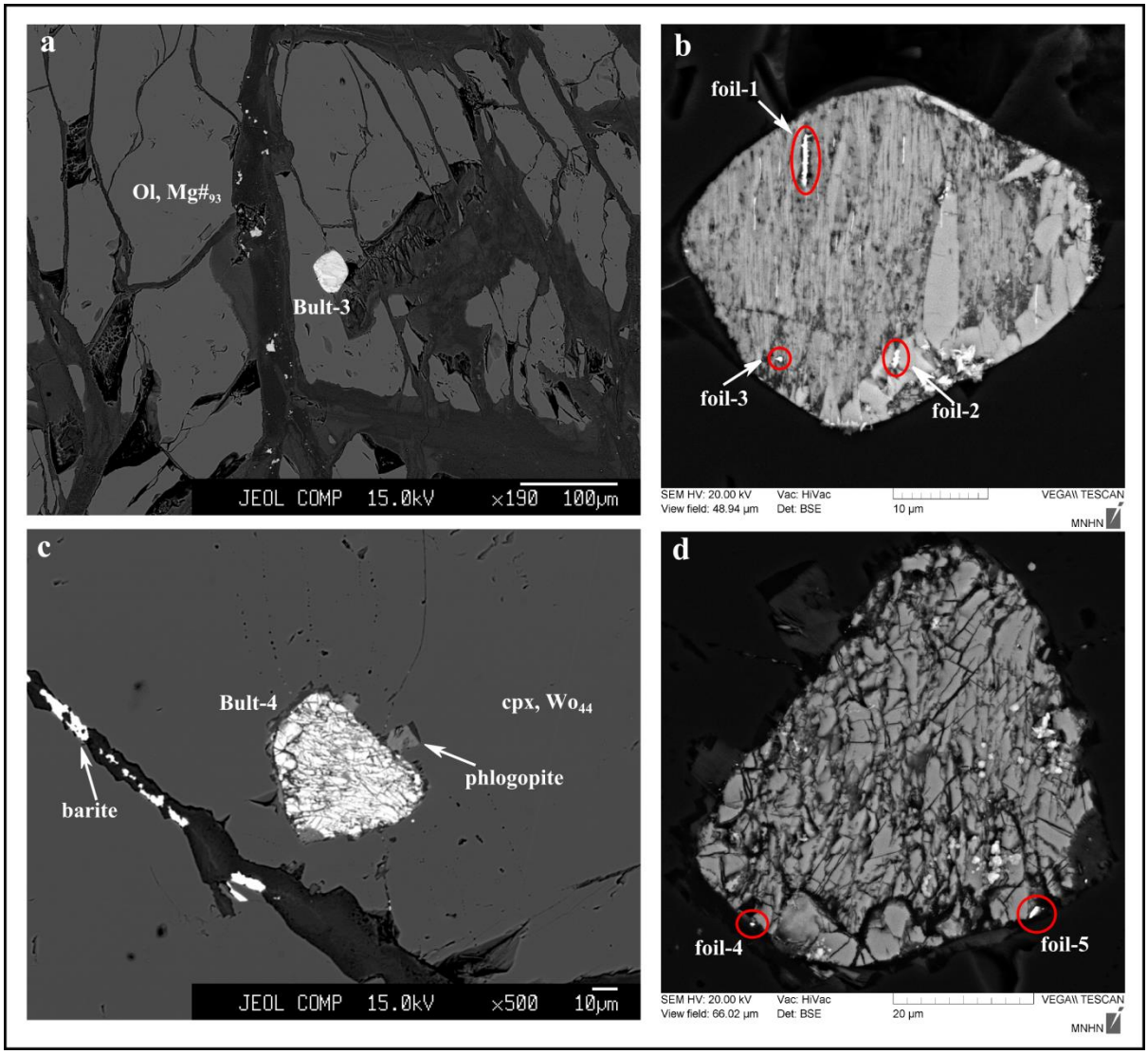

Figure 3.4. Back scattered electron (BSE) images for BMS Bult-3 and Bult-4. a) Silicate textural association of pentlandite Bult-3. The highly altered nature of the host olivine is clearly seen, however the olivine has a consistent Mg# of 93. b) BSE image of Bult-3 obtained by HR-SEM, showing the highly altered nature of the pentlandite. Red circles denote alloys extracted by FIB. Alloys that were not extracted in this study can also be seen lying parallel to one another as thin bright lines within the pentlandite matrix. c) Silicate textural association of pentlandite Bult-4. The pentlandite is enclosed within a clinopyroxene with a Wo of 44, small phlogopite grains are located around the vicinity of the pentlandite. An alteration vein is seen traversing the cpx, with barite deposited within. d) HR-SEM BSE image of Bult-4, the highly fractured nature of the pentlandite can clearly be seen. The two red circles denote the two alloys found within this pentlandite, both of which were subsequently extracted for HSE and $^{187}Os/^{188}Os$ analysis.

PGM that also contains minor Rh displaying significantly less Fe (Figure 3.5). The Ir/Pt varies slightly between the two analysed PGM in foil-2 due to an increase in Ir (Figure 3.5). The spectra for the PGM in foil-4 indicate that the composition is fairly homogenous, with no variability in Fe/Pt from three separate analyses. Osmium was not detected in any of the alloys on the TEM, despite being detected by both the SEM and EMP (see Figure A.1).

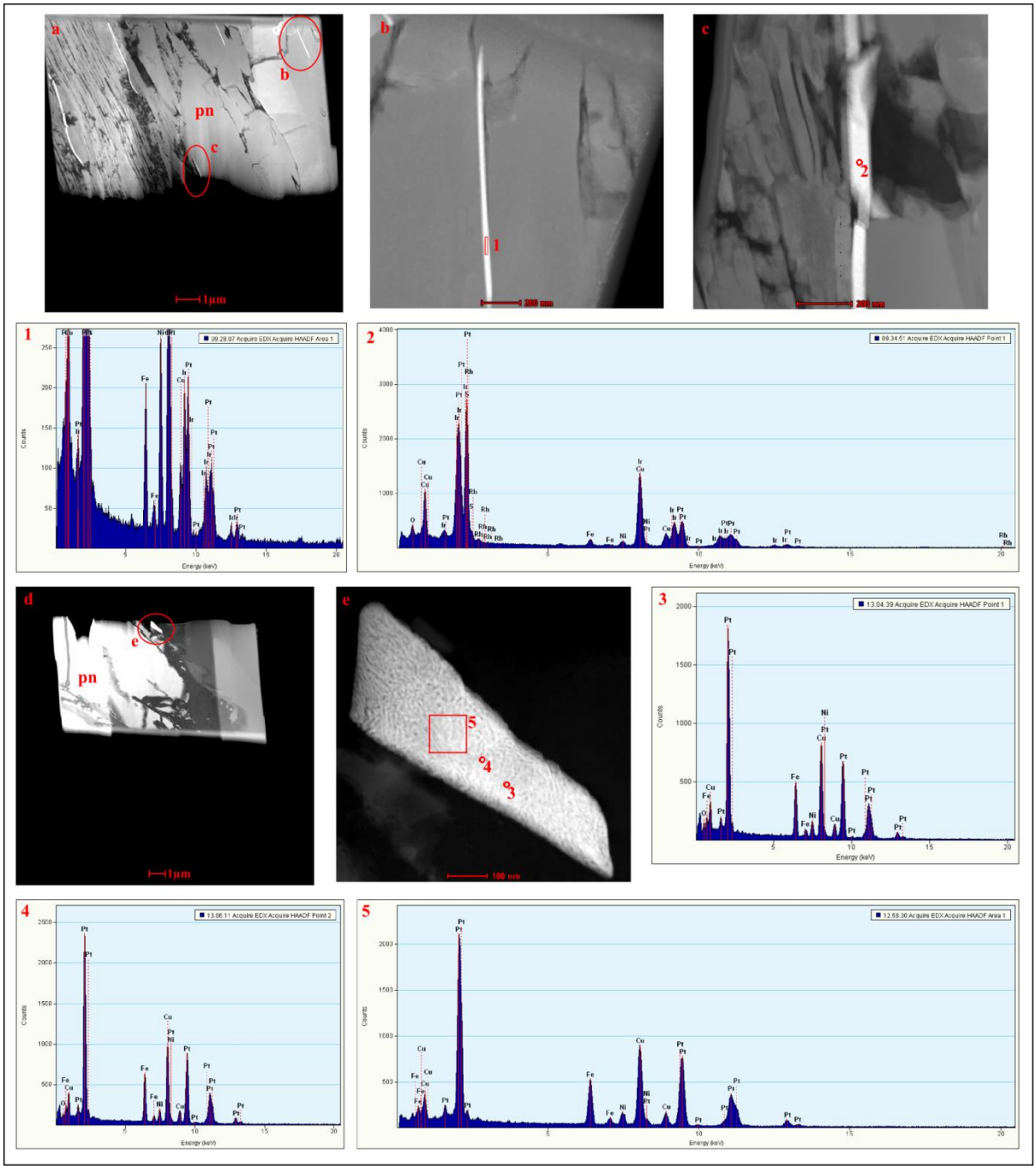

Figure 3.5. HR-TEM images and EDX spectrums for alloy-2 and alloy-4. a) HR-TEM image of entire foil-2, clearly showing multiple nano-meter thick alloys lying parallel to one another. The two red circles denote the alloys shown in b and c. b) HR-TEM image from foil-2, small square labelled "1" corresponds to the EDX-spectrum labelled 1 below. The EDX-spectrum 1 displays the Pt-Fe-Ir composition of this alloy inclusion. c) HR-TEM image of a different alloy from foil-2, small circle labelled "2" corresponds to EDX-spectrum labelled 2 below. This spectrum shows the more enriched Ir content of this alloy, as well as the association of Rh and depletion in Fe. d) HR-TEM image of entire foil-4 foil. Here, the alloy is one single cluster, shown in the red circle. e) HR-TEM image of the alloy seen in foil-4. This image shows the Chinese script texture of the alloy, the two circles and square labelled 3, 4 and 5, correspond to the subsequent EDX-spectrum. These spectrum show the homogeneous Pt-Fe composition of this alloy, with no association of Ir or Rh.

However, this may have been due to either the low detection limit of HSE by TEM (>700 ppm, Wirth et al., 2014), or due to the overlap of the KβCu peak on the LαOs peak as I used of a Cu grid on the TEM foils. Diffraction patterns obtained from foil-4 demonstrate that the PGM is not a single discrete grain but is composed of small nanoparticle platelets stacked on-top of one another. This is revealed by the circular nature of the selected area diffraction pattern (SAED; Figure 3.6a), and the variable patterns obtained from single point diffraction (Figure 3.6b-c-d).

Prior to separation of the HSE a 20% split of the alloy digestion was spiked to enable the determination of inter-elemental HSE ratios. Due to the difficulty in manipulating sub-micron grains, foil-1 was not successfully analysed. For foil-3 (from Bult-3) Pt is extremely enriched with a Pt/Ir of 27.04 and a Pt/Pd of 27.19, however Ir, Pd and Re occur in similar quantities, with a Pd/Ir of 0.99 and a Re/Ir of 0.88 (Table 3.2), such that Ir ≈ Pd ≈ Re ≪ Pt (Figure 3.2b). Foil-5 (Bult-4) is slightly different in composition compared to foil-3, with a Pt/Ir ratio of 5.18 and an Pd/Ir ratio of 0.39, however the Ir/Re ratio is 1.10. Therefore in the alloy from foil-5 the HSE follow Pd < Re ≈ Ir < Pt (Figure 3.2b). When normalised to Ir and CI-Chondrite (Anders and Grevesse, 1989) foil-3 and foil-5 show significant Re enrichment (Re_N/Ir_N = 11.64 and 14.48, respectively) and slight Pd depletions (Pd_N/Ir_N = 0.85 and 0.34, respectively; Table 3.2; Figure 3.2c).

For the two BMS $^{187}Os/^{188}Os$ compositions were obtained of 0.1084 ± 0.0006 for Bult-3 and 0.1066 ± 0.0003 for Bult-4 (Table 3.2). However, the PGM yield a systematically more radiogenic $^{187}Os/^{188}Os$ composition of 0.1294 ± 0.0012 for foil-3 (from Bult-3) and 0.1342 ± 0.0019 for foil-5 (from Bult-4). Rhenium depletion (T_{RD}) model ages were calculated for the BMS and PGM with ages of 2.86±0.16 and 3.09±0.09 Ga obtained for Bult-3 and Bult-4 respectively (Table 3.2). A very young age is obtained for foil-3 of 30±340 Ma, whilst foil-5 gives a future age (-643±516). The age of the BMS Bult-3 is within error of the average whole-rock T_{RD} age (2.73±0.03 Ga), whilst the BMS Bult-4 is within error of the average whole-rock T_{MA} (3.26±0.14).

3.4. Discussion

3.4.1. Origin of base metal sulphides and platinum alloys

The two BMS have different textural habits with the modally major silicates. Bult-3 is located along the rim of a highly serpentinised olivine, within the serpentinisation vein. This spatial association to serpentinisation likely resulted in the oxidation and break-down of the pentlandite into magnetite, due to desulphurisation (Lorand and Grégoire, 2006). However,

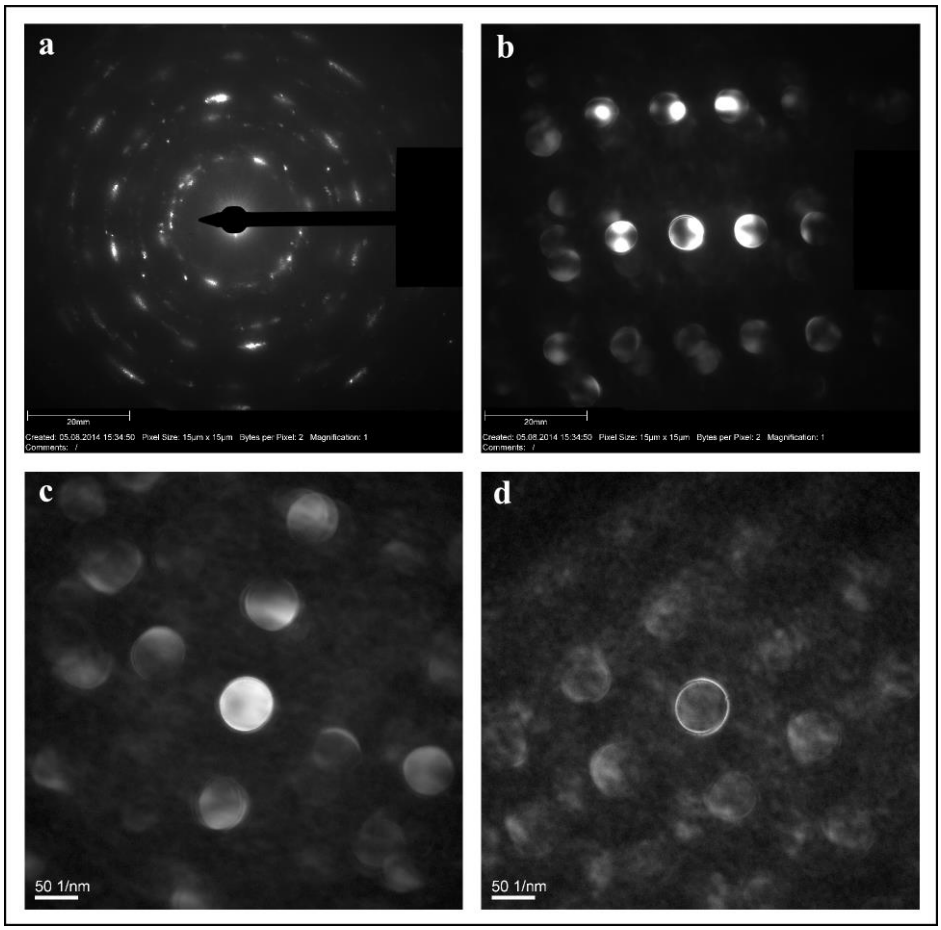

Figure 3.6. HR-TEM diffraction patterns obtained from alloy-4. a) A single area diffraction pattern from alloy-4 displaying an almost complete ring. Diffraction rings occur when multiple crystals are stacked on top of one another in different directions. This infers that alloy-4 is a cluster of nanoparticles. The point diffraction patterns in b, c and d are further proof of the nanoparticle structure of alloy-4, due to the constantly changing orientation of the spot diffraction patterns obtained.

prior to this serpentinisation the BMS Bult-3 was likely an inclusion within the olivine, due to the optical continuity of the olivine-serpentine on all side of the BMS. The BMS Bult-4 is an isolated inclusion hosted within a secondary clinopyroxene and is rimmed by very small phlogopite crystals signifying the metasomatic origin of the clinopyroxene. This entrapment in the clinopyroxene either suggests the BMS was already present in the peridotite and was included into the growing clinopyroxene during silicate metasomatism or that the BMS formed at the same time from a sulphide matte associated to the silicate metasomatism. The large size of the clinopyroxene (0.2 mm in diameter) and the alteration by cross cutting fractures filled with barite suggests that the clinopyroxene formed prior to the entrainment of the peridotite in the kimberlite. That is, the metasomatic event that formed the clinopyroxene and potentially the BMS was distinct from the kimberlite infiltration.

The predominance of Ni-rich BMS and the lack of Fe-rich BMS indicates that the BMS are not a primary feature of the peridotite and have been reintroduced by a metasomatic process. Ni-rich sulphide mattes occur in the mantle as an evolved form of an Fe-rich sulphide matte (Craig, 1973; Peregoedova et al., 2004; Lorand and Grégoire, 2006) and can occur due to fractional crystallisation of the sulphide matte (Peregoedova et al., 2004). The whole-rock major and trace element systematics of 09-BOS-05 also attest to the likelihood that the BMS are a secondary feature. Its high Mg# in olivine, low Lu and Al_2O_3 abundance infer a high degree of partial melting (i.e. >45%, cf. Chapter 2.5.1) which at least partly took place at 2-3 GPa. Also, the fertile mantle will be depleted of S with >25% partial melting, at shallow pressures where the S solubility in melt is ca. 1000 ppm (Mavrogene and O'Neill, 1999) thereby depleting the residue of primary BMS (cf. Lorand et al., 1999; Pearson et al,. 2004), as such, any BMS occurring in 09-BOS-05 cannot be of primary origin and have formed through metasomatic processes.

The PGM inclusions within the BMS could either have been formed in the residue due to partial melting or they could be secondary minerals formed in relation to the sulphide metasomatism. The nanocluster form of the PGM in foil-5 is the first time such a formation has been described in cratonic peridotite. The formation of HSE nanoparticles has been suggested by Ballhaus and Sylvester (2000) as a method for the formation of PGE (platinum group elements) deposits. This has subsequently been demonstrated as a possibility through the discovery of Ru-Rh nanoclusters in the Bushveld complex (Wirth et al., 2013) and through experiments (Helmy et al., 2013). Wirth et al. (2013) conclude that the Ru-Rh nanoclusters, found within pentlandite, formed at high temperature prior to the crystallisation of the sulphide and subsequent sub-solidus re-equilibration to pentlandite. This follows the model of Ballhaus and Sylvester (2000), whereby a S-undersaturated silicate melt becomes HSE-oversaturated, causing the least soluble metals (e.g. Pt) to form complexes with other PGE and ligands such as Fe, Bi and Te (Tredoux et al., 1995). Once S saturation has occurred immiscible sulphide droplets form, which then scavenge the PGM due to the lower surface tension, thereby concentrating the PGM. It is thus very likely that these PGM formed at high temperature from a silicate metasomatic melt as proposed by Ballhaus and Sylvester (2000). This is further supported by the stability of Pt-Fe alloys at temperatures up to 1350°C in S-free systems (Makovicky, 2002).

The Pt-alloys associated with Bult-3 are all aligned parallel to one another, regardless of size. This is observed at the micron scale and the nanometre scale within this BMS (Figure 3.4b and 3.5a), signifying a crystallographic relationship between the Pt-alloy and BMS

phase. This texture could be formed due to the crystallisation of the pentlandite, as the Pt-Fe nanoclusters are impurities in the structure of the pentlandite they will not be accommodated (Makovicky et al., 1986; Ballhaus and Ryan, 1995). As such, they form clusters along crystallographically weak layers and form thin orientated crystals. The lack of such orientation in the BMS Bult-4 may be due to the orientation of the pentlandite within the thin section, enabling only a 2D view of a 3D structure.

3.4.2. Osmium systematics of single grain BMS and platinum-alloys

Both BMS dated within this study have a small range in $^{187}Os/^{188}Os$ compositions (0.10659-0.10840). However, the Pt-alloys have a significantly more radiogenic $^{187}Os/^{188}Os$ composition of 0.12938-0.13424. This dichotomy can only be explained by a difference of Re/Os between the BMS and the Pt-alloys. Re has been shown to be siderophile in metal-silicate partitioning experiments (Mann et al., 2012), although the metal composition of the Pt-alloys from this study are not the same as those from the experiments, the siderophile nature of Re could be proposed to still take place. Therefore, if the alloys formed at high temperature in a S-undersaturated silicate melt, as was argued in Section 3.4.1, then Re within the silicate melt would partition into the Pt-alloy. Therefore, the alloy would have a high Re/Os and any subsequent sulphide matte would potentially have a lower Re/Os. Assuming that the present day $^{187}Os/^{188}Os$ composition of the BMS is close to that of the initial entire silicate-sulphide melt system, and that the BMS T_{RD} age (i.e. 3.09 Ga) dates the formation of the Pt-alloys, it is possible to calculate the amount of $^{187}Re/^{188}Os$ (and the Re/Os) required in the alloy to create the present day $^{187}Os/^{188}Os$ composition seen. This is achieved through the following equation:

$$\left[\frac{^{187}Os}{^{188}Os}\right]_{initial} = \left[\frac{^{187}Os}{^{188}Os}\right]_{Pt-alloy} - \left[\frac{^{187}Re}{^{188}Os}\right]_{Pt-alloy} \times \left[e^{\lambda t} - 1\right]$$

Where $^{187}Os/^{188}Os_{initial}$ is the present day composition of the BMS, $^{187}Os/^{188}Os_{Pt\text{-}alloy}$ is the present day composition of the Pt-alloy, $^{187}Re/^{188}Os_{Pt\text{-}alloy}$ is the unknown, λ is the Re-Os decay constant ($\lambda = 1.666 \times 10^{-11}$, Smoliar et al., 1996) and *t* is the time since the formation of the alloys i.e. the T_{RD} age of the BMS (3.09 Ga and 2.86 Ga). These calculations indicate that for foil-3 an $^{187}Re/^{188}Os$ composition of 0.48 is required, whilst for foil-5 0.52 is needed, with a corresponding Re/Os of 0.015 and 0.016 respectively. However, these high $^{187}Re/^{188}Os$ compositions are not seen within the literature in HSE-alloys (Bird et al., 1999; Meibom and Frei, 2002; Meibom et al., 2002; Walker et al, 2005; Luguet et al., 2008b; Coggon et al.,

2011), with the only data available indicating very low $^{187}Re/^{188}Os$ (i.e. < 0.001). This does not, however, preclude the possibility that HSE-alloys can contain high $^{187}Re/^{188}Os$. The alloys investigated in previous studies have been predominately sampled from placer-deposits related to ophiolites (Bird et al., 1999; Meibom and Frei, 2002; Meibom et al., 2002; Walker et al, 2005; Luguet et al., 2008b; Coggon et al., 2011). These alloys have been interpreted as exsolution products due to extensive partial melting events in a supra-subduction environment (Brenker et al., 2003) and are therefore residual in origin. This type of formation would create low to non-existent Re concentrations within the alloy, as it would have been removed during the partial melting event/s due to its higher incompatibility (McDonough, 1994; Reisberg and Lorand, 1995). The high Re concentration required in the Pt-alloys from 09-BOS-05 therefore supports the model of their formation in a silicate melt and subsequent entrainment into the BMS.

3.4.3 Mineralogical effects on the whole-rock HSE systematics and osmium compositions

The whole-rock HSE systematics show high variability, regardless of the quantity of sample analysed. A comparison of the HSE chondrite normalised patterns of the whole-rock and the Pt-alloys (Figure 3.2c) clearly shows the control the alloys have over the whole-rock Pt content, with the variability of Pt at the whole-rock scale similar to that of the Pt-alloys. Due to the lack of specific concentrations for the Pt-alloys, all of the HSE have been normalised to Ir as well as to CI-chondrite for both the Pt-alloy and the whole-rock (Figure 3.2c). The CI-chondrite normalised patterns of the Pt-alloys show a strong, yet variable, enrichment of Pt over Ir, Re over Ir and depletion of Pd. This variability is to a certain extent mimicked in the whole-rock data, as the two whole-rock patterns with the lowest Pt_N/Ir_N also have the lowest Pd_N/Ir_N. However, the whole-rock aliquots are not as enriched in Re as the Pt-alloys, and the whole-rock with the highest Pt_N/Ir_N has a markedly low Pd_N/Ir_N, signifying that in the whole-rock aliquots the Pt-Pd do not always vary together as they do in the Pt-alloys. This suggests the possibility of a third component in the system, as can also be seen in the diagram of 1/Os vs $^{187}Os/^{188}Os$ (Figure 3.3) which indicates that the variability seen in the Os composition is not a simple two-component mixing. Further support for a third component is seen in the whole-rock PGE concentration diagrams of Ir vs. Pt and Pd, with the Pt-alloy compositions and a field for metasomatic pentlandite indicated (Figure 3.7). Whilst the ratio of Pd/Ir from foil-5 is somewhat similar to the trend in the whole-rock concentrations, the Pt/Ir clearly indicates that the whole-rock is enriched in Ir compared to the Pt-alloys. The trends in Figure 3.7 also show that for the alloys Pt and Pd vary together, whilst this is not

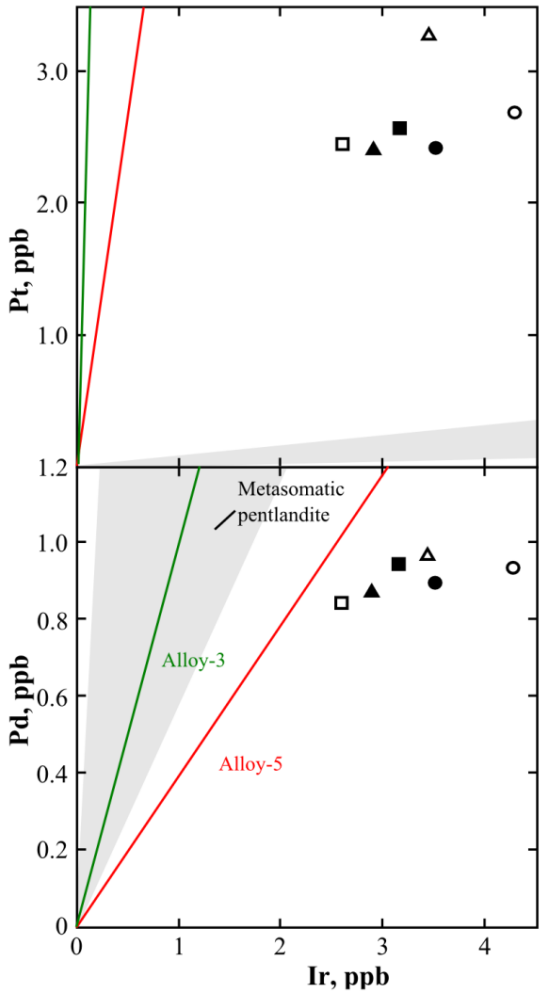

Figure 3.7. Bivariate PGE concentration plots of the whole-rock aliquots with the compositional trend of the two alloys and the zone for metasomatic pentlandite from Lherzolite LI-X of Alard et al. (2005). Symbols as in Figure 3.1, red line is alloy-5, green line is alloy-3, grey shaded area is metasomatic pentlandite. For Pt vs. Ir the alloys cannot account for the high Ir seen at the whole-rock scale. Whilst for Pd vs. Ir alloy-5 has a very similar trend to the one seen for four of the whole-rock digestions. In the alloys Pt and Pd vary together, this is not mimicked by the whole-rock and may be accounted for by metasomatic pentlandite which display high Pd and low Pt.

mimicked by the whole-rock aliquots. However, metasomatic pentlandite (Alard et al., 2005) exhibits a significant enrichment in Pd over Pt and they may account for this offset of Pt-Pd in the whole-rock aliquots and could therefore be the third component in the system. This is likely as BMS have been shown to control the whole-rock HSE budget (cf. Alard et al., 2000; Luguet et al., 2003). Nevertheless, the variable supra-chondritic Os_N/Ir_N of the whole-rock cannot be explained by metasomatic BMS. Suprachondritic Os_N/Ir_N have been interpreted as signatures of partial melting, due to the partitioning of Os and Ir into separate minerals after the extraction of S. Due to the micro-metric size of these minerals a sampling bias can occur during digestion that artificially fractionates the Os and Ir, creating variable Os_N/Ir_N in

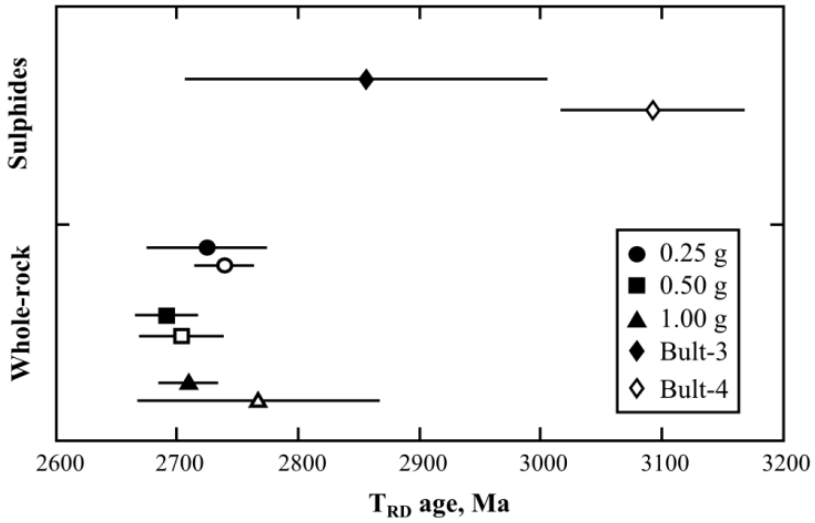

Figure 3.8. Re-Os T_{RD} ages for the whole-rock aliquots and the two BMS analysed. Black bars are the 2-sigma propagated errors after Sambridge and Lambert (1997). The variability in the whole-rock aliquots is clearly shown to be within error of one another. The large error obtained on Bult-3 also places it within error of the whole-rock, whilst Bult-4 is clearly an outlier, denoting that its Re-Os age may be recording a separate event.

duplicate analysis of the same sample (Luguet et al, 2007). Accordingly, the whole-rock Os_N/Ir_N indicates that this peridotite most likely also contains residual PGM, as expected from the high degrees of partial melting.

3.4.4 Significance of the T_{RD} ages

The T_{RD} ages obtained for the Pt-alloys have no geological implications, as due to their high Re/Os (see section 3.4.2.) the T_{RD} age is greatly impacted by the ingrowth of ^{187}Os, which has not been corrected for. However, the T_{RD} age of BMS likely reflects the age at which the Pt-alloys formed, as the BMS would have had a lower Re/Os than the Pt-alloys. It can therefore be inferred, that the 3.09 and 2.86 Ga ages signify the timing of localised silicate melt percolation. The similarity of the whole-rock T_{RD} (2.70-2.78 Ga) and T_{MA} (3.10-3.47 Ga) with these BMS ages (Figure 3.8) further indicates the likelihood of a significant event at this time. It has been shown that the eastern and western blocks of the Kaapvaal Craton were sutured between 2.93-2.88 Ga (Schmitz et al., 2004), along the Colesburg-lineament, which is <100 km from the Bultfontein kimberlite. It is therefore likely, that the BMS ages obtained in this study are reflecting this event or at least the presence of new silicate melt generated by this event. This highlights that the BMS ages obtained do not reflect partial melting events, but rather addition of new material to the lithospheric mantle.

The Western Terrane of the Kaapvaal craton has a 3.1 Ga age of stabilisation, based on crustal and mantle ages (cf. Schmitz et al., 2004). However, if a metasomatic event

between 2.9-3.1 Ga led to the formation of the Pt-alloys then the lithosphere must have been extensively depleted prior to this time. This implies that the high degree of partial melting, resulting in the depleted Al_2O_3, CaO and Lu and the potential formation of Os-Ir alloys must have occurred before 3.1 Ga. For this to be the case the stabilisation of the lithosphere must have occurred earlier, inferring that the Western Terrane is older than currently envisaged.

5. Conclusion

Sub-microscopic Pt-alloys included within metasomatic pentlandite display highly radiogenic $^{187}Os/^{188}Os$ compositions compared to the host BMS. This dichotomy can only be explained through a difference in Re/Os between the Pt-alloy and the host BMS. The Pt-alloys are formed as small nanoclusters, which can be explained through their formation at high temperature in a HSE-saturated silicate melt (Ballhaus and Sylvester, 2000). The parallel orientation of the alloys within the BMS indicate that the alloys and BMS are co-genetic, thereby indicating that the heterogeneous distribution of Re/Os must have occurred at the time of crystallisation due to the siderophile nature of Re. The Archean T_{RD} age obtained for the host metasomatic BMS signifies that this formation event took place between 2.8-3.1 billion years ago, signifying that the T_{RD} ages obtained from BMS containing Pt-alloys date addition of new material and not partial melting.

The heterogeneous distribution of Pt-alloys within xenolith 09-BOS-05 cannot fully account for the large variability in Os-Ir-Pt-Pd seen in multiple aliquots of the whole-rock. The heterogeneous distribution of the Pt-alloys within the peridotite can account for the variability in the Pt concentration seen at the whole-rock scale, however, they do not account for the variation seen in Ir and Pd. The enrichment in Pd can be accounted for by the heterogeneous distribution of metasomatic BMS through-out the peridotite and may also account for the variable Ir concentration. However, the variability in both Os and Ir and Os_N/Ir_N can also be accounted for by a fourth phase that was not discovered within the course of this study, Os-Ir alloys. Due to the high degree of partial melting this peridotite has undergone, it is likely that Os-Ir-alloys are present.

The highly depleted nature of the peridotite coupled with the Archean T_{RD} ages obtained from the metasomatic BMS imply that the host peridotite had already undergone an extreme degree of partial melting prior to the metasomatic event at least 2.8 b.y.a. This implies that the stabilisation of the lithosphere of the Western Terrane (Kaapvaal Craton) occurred much earlier than the currently accepted age of 2.9-3.2 Ga.

Chapter 4

Cryptically and modally metasomatised peridotite from Letlhakane: Insights from coupling petrography and Re-Os dating of base metal sulphides

4.1. Introduction

Archean cratons are the oldest example of the Earth's early continents, and are underlain by thick cratonic roots. As such, they are a repository of geological processes active during the Earth's early history, and also detail the link between the formation and growth of the early crust and lithospheric mantle keels. Geochemical investigations regarding the chemical composition of these lithospheric roots coupled with whole-rock isotopic dating using the Re-Os chronometer (^{187}Re->^{187}Os, $T_{1/2}$=42.3 Ga, Smoliar et al., 1996) have led to two conceptual hypotheses for craton formation (Pearson, 1999), both of which are still highly debated (Lee et al., 2011; Aulbach, 2012; Pearson and Wittig, 2013 and references therein). In brief, the first hypothesis invokes a large mantle plume as the source of partial melting and consequent extensive depletion and stabilisation of the cratonic lithosphere. Such a mechanism would be expected to result in a homogeneous distribution of Re-Os ages with depth (Griffin et al., 1999; Aulbach et al., 2007). The second model involves shallow lateral accretion processes, such as subduction, to thicken the lithosphere as a whole (Jordan, 1988; Helmsteadt & Schulze, 1989). Unlike the plume hypothesis, this would result in a complex variation of the Re-Os ages with depth as well as laterally (Parman et al., 2004; Lee, 2006; Simon et al., 2007).

There is, however, a major issue that hinders progress on the resolution of the plume vs. subduction debate for the origin of cratons. The cratonic mantle samples that possibly hold the answers needed to resolve this debate have undergone an exceedingly complex history, which has obscured much of the information on the primary processes that led to their formation (Carlson et al., 1999; Griffin et al., 1999; 2004; Pearson et al., 2003). The Re-Os isotopic system has been shown to be more robust than the lithophile-based isotopic systems to re-enrichment and rehydration of the cratonic roots (e.g. Walker et al., 1989; Pearson et al., 1995). However, this system is still sensitive to such processes via the addition of incompatible Re or the precipitation of metasomatic Os-(Re)-bearing base-metal sulphides (BMS: Fe-Ni-Cu sulphides). Both of these processes, although strongly dependent on the

extent of Re addition and its timing, will likely lead to the rejuvenation of cratonic mantle roots (Luguet et al., submitted). This will lead to an apparent decoupling of the age of the cratonic crust and lithospheric mantle, resulting in uncertainty of their genetic relationships. For example, Re-Os geochronological studies on cratonic peridotites have a statistical peak in the Neoarchean (Griffin et al., 2004; Pearson and Wittig, 2008). However, on cratons with crustal rocks of Eoarchean age, there are few, if any, corresponding mantle ages. This crust-mantle decoupling of timing of their formation is highlighted in the Zimbabwe craton where the peak in cratonic mantle Re-depletion ages falls between 2.7 and 2.9 Ga (Carlson et al., 1999; Shirey et al., 2001; Smith et al., 2009; Luguet et al., submitted) yet the oldest crustal rocks and detrital zircons are 3.5 Ga and 3.8 Ga respectively (Moorbath et al., 1976; Dodson et al., 1988; Taylor et al., 1991; Nägler et al., 1997; Horstwood et al., 1999). The reasons for this decoupling might be geological but may also be an artefact of the dating methods and lithologies available for analysis.

An alternative approach to whole-rock dating using the Re-Os isotopic system is to investigate the distribution of the Re-Os ages at the scale of the phases, which may host Os and Re. In fertile to moderately depleted peridotites the main highly siderophile element (HSE: Os, Ir, Ru, Rh, Pt, Pd and Re) hosts would be base metal sulphides, whereas in depleted peridotites, of which cratonic peridotites are an extreme end-member, refractory platinum group minerals (PGM) such as laurite, erlichmanite and Os-alloys are proven major hosts (Luguet et al., 2007; Lorand et al., 2008). When combined with detailed petrographical investigations, the Re-Os signatures in HSE carriers allows us to differentiate between the residual and metasomatic origin of these highly siderophile element (HSE)-host phases and hence provide a more robust understanding of their Re-Os ages. Pioneering *in situ* studies in cratonic samples using laser-ablation MC-ICP-MS (e.g. Aulbach et al., 2004; Griffin et al., 2004) highlighted that residual base metal sulphides constitute the most robust age archive, as the latter yield Re-Os model ages up to 1.0-1.5 Ga older than the whole-rocks. As such, if they are present, residual BMS are the prime targets to address lithospheric root stabilisation in cratonic peridotites. They are thus a potential key to resolving the debate over craton formation processes and the possible genetic relationships between cratonic crust and their lithospheric mantle roots. Nevertheless, one potential drawback of *in situ* techniques is that Re-Os fractionation has been demonstrated between different sulphide mineralogical phases (e.g. chalcopyrite and pentlandite) that lead to time-integrated differences in $^{187}Os/^{188}Os$ (Richardson et al., 2001). Hence, unless the entire sulphide is analysed it is difficult to be ensure that the analysis is a faithful record of the Re-Os systematics of the sulphide grain.

Here, I present a combined investigation of detailed BMS petrography and single BMS grain Re-Os dating using N-TIMS after simultaneous whole-sulphide digestion and Os micro-distillation in three spinel and garnet-phlogopite peridotites from the Letlhakane cratonic xenolith suite (Botswana; see Luguet et al., submitted). These three peridotite samples were selected on the basis of their progressive metasomatic overprinting in terms of silicate/lithophile (cryptic to modal metasomatism) and HSE metasomatism (whole-rock Pt, Pd, Se, Te enrichments and metasomatic BMS and PGM). I show that independent of the degree of silicate/HSE/BMS/PGM metasomatism, the ages of single sulphide grains are 0.5-2.5 Ga older than the whole rock, and push the age of initial lithosphere stabilisation back towards the age of crust formation in the Zimbabwe craton.

4.2. Regional Geology and Sample Description

The Letlhakane kimberlite is located in eastern Botswana and is part of the Orapa Kimberlite field (Figure 4.1). It intrudes the Paleoproterozoic (1.8-2.0 Ga) Magondi Belt (Stowe et al., 1989), which separates the Zimbabwe craton and the cratonised Limpopo mobile belt in the East from the Pan African orogenic belts in the West.

The Orapa diamondiferous kimberlite lies 40 km to the north-west and has been dated at 93Ma (Davis, 1977), the Letlhakane pipe is assumed to be of a similar age. Whole-rock geochemical investigations of peridotitic samples and whole-rock Re-Os dating of eclogite, lherzolite and harzburgite samples from both Orapa and Letlhakane indicates that despite the Proterozoic age of the exposed crust, this region overlies Archean subcontinental lithospheric mantle (Carlson et al., 1999; Shirey et al., 2001; Luguet et al., submitted). This Archean root, underlying the Mesoproterozoic Magondi Belt, is of disputed origin, and might represent a possible south-western extension of the Zimbabwe craton (Miensopust et al. 2011; Khoza et al., 2013) or west-north-west continuation of the Archean Limpopo Mobile Belt (Ranganai et al., 2002).

The Letlhakane kimberlite samples a variety of mantle lithologies in the form of xenoliths, namely eclogites, pyroxenites, megacrysts, glimmerites and MARID (Mica-Amphibole-Rutile-Ilmenite-Diopside) peridotites (Stiefenhofer et al., 1997; van Achterbergh et al., 2001; Luguet et al., submitted). Specifically, the peridotite suite consists of spinel-bearing, garnet-free and garnet ± phlogopite-bearing harzburgites and lherzolites, which have experienced 25-38% of polybaric partial melting (5 GPa to 1-2 GPa- Luguet et al., submitted). From this suite, the spinel peridotites appear to have suffered only cryptic metasomatism while the garnet peridotites represent a progressively increasing modally

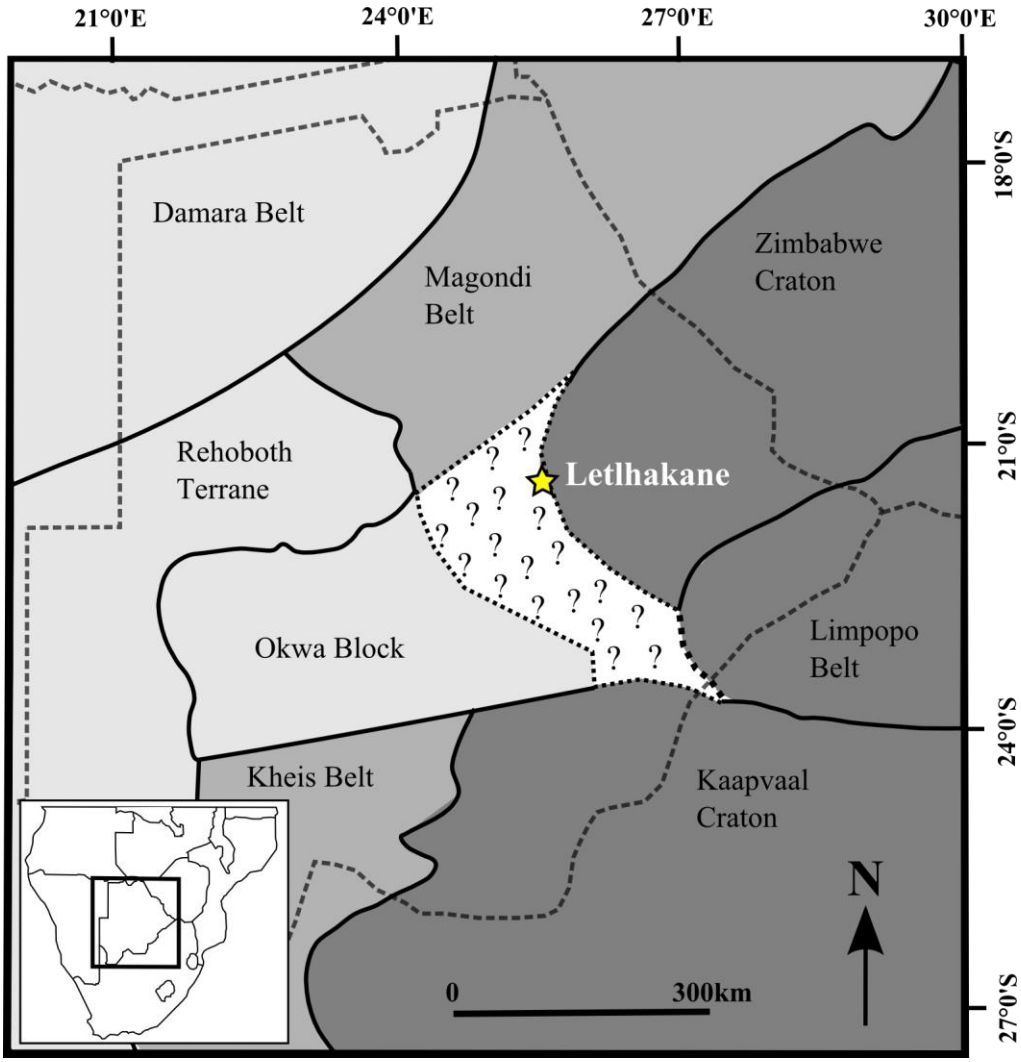

Figure 4.1. Locality map of Letlhakane kimberlite pipe, after Khoza et al. (2013). *Star* – Letlhakane kimberlite, *stippled line* – political boundaries, *solid line* – terrane boundaries, *dotted line* – assumed terrane boundaries

metasomatic sequence from phlogopite-free garnet peridotites to garnet-free phlogopite peridotites (Stiefenhofer et al., 1997; van Achterbergh et al., 2001). As in the Kimberley peridotites (Erlank et al., 1987), this modal metasomatism is marked by addition of secondary phlogopite, clinopyroxene, ilmenite and spinel at the expense of garnet and orthopyroxene, and is ascribed to the interaction with asthenosphere-derived alkaline basic silicate melts (van Achterbergh et al., 2001).

The three Letlhakane peridotites investigated in our study (MB3, MB6 and MB2) are part of a larger suite studied by Luguet et al. (submitted) for whole-rock chalcogenides (Se, Te) and highly siderophile element signatures, as well as Re-Os isotopic systematics. These three xenoliths show a variable range of whole-rock Se-Te-HSE systematics and Re-Os model ages, which taken together evolve in combination with the silicate metasomatic overprinting. Specifically, the **spinel peridotite (SP) MB3** is only slightly serpentinised and

shows typical whole-rock major element contents (e.g. low CaO, Al_2O_3) and Pd-Pt-depleted HSE signatures (Pd_N/Ir_N=0.01, N = CI-chondrites normalised after Anders and Grevesse, 1989) of highly depleted residual peridotites. Interestingly, its Os_N/Ir_N (1.52) is suprachondritic, as seen by the whole Letlhakane spinel peridotites (1.5-2.5), likely denoting the occurrence of Os-rich alloys, which exsolved in response to the extensive partial melting degree. MB3's Re-Os isotopic signature yields an Archean Re-Os T_{RD} age of 2751 Ma ($^{187}Os/^{188}Os$ of 0.1093). Despite this, its Re contents (0.012 ppb), Fe-richer olivine rims and incompatible element enriched trace element patterns indicate that the MB3 spinel peridotite suffered cryptic metasomatism.

The **Garnet-Phlogopite Peridotite (GPP) MB6** represents the first increment of modal metasomatism characterised by the breakdown of garnet to phlogopite + clinopyroxene + spinel. In addition, the garnet grains show large kelyphite reaction zones with only small intact cores remaining. While whole-rock major elements and the chemical composition of olivine ($Mg\#_{92}$, where Mg#=molar Mg/(Mg+Fe)) support MB6 as having experienced a high degree of partial melting; the occurrence of phlogopite, secondary spinel and clinopyroxene, the extensive kelyphitisation of the garnet, incompatible trace element enrichment (e.g.: Ba, La and Pd, Re, respectively) and the HSE systematics (Pd_N/Ir_N=0.16, Re=0.85 ppb) clearly argue for metasomatic overprinting. Addition of metasomatic Pt-Bi-bearing tellurides is evidenced by the minor Pd_N/Ir_N variations at sub-chondritic Pd_N/Ir_N ratios but large Se/Te scattering in the whole garnet-phlogopite peridotites group. Modelling also suggests the possible addition of a very minor amount of metasomatic sulphides (<0.01 wt. % = 30 ppm S). The $^{187}Os/^{188}Os$ ratio is 0.1102, which corresponds to a Re-Os T_{RD} age of 2627 Ma. Both remain relatively close to those obtained for the most residual less extensively metasomatised spinel peridotites, revealing that the addition of metasomatic tellurides and <0.01 wt. % sulphides did not significantly alter the Os isotopic composition of the whole-rock.

At the most metasomatised end of the spectrum is the **phlogopite peridotite (PP) MB2**, where no garnet is observed. The xenolith is interspersed with large (>2 mm) phlogopite grains of a seemingly primary origin. However, many are associated with clinopyroxene and may be secondary. This xenolith is also distinct from the other Letlhakane xenoliths as it displays enriched FeO_t (11.86 wt. %) and K_2O (0.56 wt. %) and the lowest olivine Mg# (86.8), all indicating significant interaction with silicate/alkaline basic silicate melt. It is characterised by the most Pd-Pt enriched HSE pattern with a primitive upper mantle (PUM)-like suprachondritic Pd_N/Ir_N of 1.39. The Se/Te vs. Pd_N/Ir_N of MB2 contrasts

with that of the garnet-phlogopite peridotite MB6, suggesting the occurrence of a significant amount (up to 0.05 wt. %, ca. 165 ppm S) of metasomatic base metal sulphides in addition to metasomatic tellurides. Compared to MB3 and MB6, the $^{187}Os/^{188}Os$ ratio of MB2 is shifted to a more radiogenic composition (i.e. 0.1203), yielding a Re-Os T_{RD} age of 1267 Ma, at least 1Ga younger than the peridotites MB3 and MB6. The radiogenic shift and apparent rejuvenation is likely reflecting the addition of ^{187}Os-rich metasomatic BMS.

4.3. Methods

4.3.1 Electron Microprobe Analysis

The composition of sulphides and silicates were determined using a JEOL JXA 8200 electron microprobe at the Steinmann Institut, University of Bonn. All samples were measured in wavelength dispersive (WDS) mode with a 15kV acceleration voltage, a 15 nA beam current and a 1 µm spot size. With the exceptions of the alkalis, all element calibrations were carried out by measuring their peak and background positions for 10 and 5 sec respectively, employing the ZAF matrix correction method. The alkalis (i.e. K_2O and Na_2O) were measured for 5 sec and 2.5 sec on the peak and background positions respectively, in order to avoid alkali migration and loss under the electron beam. For BMS, Fe and S were calibrated on a Canyon Diablo troilite, whereas Ni, Cu and Co were calibrated using pure alloys. Oxygen was measured using a LDE1 light element detector and calibrated by measuring the peak and background positions of its Kα x-ray line on a synthetic MgO standard. Oxygen calibrations were tested by measuring magnetite and ferro-chromite as a check for reproducibility. Major elements for the silicate minerals were calibrated using natural samples (e.g. San Carlos olivine; augite; natural pyrope and andradite; microcline), and a jadeite-diopside eutectic glass in the case of Na_2O.

4.3.2 Sulphide Extraction

BMS were extracted from thick sections (approximately 200 µm thick) in one of two ways; either with a New Wave Micro-drill to drill around the BMS or using a Resonetics RESOlution M50-E 193nm Excimer Laser operating at 30 Hz frequency, to ablate a path around the sulphide (Bragagni *et al.*, 2013). These techniques enabled us to extract almost the entire BMS with as little of the surrounding silicate as possible. Furthermore, the digestion technique used in this study will also not fully digest any of the silicates present. This, combined with the very low Os abundance present in silicates (Hart and Ravizza, 1996;

Burton et al., 1999; 2000; Handler and Bennett, 1999; Luguet et al., 2007) makes the possible contribution of silicates to the Os concentration and ^{187}Os signature determined from the single-grain sulphide digestion unlikely. The ablated/drilled path was further widened by hand using a diamond scribe under a binocular scope, to enable the complete removal of the BMS. The BMS was then freed from the section and carefully moved to a containment vessel.

4.3.3 $^{187}Os/^{188}Os$ Analysis

The extracted BMS were then micro-distilled for Os following the procedure described in Pearson et al. (1998). However, due to the small size of the BMS grains it was not possible to weigh them or to spike them. The digestion procedure of Pearson et al. (1998) for BMS grains occurs at low temperature (90°C) and at atmospheric pressure. Therefore, any Os-bearing alloy present within the BMS grain would not be digested (Meisel et al., 2003; Lorand et al., 2008) and all $^{187}Os/^{188}Os$ compositions are purely from the BMS. The $^{187}Os/^{188}Os$ ratios were determined using a Thermo-Finnigan Triton N-TIMS of the Northern Centre for Isotopic and Element Tracing (NCIET) at University of Durham (UK) following the procedures of Dale et al. (2008), apart from samples AW22 and AW24, which were analysed with the same model instrument at the University of Vienna. Sample analyses had an average ^{192}Os signal of 11,275 cps, ^{187}Os beams range from 30 to 2100 cps (240/233 ratio of 200-225,000), leading to an 1-std absolute error range of 0.00012-0.00201. Full procedural blanks (n = 3) for Os are 40 fg ± 3 including filament blank, with an average ^{192}Os beam of 45 cps. Reproducibility of $^{187}Os/^{188}Os$ for measurements of the Durham Romil Osmium Standard (DROsS) Solution range from 0.8-1.4‰. Over the course of this study, the DROsS solution was run 11 times with a load size of 10 pg yielding a mean $^{187}Os/^{188}Os$ of 0.16094 ± 0.00064 (2 std dev). This is in agreement with the values obtained by Luguet et al. (2008) for 10-100 ng loads (0.160924±4). The larger error obtained on the DROsS $^{187}Os/^{188}Os$ in this study is a result of the analysis of much smaller load sizes.

4.4. Results

4.4.1 Base metal sulphide modal abundances and occurrences

4.4.1.1 Modal abundances and distribution of the BMS

All three Letlhakane peridotites contain BMS, of which the modal abundances increase from the spinel peridotite MB3, to the garnet-phlogopite peridotite MB6 to the phlogopite peridotite MB2 (see Table 4.1). This trend correlates with the incompatible HSE

Table 4.1. Textural habit, composition and number of sulphides across each three xenolith investigated. See Section 4.4.2 for complete habit description and Section 4.4.3 for description of sulphide compositions.

sample	habit					
	inclusion			interstitial		pool (vi)
	isolated (i)	connected - small (ii)	connected - large (iii)	clusters (iv)	isolated (v)	
MB3	xxx pn, cp				xxxxxx hz	
MB6	xxx pn, cp, mss1	xx hz	xxx pn, hz + Cu-hz, pn + hz + Cu	xxxx hz, hz + mt	++ hz, hz + O-hz	
MB2	xx pn, mss1	xx po, O-mss + Cu-mss	xxxxxxxx pn, pn + Cu-pn, pn + O-mss, pn + mt, pn + cc, hz + cc	xxxx hz, hz + mt	x hz	xxxx hz, hz + mt, hz + cc

X denotes number found in each xenolith of specific habit

enrichment and the shift toward more radiogenic ^{187}Os signatures observed at the whole-rock scale and also follows the increasing metasomatic sequence highlighted by the trace elements and the modal abundances of the metasomatic silicates. Investigation of multiple thin sections (between 9-12 thin sections) for a given sample reveals the extremely heterogeneous distribution of BMS at the thin section scale. For both MB3 and MB6, between half and one third of the thin sections were BMS-free. When BMS were observed in these samples, they are clustered over 1 to 2cm. In contrast, all MB2 thin sections contain BMS but they are also heterogeneously distributed throughout each section, i.e. they cluster together along serpentinisation veins or in pools (Figure 4.2 vi).

4.4.1.2. Textural habits of BMS

Base metal sulphides in the Letlhakane peridotites occur as either inclusions or interstitial grains. Overall, six different textural habits with modally-major minerals can be distinguished. Habits (i) to (iii) are inclusions in host minerals whereas habits (iv) to (vi) represent interstitial BMS occurrences. The overall textural associations can be summarised as:

(i-ii) Small (< 30 μm) BMS inclusions are found within silicate minerals, generally olivine but occasionally phlogopite, orthopyroxene and garnet. These inclusions are systematically associated with silicate-phase rims, some being completely enclosed (habit i

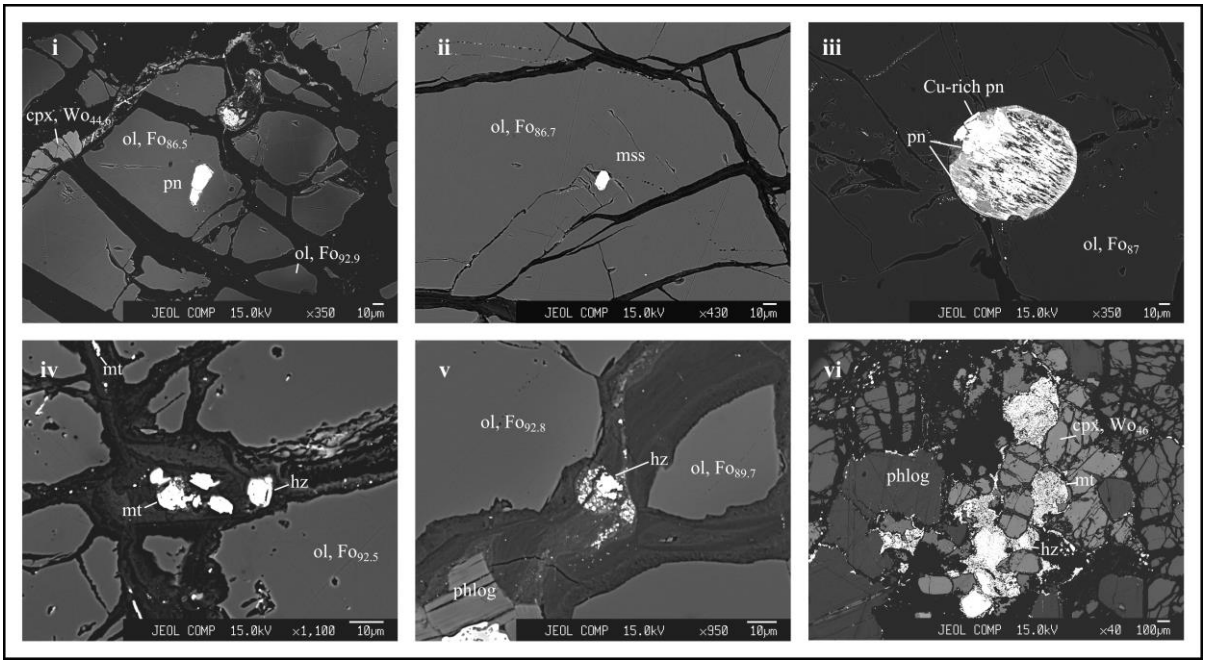

Figure 4.2. Textural habit of the Letlhakane BMS within the modally major silicates. i) inclusion, isolated, ii) inclusion small connected, iii) inclusion large connected, iv) interstitial clusters, v) interstitial isolated, vi) interstitial pool. See Section 4.4.2 for details. Abbreviations are: *pn* – pentlandite; *hz* – heazlewoodite; *mt* – magnetite; *ol* – olivine; *cpx* – clinopyroxene; *phlog* – phlogopite.

Figure 4.2 i) while others are connected to fractures or cracks, and ultimately are in contact with the interstitial medium of the peridotites (habit ii) (Figure 4.2 ii). The morphology of both these small inclusion occurrences is variable, ranging from euhedral to a globule-like shape.

(iii) Isolated, large (>50 µm), globular BMS grains, connected to cracks and fractures (Figure 4.2 iii), are found in the serpentine zones of optically continuous olivine and orthopyroxene grains. These BMS grains will be referred to as "pseudo-inclusions", as they were likely to represent former inclusions. In contrast to habits (i) and (ii) they are strongly altered, with generally less than 50% of the original BMS grain being preserved.

(iv-v) Interstitial BMS are observed at the grain boundaries between silicates or disseminated within the serpentine veins, which crosscut the peridotitic matrix. They occur either as small (<30 µm) BMS grains (i.e. habit iv, Figure 4.2 iv) occurring as clusters of up to 10 grains and are always associated with oxides or as larger but single BMS grains (>10-50µm) (i.e. habit v, Figure 4.2 v). This latter occurrence is variably altered, with some grains showing no visible alteration and others already partially replaced by magnetite.

(vi) Interstitial BMS grains also occur within interstitial "pools", exclusively associated with large (up to 1 cm long) phlogopite and clinopyroxene grains, which have

been interpreted as metasomatic silicates (Figure 4.2 vi). The pools are large blobs (>50 µm) made up of a ca. 80% oxides (i.e. magnetite) and ca. 20% small (<30 µm) BMS. The morphology of the pool with the surrounding silicate minerals exhibit low dihedral angle and contorted rims moulding the surrounding silicates. Interestingly, some pools can also be rimmed or contain a calcium-rich carbonate phase (Figure 4.3D-E-F).

In the spinel peridotite MB3, only isolated small inclusions (habit i) and small isolated interstitial grains (habit v) have been observed, with the latter habit being predominant (Table 4.1). Interestingly these isolated inclusions can be associated with metasomatised silicates, such as AW27, which shows an obvious and distinct compositional change in the olivine (Figure 4.3A-B-C) from Mg-rich (Mg# 92.7) to Fe-rich (Mg# 85.5), with the BMS associated to the Fe-rich olivine rim..

The garnet-phlogopite peridotite MB6 contains inclusions and interstitial BMS displaying textural habits (i) to (v) in relatively similar proportions. This xenolith is also host to the only inclusion of habit (ii) in a garnet; this inclusion lies within the large kelyphitised rim within 200 µm of the relic garnet core.

Finally, MB2, the most modally-metasomatised peridotite from our Letlhakane suite is the only xenolith containing BMS from the six different textural habits identified and thus is the only sample containing the oxide-BMS pools (habit vi). In this sample, the dominant BMS occurrences are large BMS pseudo-inclusions (habit iii), clusters of small interstitial grains (habit iv) and the large pools (habit vi). Additionally, a large amount (>100) of sub-microscopic (<2 µm) BMS, not classified in term of textural habit and composition, are also disseminated through-out the alteration veins in this xenolith.

4.4.2. BMS mineral assemblages and chemical composition

4.4.2.1. BMS assemblages

The amount and variability of BMS minerals increases from MB3 through MB6 to MB2 (Table 4.1, Figure 4.4), and tends to follow the extent of both silicate and HSE-Se-Te metasomatic overprinting.

The BMS assemblages differ with respect to the textural relationships they display with the silicates. The small isolated BMS inclusions (habit i) are a one-phase assemblage (Table 4.2), mainly consisting of either pentlandite (pn), monosulphide solid solution (mss) or chalcopyrite (cp). This is typically interpreted as the subsolidus re-equilibration of the high-temperature magmatic sulphide phase (Craig and Kullerud, 1969; Lorand and Grégoire,

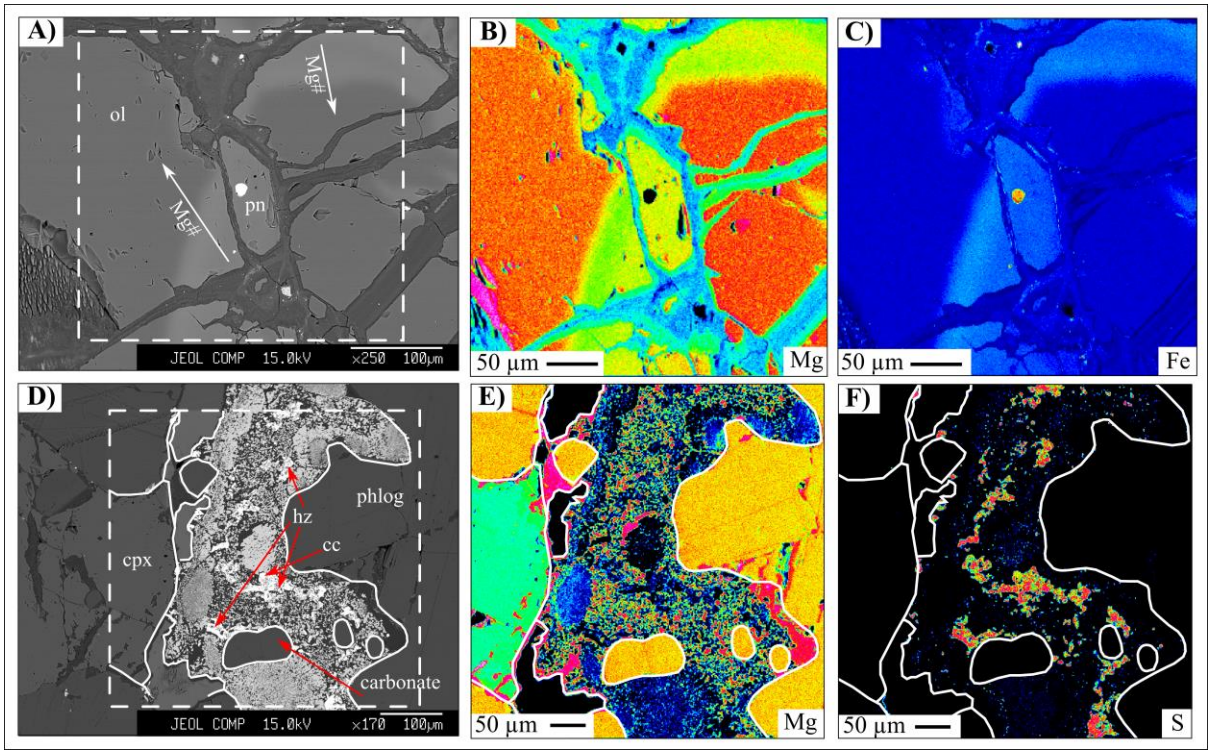

Figure 4.3. BSE images and false colour qualitative elemental maps – warm colours represent high intensity, cold colours are low intensity. *A* – BSE image of AW27, showing compositional change, two arrows represent the decrease in Mg# described in Section 4.4.2. Dashed line represents area analysed in B and C; *B* - AW27, Mg, dark area is the BMS inclusion; *C* – AW27, Fe, bright spot is BMS; *D* – BSE image of pool BMS AW24, showing interaction of silicate minerals with the sulphide and oxide pool, dashed line represents area analysed in E and F. White lines are the outline of the modally-major silicates; *E* – AW24, Mg, this image shows the complimentary nature of the metasomatic silicates with the BMS (compare to f), white line as in D; *F* – AW24, S, distribution of the small BMS minerals within the metasomatic silicate and oxide matrix, white line as in D. Abbreviations as in Figure 4.2, additionally *cc* – chalcocite.

2006). In contrast, the connected small and large inclusions as well as the three habits of interstitial BMS are made up from one to three phases per grain (Table 4.2), which are mainly heazlewoodite (hz), pn, chalcocite (cc), native copper, mss and magnetite. Overall, the Cu-rich BMS or minerals (e.g. native copper) only account for <5 vol. % of the total BMS in MB3 and MB6 and reaches ca. 10 vol. % in MB2. When present in a given BMS, chalcocite is generally located towards the rim as a single discrete grain (see Figure 4.5H and L). Native copper is found as single-phase grain as well as in association with pn and hz, in a pseudo-inclusion of the garnet peridotite MB6, where it occurs as a well-defined individual phase (Figure 4.5F).

Table 4.2. Representative electron-microprobe results for the base metal sulphides.

Sample	Habit	O	S	Cu	Ni	Fe	Co	Total	Metal/ Sulphur	Mineral
MB3										
AW27	i	0.34	32.92	0.00	41.20	25.15	0.25	99.86	1.13	Pentlandite
AW28	v	0.47	26.27	0.00	68.57	2.01	0.07	97.40	1.47	Heazlewoodite
		1.45	26.53	0.48	65.46	2.89	1.66	98.46	1.45	Heazlewoodite
n/a	v	0.06	26.64	0.00	72.61	1.35	0.03	100.68	1.52	Heazlewoodite
		0.14	27.05	0.00	71.96	1.44	0.00	100.60	1.48	Heazlewoodite
MB6										
AW29	ii	0.13	26.63	0.46	69.63	2.57	0.10	99.52	1.49	Heazlewoodite
		0.01	27.36	0.00	71.24	2.51	0.08	101.21	1.48	Heazlewoodite
		0.24	26.93	0.00	71.00	3.19	0.06	101.43	1.51	Heazlewoodite
AW31	iii	0.21	33.18	0.00	35.27	28.85	1.50	99.01	1.10	Pentlandite
AW32	i	0.00	33.52	33.50	1.82	30.18	0.00	99.03	1.05	Chalcopyrite
n/a	iv	1.45	26.40	0.00	69.10	2.03	0.52	99.49	1.48	Heazlewoodite
		0.96	26.01	0.00	68.55	2.20	0.13	97.85	1.49	Heazlewoodite
		29.37	0.07	0.04	0.33	68.14	0.14	98.08	-	Magnetite
n/a	ii	0.15	26.80	1.92	68.31	0.00	0.15	97.33	1.44	Heazlewoodite
MB2										
AW10	iii	0.23	32.80	0.00	38.68	27.26	0.79	99.76	1.13	Pentlandite
		24.58	6.16	0.18	0.85	69.65	0.12	101.54	-	Magnetite
		0.58	32.83	0.20	38.31	27.84	0.84	100.60	1.14	Pentlandite
		0.33	33.44	0.00	39.46	26.51	1.09	100.82	1.12	Pentlandite
AW11	i	0.20	32.16	3.96	36.58	25.23	1.03	99.15	1.15	Pentlandite
AW21	i	0.63	39.30	0.04	4.27	57.31	0.15	101.70	0.90	mss
AW25	ii	0.63	35.79	0.00	0.17	63.82	0.05	100.45	1.03	Pyrrhotite
n/a	iii	1.29	27.29	48.81	19.07	3.26	0.01	99.74	1.35	
		0.55	21.93	72.38	0.63	3.78	0.15	99.41	1.78	Chalcocite
		0.39	29.41	0.00	68.22	4.78	0.01	102.81	1.36	Heazlewoodite
n/a	iv	0.10	28.12	0.00	70.30	2.62	0.03	101.18	1.42	Heazlewoodite
n/a	iii	0.33	32.07	11.30	31.00	25.53	1.09	101.31	1.18	Cu rich pentlandite
		0.25	33.36	0.00	36.18	29.97	0.81	100.57	1.12	Pentlandite
		0.56	32.83	0.83	36.57	28.24	1.08	100.09	1.13	Pentlandite
n/a	vi	28.26	0.01	0.03	0.18	72.79	0.05	101.30	-	Magnetite
		0.59	27.18	0.00	71.95	1.39	0.12	101.22	1.48	Heazlewoodite

Habits: (i) inclusion, isolated; (ii) inclusion, small connected to fracture; (iii) inclusion, large connected to fractures; (iv) interstitial, clustered; (v) interstitial, isolated; (vi) pool; see Section 4.4.2 for full details.

4.4.2.2 BMS chemical composition

Isolated BMS inclusions (habit i) have generally experienced a low degree of oxidation as revealed by their low O contents (<0.6 wt. %; Table 4.2). Only one pn inclusion

yields an O content of ca. 4 wt. %. Because primary, Ni-rich, sulphide melts are less prone to dissolving O (cf. Fonseca et al., 2008; Wohlgemuth-Ueberwasser et al., 2013), it is unlikely that the composition of this pentlandite or any oxidised Ni-rich sulphide phase is representative of a primary process, and thus will not be further considered. **Pentlandite** (n = 2) found as isolated inclusions (habit i) has a high metal/sulphur (M/S=(Fe+Ni+Cu+Co)/S) atomic ratio (M/S = 1.13-1.15). Whilst their Fe contents do not vary, their Ni content ranges from 36.6 to 41.2 wt. % (Figure 4.4). The isolated pn inclusion with 36.6 wt. % Ni, also contains ca. 1 wt. % Co and close to 4 wt % Cu (Table 4.2). This high Cu content could reflect possibly the occurrence of very fine and non-detected chalcopyrite lamellae within the pentlandite. The **mss** of textural occurrence (i) (n = 2) are similar in composition to the Ni-poor mss-1 of Stone et al. (1989), Farrell and Fleet (2002) and Lorand and Grégoire (2006) (Figure 4.4) and have a low M/S ratio (0.87-0.9). Their Fe contents show large variations, from 51.9 to 57.3 wt. %, that negatively correlate with Ni content (3.4-8.4 wt. %, Table 4.2). These mss are also Cu-free (<0.04 wt. %) and Co-poor (<0.2 wt. %). The isolated **chalcopyrite** inclusions (n = 3), which display a M/S ratio close to 1, show little compositional variation: 32.9-33.5 wt. % Cu, 29.5-30.2 wt. % Fe and 1.8-2.8 wt. % Ni (Table 4.2).

The BMS from textural occurrences ii to vi have a large range of O contents, from 0.01 up to 9.4 wt. %, and on average are much higher than those in isolated BMS inclusions (Table 4.2). Due to their interstitial/connected habit the high O content most likely reflects the open-system evolution of these BMS assemblages, having likely reacted to the redox conditions imposed by the silicates (i.e. from serpentinising fluids). This secondary oxygen enrichment leads to the desulphurisation of the BMS, elevating the M/S to higher values. Therefore, only BMS with O contents below 1 wt. % will be described here, as the M/S ratio in oxidised BMS are systematically shifted and thus not representative of the original BMS composition.

In textural occurrence ii **mss** (n=1) has a slightly elevated M/S of 1.05 and is Cu-rich (5.6 wt. %; AW2, Table 4.3). This is coupled with a high Ni content (10.5 wt. %) and compensated by the low Fe content (49.7 wt. %). **Pyrrhotite** from occurrence (ii) (n=1) is close to stoichiometric with a M/S ratio of 1.03 and Fe and S contents of 63.8 and 35.8 wt. % respectively (Figure 4.4). **Pentlandite** from textural habit (iii) (n=11) has slightly lower Ni content when compared to isolated inclusions (35.2-39.5 wt. % vs. 36.6-41.2 wt. %; Table 4.2). They also have generally low Cu and Co contents (<0.01 wt. % Cu for 8 analyses, 0.2-

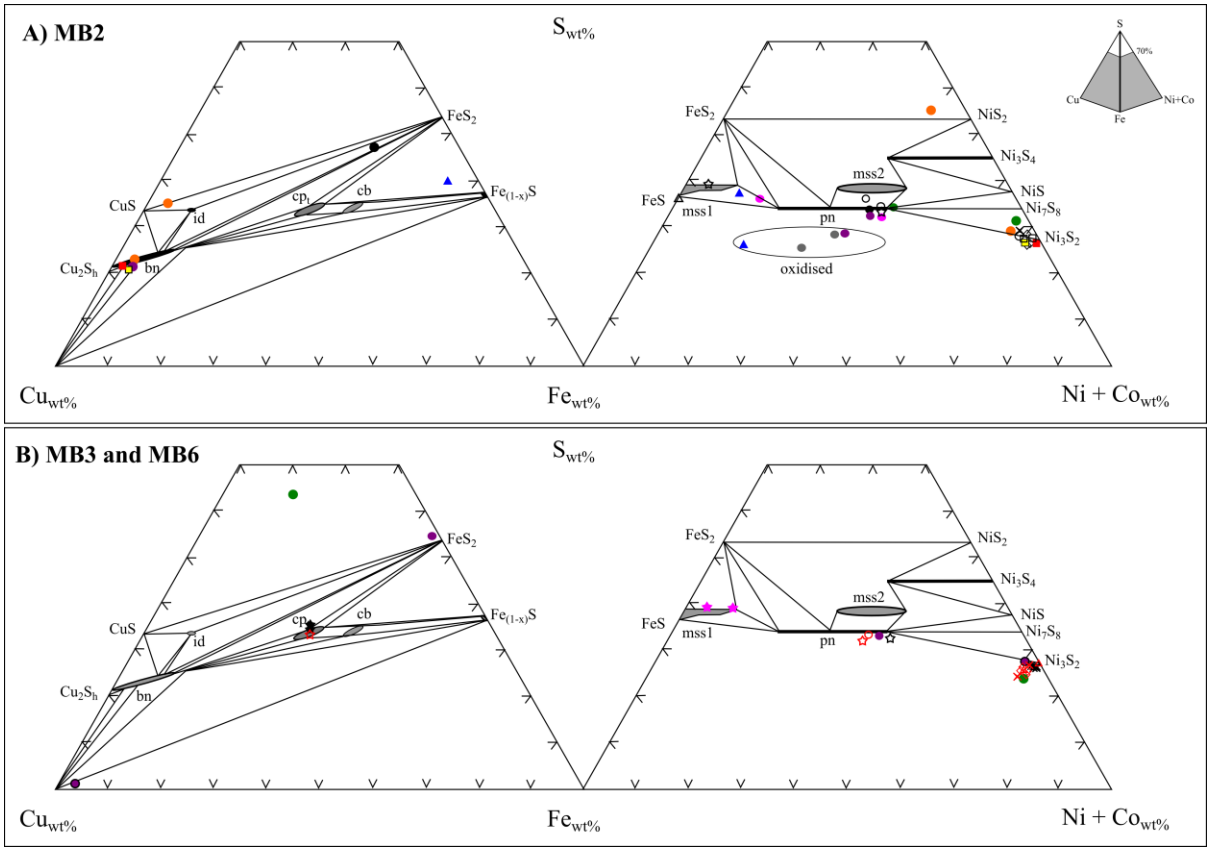

Figure 4.4. BMS compositions in the Cu-Fe-Ni-S system at 300°C (after Craig, 1973; Yund and Kullerud, 1966). Symbols of the same colour represent multi-phase BMS, grey field are for solid solutions of mss1, mss2, cubanite (cb), chalcopyrite (cp), idanite (id), and bornite (bn), solid lines represent tie-lines between different compositions. *star* – habit i, *triangles* – habit ii, *circles* – habit iii, *diamonds* – habit iv, *cross* – habit v, *squares* – habit vi (See Section 4.4.2 for habit descriptions). Symbols plotting in the Cu-Fe-S side that do not correlate to a specific mineral composition represent Ni-Fe sulphides with minor Cu (e.g. both green circles are the same in B). In B) red and coloured symbols are from MB6, black symbols are from MB3 as all BMS in this xenolith are single phase.

0.8 wt. % Cu in 3 analyses; 0.6-1.1 wt. % Co). Exceptionally, in one outlier, pn with a slightly higher M/S (1.18) has a high Cu content of 11.3 wt. % (Table 4.2). **Native Copper** in association with pn and hz (AW8, textural habit iii) contains 96 wt. % Cu along with minor Fe (<3.3 wt. %) and Ni (<1.5 wt. %; Table 4.3). **Chalcocite** from habit (iii) is systematically lower in Cu (72-74 wt. %) compared to textural occurrence (vi) (77-78 wt. %) but their S contents vary independently of textural habit (20.1-21.9 wt. %), as do the Ni (<0.7 wt. %) and Fe (2.4-4.2 wt. %) contents (Figure 4.4). **Heazlewoodite** from habits (ii) through (vi) show relatively homogeneous chemical compositions with M/S ratios of 1.43-1.54 (average 1.49 ± 0.09 over 36 analyses, cf. Table 4.2). The slight variations are independent of textural habit and may be found within a single BMS grain. Their Ni contents average, 70.3 ± 3.9 wt. % (2

stdev) with S contents averaging 27.0 ± 1.8 wt. % plus minor Fe (2.3 ± 2.1 wt. %). Additionally, some hz grains (n=3) show relatively high Cu contents (up to 1.9 wt. % compared to the usual <0.01 wt. %, Table 4.2) however one oxidised sample has 7.2 wt. % Cu, without being associated with any Cu-bearing phases (e.g. native Cu, cc) in the same BMS grain. The Co contents are low and variable (0.25 ± 0.99, 2 stdev), with the variability controlled by three hz containing between 0.8 to 2.9 wt. % Co. The remaining 33 hz grains contain <0.5 wt.% Co (Table 4.2).

4.4.3 $^{187}Os/^{188}Os$ isotopic compositions of the BMS from the Letlhakane peridotites

Of the 28 BMS extracted for Os analysis, only 12 were successfully analysed (no habit iv analysed, see Table 4.3). The extremely small size of the grains led to difficulties during extraction and manipulation prior to digestion. In addition, it seems likely that their small size is also synonymous with low osmium contents (see section 3.3) which translates into much larger resulting uncertainties in the Os isotopic measurements (rsd up to 17%). Despite the high uncertainty of some analyses, a clear distinction in the $^{187}Os/^{188}Os$ composition of the BMS can be resolved (Figure 4.6).

The $^{187}Os/^{188}Os$ isotopic compositions covered a wide range in all three xenoliths, ranging from non-radiogenic ($^{187}Os/^{188}Os$ = 0.1016) to extremely radiogenic values (0.6109) (Table 4.3, Figure 4.6). Overall, there is no systematic relationship between BMS ^{187}Os isotopic composition and textural habit (see Table 4.3 and Figure 4.6), however, a clear relationship between BMS composition and ^{187}Os isotopic composition exists. The most radiogenic $^{187}Os/^{188}Os$ compositions (>0.1729) are systematically associated to a BMS assemblage dominated by Fe or Cu-rich phases (mss, chalcopyrite). In contrast, BMS containing heazlewoodite or pentlandite (Ni-rich phases) are less radiogenic (<0.1485) to very unradiogenic (<0.1203).

In the cryptically metasomatised spinel peridotite MB3, three heazlewoodite grains, of the same textural habit (v) and similar composition show significant ^{187}Os variations (Table 4.3). Grain AW4 (Figure 4.5A), which is interstitial to olivine, has a similarly radiogenic $^{187}Os/^{188}Os$ (0.1466) to grain AW5 (0.1485) (Figure 4.5B), although secondary clinopyroxene is found in the vicinity of the latter. In contrast, grain AW14 (Figure 4.5D), interstitial to olivine with striking core to rim Mg# variations (89.2-92.8) has an unradiogenic $^{187}Os/^{188}Os$ ratio (0.1042). Finally, an isolated chalcopyrite (AW6, Figure 4.5C) included in olivine has a radiogenic $^{187}Os/^{188}Os$ of 0.1894.

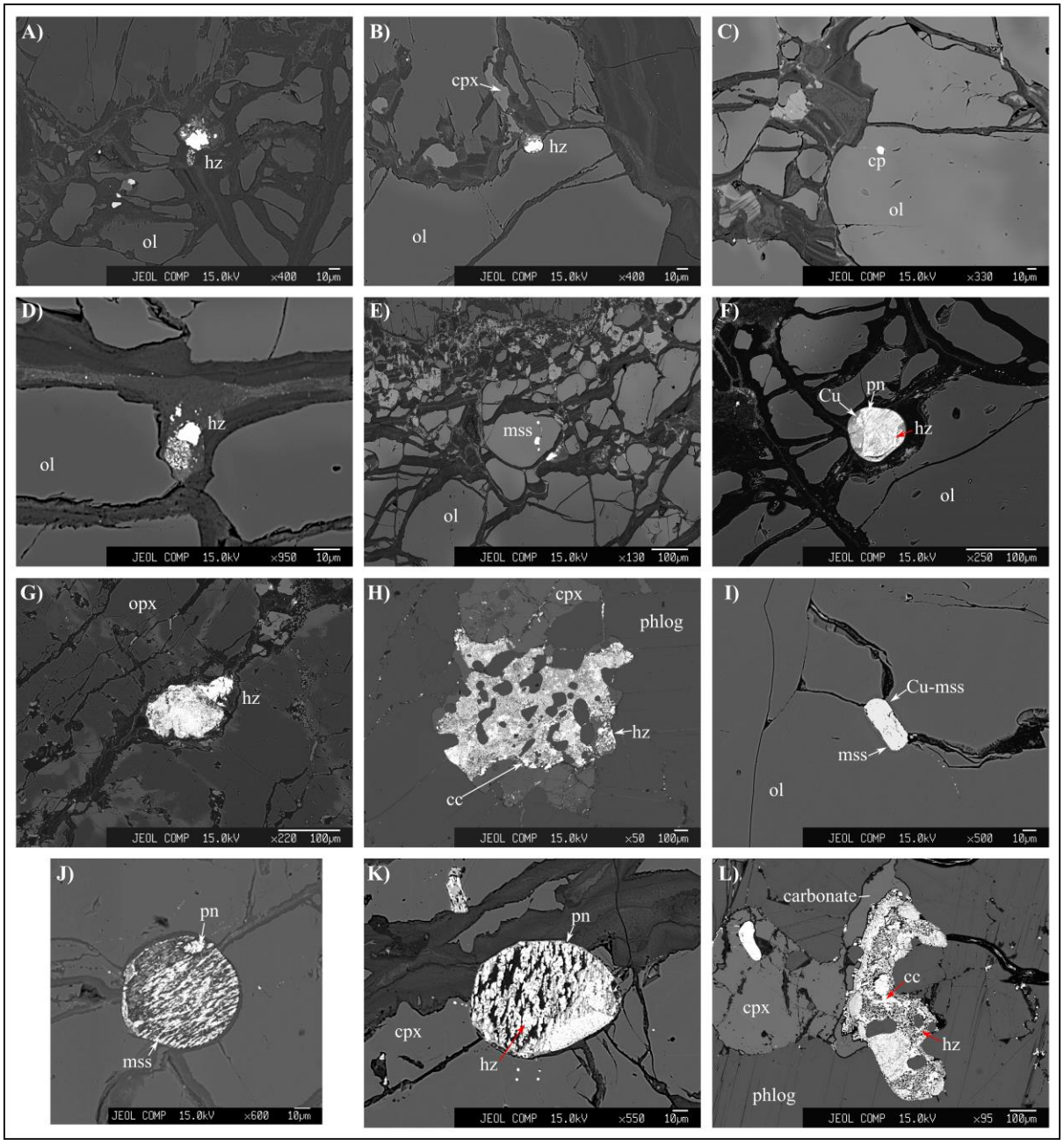

Figure 4.5. The 12 BMS samples analysed for $^{187}Os/^{188}Os$. Xenolith; MB3: *A* – AW4, *B* – AW5, *C* – AW6, *D* – AW14, MB6: *E* – AW7, *F* – AW8, *G* – AW9 and MB2: *H* – AW1, *I* – AW2, *J* – AW3, *K* – AW22, *L* – AW24. Abbreviations as in Figure 4.2 and 4.3, *cp* – chalcopyrite.

In the weakly modally metasomatised peridotite MB6, grains AW8 (Figure 4.5F) and AW9 (Figure 4.5G) consist mostly of heazlewoodite and/or pentlandite and have similar unradiogenic $^{187}Os/^{188}Os$ (0.1133 to 0.1113, respectively), independent of their different textural habit (pseudo inclusion, iii vs. isolated interstitial, iv; Table 4.3). In contrast, the isolated mss inclusion (i) AW7 (Figure 4.5E), found in an olivine crystal, has a radiogenic ^{187}Os isotopic composition (0.1727).

Interestingly, MB2, the most metasomatised peridotite in terms of silicate/oxide minerals and lithophile trace elements and Se-Te-HSE systematics, contains BMS with both the lowest and the highest $^{187}Os/^{188}Os$ isotopic compositions of the whole suite (Table 4.3). The BMS pool (habit vi) grains AW1 (Figure 4.5H) and AW24 (Figure 4.5L), located within phlogopite and associated to clinopyroxene, magnetite and carbonate, both yield unradiogenic osmium compositions, with $^{187}Os/^{188}Os$ of 0.1104 and 0.1100, respectively. Both pools contain BMS composed of heazlewoodite and chalcocite (5-30 µm in size) in a magnetite matrix; the entire area of BMS and oxide, which was fully analysed for Os isotopes, was approximately 1250 x 875 µm in AW1 and 150 x 750 µm in AW24. Two pseudo inclusions (habit iii; AW3, Figure 4.5J and AW22, Figure 4.5K), dominantly made up of pn and/or hz sometimes with minor amounts of oxidised mss (i.e. AW3) yield different but still unradiogenic $^{187}Os/^{188}Os$ ratios (0.1203 and 0.1016, respectively). At the opposite end of the spectrum, the small inclusion of oxidised mss and Cu-bearing mss AW2 (Figure 4.5I) has the most radiogenic ^{187}Os composition analysed during this study (0.6109).

As the rhenium concentration was not obtained for these BMS due to the impossibility of weighing and spiking such small BMS grains accurately, the $^{187}Os/^{188}Os$ isotopic ratios have been used to calculate the "rhenium depletion" (T_{RD}) model ages (Figure 4.6B). This approach produces a conservative estimate of the age of the BMS because it yields a minimum age compared to T_{MA} and T_{RD} eruption ages which use the measured Re concentrations (cf. Walker et al., 1989).

The T_{RD} model ages for the Letlhakane BMS vary from future ages, produced by the Cu and Fe-rich BMS assemblages (AW6, AW7 and AW2), to early Archean ages (i.e. 3.75 Ga for grain AW22) (see Table 4.3), with the corresponding whole-rock T_{RD} model occurring in the middle of the BMS age span (Figure 4.6B). Although the BMS T_{RD} ages are quite scattered over the whole range, four grains of pentlandite/heazlewoodite define a cluster of Neoarchean-Paleoproterozoic model ages between 2.65 and 2.20 Ga.

Some care should be exercised when interpreting the T_{RD} model ages determined for BMS measured in this study. Because the T_{RD} calculation does not correct for the ^{187}Os ingrowth due to the radioactive decay of Re since the BMS crystallisation/segregation, and because most BMS have a high distribution coefficient for Re, the T_{RD} model ages of high Re/Os BMS may be dramatically underestimated. This is possibly the case for the Fe and Cu-rich BMS assemblages (Mss, chalcopyrite) as these BMS are, on average, characterised by a higher Re/Os ratio than the Ni-rich BMS mineralogies (i.e. pentlandite and heazlewoodite; e.g., Godel and Barnes, 2008). Therefore, in the following section, the discussion regarding

Table 4.3. $^{187}Os/^{188}Os$ and EMP results for the twelve base metal sulphides successfully analysed.

Sample	Xenolith	Thin Section	Habit	size, µm	O	S	Cu	Ni	Fe	Co	Total	Metal/ Sulphur	Sulphide composition	$^{187}Os/^{188}Os$ corrected	1-Std error (abs)	T_{RD}, Ga	2 sigma error, Ga
AW4	MB3	5	v	15	0.28	26.39	0.06	70.56	1.32	0.89	99.50	1.51	Heazlewoodite	0.1466	0.0004	-2.99	0.13
AW5	MB3	7	v	20	0.53	26.49	0.00	71.91	1.38	0.11	100.43	1.52	Heazlewoodite	0.1485	0.0006	-2.67	0.18
AW6	MB3	12	i	10	0.24	33.26	32.92	2.83	29.56	0.10	98.89	1.06	Chalcopyrite	0.1894	0.0035	-9.26	1.13
AW14	MB3	7	v	10	0.29	26.17	0.00	71.78	1.61	0.11	99.96	1.54	Heazlewoodite	0.1042	0.0011	3.41	0.28
					0.23	26.21	0.00	70.66	1.74	0.42	99.26	1.52					
					0.44	26.05	0.00	67.76	1.97	2.96	99.18	1.53					
AW7	MB6	4	i	30	0.14	39.60	0.00	8.37	51.93	0.19	100.22	0.87	Mss	0.1727	0.0013	-6.26	0.40
					0.12	39.33	0.00	3.46	56.30	0.12	99.34	0.87					
AW8	MB6	5	iii	50	0.50	33.08	0.80	38.04	26.69	0.99	100.10	1.12	Pentlandite + Heazlewoodite + Copper	0.1133	0.0001	2.20	0.03
					0.65	0.35	96.00	1.52	3.31	0.07	101.90	20.83					
					0.33	26.62	0.00	70.67	3.35	0.16	101.14	1.53					
AW9	MB6	7	v	50	0.36	26.42	0.00	69.57	3.41	0.09	99.84	1.51	Heazlewoodite	0.1113	0.0001	2.47	0.03
					0.06	27.35	0.00	71.91	1.04	0.16	100.52	1.46					
					0.26	27.10	0.00	72.21	1.11	0.10	100.78	1.48					
AW1	MB2	2	vi	5-30	0.07	27.48	0.00	73.18	0.73	0.07	101.53	1.47	Heazlewoodite + Chalcocite + Magnetite	0.1104	0.0002	2.59	0.05
					0.18	26.73	0.00	72.98	1.55	0.09	101.53	1.53					
					0.16	20.74	77.12	0.00	2.43	0.06	100.51	1.94					
					0.19	26.78	0.00	73.62	0.60	0.05	101.23	1.52					
AW2	MB2	7	ii	30	8.66	23.33	0.57	15.70	51.36	0.39	100.02	1.65	oxidised Mss + Cu-mss	0.6109	0.0051	-	-
					0.20	35.50	5.56	10.50	49.73	0.30	101.79	1.05					
AW3	MB2	8	iii	50	3.75	29.81	0.59	37.26	24.94	1.02	97.37	1.19	Pentlandite + oxidised-Mss	0.1203	0.0003	1.28	0.08
					9.44	31.84	0.87	13.53	43.46	0.51	99.65	1.04					
AW22	MB2	8	iii	90	0.33	30.07	0.00	65.09	2.51	0.06	98.07	1.50	Heazlewoodite + Pentlandite	0.1016	0.0020	3.75	0.52
					0.58	33.06	0.00	39.77	23.69	1.28	98.39	1.09					
AW24	MB2	8	vi	5-30	0.15	20.94	78.24	0.71	4.22	0.07	104.33	2.02	Heazlewoodite + Chalcocite + Magnetite	0.1100	0.0018	2.65	0.46
					0.80	26.70	0.00	69.33	2.95	0.43	100.21	1.49					
					0.33	27.03	0.00	72.25	2.57	0.12	102.29	1.52					

habits: (i) inclusion, isolated; (ii) inclusion, small connected to fractures; (iii) inclusion, large connected to fractures; (iv) interstitial; clustered; (v) interstitial, isolated; (vi) pool; see Section 4.4.2 for full details. T_{RD} were calculated using the present-day primitive mantle $^{187}Os/^{188}Os$ and $^{187}Re/^{188}Os$ compositions of 0.1296 and 0.435 (Becker et al., 2006).

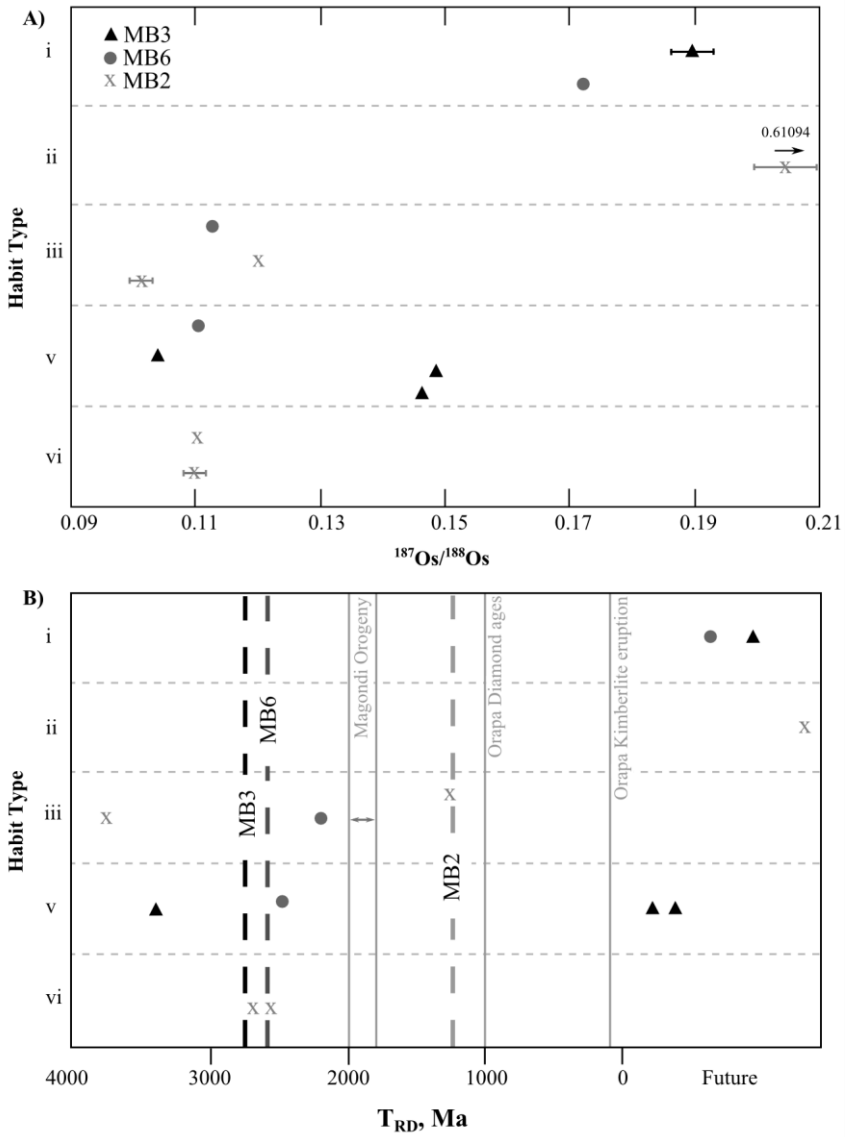

Figure 4.6. A) Osmium systematics for Letlhakane BMS. Errors smaller than symbol size unless indicated. B) Osmium T_{RD} model ages for Letlhakane BMS and whole rock xenoliths versus textural habit. Symbols as in a, stippled lines are whole rock T_{RD} ages, solid grey lines are regionally significant ages (Magondi Orogeny from McCourt et al., 2001 and Majaule et al., 2001; Orapa Diamond ages from Shirey et al., 2004; Orapa Kimberlite eruption from Davis, 1977) see section 4.4.2 for habit descriptions.

the T_{RD} ages will exclusively focus on the low Re/Os, Ni-rich pentlandite and heazlewoodite grains, which are more likely to yield meaningful T_{RD} model ages.

4.5. Discussion

4.5.1 Residual vs. metasomatic origin of the BMS

In the Letlhakane peridotites, BMS blebs isolated within the most refractory silicates (olivine and orthopyroxene) show the distinctive mss ± pentlandite ± chalcopyrite assemblage that is typically interpreted as sub-solidus re-equilibration of a high temperature

sulphide melt that crystallised first mss and then Cu-rich intermediate solid solution (i.e. iss; Dromgoole and Pasteris, 1987; Lorand and Grégoire, 2006). The small BMS inclusions now connected to the interstitial medium or classified as large pseudo inclusions, as well as all the interstitial BMS generally display a different paragenesis, characterised by a higher M/S and mainly comprising pn, hz, cc and magnetite. This sequence follows the transition of the original mss-iss, to its sub-solidus phases (pn + cp) followed by a desulphurisation caused by the reducing conditions imposed during serpentinisation of the mantle rocks (Lorand, 1985; Abrajano and Pasteris, 1989; Lorand and Grégoire, 2006; Klein and Bach, 2009).

Inclusions and interstitial BMS can have two distinct origins: 1) they could be residual and have survived *in situ* the partial melting event(s) experienced by the peridotites; 2) they could be metasomatic, having been reintroduced into the highly depleted residues after partial melting. Several arguments point towards a metasomatic origin for the BMS inclusions (habits i-iii) in addition to the interstitial pools (habit vi) found in the Letlhakane peridotites.

1) From a textural point of view, inclusions and interstitial BMS can be found within or associated with minerals that have a clear metasomatic origin (i.e. phlogopite, secondary clinopyroxene, carbonates) or those taking an active role in the metasomatic reaction (i.e. garnet; see also Luguet et al., submitted). When present within seemingly primary and refractory mantle minerals like olivine and orthopyroxene, inclusions are systematically found in the rims of these silicates. More importantly, in some cases olivine rims show clear chemical modifications toward Fe enrichment (see Figure 4.3 A-B-C), highlighting that even the most refractory silicates (whose rims contain BMS inclusions) have reacted to the infiltration of the metasomatising agent.

2) The BMS-oxide pools (habit vi) displays a typical melt-like morphology characterised by low dihedral angle and cuspate extensions within the grain boundaries of metasomatic silicates (e.g. phlogopite, Fig. 5L).

3) The increase in BMS modal abundances follows the defined metasomatic overprinting sequence progressing from the spinel peridotites (MB3) to the garnet phlogopite peridotites (MB6) and ultimately to the phlogopite peridotites (MB2). Strikingly, the overall modal increase of the BMS is exclusively reflected by a modal increase of the larger pseudo-inclusions (habit iii) from MB3 through MB6 to MB2 and the sudden appearance of the large interstitial BMS+oxide pools in the phlogopite peridotite MB2.

4) The textural evidence is supported by the origin of the whole-rock HSE-Se-Te signatures. Luguet et al. (submitted), argued on the basis of the suprachondritic Os/Ir ratios of

the spinel peridotites that the original post-melting protoliths of the Letlhakane peridotites was a highly depleted S-free harzburgite, with no primary mantle BMS left after partial melting. Such supra-chondritic Os/Ir ratios are characteristic of high-temperature PGM such as laurite and/or Os-bearing alloys (e.g. Malitch and Merkle, 2004), which form in partial melting residues, when the partial melting degree allows a near to complete or complete extraction of the primary mantle BMS within the partial melts (Luguet et al., 2007, Fonseca et al. 2012). The complete consumption of primary mantle BMS is also attested by the whole-rock supra-chondritic Se/Te and extreme Pd depletions.

The textural relationships between BMS and major minerals and whole-rock HSE-Se-Te systematics, along with the modal abundance variations of the BMS within the Letlhakane peridotites, rule out a residual origin for both inclusions and interstitial BMS. Rather, their presence confirms the addition of metasomatic BMS to the highly depleted protoliths during metasomatic events. This raises the question of what Re-Os ages on the metasomatic BMS represent.

4.5.2 Significance of BMS Re-Os T_{RD} ages

The T_{RD} ages of the Letlhakane pentlandite-heazlewoodite dominated BMS vary widely from Eoarchean to future ages but cluster around three time periods, the Eoarchean-Paleoarchean, Neoarchean-Paleoproterozoic and future ages (Figure 4.6B). This spectrum of model ages can be obtained within a single peridotite hand sample. Such a large range of T_{RD} ages and the close spatial association of the BMS exhibiting these ages needs to be reconciled with both the Os-host minerals expected to be present and the petrological history of the Letlhakane peridotites.

Letlhakane peridotites have experienced close to 35% polybaric partial melting, which at least partly took place in the spinel-stability field in order to explain the low whole-rock heavy rare earth element (e.g. Lu) abundances (see Luguet et al., submitted). Such a partial melting event led to the full consumption of the mantle BMS and the concomitant exsolution of high-temperature and highly refractory PGM (laurite and/or Os-bearing alloys). These minerals, owing to their chemical inertness as well as their extremely high Os contents (up to 70 wt. %; e.g. Malitch and Merkle, 2004) are known to preserve their original ^{187}Os isotopic composition even through several partial melting or subduction events (Malitch and Merkle, 2004; Pearson et al., 2007; Coggon et al., 2013 and references therein). The non-detection of these laurites and/or Os-bearing alloys in our three Letlhakane peridotites could result either from their extremely small size and heterogeneous distribution, or their

"disappearance" due to the subsequent metasomatic BMS enrichment experienced by the Letlhakane peridotites. It could be envisaged that while originally present after the large partial melting event, these residual PGM have been redissolved within the metasomatic BMS. Such a scenario is supported by the high experimentally-determined Os solubility in sulphide melt (tens of ppm level, cf. Fonseca et al., 2012). Residual PGM dissolution by metasomatic BMS would lead to the newly-introduced metasomatic BMS phases inheriting the older isotopic signatures of the residual PGM. If these residual PGM were to dominate the Os budget of a given BMS grain, then these BMS would record the earliest large-degree melting events to affect these peridotites. Such a process could then account for the existence of Paleoarchean T_{RD} ages (3.7-3.4 Ga, see Table 4.3) in metasomatic BMS, which are much older than the respective whole-rock T_{RD} ages of the peridotites selected for our study.

However, if the Os budget at the sulphide grain level is dominated by Os from the in-coming sulphide melt that is responsible for the metasomatic BMS, then the residual PGM signals will be diluted and the resulting $^{187}Os/^{188}Os$ composition of the BMS grain will be a mixture, shifted toward more radiogenic values and hence producing younger T_{RD} ages. This shift to more radiogenic Os isotope compositions is due to the fact that compared to residual PGM, the metasomatic BMS (chiefly pn ± hz) either contain Re (cf. Alard et al., 2005), which would then decay into ^{187}Os with time, and/or could derive from a reservoir with an already long-term elevated Re/Os. In this scenario, the composition of the metasomatic BMS end-member is best represented by the $^{187}Os/^{188}Os$ composition of the interstitial heazlewoodite grains of habit (v) analysed in the spinel peridotite MB3 (0.1466-0.1485, see Table 4.3). Therefore, the small cluster of Neoarchean-Paleoproterozoic T_{RD} ages as well as the Mesoproterozoic and future ages could then reflect the grain-scale Os budget becoming progressively dominated by metasomatic BMS-derived Os.

Alternatively, the T_{RD} ages than range from Neoarchean to future could also reflect single individual events in terms of BMS addition. However, this scenario seems less plausible on the basis that 1) the Neoarchean-Paleoproterozoic age peak is not sharp enough to represent a single event, but rather reflects a mixture and 2) that there are no known Neoarchean-Paleoproterozoic or Mesoproterozoic events in the Magondi Belt or in the Letlhakane or Orapa mantle roots (e.g. diamond-formation events) (Figure 4.6B).

5.2.2 Single grain BMS vs whole-rock T_{RD} ages – implications for the whole-rock Os budget of the Letlhakane peridotites

The range of the $^{187}Os/^{188}Os$ composition and T_{RD} ages of the BMS grains is always

much larger (up to 6.3 Ga time span if future ages are taken into account) than the respective whole-rocks (Figure 6B). Interestingly, the largest range of T_{RD} ages is observed for sample MB3, even though this sample is considered the least metasomatised from a silicate modal metasomtism perspective. This relationship indicates that silicate modal metasomatism (i.e. addition of phlogopite, clinopyroxene) is not necessarily the best indicator of metasomatic addition of BMS and PGM and that there is no substitute for a thorough examination of the HSE-host phase (BMS and PGM) petrology.

Additionally, for both the most refractory (MB3) and most metasomatised (MB2) peridotites analysed here, single BMS grains exhibit T_{RD} ages older than their respective whole-rock by up to 0.7 Ga for MB3 and more than 2.5 Ga for MB2. A maximum difference of 1 Ga between BMS and their respective whole-rock was previously reported by Griffin et al. (2004) in Kaapvaal peridotites but this is, to our knowledge, the first time that differences of up to 2.5 Ga between whole-rock and BMS are found.

The comparison of the BMS and whole-rock T_{RD} model ages in this study has a number of implications. The whole-rock compositions of the three peridotites analysed, in terms of $^{187}Os/^{188}Os$, clearly represent mixtures between several populations of Os-host phases such as residual high temperature PGM (i.e. laurite or Os-bearing alloys) and metasomatic BMS. Metasomatic PGM (i.e. Pt-tellurides) do not influence the mass balance for the Os isotopic composition at the whole-rock or even at the single grain scale as they are likely Os and Re free. As discussed previously, the Os-rich residual minerals will likely display an unradiogenic $^{187}Os/^{188}Os$ composition while the metasomatic BMS show more radiogenic signatures, as high as 0.1485 in this study (see Section 5.2). The whole-rock $^{187}Os/^{188}Os$ composition of a given peridotite will then just reflect the relative proportion of these two populations at the whole-rock scale. For example, the whole-rock T_{RD} age of MB3 is ca. 1.5 Ga older than that of MB2, while they both show a similar range of T_{RD} ages at the BMS scale. Such observations imply that MB2 is richer in metasomatic BMS and the whole-rock Os budget is predominantly controlled by metasomatic BMS. In contrast, in spinel peridotite MB3, the whole-rock Os budget is more dominated by unradiogenic Os carrier-phases, which could have originally be expressed as laurite or Os-bearing alloys (i.e. residual PGM), now likely redissolved within some metasomatic BMS.

A simple two-component mixing trend (Figure 7) has been calculated to determine the proportion of metasomatic BMS vs. residual PGM required to explain the whole rock $^{187}Os/^{188}Os$ compositions. The model was calculated using the most radiogenic and unradiogenic BMS grains from this study (i.e. AW5: 0.1485 and AW22: 0.1016), coupled

with an Os concentration for the radiogenic end-member of 4 ppm, (similar to BMS grain LI 129-15 of Alard et al. (2005)), and for the unradiogenic end member a higher but very conservative 40 ppm Os, typical of BMS found in cratonic peridotites (cf. Aulbach et al., 2004; Griffin et al., 2004). This model demonstrates that, if the BMS we have sampled are representative of the whole population present in each sample, the Os carriers are 66% and 87% metasomatic BMS in MB3 and MB2 respectively (Figure 7). Of course, if the Os concentrations in the unradiogenic and radiogenic end-members are different, the relative proportion of the residual PGM and metasomatic BMS will change. Nevertheless, the whole-rock Os isotopic composition of MB2 will still require a higher proportion of metasomatic BMS than the spinel peridotite MB3.

Interestingly MB2, the most metasomatised peridotite found in our Letlhakane suite, contains the oldest BMS grain with a T_{RD} age of 3.75 +/- 0.52 (2-sigma) Ga, much older than any whole-rock Letlhakane peridotites, even when the error propagation of the age calculation is taken into account. The preservation of an Eoarchean age in MB2 suggests that this sample contained laurite and/or Os-bearing alloys as the Os-carrier as a result of extensive partial melting. Which provides further support for the fact that the garnet, garnet-phlogopite and phlogopite peridotites of Letlhakane are metasomatised spinel peridotites which suffered metasomatic addition of PGM (tellurides), BMS and concomitant enrichments in Se-Te-HSE-^{187}Os, as previously demonstrated by Luguet et al. (submitted). Furthermore, the preservation of an old T_{RD} age within a BMS from such a metasomatised sample, which has a whole-rock T_{RD} age 2.5 Ga younger, demonstrates how robust the Os isotopic signatures within single residual Os-carrier-phases can be. This analysis also reveals that even highly metasomatised peridotites may preserve, at the micro-scale, evidence of their ancient origins that is obscured at the whole rock scale by the complexity of multiple petrological events. This emphasizes that, when available, BMS grains constitute better time-capsules than the whole-rock, especially if the latter has been subjected to intense post-melting modifications involving BMS addition.

5.3 Regional Significance of the T_{RD} ages

The Re-Os T_{RD} model ages determined in the BMS grains coupled with the whole rock results of Luguet et al. (submitted) and Carlson et al. (1999) clearly indicates that the Letlhakane kimberlite sampled Eoarchean sub-continental lithospheric mantle (SCLM). The SCLM had ultimately suffered a complex petrological history involving large degree melt

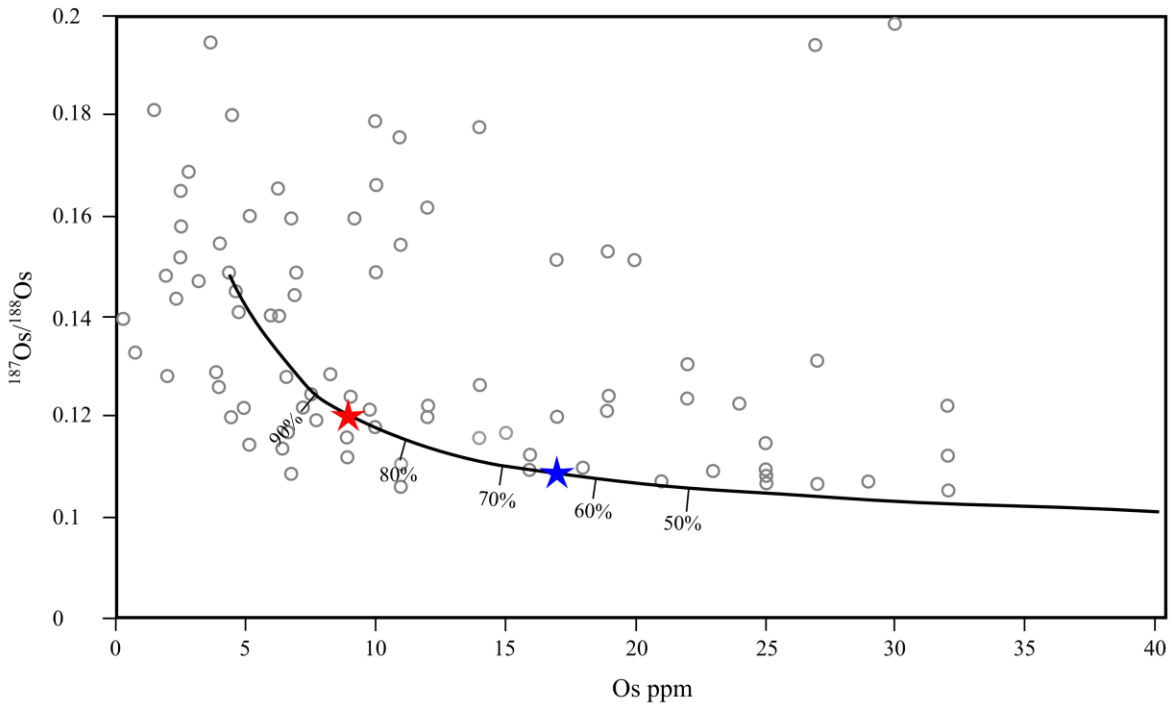

Figure 4.7. Two component mixing model for the Letlhakane peridotites, showing relationship between whole-rock and BMS Os compositions. Mixing was calculated using the most radiogenic and unradiogenic Ni-rich BMS from the Letlhakane peridotites ($^{187}Os/^{188}Os$ of 0.10159 and 0.14850) with assumed Os concentrations (high 40 ppm for unradiogenic residual PGM composition, and 4 ppm for radiogenic the BMS after sample LI 129-15 of Alard et al., 2005). Percentages refer to amount of metasomatic BMS mixed into the residual PGM component. The blue star is the whole rock composition of MB3 and the yellow star is for MB2. Grey circles are data for *in situ* Fe-rich sulphides (Griffin et al., 2004).

extraction to stabilise residual Os-rich PGM followed by metasomatism-related re-enrichments in lithophile and chalcophile/siderophile elements. This Archean age along with the whole rock model ages presented previously, brings further support to the cratonic origin of the Letlhakane lithospheric root, which is in agreement with the magnetotelluric data of Miensopust et al. (2011) and Khoza et al. (2013) that shows a thick resistive lithosphere beneath the region. Our data signify that the age of initial stabilisation of the lithosphere is in closer agreement to the oldest crustal samples from the Zimbabwe Craton (Moorbath et al., 1976; Dodson et al., 1988; Taylor et al., 1991; Nägler et al., 1997; Horstwood et al., 1999), which likely extends under the Magondi mobile belt. Moreover, the Paleoarchean age for the Letlhakane mantle root also implies that there is no crust-mantle genetic link between the Proterozoic Magondi mobile belt and its underlying mantle keel. This conclusion strengthens the evidence for the crust-mantle decoupling in this region originally based on the whole-rock Re-Os ages form the Letlhakane peridotites and suggests that the events recorded by the Letlhakane peridotites do not have a locally exposed crustal link.

Age data for the Kaapvaal Craton suggests that the eastern segment was formed between 3.2-3.7 Ga whilst the west is younger at 2.9-3.2 Ga, resulting in an east-west dichotomy (Carlson and Moore, 2004; Griffin et al., 2004; Schmitz et al, 2004). This east-west divide has also been reported for the Zimbabwe Craton on the basis of extensive older crust in the eastern part (Moorbath et al., 1976; Dodson et al., 1988; Taylor et al., 1991; Nägler et al., 1997; Horstwood et al., 1999) and a 3.4 Ga T_{RD} age obtained in a BMS inclusion from a diamond of the Murowa Kimberlite (Smith et al. 2009). The ages obtained from Letlhakane dispute this east-west dichotomy in the Zimbabwe Craton, as we report similarly old ages in Letlhakane (west) and Murowa (east) BMS. Therefore, the east-west divide seen in the Kaapvaal craton does not extend into the Zimbabwe Craton.

7. Conclusion

The Letlhakane peridotites have experienced variable degrees of metasomatism which has led to a re-enrichment in the HSE-Se-Te systematics at the whole rock scale of the original highly depleted mantle residues. The HSE carriers in these metasomatised peridotites are associated with chemically modified mineral rims or clearly metasomatism-related phlogopite, garnet and clinopyroxene. However, strikingly their $^{187}Os/^{188}Os$ ratios covers a large compositional span from unradiogenic to radiogenic (0.10159-0.61094) yielding Re-Os T_{RD} model ages from Paleoarchean to future ages. These results demonstrate that even metasomatic BMS from strongly metasomatised xenoliths can preserve non-radiogenic osmium compositions and act as robust time capsules despite the complex petrogenetic history of their host mantle rocks. There is then no rule of thumb between the isotopic composition/preservation and the textural relations and origin of the Os-carriers. Therefore Re-Os studies on cratonic peridotites should not be limited to samples and BMS that appear to be 'residual', all xenolith types and Os-bearing minerals should be investigated thoroughly in order to constrain the timing of the lithosphere stabilisation.

The unradiogenic composition of the metasomatic BMS is likely the result of the re-dissolution into the metasomatic sulphide melt of residual Os-bearing alloys, which were the Os-host phases in the highly depleted mantle residues before they suffered metasomatic overprinting. Nevertheless, the occurrence of radiogenic ^{187}Os compositions and respective future ages in metasomatic BMS argue for a dominant contribution at the grain scale of metasomatically derived osmium, originating from a source characterised by a high Re/Os composition. Of course, this mixing of the different osmium compositions has a profound effect on the whole rock Re-Os systematic; with BMS from the Letlhakane peridotites

retaining Re-Os T_{RD} ages more than 2.5 Ga older than the whole rock, questioning the robustness and meaning of the whole-rock Re-Os isotopic dating in such samples.

Ultimately, the Archean ages obtained in the BMS from Letlhakane peridotites confirm the presence of Archean mantle under the Proterozoic Magondi mobile belt and provide further evidence for crust-mantle age decoupling in Letlhakane. The BMS T_{RD} ages push the age of initial stabilisation of the lithosphere under Letlhakane back to 3.7 Ga, possibly establishing a genetic linkage between the Letlhakane mantle root and the Zimbabwe craton, as this age is similar to the age of the oldest Zimbabwe cratonic crustal rocks.

Chapter 5

Conclusions

The Kaapvaal peridotites studied in this thesis are lherzolites and harzburgites. They have all experienced high degrees of melt depletion as evidenced by their low Al_2O_3 and CaO contents. They also have low Lu contents, which signify that the Kaapvaal peridotites experienced partial melting within the spinel stability field. This is further conveyed by the Lu and Yb systematics which indicate pressures of between 2-3 GPa. The high Mg# in olivine has been used to model the degree of partial melting, and indicates that all of the Kaapvaal peridotites have experienced >20% partial melting, with only four <35%.

Nevertheless, the Kaapvaal peridotites are characterised by enrichment in the incompatible trace elements, with enrichments up to 30 times higher than primitive mantle for the most incompatible elements. This enrichment represents the pervasive cryptic metasomatism that has affected these peridotites, most likely due to interaction with the kimberlite melt. The presence of metasomatic minerals, such as phlogopite and amphibole, in half of the peridotites support enrichment from the kimberlitic melt and indicate that the peridotites have also experienced modal metasomatism.

The presence of base metal sulphides (BMS: Fe-Ni-Cu-sulphides) within residues of high degrees of partial melting at shallow pressures is not expected. Yet, 17 of the peridotites contain BMS, signifying that metasomatic BMS have also been added to the highly depleted peridotites. Due to the control BMS retain over the highly siderophile elements (HSE: Os, Ir, Pt, Pd, Re) the whole-rock HSE systematics reflect this metasomatic enrichment. With variable degrees of enrichment in Pt-Pd-Re over what is expected in residues of partial melting. Due to the presence of Re in such metasomatic BMS the Re-Os systematics of the whole-rock have also been disturbed. Consequently, Re-Os model ages do not provide ages of partial melting, but rather are integrations of multiple generations of Os-bearing minerals. Therefore, the ages obtained on the whole-rock of the Kaapvaal peridotites are unable to provide geologically significant information regarding the timing of lithosphere formation and stabilisation. Nevertheless, the presence of Archean T_{RD} ages in single grain BMS from these highly depleted peridotites infers that the addition of the BMS occurred at least 3.2 b.y.a. As such, the Kaapvaal peridotites had already experienced high degrees of partial melting prior to this metasomatic event.

While the HSE systematics have been disturbed by the addition of metasomatic BMS, the HSE variability can be used as indicators for the presence of specific platinum-group minerals (PGM). The suprachondritic Os_N/Ir_N (sub-script N denotes concentration normalised to CI-chondrite) of a number of peridotites may represent the signature of residual PGM. During partial melting, after sulphur has been depleted from the residue, Os and Ir partition into separate PGM such as erlichmanite and Pt-Ir alloys. As these minerals are generally small (<1 µm) and heterogeneously distributed through-out the peridotite, a sampling bias or 'nugget-effect' can occur during digestion, such that an artificial fractionation of Os and Ir occurs. Therefore, the Kaapvaal peridotites most likely contain residual alloys, as would be expected due to the high degrees of partial melting that these rocks experienced. The variable Pt-Pd within the Kaapvaal peridotites may also be due to a nugget-effect. It is expected that Pt and Pd would have been enriched in the metasomatic sulphide melt. Upon crystallisation and sub-solidus re-equilibration of the precipitated metasomatic BMS into pentlandite, Pt is no longer retained within the crystalline structure of pentlandite. As such, Pt will fractionate into Pt-minerals (e.g. Pt-Fe-alloys, Pt-tellurides, Pt-arsenides) whilst Pd is retained within the BMS. This difference in mineralogy can again create a 'nugget-effect' and cause variation in the degree of enrichment of Pt and Pd.

In one of the Kaapvaal peridotites – 09-BOS-05 – a number of Pt-alloy micro-inclusions were identified within two separate BMS. This provided a unique opportunity to investigate the effect these minerals had at the whole-rock scale. Replicate aliquots of the whole-rock display variability in Os-Ir-Pt-Pd concentrations. These concentrations do not vary systematically with the concentration of the HSE in the Pt-alloys. Therefore the Pt-alloys are not the only control on the HSE systematics at the whole-rock scale. The variable suprachondritic Os_N/Ir_N support the presence of residual alloys within this peridotite, whilst the variable Pd_N/Ir_N most likely indicates the presence of metasomatic sulphides. This signifies the highly heterogeneous distribution of PGM and BMS minerals within the peridotite.

The $^{187}Os/^{188}Os$ compositions of the Pt-alloys are quite different from the $^{187}Os/^{188}Os$ compositions of the host BMS, with the alloys being radiogenic ($^{187}Os/^{188}Os$ 0.1294 - 0.1342) and the BMS being unradiogenic ($^{187}Os/^{188}Os$ 0.1066 - 0.1084). The alloys are hosted within the BMS as inclusions either at the edge of the grain or as oriented needles within the BMS grain. Diffraction patterns obtained on the Pt-alloys demonstrate their nanoparticle nature, whilst EDX spectra infer that the Pt-alloys are composed of Pt-Fe ± Ir ± Rh. The combination of the texture, nanoparticle nature, Pt-Fe composition and the dichotomy between the Pt-

alloys and the host BMS $^{187}Os/^{188}Os$ compositions imply that the Pt-alloys and BMS were formed due to the percolation of a HSE-Si-rich, S-undersaturated melt. The Pt-alloys formed as nanoparticle ligands within the Si-rich melt. Upon reaching S-saturation, a sulphide melt formed and scavenged the Pt-alloys. The dichotomy in $^{187}Os/^{188}Os$ between the Pt-alloy and the BMS infers that any Re available in the system partitioned into the Pt-alloys rather than the BMS. Therefore, the BMS did not experience a high degree of ^{187}Os ingrowth and the T_{RD} ages obtained from the BMS (2.9 and 3.1 Ga) most likely provide a minimum estimate on the timing of the percolation of the metasomatic silicate melt.

The T_{RD} ages of the Kaapvaal peridotites do not provide information on the formation and stabilisation of the Kaapvaal lithosphere due to pervasive metasomatism. However, despite significant metasomatism, ages related to lithosphere formation can still be obtained, as shown with the Letlhakane peridotites. These peridotites have experienced variable degrees of silicate-HSE-Se-Te-metasomatism. Nevertheless, single grain BMS ages obtained from these peridotites pre-date the whole-rock by up to 2.5 Ga. Such old ages within metasomatic BMS indicate that residual PGM within the peridotites can be entrained by the BMS. Mass balance modelling indicates that for the most metasomatised peridotite (MB2) the metasomatic BMS account for 87% of the whole-rock $^{187}Os/^{188}Os$ composition. In the least metasomatised peridotite (MB3), the metasomatic BMS account for 66% of the whole-rock $^{187}Os/^{188}Os$ composition. This signifies that peridotites which experienced minor degrees of metasomatism can still have $^{187}Os/^{188}Os$ compositions dominated by metasomatic minerals. As such, whole-rock Re-Os model ages should be interpreted with caution.

The ability of metasomatic sulphides to retain unradiogenic Re-Os due to entrainment of PGM, demonstrates that no rules can be applied to the selection of BMS for single grain analysis. With BMS which retain un-radiogenic $^{187}Os/^{188}Os$ being of Ni-rich compositions (e.g. heazlewoodite) and are located interstitial to secondary minerals such as clinopyroxene and phlogopite,. The oldest T_{RD} age of 3.7 Ga obtained on a BMS from the Letlhakane peridotite, pushes the age of the initial stabilisation of the mantle in the Zimbabwe craton back towards the ages of the oldest crustal rocks.

The results obtained in this study demonstrate that the Re-Os system should be carefully applied to whole-rock peridotites. Due to pervasive metasomatic enrichment of the HSE, the Re-Os systematic at the whole-rock scale is an integration of multiple generations of Os-bearing minerals. The combination of HSE systematics with Re-Os geochronology allows for an accurate interpretation of the obtained ages. The utility of the Re-Os system lies in the ability to distinguish between metasomatic events and partial melting. Through the

determination of Os compositions on different constituents within peridotites, it is possible to differentiate between the different populations and obtain geologically significant information.

Chapter 6

References

Abrajano Jr., T.A. and Pasteris J.D. (1989) Zambales ophiolite, Philippines. *Contrib. Mineral. Petrol.* **103**, 64-77

van Achterbergh E., Griffin W.L., and Stiefenhofer J. (2001) Metasomatism in mantle xenoliths from the Letlhakane kimberlites: estimation of element fluxes. *Contrib. Mineral. Petrol.* **141**, 397-414

Alard O., Griffin W.L., Lorand J.-P., Jackson S.E. and O'Reilly S.Y. (2000) Non-chondritic distribution of the highly siderophile elements in mantle sulphides, *Nature*, **407**, 891-894

Alard O., Griffin W.L., Pearson N.J., Lorand J.-P. and O'Reilly S.Y. (2002) New insights into the Re-Os systematics of sub-continental lithospheric mantle from in situ analysis of sulphides. *Earth Planet. Sci. Lett.*, **203**, 651-663

Alard O., Luguet L., Pearson N.J., Griffin W.L., Lorand J.-P., Gannoun A., Burton K.W. and O'Reilly S.Y. (2005) In Situ Os isotopes in abyssal peridotites bridge the isotopic gap between MORBs and their source mantle, *Nature*, **436,** 1005-1008

Allsopp H.L. and Barrett D.R. (1975) Rb-Sr age determinations on South African kimberlite pipes, *Phys. Chem. Earth,* **9**, 605-617

Anders E. and Grevesse, N. (1989) Abundances of the elements: Meteoritic and solar, *Geochim. Cosmochim. Acta,* **53**, 197-214

Armstrong R.A., Compston W., de Wit M.J. and Williams I.S. (1990) The stratigraphy of the 3.5-3.2 Ga Barberton Greenstone Belt revisted: a single zircon ionprobe study, *Earth Planet. Sci. Lett*, **101**, 90-106

Aulbach S. (2012) Craton nucleation and formation of thick lithospheric roots. *Lithos* **149**, 16-30

Aulbach S., Griffin W.L., Pearson N.L., O'Reilly S.Y., Kivi K. and Doyle, B.J. (2004) Mantle formation and evolution, Slave Craton: constraints from HSE abundances and Re-Os isotope systematics of sulfide inclusions in mantle xenocrysts. *Chem. Geol.* **208**, 61-88

Aulbach S., Griffin W.L., Pearson N.J., O'Reilly S.Y. and Doyle B.J. (2007) Lithosphere formation in the Central Slave Craton (Canada): plume accretion or lithospheric accretion. *Contrib. Mineral. Petrol.* **154**, 409-428

Baker M.B. and Stolper E.M. (1994) Determining the composition of high-pressure mantle melts using diamond aggregates, *Geochim. Cosmochim. Acta*, **58**, 2811-2827

Ballhaus C. and Ryan C.G. (1995) Platinum-group elements in the Merensky Reef. I. PGE in solid solution in base metal sulfides and the down-temperature equilibration history of Merensky ores. *Contrib. Mineral. Petrol.*, **122**, 241-251

Ballhaus C. and Sylvester P. (2000) Noble metal enrichment processes in the Merensky Reef, Bushveld Complex, *J. Petrol.*, **41**, 545-561

Ballhaus C., Bockrath C., Wohlgemuth-Ueberwasser C., Laurenz V. and Berndt J. (2006) Fractionation of the noble metals by physical processes, *Contrib. Mineral. Petrol.*, **15**, 667-684

Barnes S.-J., Prichard H.M., Cox R.A., Fisher P.C. and Godel B. (2008) The location of the chalcophile and siderophile elements in platinum-group element ore deposits (a textural, microbeam and whole rock geochemical study): Implications for the formation of the deposits, *Chem. Geol.*, **248**, 295-317

Becker H., Horan M.F., Walker R.J., Gao S., Lorand J.-P. and Rudnick, R.L. (2006) Highly siderophile element composition of the Earth's primitive upper mantle: Constraints from new data on peridotite massifs and xenoliths. *Geochim. Cosmochim. Acta,* **70**, 4528-4550

Bell D.R., Grégoire M., Grove T.L., Chatterjee N., Carlson R.W. and Buseck P.R. (2005) Silica and volatile-element metasomatism of Archean mantle: a xenolith-scale example from the Kaapvaal Craton, *Contrib. Mineral. Petrol.*, **150**, 251-267

Bird J.M., Meibom A., Frei T. and Naegler T.F. (1999) Osmium and lead isotopes of rare OsIrRu minerals: derivation from the core-mantle boundary region? *EPSL*, **170**, 83-92

Bockrath C., Ballhaus C. and Holzheid A. (2004) Fractionation of the Platinum-Group Elements During Mantle Melting, *Science*, **305**, 1951-1953

Bowring S.A., Williams I.S. and Compston W. (1989) 3.96 Ga gneisses from the Slave province, Northwest Territories, Canada, *Geology*, **17**, 971-975

Boyd F.R. (1989) Compositional distinction between oceanic and cratonic lithosphere, *Earth Planet. Sci. Lett.*, **96**

Boyd F.R. (1997) Correlation of orthopyroxene abundance with the Ni content of coexisting olivine in cratonic peridotites. *Eos Trans. Amer. Geophys. Union*, **78**, F746

Boyd F.R. and Nixon P.H. (1978) Ultramafic nodules from the Kimberley pipes, South Africa, *Geochim. Cosmochim. Acta,* **42**, 1367-1382

Bragagni A., Luguet A., Pearson D.G., Fonseca R.O.C. and Kjarsgaard B.A. (2013) Insight on formation and evolution of cratonic mantle: Re-Os dating of single sulfides from Somerset mantle xenoliths (Rae Craton, Canada). *Goldschmidt Conference Abstracts,* **760**

Brenker F.E., Meibom A. and Frei R. (2003), On the formation of peridotite-derived Os-rich PGE alloys, *Am. Min.,* **88**, 1731-1740

Brey G.P. and Köhler T. (1990) Geothermobarometry in Four-phase lherzolite II. New Thermobarometers, and Practical Assessment of Existing Thermobarometers, *J. Petrol.*, **31**, 1353-1378

Burton K.W., Schiano P., Birck J.L. and Allègre C.J. (1999) Osmium isotope disequilibrium between mantle minerals in a spinel-lherzolite. *Earth Planet. Sci. Lett.* **172**, 311-322

Burton K.W., Schiano P., Birck J. L., Allegre C. J., Rehkämper M., Halliday A. N., & Dawson J. B. (2000) The distribution and behaviour of rhenium and osmium amongst mantle minerals and the age of the lithospheric mantle beneath Tanzania. *Earth Planet. Sci. Lett.* **183**, 93-106.

Canil D. (1991) Experimental evidence for the exsolution of cratonic peridotite from high-temperature harzburgite, *Earth Planet. Sci. Lett.,* **106**, 64-72

Canil D. (2004) Mildly incompatible elements in peridotites and the origins of mantle lithosphere, *Lithos,* **77**, 375-393

Carlson R.W. and Moore R.O. (2004) Age of the Eastern Kaapvaal mantle: Re-Os isotope data for peridotite xenoliths from the Monastery kimberlite. *S. Afr. J. Geol.* **107**, 81-90

Carlson R. W., Pearson D. G., Boyd F. R., Shirey S. B., Irvine G., Menzies A. H. & Gurney J. J. (1999) Re–Os systematics of lithospheric peridotites: implications for lithosphere formation and preservation. *7th Int. Kimberlite Conf.,* Red Roof Design, Cape Town. pp. 99-108.

Chapman D.S. and Pollack H.N. (1977) Regional geotherms and lithospheric thicknesses, *Geology*, **5**, 565-568

Coggon J.A., Nowell G.M., Pearson D.G. and Parman S.W. (2011) Application of the 190Pt-186Os isotope system to dating platinum mineralization and ophiolite formation: An example from the Meratus mountains, Borneo, *Econ. Geol.,* **106**, 93-117

Coggon J.A., Luguet A., Nowell G.M. and Appel P.W.U. (2013) Hadean mantle melting recorded by southwest Greenland chromitite ^{186}Os signatures, *Nat. Geosci.*, **6**, 871-874

Cohen A.S. and Waters F.G. (1996), Separation of osmium from geological materials by solvent extraction for analysis by thermal ionisation mass spectrometry, *Anal. Chim. Acta,* **332**, 269-275

Craig J.R. (1973) Pyrite-Pentlandite assemblages and other low temperature relations in the Fe-Ni-S system, *Am. J. Sci.,* **273A**, 496-510

Craig J.R. and Kullerud G. (1969) Phase relations in the Cu-Fe-Ni-S System and their Application to Magmatic Ore Deposits. In: *Symposium on Magmatic Ore Deposition, Econ. Geol. Mono.,* **4**. 344-358

Dale C.W., Luguet A., Macpherson C.G., Pearson D.G. and Hickey-Vargas R. (2008) Extreme platinum-group element fractionation and variable Os isotope compositions in Philippine Sea Plate basalts: Tracing mantle source heterogeneity. *Chem Geol.*, **248**, 213-238

Davis G.L. (1977) The ages and uranium content of zircons from kimberlites and associated rocks, extended abstract. *Second Int. Kimberlite Conf.* (unpaginated)

Dawson J.B. and Stephens W.E. (1976) Statistical classification of garnets from kimberlite and associated xenoliths, *J. Geology*, **53**, 589-607

Dodson M.H., Compston W., Williams I.S. and Wilson J.F. (1988) A search for ancient detrital zircons in Zimbabwean sediments. *J. Geol. Soc.,* **145**, 977-983

Drennen G.R., Robb L.J., Meyer F.M., Armstrong R.A. and de Brulyn H. (1990) The nature of the Archean basement in the hinterland of the Witwatersand Basin: II. A crustal profile west of the Welkom Goldfield and comparisons with the Vredefort crustal profile. *S. Afr. J. Geol.*, **93**, 41-53

Dromgoole E.L. and Pasteris J.D. (1987) Interpretation of the sulfide assemblages in a suite of xenoliths from Kilbourne Hole, New Mexico. *Geol. S. Am. S.*, **215**, 25-46

Erlank A.J., Waters F.G., Hawkesworth C.J., Haggerty S.E., Allsopp H.L., Rickard R.S. and Menzies M.A. (1987) Evidence for mantle metasomatism in peridotite nodules from the Kimberlite piper, South Africa. In: *Mantle Metasomatism, Academic Press, London* (pp. 221-311)

Farrell S.P and Fleet M.E. (2002) Phase separation in $(Fe,Co)_{1-x}S$ monosulfide solid-solution below 450°C, with consequences for coexisting pyrrhotite and pentlandite in magmatic sulfide deposits. *Can. Mineral.* **40**, 33-46

Farrow C.E.G. and Watkinson D.H. (1997) Diversity of precious-metal mineralization in footwall Cu-Ni-PGE deposits, Sudbury, Ontario: Implications for hydrothermal models of formation, *Can. Mineral.*, **35**, 817-839

Fischer-Gödde M., Becker H. and Wombacher F. (2011) Rhodium, gold and other highly siderophile elements in orogenic peridotites and peridotite xenoliths, *Chem. Geol.*, **280**, 365-383

Fleet M.E., Chryssoulis S.L., Stone W.E. and Weisener C.G. (1993) Partitioning od platinum-group elements and Au in the Fe-Ni-Cu-S system: experiments on the fractional crystallisation of sulfide melt, *Contrib. Mineral. Petrol.*, **115**, 36-44

Fonseca R.O.C., Mallmann G., O'Neill H.St.C. and Campbell I.H. (2007) How chalcophile is rhenium? An experimental study of the solubility of Re in sulfide mattes, *EPSL*, **260**, 537-548

Fonseca, R.O.C., Campbell, I.H., O'Neill, H.St.C., Fitzgerald, J.D., (2008). Oxygen solubility and speciation in sulfide-rich mattes. *Geochim. Cosmochim. Acta* **72**, 2619-2635

Fonseca R.O.C., Mallmann G., O'Neill H.St.C., Campbell I.H. and Laurenz V. (2011) Solubility of Os and Ir in sulfide melt: Implications for Re/Os fractionation during mantle melting, *Earth Planet. Sci. Lett.*, **331**, 339-350

Fonseca R.O.C., Laurenz V., Mallmann G., Luguet A., Hoehne N. and Jochum K.P. (2012) New constraints on the genesis and long-term stability of Os-rich alloys in the Earth's mantle, *Geochim. Cosmochim. Acta*, **87**, 227-242

Gibson S.A., Malarkey J. and Day J.A., (2008) Melt depletion and enrichment beneath the Western Kaapvaal Craton: Evidence from Finsch Peridotite Xenoliths, *J. Petrol.*, **49**, 1817-1582

Godel B. and Barnes S.-J. (2008) Platinum-group elements in sulfide minerals and the whole rocks of the J-M Reef (Stillwater Complex): Implication for the formation of the reef. *Chem. Geol.* **248**, 272-294

Grégoire M., Bell D.R. and le Roux A.P., (2003) Garnet lherzolits from the Kaapvaal Craton (South Africa): Trace element evidence for a metasomatic history, *J. Petrol.*, **44**, 629-657

Grégoire M., Tinguely C., Bell D.R. and le Roux A.P. (2005) Spinel lherzolite xenoliths from the Premier kimberlite (Kaapvaal craton, South Africa): Nature and evolution of the shallow upper mantle beneath the Bushveld complex, *Lithos*, **84**, 185-205

Griffin W.L., Shee S.R., Ryan C.G., Win T.T. and Wyatt B.A. (1999). Harzburgite to lherzolite and back again: Metasomatic processes in ultramafic xenoliths from the Wesselton kimberlite, Kimberley, South Africa. *Contr. Mineral. Petrol*. **134**, 232-250.

Griffin W.L., O'Reilly S.Y., Natapov L.M. and Ryan C.G. (2003) The evolution of lithospheric mantle beneath the Kalahari Craton and its margins, *Lithos*, **71**, 215-241

Griffin W.L., Graham S., O'Reilly S.Y. and Pearson N.J. (2004) Lithosphere evolution beneath the Kaapvaal Craton: Re–Os systematics of sulfides in mantle-derived peridotites. *Chem. Geol.* **208**, 89-118.

Grütter H., Latti D. and Menzies A. (2006) Cr-saturation arrays in concentrate garnet compositions from kimberlite and their use in mantle barometery, *J. Petrol.*, **47**, 801-820

Handler M.R. and Bennett V.C. (1999) Behaviour of platinum-group element in the subcontinental mantle of eastern Australia during variable metasomatism and depletion. *Geochim. Cosmochim. Acta* **63**, 3597-3618

Harrison T.M. (2008) The Hadean Crust: Evidence from >4 Ga Zircons, *Annu. Rev. Earth Plant. Sci.*, **37**, 479-505

Hart S.R. and Ravizza G.E. (1996) Os partitioning between phases in lherzolite and basalt. In: *Earth Processes: Reading the Isotopic Code, American Geophysical Union,* (pp. 123-134)

Hattori K. and Cabri L.J. (1992) Origin of platinum-group mineral nuggets inferred from an osmium isotope study, *Can. Mineral*, **30**, 289-301

Hawkesworth C.J., Erlank A.J., Kempton P.D. and Water F.G. (1990) Mantle metasomatism: Isotope and trace-element trends in xenoliths from Kimberley, South Africa, *Chem. Geol.*, **85**, 19-34

Helmsteadt H. and Schulze D.J. (1989) Southern African kimberlites and their mantle sample-implication for Archean tectonics and lithosphere evolution. *Geol. Soc. Aust.* **14**, 358-422

Helmy H.M., Ballhaus C., Fonseca R.O.C., Wirth R., Nagel T. and Tredoux M. (2013) Noble metal nanoclusters and nanoparticles precede mineral formation in magmatic sulphide melts, *Nat. Commun.*, **4:2405**

Herzberg C. (1999) Phase equilibrium constraints on the formation of cratonic mantle. In: *Mantle Petrology, Field Observations and High Pressure Experimentation: A tribute to Francis R. Boyd* (Eds. Fei Y., Bertka C. and Mysen B.), The Geochemical Soc. Spec. Pub. Houston, 225-239

Herzberg C. (2004) Geodynamic information in peridotite petrology, *J. Petrol.*, **45**, 2507-2530

Holwell D.A. and McDonald I. (2010) A review of the behaviour of Platinum Group Elements within natural magmatic sulfide ore systems, *Platinum Metals Rev.*, **54**, 26-36

Horstwood M.S.A., Nebitt R.W., Noble S.R. and Wilson J.F. (1999) U-Pb zircon evidence for the extensive early Archean craton in Zimbabwe: A reassessment of the timing of craton formation, stabilization, and growth. *Geology* **27**, 707-710

Irvine G.J., Pearson D.G. and Carlson R.W. (2001) Lithspheric mantle evolution of the Kaapvaal Craton: A Re-Os isotope study of peridotite xenoliths from Lesotho kimberlites¸ *Geophys. Research Lett.*, **28**, 2505-2508

Irvine G.J., Pearson D.G., Kjarsgaard B.A., Carlson R.W., Kopylova M.G. and Dreibus G. (2003) A Re-Os isotope and PGE study of kimberlite-derived peridotite xenoliths from Somerset Island and a comparison to the Slave and Kaapvaal cratons, *Lithos*, **71**, 461-488

Ishikawa A., Senda R., Suzuki K., Dale C.W. and Meisel T. (2014) Re-evaluating digestion methods for highly siderophile element and ^{187}Os isotope analysis Evidence from geological reference materials, *Chem. Geol.*, **384**, 27-46

James D.E. and Fouch M.J. (2002) Formation and evolution of Archean cratons: insights from southern Africa, In: *The Early Earth, Physical, Chemical and Biological Development* (Fowler C.M.R., Ebiner C.J. and Hawkesworth C.J. (eds)), Geol. Soc., London, Special Publication **199,** 1-26

Jordan T.H. (1988) Structure and Formation of the Continental Tectosphere, *J. Petrol.,* **Spec. Vol. 1,** 11-37

Kelemen P.B., Hart S.R. and Bernstein S. (1998) Silica enrichment in the continental upper mantle via melt/rock reaction, *Earth Planet. Sci. Lett.*, **164**, 387-406

Kesson S.E. and Ringwood A.E. (1989) Slab-mantle interactions 2. The formation of diamonds, *Chem. Geol.,* **75**, 97-118

Khoza D., Jones A.G., Muller M.R., Evans R.L., Webb S.J., Miensopust M., the SAMTEX team (2013) Tectonic model of the Limpopo belt: Constraints from magnetotelluric data. *Precamb. Research* **226**, 143-156

Klein F. and Bach W. (2009) Fe-Ni-Co-O-S Phase relations in peridotite-seawater interactions. *J. Petrol.*, **50**, 37-59

König S., Luguet A., Lorand J.-P., Wombacher F. and Lissner M. (2012). Selenium and tellurium systematics of the Earth's mantle from high precision analyses of ultra-depleted orogenic peridotites. *Geochim. Cosmochim. Acta* **86**, 354-366

Kröner A., Compston W. and Williams I.S., (1989) Growth of early Archean crust in the Ancient Gneiss complex of Swaziland as revealed by single zircon dating, *Tectono.,* **161**, 271-298

Kröner A., Hegner E., Wendt J.I. and Byerly G.R. (1993) The oldest part of the Barberton granitoid-greenstone terrain, South Africa: evidence for crust formation between 3.5 and 3.7 Ga. *Precamb. Research,* **78**, 105-124

Lazarov M., Brey G.P. and Weyer S. (2009a) Time steps of depletion and enrichment in the Kaapvaal craton as recorded by subcalcic garnets from Finsch (SA), *Earth Planet. Sci. Lett.,* **279**, 1-10

Lazarov M. Woodland A.B. and Brey G.P., (2009b) Thermal state and redox conditions of the Kaapvaal mantle: A study of xenoliths from the Finsch mine, South Africa. *Lithos,* **112S**, 913-923

Lee C.-T.A. (2006) Geochemical/petrological constraints on the origin of cratonic mantle. In *Archean Geodynamics and Environments*, (ed. K. Benn, J.-C. Mareschal, K.C. Condie), *Geophys. Monogr*. **164,** 89–114

Lee C.-T.A., Luffi P. and Chin E.J. (2011) Building and Destroying Continental Mantle. *Annu. Rev. Earth Planet. Sci.* **39**, 59-90

Li C. and Ripley E.M. (2006) Formation of Pt-Fe alloy by desulfurization of Pt-Pd sulfide in the J-M Reed of the Stillwater Complex, Montana, *Can. Mineral.,***44**, 895-903

Lissner M., König S., Luguet A., le Roux P.J., Schuth S., Heuser A., le Roex A.O. (2014) Selenium and Tellurium systematics in MORBs from the southern Mid-Atlantic Ridge (47-50°S). *Geochim. Cosmochim. Acta.* in press *DOI: 10.1016/j.gca.2014.08.023*

Lorand J.-P. (1985) The behaviour of the upper mantle sulfide component during incipient alteration of "Alpine"-Type peridotites as illustrated by the Beni Bousera (Northern Morocco) and Ronda (Southern Spain) ultramafic bodies. *Tschermaks Min. Petr. Mitt.* **34**, 183-209

Lorand J.-P. and Grégoire M. (2006), Petrogenesis of base metal sulphide assemblages of some peridotites from the Kaapvaal craton (South Africa). *Contrib. Mineral. Petrol.,* **151**, 521-538

Lorand J.-P., Pattou L. and Gros M. (1999) Fractionation of Platinum-group elements and Gold in the Upper Mantle: A detailed study in Pyrenean Orogenic Lherzolites, *J. Petrol.*, **40**, 957-981

Lorand J.-P., Delpech G., Grégoire M., Moine B., O'Reilly S.Y. and Cotton J.-Y. (2004) Platinum-group elements and the multistage metasomatic history of Kerguelen lithospheric mantle (South Indian Ocean), *Chem. Geol.,* **208**, 195-215

Lorand J.-P., Luguet A., Alard O., Bezos A. and Meisel T. (2008) Abundance and distribution of platinum-group elements in orogenic lherzolites; a case study in a Fontete Rouge lherzolite (French Pyrénées). *Chem. Geol.*, **248**, 174-194

Lorand J.-P., Luguet A. and Alard O. (2013) Platinum-group element systematics and petrogentic processing of the continental upper mantle: A review, *Lithos*, **164-167**, 2-21

Luguet A., Alard O., Lorand J.-P., Pearson N.J., Ryan C. and O'Reilly S.Y. (2001) Laser-ablation microprobe (LAM)-ICPMS unravels the highly siderophile element geochemistry of the oceanic mantle, *Earth Planet. Sci. Lett.*, **189**, 285-294

Luguet A., Lorand J.-P. and Seyler M. (2003) Sulfide petrology and highly siderophile element geochemistry of abyssal peridotites: A couple study of samples from the Kane Fracture Zone (45°W 23°20N, MARK Area, Atlantic Ocean). *Geochim. Cosmochim. Acta*, **67**, 1553-1570

Luguet A., Lorand J.-P., Alard O. and Cottin J.-Y. (2004) A multi-technique study of platinum group element systematic in some Ligurian ophiolite peridotites, Italy. *Chem. Geol.*, **208**, 175-194

Luguet A., Shirey S.B., Lorand J.-P., Horan M.F. and Carlson R.W. (2007) Residual platinum-group minerals from highly depleted harzburgites of the Lherz massif (France) and their role in HSE fractionation of the mantle. *Geochim Cosmochim. Acta* **71**, 3082-3097

Luguet A., Nowell G.M. and Pearson D.G. (2008a) $^{187}Os/^{188}Os$ and $^{186}Os/^{188}Os$ measurements by Negative Thermal Ionisation Mass Spectrometry (N-TIMS): Effects of interfering element and mass fractionation corrections on data accuracy and precision. *Chem. Geol.* **248**, 342-362

Luguet A., Pearson D.G., Nowell G.M., Dreher S.T., Coggon J.A., Spetsius Z.V. and Parman S.W. (2008b), Enriched Pt-Re-Os isotope systematics in plume lavas explained by metasomatic sulphides, *Science*, **319**, 453-456

Luguet A., Jaques A.L., Pearson D.G., Smith C.B., Bulanova G.P., Roffey S. L., Rayner M.J. and Lorand J.-P. (2009) An integrated petrological, geochemical and Re-Os isotope study of peridotite xenoliths from the Argyle lamporite, Western Australia and implications for cratonic diamond occurrences, *Lithos*, **112S**, 1096-1108

Luguet A., Behrens M., Pearson D.G., König S. and Herwartz D. (submitted) Significance of the whole-rock Re-Os ages in cryptically and modally metasomatised cratonic peridotites - Part 1: HSE-Se-Te systematics as discriminant tools

Majaule T., Hanson R.E., Key R.M., Singletary S.J., Martin M.W. and Bowring S.A. (2001) The Magondi Belt in northeast Botswana: regional relations and new geochronological data from the Sua Pan area. *J. Afr. Earth Sci.,* **32**, 257-267

Makovicky E. (2002), Ternary and Quaternary Phase Systems with PGE, In: *The Geology, Geochemistry, Mineralogy and Mineral Benefication of Platinum-group elements, Canadian Institute of Mining, Metallurgy and Petroleum* (Cabri L.J., eds), Montreal, **Special vol. 54**, 131-175

Makovicky M., Makovicky E. and Rose-Hanson J. (1986) Experimental studies on the solubility and distribution of platinum group elements in base-metal sulphides in platinum deposits. In: *Metalogeny of basic and ultrabasic rocks,* **The Institution of Mining and Metallurgy**, (Gallagher M.J., Ixer R.A., Neary C.R. and Prichard H.M. eds), London, 415-425

Malitch K.N. and Thalhammer O.A.R. (2002) Pt-Fe nuggets derived from clinopyroxenite-dunite massifs, Russia: A structural, compositional and osmium-isotope study, *Can. Mineral.,* **40**, 395-418

Malitch K.N. and Merkle R.K.W. (2004) Ru-Os-Ir-Pt and Pt-Fe alloys from the Evander goldfield, Witwatersrand Basin, South Africa: Detrital origin inferred from compositional and osmium-isotope data, *Can. Mineral.*, **42**, 631-650

Mann U., Frost D.J., Rubie D.C., Becker H. and Audétat A. (2012) Partitioning of Ru, Rh, Pd, Re, Ir and Pt between liquid metal and silicate at high pressures and temperatures – Implications for the origin of highly siderophile element concentrations in the Earth's mantle, *Geochim. Cosmochim. Acta,* **84**, 593-613

Mavrogenes J.A. and O'Neill H.St.C., The relative effects of pressure, temperature and oxygen fugacity on the solubility of sulfide in mafic magmas, *Geochim. Cosmochim. Acta,* **63**, 1173-1180

McCourt S., Hilliard P., Armstrong R.A. and Munyanyiwa H. (2001) SHRIMP U-Pb zircon geochronology of the Hurungwe granite northwest Zimbabwe: Age constrains on the timing of the Magondi orogeny and implications for the correlation between the Kheis and Magondi Belts. *S. Afr. J. Geol.,* **104**, 39-46

McDonough W.F. (1994) Chemical and isotopic systematics of continental lithospheric mantle. In: *Proceedings Fifth International Kimberlite Conference*, Meyer H.O.A. and Leonardos O. (eds), CPRM, Brasilia, 478-485

McDonough W.F. and Sun S.-s. (1995) The composition of the Earth, *Chem. Geol.,* **120**, 223-253

Meibom A. and Frei R. (2002) Evidence for an Ancient Osmium Isotopic Reservoir in Earth, *Science*, **296**, 516–518.

Meibom A., Sleep N.H., Chamberlain C.P., Coleman R.G., Frei R., Hren, M.T. and Wooden J.L. (2002) Re-Os isotopic evidence for long-lived heterogeneity and equilibrium processes in Earth's upper mantle, *Nature*, **419**, 705–708

Meisel T. and Moser J. (2004) Reference materials for geochemical PGE analysis: new analytical data for Ru, Rh, Pd, Os, Ir, Pt and Re by isotope dilution ICPMS in 11 geological reference materials, *Chem. Geol.*, **208**, 319-338

Meisel T., Reisberg L., Moser J., Carignan J., Melcher F. and Brügmann G. (2003) Re-Os systematics of UB-N, a serpentinised peridotite reference material. *Chem. Geol.,* **201**, 161-179

Miensopust M., Jones A.G., Muller A.G., Garcia X. and Evans R.L. (2011) Lithospheric structures and Precambrian terrane boundaries in north-eastern Botswana revealed through magnetotelluric profiling as part of the Southern African magnetotelluric experiment. *J. Geophys. Res.* **116**, B02401

Menzies, A.H., Carlson, R.W., Shirey, S.B. and Gurney, J.J., 1999. Re-Os systematics of Newlands peridotite xenoliths: implications for diamond and lithosphere formation. In:), 7th Int. Kimberlite Conf., J.J. Gurney, J.L. Gurney, M.D. Pascoe and S.H. Richardson (Eds.) Red Roof Design, Cape Town, South Africa, 566-573.

Moorbath S., Wilson J.F. and Cotterill P. (1976) Early Archean age for the Sebakwian group at Selukwe, Rhodesia. *Nature* **264**, 536-538

Nägler Th.F., Kramers J.D., Kamber B.S., Frei R. and Prendergast M.D.A. (1997) Growth of subcontinental lithospheric mantle beneath Zimbabwe started at of before 3.8 Ga: Re-Os study on chromites. *Geology* **25**, 983-986

Nickel K.G. and Green D.H. (1985) Empirical geothermobarometry for garnet peridotites and implications for the nature of the lithosphere, kimberlites and diamonds, *Earth Planet. Sci. Lett.,* **73**, 158-170

Nimis P. and Grütter H. (2010) Internally consistent geothermometers for garnet peridotites and pyroxenites, *Contrib. Mineral. Petrol.*, **159**, 411-427

Nimis P. and Talyer W.R. (2000) Single clinopyroxene thermobarometry for garnet peridotites. Part I. Calibration and testing of a Cr-in-Cpx barometer and an enstatite-in-cpx thermometer, *Contrib. Mineral. Petrol.,* **139**, 541-554

Nowell G.M., Pearson D.G., Parman S.W., Luguet A. and Hanski E. (2008) Precise and accurate $^{186}Os/^{188}Os$ and $^{187}Os/^{188}Os$ measurements by Multi-collector Plasma Ionisation Mass Spectrometry, part II: Laser ablation and its application to single-grain Pt-Os and Re-Os geochronology, *Chem. Geol.*, **248**, 394-426

O'Neil J., Carlson R.W., Francis D. and Stevenson R.K. (2008) Neodymium-142 Evidence for Hadean Mafic Crust, *Science*, **321**, 1828-1831

Parman S.W., Grove, T.L., Dann J.C. and de Wit M.J. (2004) A subduction origin for komatiites and cratonic lithospheric mantle. *S. Afr. J. Geol.*, **107**, 107-118

Pearson D.G. (1999) The age of continental roots, *Lithos*, **48**, 171-194

Pearson D.G. and Woodland S.J. (2000) Solvent extraction/anion exchange separation and determination of PGEs (Os, Ir, Pt, Pd, Ru) and Re-Os isotopes in geological samples by isotope dilution ICP-MS, *Chem. Geol.*, **165**, 87-107

Pearson D.G. and Wittig N. (2008) Formation of Archaean continental lithosphere and its diamonds: the root of the problem. *J. Geol. Soc.* **165**, 895-914

Pearson D.G. and Wittig N. (2013) The formation and evolution of cratonic mantle lithosphere—Evidence from mantle xenoliths. In *Treatise in Geochemistry, vol. 3, The Mantle* (ed. R.W. Carlson). Elsevier, Amsterdam, pp. 255-292

Pearson D.G., Carlson R.W., Shirey S.B., Boyd F.R. and Nixon P.H. (1995) The stabilisation of Archean lithospheric mantle: a Re-Os isotope study of peridotite xenoliths from the Kaapvaal craton, *Earth Planet. Sci. Lett.*, **134**, 341-357

Pearson D.G., Shirey S.B., Harris J.W. and Carlson R.W., (1998) Sulphide inclusions in diamonds from the Koffiefontein kimberlite, S Africa: constraints on diamond ages and mantle Re-Os systematics. *Earth Planet. Sci. Lett.* **160**, 311-326

Pearson D.G., Canil D., Shirey S.B., (2003) Mantle samples included in volcanic rocks: xenoliths and diamonds. In *Treatise in Geochemistry, vol. 2, The Mantle* (ed. R.W. Carlson). Elsevier, Amsterdam, pp. 171-276

Pearson D.G., Irvine G.J., Ionov D.A., Boyd F.R. and Dreibus G.E. (2004) Re-Os isotope systematics and platinum group element fractionation during mantle melt extraction: a study of massif and xenolith peridotite suites, *Chem. Geol.*, **208**, 29-59

Pearson D.G., Parman S.W. and Nowell G.M. (2007) A link between large mantle melting events and continent growth seen in osmium isotopes, *Nature*, **449**, 202-205

Peregoedova A., Barnes S.-J. and Baker D.R. (2004) The formation of Pt-Ir alloys and Cu-Pd-rich sulfide melts by partial desulfurization of Fe-Ni-Cu sulfides: results of experiments and implications for natural systems, *Chem. Geol.,* **208**, 247-264

Putnis A. (2002) An Introduction to Mineral Sciences, Cambridge University Press

Ranganai R.T., Kampunzu A.B., Atekwana A., Paya B.K., King J.G., Koosimile D.I. and Stettler E.H. (2002) Gravity evidence for a larger Limpopo Belt in southern Africa and geodynamic implications. *Geophys. J. Int.,* **149**, F9-F14

Reisberg L. and Lorand J.-P. (1995) Longevity of sub-continental mantle lithosphere from osmium isotope systematics in orogenic peridotite massifs, *Nature*, **376**, 159-162

Reisberg L. and Meisel T. (2002) The Re-Os Isotopic System: A review of analytical techniques, *Geostandard Newslett.,* **26**, 249-267

Richardson S.H., Shirey S.B., Harris J.W. and Carlson R.W. (2001) Archean subduction recorded by Re-Or isotopes in eclogitic sulfide inclusions in Kimberley diamonds. *Earth Planet. Sci. Lett.,* **191**, 257-266

Ringwood A. (1975) *Composition and Petrology of the Earth's Upper Mantle*, London: McGraw Hill.

de Ronde C.E.J. and de Wit M.J. (1994) Tectonic history of the Barberton greenstone beltm South Africa: 490 million years of Archean crustal evolution, *Tectonics*, **13**, 983-1005

Rudnick R.L. and Nyblade A.A. (1999) The thickness and heat production of Archean lithosphere: constraints from xenolith thermobarometry and surface heat flow. In: *Mantle Petrology: Field Observations and High Pressure Experimentation: A Tribute to Francis R. (Joe) Boyd* (Fei Y., Bertka C.M. and Mysen B.O., Eds.), The Geochemical Society Special Publications, 3-12

Rudnick R.L., McDonough W.L. and Orpin A. (1994) Northern Tanzanian peridotite xenoliths: a comparison with Kaapvaal peridotites and inferences on metasomatism interactions. In: *Kimberlites, Related Rocks and Mantle Xenoliths,* (Meyer H.O.A., and Leonardos O.H., Eds), CPRM Spec. Publ. Brazil, 336-353

Sambridge M. and Lambert D.D. (1997) Propagating errors in decay equations: Examples from the Re-Os isotopic system, *Geochim. Cosmochim. Acta*, **61**, 3019-3024

Schmitz M.D., Bowring S.A., de Wit M.J. and Gartz V. (2004) Subduction and terrane collision stabilize the western Kaapvaal craton tectosphere 2.9 billion years ago, *Earth Planet. Sci. Lett.,* **222**, 363-376

Simon N.S.C, Irvine G.J., Davies G.R., Pearson D.G. and Carlson R.W. (2003) The origin of garnet and clinopyroxene in depleted Kaapvaal peridotites. *Lithos*, **71**, 289-322

Simon N.S.C., Carlson R.W., Pearson, D.G. and Davies G.R. (2007) The origin and evolution of the Kaapvaal cratonic lithospheric mantle. *J. Petrol.* **48**, 589-625

Shirey S.B., Carlson R.W., Richardson S.H., Menzies A., Gurney J.J., Pearson D.G., Harris J.W. and Wiechert U. (2001) Archean emplacement of eclogitic components into the lithospheric mantle during formation of the Kaapvaal Craton. *Geophys. Res. Lett.* **28**, 2509-2512

Shirey S.B., Richardson S.H. and Harris J.W. (2004) Integrated models of diamond formation and craton evolution. *Lithos*, **77**, 923-944

Smith C.B. (1983) Pb, Sr and Nd isotopic evidence for sources of southern African Cretaceous kimberlites, *Nature*, **304**, 51-54

Smith C.B., Pearson D.G., Bulanova G.P., Beard A.D., Carlson R.W., Wittig N., Sims K., Lovemore C. and Muchemwa E. (2009) Extremely depleted lithospheric mantle and diamonds beneath the southern Zimbabwe Craton, *Lithos*, **112S**, 1120-1132

Smoliar M.I., Walker R.J. and Mrgan J.W. (1996) Re-Os Ages of Group IIA, IIIA, IVA, and IVB Iron Meteorites, *Science*, **271,** 1099-1102

Stiefenhofer J., Viljoen K.S. and Marsh J.S (1997) Petrology and Geochemistry of peridotite xenoliths from the Letlhakane kimberlites, Botswana. *Contrib. Mineral. Petrol.* **127**, 147-158

Stone W.E., Fleet M.E. and MacRae N.D. (1989) Two-phase nickeliferous monosulfide solid solution (mss) in megacrysts from Mount Shasta, California: A natural laboratory for nickel-copper sulfides. *Am. Mineral.* **74**, 981-993

Stowe C. W. (1989) The Proterozoic Magondi mobile belt in Zimbabwe; discussion. *S. Afr. J. Geol.* **92**, 69-71

Tainton K.M. and McKenzie D. (1994) The generation of kimberlites, lamproites, and their source rocks, *J. Petrol.*, **35**, 787-817

Taylor W.R. (1998) An experimental test of some geothermometer and geobarometer formulations for upper mantle peridotites with application to the thermobarometry of fertile lherzolite and garnet websterite. *N Jahrb Mineral Abh*, **172**, 381-408

Taylor P.N., Kramers J.D., Moorbath S., Wilson J.F., Orpen J.L. and Martin A. (1991) Pb-Pb, Sm-Nd and Rb-Sr geochronology in the Archean Craton of Zimbabwe. *Chem. Geol.* **87**, 175-196

Tredoux M., Lindsay M.N., Davies G. and McDonald I. (1995) The fractionation of platinum-group elements in magmatic systems, with the suggestion of a novel casual mechanism. *S. Afr. J. Geol.,* **98**, 157-167

Walker R.J., Carlson R.W., Shirey S.B. and Boyd F.R. (1989) Os, Sr, Nd, and Pb isotope systematics of southern African peridotite xenoliths: Implications for the chemical evolution of subcontinental mantle. *Geochim. Cosmochim. Acta,* **53**, 1583-1595

Walker R.J., Brandon A.D., Bird J.M., Piccoli P.M., McDonough W.F. and Ash R.D. (2005) ^{187}Os-^{186}Os systematics of Os-Ir-Ru alloy grains from southwestern Oregon, *Earth Planet. Sci. Lett.*, **230**, 211-226

Walter M.J. (1998) Melting of garnet peridotite and the origin of komatiite and depleted lithosphere, *J. Petrol*, **39**, 29-60

Wirth R., Reid D. and Schreiber A. (2013) Nanometer-sized platinum-group minerals (PGM) in base metal sulfides: New evidence for an orthomagmatic origin of the Merensky Reef PGE ore deposit, Bushveld Complex, South Africa, *Can. Mineral.,* **51**, 143-155

de Wit M.J., Roering C., Hart R.J., Armstrong R.A., de Ronde C.E.J., Green R.W.E., Tredoux M., Peberdy E. and Hart R.A. (1992) Fromation of an Archean continent, *Nature,* **357**, 553-562

Wittig N., Pearson D.G., Webb M., Ottley C.J., Irvine G.J., Kopylova M., Jensen S.M. and Nowell G.M. (2008) Origin of cratonic lithospheric mantle roots: A geochemical study of peridotites from the North Atlantic Craton, West Greenland, *Earth Planet. Sci. Lett.,* **274,** 24-33

Wohlgemuth-Ueberwasser C.C., Fonseca, R.O.C., Ballhaus C. and Berndt, J. (2013) Sulfide oxidation as a process for the formation of copper-rich minerals. *Miner. Deposita* **48**, 115-127

Yund R.A. and Kullerud G. (1966) Thermal stability of assemblages in the Cu-Fe-S system. *Ibid*, **7**, 454-488

Glossary of Terms

Base metal sulphides (BMS) sulphide minerals composed of Fe-Ni-Cu-S

Cc abbreviation for chalcocite, Cu_2S

Cp abbreviation for chalcopyrite, $CuFeS_2$

Cpx abbreviation for clinopyroxene

Cr# ratio of Cr and Al in a given sample (rock or mineral) utilising atomic compositions in the following the equation. Cr# = Cr / (Cr + Al) x 100

En determines how close a pyroxene is to the enstatite end-member, based on the atomic amounts of Mg, Fe and Ca. En = Mg / (Mg + Fe + Ca) x 100

Grt abbreviation for garnet

Harzburgite a sub-class of peridotite that is composed of olivine + orthopyroxene ± garnet ± spinel, and has an Al_2O_3 composition of <2%.

HFSE the high field strength elements, e.g. Zr, Hf

HSE the highly siderophile elements, e.g. Os, Ir, Pt, Pd, Re

HREE the heavy rare earth elements, Eu-Lu

Hz abbreviation for heazlewoodite, Ni_3S_2

Iss intermediate solid solution, composed of Cu-Ni-S±Fe

Lherzolite a sub-class of peridotite this is composed of olivine + orthopyroxene + clinopyroxene ± garnet ± spinel and has an Al_2O_3 composition >2%

LILE Large ion lithophile element, e.g. K, Rb, Ce, Sr, Ba

LREE the light-rare earth elements, La-Sm

Metal/Sulphur (M/S) the ratio of the metal portion of a sulphide to the sulphur in atomic %, i.e. (Fe + Ni + Cu + Co) / S

Metasomatism is the modification of the depleted mantle by the addition of elements, usually incompatible elements; this can either occur by fluids or melt. Metasomatism can occur to different extents: *cryptic* metasomatism is when the metasomatic agent does not modify the modal mineral content of the rock, but only slightly modifies the elements hosted by the minerals (e.g. addition of Fe to depleted forsteritic olivine). *Modal* metasomatism is the process where the metasomatic agent actively breaks down a primary mineral into different minerals (e.g. garnet + fluid = phlogopite + spinel + clinopyroxene + fluid), or adds minerals to the rock (e.g. clinopyroxene).

Mg# ratio of Mg and Fe in a given sample (rock or mineral) utilising atomic compositions in the following the equation. Mg# = Mg / (Mg + Fe) x 100

Mss abbreviation for Monosulphide solid solution, composed of Fe+Ni+S

Mt abbreviation for magnetite

N as a sub-script character, denotes concentration normalised to CI-chondrite

Ol abbreviation for olivine, $(Mg,Fe^{2+})_2SiO_4$

Opx abbreviation for orthopyroxene

Phl abbreviation for phlogopite, $KMg_3(AlSi_3O_{10})(OH,F)_2$

PGM abbreviation for platinum-group mineral

PM abbreviation for primitive mantle, as sub-script denotes concentration normalised to primitive mantle

Pn abbreviation for pentlandite, $(Fe,Ni)_9S_8$

Po abbreviation for pyrrhotite, FeS

REE the rare earth elements La-Lu

Sp abbreviation for spinel

Sulphur fugacity (fS_2) the activity of the available sulphur within a melt

Wo determines how close a pyroxene is to the wollastonite end-member, based on the atomic amounts of Mg, Fe and Ca. Wo = Ca / (Mg + Fe + Ca) x 100

XFs determines how close a pyroxene is to the ferrosilite end-member, based on the atomic amounts of Mg, Fe and Ca. XFs = Fe / (Mg + Fe + Ca) x 100

Acknowledgements

The first acknowledgement goes to my supervisor, Ambre Luguet. Thankfully, she took a chance on an Aussie girl she'd never even laid eyes on. Ambre opened up a whole new world of geochemical wonders to me, for which I will be forever grateful. I am also indebted to the help and advice given through-out my time in Bonn. I can honestly say she helped me think about things in a way I hadn't before.

To the committee members, Dr. Raúl Fonseca, Dr. Chris Ballhaus and Dr. Johannes Beck, thank you for taking the time to read this manuscript and being part of the process.

The scientific work obtained in this thesis would not have been possible without the help and support of so many people, thank you to everyone who in any way, shape, or form contributed to this thesis:

- Graham Pearson for generously supplying the Letlhakane peridotites for analysis and for his detailed and helpful feedback on manuscripts and abstracts.
- Phil Janney for allowing Ambre access to the mantle room for the selection of peridotites. Also, for taking the time to analysis the 22 Kaapvaal peridotites for trace elements, in what ended up being quite a rush, sorry for that!
- To my fellow Os-group colleagues, Alessandro Bragagni, Jude Coggon, Moritz Lissner, David van Acken and all the hewes, thank you for providing an awesome working environment and for allowing me to constantly bounce ideas off you, not to mention keeping the lab going and in tip top shape!
- Raúl Fonseca, thank you for many calibrations on the microprobe, countless laser shots and hours of conversation, both scientific and not.
- To Geoff Nowell for all your help in the analysis of osmium on a TIMS, and taking the time to explain to me how the machines work.
- Alex Hauser for the management of the element, and for not getting too exasperated every time I knocked on his door with yet another problem.
- Nils Jung, for making countless thin sections to my exacting specifications.
- Radegund Hoffbauer for the major element analysis, which was done so quickly!
- Anja Schreiber for four days of FIB work, in what ended up being a quite challenging task of extracting PGM!
- Sylvain Pont for a whole day spent looking for mostly non-existent PGM.
- Richard Wirth for the analyses with the HR-TEM.

On a personal note, special thanks to my family in supporting my move to the other side of world and for providing me with the tools to not only survive, but to thrive. Special thanks to Mortiz Lissner for acting as translator for all of the bureaucratic nonsense upon my arrival. To all the people who welcomed me with open arms upon my arrival and since (you know who you are!), you made my transition to this foreign land painless and easy. You have all gone on to make it my home. The countless people I have met and befriended over the past three years have made this the most amazing experience and have truly added to my life.

And finally, Freddi Kirst. You are my moonshine, the light that brightens the darkest hours. I am not sure what I would have done without your love and support, you helped keep this whole thing as painless as possible.

Ashlea.

Appendix

Table A.1. Trace element analysis of USGS standards.

	PCC-1		BIR-1		AGV-1	
	mean, n=4	%RSD	mean, n=8	%RSD	mean, n=4	%RSD
Sc (ppm)	7.6	4.5	41.4	1.7		
V (ppm)	26	4.8	353	2.3		
Cr (ppm)	2417	6.0	385	2.0		
Co (ppm)	74	5.1	46	4.3		
Ni (ppm)	1937	6.7	160.6	1.9		
Cu (ppm)	5.1	11.9	105.7	3.7		
Zn (ppm)	24	23.9	67	10.6		
Rb (ppm)			0.175	6.8	58.0	2.5
Ba (ppm)			6.08	0.7	1037	3.0
Nb (ppm)			0.53	4.9	13.3	3.3
La (ppm)			0.60	2.6	34.05	4.4
Ce (ppm)			1.91	1.0	61.26	1.5
Pr (ppm)			0.38	1.0	7.53	3.9
Sr (ppm)			100.9	1.4	687	4.0
Nd (ppm)			2.44	1.9	28.3	3.5
Sm (ppm)			1.14	2.5	5.31	4.2
Zr (ppm)			14.2	0.8	226	1.7
Eu (ppm)			0.491	1.8	1.41	3.5
Ti (ppm)	19.7	3.0	5679	1.2		
Gd (ppm)			1.74	1.8	4.21	2.7
Tb (ppm)			0.335	1.2	0.610	2.1
Dy (ppm)			2.43	1.3	3.29	2.5
Y (ppm)			15.5	0.7	19.3	3.1
Ho (ppm)			0.536	1.2	0.653	3.7
Er (ppm)			1.64	1.0	1.69	3.0
Th (ppb)			29	12.7	6307	4.0
U (ppb)			11.6	9.1	1871	2.8
Pb (ppb)			2631	2.2	36136	0.4
Tm (ppb)			240	1.5	234	4.5
Hf (ppb)			562	1.8	4859	1.3
Yb (ppb)			1574	1.3	1574	2.5
Lu (ppb)			256	2.2	246	6.1

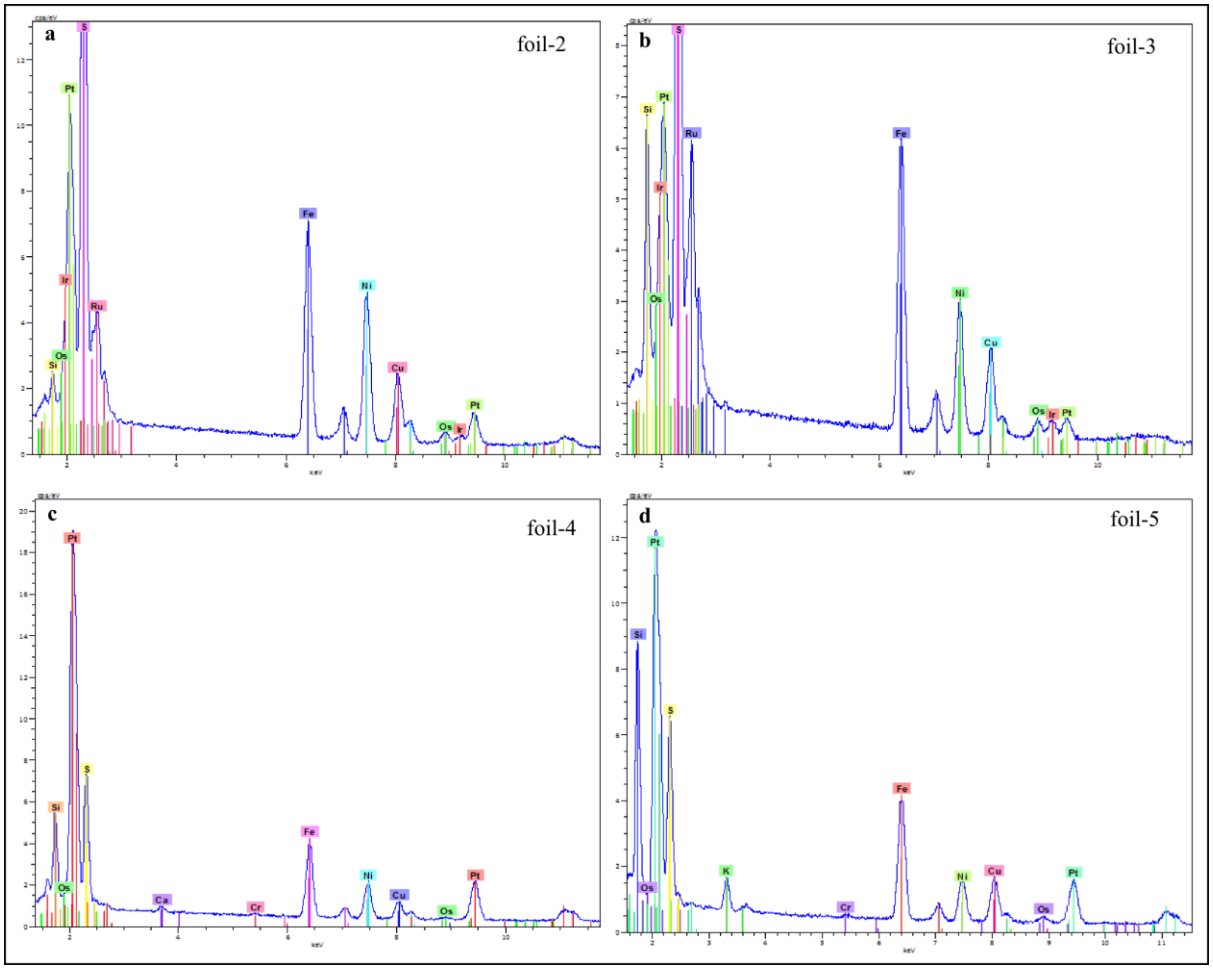

Figure A.1. EDS spectra from the FEG-SEM for the four analysed Pt-alloys. A small Os peak is resolvable in every spectra, signifying its presence.